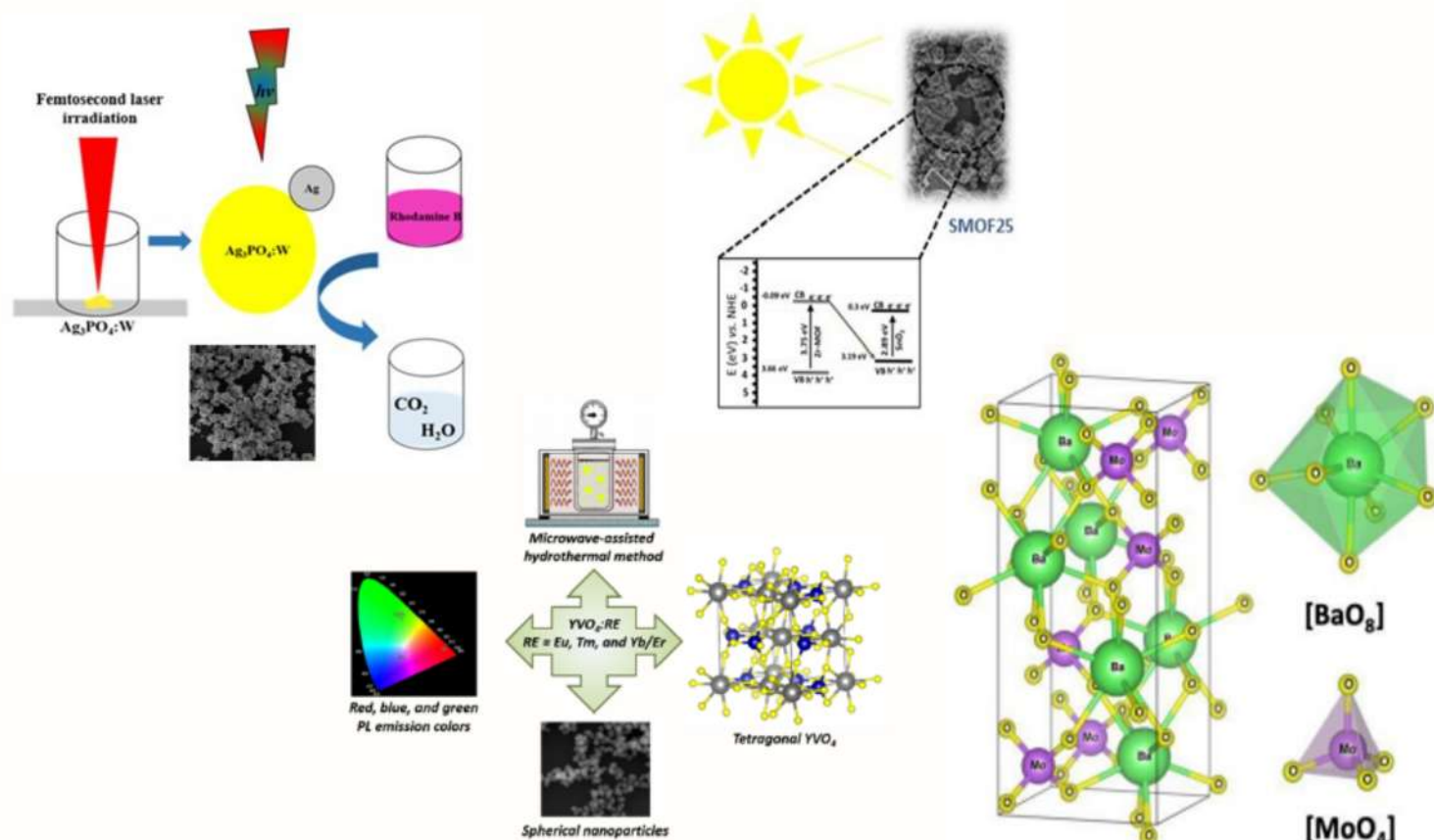


Eclética Química Journal

Volume 47 • special issue 1 • year 2022



Ag/Ag₃PO₄:W - photocatalytic activity

BaMoO₄ crystals - photocatalytic activity

TiO₂/Au catalyst - benzyl alcohol oxidation

Ca_{1-x}ZrO₃:Eu_x - luminescence and structural properties

YVO₄:rare earth NPs - photoluminescence application

Laser-irradiated α -Fe₂O₃ - MB dye discoloration

BNZ@BNNT, BNZ@CNT complexes - quantum chemistry study

Coupling Zr-MOF and SnO₂ - photoelectrode in solar cell

Pumpkin seeds - activated carbon for ORP applications

Cu-doped TiO₂ - structural and photocatalytic properties



UNIVERSIDADE ESTADUAL PAULISTA

Reitor

Pasqual Barretti

Vice-Reitora

Maysa Furlan

Pró-Reitora de Graduação

Celia Maria Giacheti

Pró-Reitora de Pós-Graduação

Maria Valnice Boldrin

Pró-Reitor de Pesquisa

Edson Cocchieri Botelho

Pró-Reitor de Extensão Universitária e Cultura

Raul Borges Guimarães

Pró-Reitor de Planejamento Estratégico e Gestão

Estevão Tomomitsu Kimpara



INSTITUTO DE QUÍMICA

Diretor

Sidney José Lima Ribeiro

Vice-Diretora

Denise Bevilaqua

Editorial Team

Editor-in-Chief

Prof. Assis Vicente Benedetti, São Paulo State University, Institute of Chemistry, Araraquara, Brazil

Editors Section

Prof. Dr. Elson Longo, São Paulo State University, Institute of Biosciences, Languages and Exact Sciences, São José do Rio Preto, Brazil

Prof. Dr. Juan Manuel Andrés Bort, University Jaume I, Department of Physical and Analytical Chemistry, Castelló, Spain.

Editors

Prof. Antonio Eduardo Mauro, São Paulo State University, Institute of Chemistry, Araraquara, Brazil

Prof. Horacio Heinzen, University of the Republic, Faculty of Chemistry, Montevideo, Uruguay

Prof. Marcos Carlos de Mattos, Federal University of Ceará, Center of Sciences, Fortaleza, Brazil

Prof. Maria Célia Bertolini, São Paulo State University, Institute of Chemistry, Araraquara, Brazil

Prof. Patrícia Hatsue Suegama, Federal University of Grande Dourados, Faculty of Exact and Technological Sciences, Dourados, Brazil

Prof. Paulo Clairmont Feitosa Lima Gomes, São Paulo State University, Institute of Chemistry, Araraquara, Brazil

Editorial Board

Prof. Bayardo Baptista Torres, University of São Paulo, Institute of Chemistry, São Paulo, Brazil

Prof. Enric Brillas, University of Barcelona, Faculty of Chemistry, Barcelona, Spain

Prof. Francisco de Assis Leone, University of São Paulo, Faculty of Philosophy, Sciences and Literature, Ribeirão Preto, Brazil

Prof. Ivano Gerardt Rolf Gutz, University of São Paulo, Institute of Chemistry, São Paulo, Brazil

Prof. Jairton Dupont, Federal University of Rio Grande do Sul, Institute of Chemistry, Porto Alegre, Brazil

Prof. José Antônio Maia Rodrigues, University of Porto, Faculty of Sciences, Porto, Portugal

Prof. Lauro Kubota, University of Campinas, Institute of Chemistry, São Paulo, Brazil

Prof. Massuo Jorge Kato, University of São Paulo, Institute of Chemistry, São Paulo, Brazil

Prof. Roberto Santana da Silva, University of São Paulo, Faculty of Pharmaceutical Sciences, Ribeirão Preto, Brazil

Prof. Verónica Cortés de Zea Bermudez, University of Trás-os-Montes and Alto Douro, School of Life and Environmental Sciences, Vila Real, Portugal

EDITORIAL PRODUCTION

Ctrl K Produção Editorial – Araraquara, Brazil

digite@ctrlk.com.br

Editorial

On May 18, 2016, the science and technology lost a real giant—José Arana Varela, who passed away at age 72. Describing him as a *giant* does not do justice to the scientist, the professor, the mentor, and the human being. It is with great pleasure that we write the preface to the Eclética Química Journal in honor of Professor José Varela. He was a close colleague, a collaborator, and, above all, a friend for nearly 50 years. This opportunity represents just an excellent excuse to celebrate a most remarkable physicist who has always been far ahead of his time, thanks to a unique combination of scientific visions, creativity, breadth, drive, and dedication. Rather than describing José's distinguished academic career, here we highlight different aspects, which we believe have given it particular impact.

Varela was born in Martinópolis, São Paulo, Brazil, on April 11, 1944, and left this world in his long-time home of Araraquara, São Paulo. Obviously, a lot of things happened in between, but this editorial is going to focus on the recollections of this giant as seen through his former colleagues and friends. He held a degree in Physics from the University of São Paulo (1968), a Master's degree in Physics from the Instituto Tecnológico de Aeronáutica (1975) and a PhD in Ceramic Materials from the University of Washington (1981). He published over 500 articles in international journals. He developed more than 35 projects and agreements with governments: federal and state and also with companies. He supervised and co-supervised more than 50 theses and dissertations. He received more than 20 awards and honorable mentions, including the Golden Epsilon Award from the Spanish Society of Ceramics and Glass. He worked on a strong exchange with national and international research institutions in Spain, France, USA, Slovenia and Italy. He focused his research in Materials and Metallurgical Engineering, with emphasis on Ceramics, worked mainly on the following topics: thin films, ferroelectric and dielectric materials, varistors, grain boundary properties and sintering.

José Varela was a true innovator who opened numerous new fields of research. A major strength of his scientific approach has always been to precisely demonstrate with rigorous methodologies and simple examples new notions, and to put these notions in much broader perspectives—often inspired by philosophy and arts—to generate paradigms of deep impact. From early works dedicated to sintering and electronic ceramics, to those of us who considered Varela a cherished friend, the fire of science burned brightly within him until the very end. To those of us who considered Varela a cherished friend, the fire of science burned brightly within him until the very end. Many of his colleagues have described him as a force of nature, which indeed he was. He was determined to do cutting edge science each and every day, even toward the end of his life. Amazingly, even several months before his death, at the ripe young age of 71, he was planning on the next project and the meeting with friend to drink a good wine. To his friends and students, Varela will be sorely missed. He was a role model who showed us not only how to be a great scientist but also a wonderful human being. He inspired us by his devotion to his craft and his passion to unlock one of the secrets of nature. He never gave up; he was passionate and truly lived a remarkable life that serves as a shining example to all his colleagues and friends.

Opening this issue the preparation of a W-doped Ag_3PO_4 with high photocatalytic activity by the chemical coprecipitation method and irradiated with a femtosecond laser (FL) is described. A higher structural disorder in the $[\text{PO}_4]$ clusters was observed for the FL irradiated sample ($\text{Ag}_3\text{PO}_4\text{:W-FL}$), indicating the formation of Ag metallic from the Ag_3PO_4 structure. The photocatalytic activity of the samples was studied by photodegradation of rhodamine B under visible light irradiation. The formation of Ag nanoparticles on the surface of $\text{Ag}_3\text{PO}_4\text{:W}$ led to a degradation rate constant 3.54 times higher than the nonirradiated sample. Follow, it is described the catalytic potential of titanium oxide (TiO_2) and gold doped titanium oxide nanoparticles applied to the selectivity benzyl alcohol oxidation. A composite nanomaterial was obtained with high synergy between gold and TiO_2 nanoparticles, resulting in high catalytic activity and selectivity for benzaldehyde formation. Selective oxidation of alcohols is one of the most significant transformations of organic chemistry since it is essential for industrial intermediates production. The next article describes the synthesis of $\text{YVO}_4\text{:RE}$ (RE = Eu, Tm, and Yb/Er) nanoparticles using the microwave-assisted hydrothermal method. Different characterization techniques have been employed to examine the structural, optical,

as well as its morphology and the photoluminescence (PL) emissions. The as-synthesized samples present different emission colors due to RE^{3+} ions, as well as nanosized spherical morphology. These materials are efficient for optical devices. Afterwards, it is presented the quantum chemistry methods used to study a boron nitride nanotube (BNNT) and a carbon nanotube (CNT) as possible carrier agents for the antichagasic benzimidazole (BNZ) to improve its water solubility and bioavailability in the organism. For the BNZ@BNNT complex, it was possible to note short interactions, at a distance of 0.215 nm, between hydrogen atoms from BNZ and nitrogen atoms from BNNT. Overall, the results demonstrate that the BNNT is a better candidate to be used as a carrier agent for BNZ than the CNT due to its higher structural and chemical stability, lower binding energy and lower solvation enthalpy. In the sequence, the production of activated carbon (AC) from pumpkin seeds by simultaneous carbonization activation for occupational respiratory protection is described. The AC is derived from carbonaceous sources and used as a technological element for various industrial purposes. Due to this context and to enhance sustainability concepts and human health in the production of materials, this study aimed to produce activated carbon from an abundant agricultural waste in northeast Brazil through a route that not only favors its simultaneous carbonization and activation but also its thermal neutralization, enhancing sustainability concepts and human health in the production of materials. The AC showed yields between 73%-78% and adsorption capacity and selectivity to ammonia gas. The morphology varied in function of the biomass interaction with the type and concentration of acid used. Follow, the readers find a study of surfactant effects in the morphology and the photocatalytic activity of the $BaMoO_4$ crystals where experimental techniques were applied to investigate the order-disorder degree of samples. The morphologies were investigated by field emission scanning electron microscopy, and the theoretical crystal morphologies were obtained through the Wulff construction. The photocatalytic activity efficiency of the $BaMoO_4$ crystals were tested against the rhodamine (RhB) dye. $BaMoO_4$ synthesized with the surfactant sodium dodecyl sulfate presented a monophasic crystal with a disordered structure. The presence of surfactant generated pores on the surfaces of the material that were responsible for the appearance of the adsorptive ability enhancing the adsorption process of the RhB dye in the absence of ultraviolet light. Subsequently, the influence of Eu^{3+} cations in the host matrix of $CaZrO_3$ is discussed by analyzing the luminescence and structural properties. The $Ca_{1-x}ZrO_3:Eu_x$ crystals were obtained by a simple sol-gel method followed by a soft thermal treatment without any surfactant. The structural characterization at short-, medium- and long-distance allowed to observe the effect of the dopant in the host matrix. The luminescence profile of the sample was investigated by analyzing the excitation and emission spectrum monitoring the emission at 614 nm and excited at 394 nm, noting that the sample Eu-doped with 0.08 mol% has greater emission intensity. The color variations of the characteristic emissions of $Ca_{1-x}ZrO_3:Eu_x$ crystals were evaluated according to the Commission Internationale de L'Éclairage, observing a red shift for all Eu-doped samples. A general luminescence scheme was proposed combining the density of state and the band structure calculations. Nowadays, the disposal of polluting substances, such as methylene blue (MB) dye, into wastewater, arouses the interest of technologies to remove these pollutants. Here, Fe_2O_3 was obtained by the conventional hydrothermal process and heat-treatment, subsequently FL-irradiated treatment. The mixture of irradiated $\alpha-Fe_2O_3$ and $\epsilon-Fe_2O_3$ phases revealed lower crystallinity than irradiated $\alpha-Fe_2O_3$ samples that together with the increase in crystallinity were crucial to improve the performance of $\alpha-Fe_2O_3$ irradiated sample in the discoloration of MB, reaching 90% in 75 min of dye solution exposure under UV irradiation. This result was attributed to the increase in active sites due to the density of defects generated, which enhance the degradation process. The next work describes the effect of coupling the Zr-metal-organic frameworks (MOFs) and SnO_2 and its potential for application as photoelectrode in solar cells. Coupling was performed by mechanical mixture followed by heat treatment and the effect of adding two amounts of Zr-MOF (25 and 50 wt%) on morphology and photoelectrochemical properties were investigated. The J-V curves show that the coupling of 25 wt% Zr-MOFs with SnO_2 improves the charge transfer characteristics under light irradiation 1.6 times compared to the pure SnO_2 . Completes this issue the research concerning the modifications of materials for improvement of its photocatalytic activity that has been widely increased due to the potential of heterogeneous photocatalysis for wastewater treatment. One of the most employed methods is the metal doping process into semiconductors, which allows the modification of their electronic structure. As observed by XRD and

Raman results, the Cu insertion into TiO₂ structure induced the stabilization of anatase phase, increasing its content in the samples in relation to the bare TiO₂. The photoluminescence spectroscopy (PL) results indicated that the Cu insertion into TiO₂ promoted a decrease in the PL emission intensity and a shift of the emission band to the blue region. The photocatalytic activity of the samples for RhB degradation under UV light irradiation indicated that the Cu-doping into TiO₂ led to an enhancement of the photocatalytic activity compared to the bare sample.

Prof. Dr. Elson Longo (Guest Editor)

Prof. Dr. Juan Manuel Andrés Bort (Guest Editor)

Editor's note

The Eclética Química Journal has a line in its scope to publish special issues in honor of scientists with relevant contributions to the scientific and technological development in Chemistry and related areas. Prof. José Arana Varela joined the Instituto de Química-UNESP, Araraquara, in 1980, coming from the Presidente Prudente Campus of UNESP, initially dedicating himself to the creation of a multidisciplinary research group, the coordination and development of several research projects in ceramic materials, thin films, ferroelectrics, dielectrics, varistors, refractories, sintering processes and chemical routes for the preparation of ceramic materials (Pechini method). All these actions have stimulated the creation of the Graduate Program in Physical Chemistry at IQ-UNESP. He worked together with other professors from the Araraquara Campus in the design and assembly of several modernly equipped research laboratories. He actively participated in the process of unifying the various graduate courses at the Instituto de Química, currently the Graduate Course in Chemistry, of which he was coordinator. He has held several administrative positions at the Instituto de Química and UNESP, all of them of special relevance to scientific development and technological innovation. He also participated in scientific-administrative activities in various development agencies, especially FAPESP, in scientific journals as a reviewer and member of the editorial board and he stood out as a researcher in the national and international scientific community that earned him several national and international awards. So, this special issue intends to pay a simple tribute to Prof. Varela and aims to recognize its enormous scientific contribution at the national and international levels as well as thank him for his dedication, teachings and collaboration in the training of qualified human resources in science and technology, and also for his futuristic vision of the materials area. It contains scientific contributions from collaborators and colleagues of Prof. Varela, especially on preparation of a W-doped Ag_3PO_4 with high photocatalytic activity, the catalytic potential of titanium oxide (TiO_2) and gold doped titanium oxide nanoparticles, quantum chemistry methods in studying boron nitride nanotube and carbon nanotube as carrier agent for the antichagasic benzimidazole, the production of activated carbon from pumpkin seeds by simultaneous carbonization activation for occupational respiratory protection, surfactant effects in the morphology and photocatalytic activity of the BaMoO_4 crystals, the influence of Eu^{3+} cations in the host matrix of CaZrO_3 by analyzing the luminescence and structural properties, Fe_2O_3 preparation by hydrothermal process, heat-treatment followed by femtosecond laser-irradiation and use in depolluting wastewater, the effect of coupling the Zr-metal-organic frameworks and SnO_2 as promising applications as photoelectrode in solar cells and materials modifications for improving the photocatalytic activity for wastewater treatment. The articles published here followed all the standard procedures used by the Eclética Química Journal and fulfilled all the qualitative requirements of selection, peer review and editing.

Prof. Dr. Assis Vicente Benedetti
Editor-in-Chief

Citation databases: Eclética Quim. J. is indexed



*Click on the images to follow the links.

EBSCO has no link available. The address is for subscribers only.

INSTRUCTIONS FOR AUTHORS

BEFORE YOU SUBMIT

1. Check *Eclét. Quim. J.*'s focus and scope

Eclética Química Journal is a peer-reviewed quarterly publication of the Institute of Chemistry of São Paulo State University (UNESP). It publishes original researches as articles, reviews and short reviews in **all areas of Chemistry**.

2. Types of papers

- a. Original articles
- b. Reviews
- c. Short reviews
- d. Communications
- e. Technical notes
- f. Articles in education in chemistry and chemistry-related areas

Manuscripts submitted for publication as full articles and communications must contain original and unpublished results and should not have been submitted elsewhere either partially or whole.

a. Original articles

The manuscript must be organized in sections as follows:

1. Introduction
 2. Experimental
 3. Results and Discussion
 4. Conclusions
- References

Sections titles must be written in bold and sequentially numbered; only the first letter should be in uppercase letter. Subsections, numbered as exemplified, should be written in normal and italic letters; only the first letter should be in uppercase letter.

Example:

1. Introduction

1.1 History

2. Experimental

2.1 Surface characterization

2.1.1 Morphological analysis

b. Reviews

Review articles should be original and present state-of-the-art overviews in a coherent and concise form covering the most relevant aspects of the topic that is being revised and indicate the likely future directions of the field. Therefore,

before beginning the preparation of a Review manuscript, send a letter (one page maximum) to the Editor with the subject of interest and the main topics that would be covered in the Review manuscript. The Editor will communicate his decision in two weeks. Receiving this type of manuscript does not imply acceptance to be published in **Eclet. Quím. J.** It will be peer-reviewed.

c. Short reviews

Short reviews should present an overview of the state-of-the-art in a specific topic within the scope of the Journal and limited to 5,000 words. Consider a table or image as corresponding to 100 words. Before beginning the preparation of a Short Review manuscript, send a letter (one page maximum) to the Editor with the subject of interest and the main topics that would be covered in the Short Review manuscript.

d. Communications

Communications should cover relevant scientific results and are limited to 1,500 words or three pages of the Journal, not including the title, authors' names, figures, tables and references. However, Communications suggesting fragmentation of complete contributions are strongly discouraged by Editors.

e. Technical notes

Descriptions of methods, techniques, equipment or accessories developed in the authors' laboratory, as long as they present chemical content of interest. They should follow the usual form of presentation, according to the peculiarities of each work. They should have a maximum of 25 pages, including figures, tables, diagrams, etc.

f. Articles in education in chemistry and chemistry-correlated areas

Research manuscript related to undergraduate teaching in Chemistry and innovative experiences in undergraduate and graduate education. They should have a maximum of 25 pages, including figures, tables, diagrams, and other elements.

3. Special issues

Special issues with complete articles dedicated to Symposia and Congresses and to special themes or in honor of scientists with relevant contributions in Chemistry and correlate areas can be published by **Eclet. Quím. J.** under the condition that a previous agreement with Editors is established. All the guides of the journal must be followed by the authors.

4. Approval

Ensure all authors have seen and approved the final version of the article prior to submission. All authors must also approve the journal you are submitting to.

ETHICAL GUIDELINES

Before starting the submission process, please be sure that **all ethical aspects mentioned below were followed.** Violation of these ethical aspects may preclude authors from submitting or publishing articles in **Eclet. Quím. J.**

a. Coauthorship: The corresponding author is responsible for listing as coauthors only researchers who have really taken part in the work, for informing them about the entire manuscript content and for obtaining their permission to submit and publish it.

b. Nonauthors: Explicit permission of a nonauthor who has collaborated with personal communication or discussion to the manuscript being submitted to **Eclet. Quím. J.** must be obtained before being cited.

c. Unbiased research: Authors are responsible for carefully searching for all the scientific work relevant to their reasoning irrespective of whether they agree or not with the presented information.

d. Citation: Authors are responsible for correctly citing and crediting all data taken from other sources. This requirement is not necessary only when the information is a result of the research presented in the manuscript being submitted to **Eclet. Chem. J.**

e. Direct quotations: The word-for-word reproduction of data or sentences as long as placed between quotation marks and correctly cited is not considered ethical deviation when indispensable for the discussion of a specific set of data or a hypothesis.

f. Do not cite: Master's Degree dissertations and PhD theses are not accepted; instead, you must cite the publications resulted from them.

g. Plagiarism: Plagiarism, self-plagiarism, and the suggestion of novelty when the material was already published are unaccepted by **Eclet. Quím. J.** Before reviewing a manuscript, the **Turnitin antiplagiarism software** will be used to detect any ethical deviation.

h. Simultaneous submissions of the same manuscript to more than one journal is considered an ethical deviation and is conflicted to the declaration has been done below by the authors.

i. Studies with humans or other animals: Before submitting manuscripts involving human beings, materials from human or animals, the authors need to confirm that the procedures established, respectively, by the institutional committee on human experimentation and Helsinki's declaration, and the recommendations of the animal care institutional committee were followed. Editors may request complementary information on ethical aspects.

COPYRIGHT NOTICE

The corresponding author transfers the copyright of the submitted manuscript and all its versions to **Eclet. Quím. J.**, after having the consent of all authors, which ceases if the manuscript is rejected or withdrawn during the review process.

When a published manuscript in **Eclet. Quím. J.** is also published in other Journal, it will be immediately withdrawn from **Eclet. Quím. J.** and the authors informed of the Editor decision.

Self-archive to institutional, thematic repositories or personal webpage is permitted just after publication. The articles published by **Eclet. Quím. J.** are licensed under the **Creative Commons Attribution 4.0 International License**.

PUBLICATION CHARGES

Eclética Química Journal is supported by the Institute of Chemistry/UNESP and publication is free of charge for authors.

MANUSCRIPT PREPARATION

COVER LETTER

We provide a template to help you prepare your cover letter. To download it, click [here](#).

The cover letter **MUST** include:

1. Identification of authors

- a. The authors' full names (they must be written in full and complete, separated by comma)

João M. José	Incorrect
J. M. José	Incorrect
João Maria José	Correct!

- b. E-mail addresses and affiliations (**neither more nor less than two instances**) of all authors;
c. ORCID ID links;
d. A plus sign (+) indicating the corresponding author.

Example:

Author Full Name¹⁺, Author Full Name²

1. University, Faculty or Institute, City, Country.
2. Company, Division or Sector or Laboratory, City, Country.

+ Author 1: address@mail.com, ORCID: <https://orcid.org/xxxx-xxxx-xxxx-xxxx>

Author 2: address@mail.com, ORCID: <https://orcid.org/xxxx-xxxx-xxxx-xxxx>

2. Authors' contribution

We request authors to include author contributions according to CRediT taxonomy standardized contribution descriptions. **CRediT (Contributor Roles Taxonomy)** is a high-level taxonomy, including 14 roles, that can be used to represent the roles typically played by contributors to scientific scholarly output. The roles describe each contributor's specific contribution to the scholarly output.

- a. Please, visit this link (<https://casrai.org/credit/>) to find out which role(s) the authors fit into;
- b. Do not modify the role names; do not write "all authors" in any role. Do not combine two or more roles in one line.**
- c. If there are any roles that no author has engaged in (such as funding in papers that were not funded), write "Not applicable" in front of the name of the role;
- d. Write the authors' names according to the **American Chemistry Society (ACS) citation style**.

Example:

Conceptualization: Foster, J. C.; O'Reilly, R. K.

Data curation: Varlas, S.; Couturaud, B.; Coe, J.; O'Reilly, R. K.

Formal Analysis: Foster, J. C.; Varlas, S.

Funding acquisition: Not applicable.

Investigation: Foster, J. C.; O'Reilly, R. K.

Methodology: Coe, J.; O'Reilly, R. K.

Project administration: O'Reilly, R. K.

Resources: Coe, J.

Software: Not applicable.

Supervision: O'Reilly, R. K.

Validation: Varlas, S.; Couturaud, B.

Visualization: Foster, J. C.

Writing – original draft: Foster, J. C.; Varlas, S.; Couturaud, B.; Coe, J.; O'Reilly, R. K.

Writing – review & editing: Foster, J. C.; Varlas, S.; Couturaud, B.; Coe, J.; O'Reilly, R. K.

4. Indication of reviewers

We kindly ask the authors to suggest **five** suitable reviewers, providing full name, affiliation, and email.

5. Other information

- a. The authors must write one paragraph remarking the novelty and relevance of the work;
- b. The corresponding author must declare, on behalf of the other authors, that the manuscript being submitted is original and its content has not been published previously and is not under consideration for publication elsewhere;
- c. The authors must inform if there is any conflict of interest.

6. Acknowledgements and funding

Acknowledgements and funding information will be requested after the article is accepted for publication.

7. Data availability statement

A data availability statement informs the reader where the data associated with your published work is available, and under what conditions they can be accessed. Therefore, authors must inform if:

Data will be available upon request;

All dataset were generated or analyzed in the current study; or

Data sharing is not applicable.

MANUSCRIPT

We provide a template to help you prepare your manuscript. To download it, click [here](#).

1. General rules

Only manuscripts written in English will be accepted. British or American usage is acceptable, but they should not be mixed. Non-native English speakers are encouraged to have their manuscripts professionally revised before submission.

Manuscripts must be sent in editable files as *.doc, *.docx or *.odt. The text must be typed using font style Times New Roman and size 12. Space between lines should be 1.5 mm and paper size A4, top and bottom margins 2.5 cm, left and right margins 2.0 cm.

All contributions must include an **abstract** (170 words maximum), **three to five keywords** and a **graphical abstract** (8 cm wide × 8 cm high).

Supplementary information: all type of articles accepts supplementary information (SI) that aims at complementing the main text with material that, for any reason, cannot be included in the article.

TITLE

The title should be concise, explanatory and represent the content of the work. The title must have only the first letter of the sentence in uppercase. The following are not allowed: acronyms, abbreviations, geographical location of the research, en or em dashes (which must be replaced by a colon). Titles do not have full point.

ABSTRACT

Abstract is the summary of the article. The abstract must be written as a running text not as structured topics, but its content should present background, objectives, methods, results, and conclusion. It cannot contain citations. The text should be written in a single paragraph with a **maximum of 170 words**.

KEYWORDS

Keywords are intended to make it easier for readers to find the content of your text. As fundamental tools for database indexing, they act as a gateway to the text. The correct selection of keywords significantly increases the chances that a document will be found by researchers on the topic, and consequently helps to promote the visibility of an article within a myriad of publications.

FIGURES, TABLES AND EQUATIONS

Figures, tables and equations must be written with initial capital letter followed by their respective number and period, in bold, without adding zero “**Table 1**”, preceding an explanatory title. Tables, Figures and Equations should appear after the first citation and should be numbered according to the ascending order of appearance in the text (1, 2, 3...).

Figures, tables, schemes and photographs already published by the same or different authors in other publications may be reproduced in manuscripts of **Eclet. Quim. J.** only with permission from the editor house that holds the copyright.

Nomenclature, abbreviations, and symbols should follow IUPAC recommendations.

DATA AVAILABILITY STATEMENT

The data availability statement informs the reader where the data associated with your work is available, and under what conditions they can be accessed. They also include links (where applicable) to the data set.

- a. The data are available in a data repository (cite repository and the DOI of the deposited data);
- b. The data will be available upon request;
- c. All data sets were generated or analyzed in the current study;
- d. Data sharing is not applicable (in cases where no data sets have been generated or analyzed during the current study, it should be declared).

GRAPHICAL ABSTRACT

The graphical abstract must summarize the manuscript in an interesting way to catch the attention of the readers. As already stated, it must be designed with 8 cm wide × 8 cm high, and a 900-dpi resolution is mandatory for this journal. It must be submitted as *.jpg, *.jpeg, *.tif or *.ppt files as supplementary file.

We provide a template to help you prepare your GA. To download it, click [here](#).

SUPPLEMENTARY INFORMATION

When appropriate, important data to complement and a better comprehension of the article can be submitted as Supplementary File, which will be published online and will be made available as links in the original article. This might include additional figures, tables, text, equations, videos or other materials that are necessary to fully document the research contained in the paper or to facilitate the readers' ability to understand the work.

Supplementary material should be presented in appropriate .docx file for text, tables, figures and graphics. All supplementary figures, tables and videos should be referred in the manuscript body as "Table S1, S2...", "Fig. S1, S2..." and "Video S1, S2 ...".

At the end of the main text the authors must inform: This article has supplementary information.

Supplementary information will be located following the article with a different DOI number from that of the article, but easily related to it.

CITATION STYLE GUIDE

From 2021 on, the **Eclet. Quim. J.** will follow the **ACS citation style**.

Indication of the sources is made by authorship and date. So, the reference list is organized alphabetically by author.

Each citation consists of two parts: the in-text citation, which provides brief identifying information within the text, and the reference list, a list of sources that provides full bibliographic information.

We encourage the citation of primary research over review articles, where appropriate, in order to give credit to those who first reported a finding. Find out more about our commitments to the principles of **San Francisco Declaration on Research Assessment (DORA)**.

What information you must cite?

- a. Exact wording taken from any source, including freely available websites;
- b. Paraphrases of passages;
- c. Summaries of another person's work;
- d. Indebtedness to another person for an idea;
- e. Use of another researchers' work;
- f. Use of your own previous work.

You do not need to cite **common knowledge**.

Example:

Water is a tasteless and odorless liquid at room temperature (common knowledge, no citation needed)

In-text citations

You can choose to cite your references within or at the end of the phrase, as showed below.

Within the cited information:

One author: Finnegan (2004) states that the primary structure of this enzyme has also been determined.
Two authors: Finnegan and Roman (2004) state that the structure of this enzyme has also been determined.
Three or more authors: Finnegan *et al.* (2004) state that the structure of this enzyme has also been determined.

At the end of the cited information:

One author: The primary structure of this enzyme has also been determined (Finnegan, 2004).
Two authors: The primary structure of this enzyme has also been determined (Finnegan and Roman, 2004).
Three or more authors: The primary structure of this enzyme has also been determined (Finnegan *et al.*, 2004).

If you need to cite more than one reference in the same brackets, separate them with semicolon and write them in alphabetic order:

The primary structure of this enzyme was determined (Abel *et al.*, 2011; Borges, 2004; Castro *et al.*, 2021).

Bibliographic references

Article from scientific journals

Foster, J. C.; Varlas, S.; Couturaud, B.; Coe, J.; O'Reilly, R. K. Getting into Shape: Reflections on a New Generation of Cylindrical Nanostructures' Self-Assembly Using Polymer Building Block. *J. Am. Chem. Soc.* **2019**, *141* (7), 2742–2753. <https://doi/10.1021/jacs.8b08648>

Book

Hammond, C. *The Basics of Crystallography and Diffraction*, 4th ed.; International Union of Crystallography Texts on Crystallography, Vol. 21; Oxford University Press, 2015.

Book chapter

Hammond, C. Crystal Symmetry. In *The Basics of Crystallography and Diffraction*, 4th ed.; International Union of Crystallography Texts on Crystallography, Vol. 21; Oxford University Press, 2015; pp 99–134.

Book with editors

Mom the Chemistry Professor: Personal Accounts and Advice from Chemistry Professors Who Are Mothers, 2nd ed.; Woznack, K., Charlebois, A., Cole, R. S., Marzabadi, C. H., Webster, G., Eds.; Springer, 2018.

Website

ACS Publications Home Page. <https://pubs.acs.org/> (accessed 2019-02-21).

Document from a website

American Chemical Society, Committee on Chemical Safety, Task Force for Safety Education Guidelines. *Guidelines for Chemical Laboratory Safety in Academic Institutions*. American Chemical Society, 2016. <https://www.acs.org/content/dam/acsorg/about/governance/committees/chemicalsafety/publications/acs-safety-guidelines-academic.pdf> (accessed 2019-02-21).

Conference proceedings

Nilsson, A.; Petersson, F.; Persson, H. W.; Jönsson, H. Manipulation of Suspended Particles in a Laminar Flow. In *Micro Total Analysis Systems 2002, Proceedings of the μ TAS 2002 Symposium*, Nara, Japan, November 3–7, 2002; The Netherlands, 2002; pp 751–753. https://doi.org/10.1007/978-94-010-0504-3_50

Governmental and legislation information

Department of Commerce, United States Patent and Trademark Office. Section 706.02 Rejection of Prior Art [R-

07.2015]. *Manual of Patent Examining Procedure (MPEP)*, 9th ed., rev. 08.2017, last revised January 2018. <https://www.uspto.gov/web/offices/pac/mpep/s706.html#d0e58220> (accessed 2019-03-20).

Patent

Lois-Caballe, C.; Baltimore, D.; Qin, X.-F. Method for Expression of Small RNA Molecules within a Cell. US 7 732 193 B2, 2010.

Streaming data

American Chemical Society. Game of Thrones Science: Sword Making and Valyrian Steel. *Reactions*. YouTube, April 15, 2015. <https://www.youtube.com/watch?v=cHRcGoje4j4> (accessed 2019-02-28).

For more information, you can access the [ACS Style Quick Guide](#) and the [Williams College LibGuides](#).

SUBMITTING YOUR MANUSCRIPT

The corresponding author should submit the manuscript online by [clicking here](#). If you are a user, register by [clicking here](#).

At the **User home** page, click in **New submission**.

In Step 1, select a section for your manuscript, verify one more time if you followed all these rules in **Submission checklist**, add Comments for the Editor if you want to, and click Save and continue.

In Step 2, you will **upload your manuscript**. Remember it will pass through a double-blind review process. So, do not provide any information on the authorship.

In Step 3, enter **submission's metadata**: authors' full names, valid e-mail addresses and ORCID ID links (with "http" not "https"). Add title, abstract, contributors and supporting agencies, and the list of references.

In Step 4, upload the **cover letter**, the **graphical abstract** and other **supplementary material** you want to include in your manuscript.

In Step 5, you will be able to check all submitted documents in the **File summary**. If you are certain that you have followed all the rules until here, click in **Finish submission**.

REVIEW PROCESS

The time elapsed between the submission and the first response of the reviewers is around three months. The average time elapsed between submission and publication is around seven months.

Resubmission (manuscripts "rejected in the present form" or subjected to "revision") must contain a letter with the responses to the comments/criticism and suggestions of reviewers/editors should accompany the revised manuscript. All modifications made to the original manuscript must be highlighted.

If you want to check our Editorial process, click [here](#).

EDITOR'S REQUIREMENTS

Authors who have a manuscript accepted in **Eclet. Quim. J.** may be invited to act as reviewers.

Only the authors are responsible for the correctness of all information, data and content of the manuscript submitted to **Eclet. Quim. J.** Thus, the Editors and the Editorial Board cannot accept responsibility for the correctness of the material published in **Eclet. Quim. J.**

Proofs

After accepting the manuscript, **Eclet. Quim. J.** technical assistants will contact you regarding your manuscript page proofs to correct printing errors only, i.e., other corrections or content improvement are not permitted. The proofs shall be returned in three working days (72 h) via email.

Appeal

Authors may only appeal once about the decision regarding a manuscript. To appeal against the Editorial decision on your manuscript, the corresponding author can send a rebuttal letter to the editor, including a detailed response to any comments made by the reviewers/editor. The editor will consider the rebuttal letter, and if deemed appropriate, the manuscript will be sent to a new reviewer. The Editor decision is final.

Contact

If you have any question, please contact our team:

Prof. Assis Vicente Benedetti
Editor-in-Chief
ecletica.iq@unesp.br

Letícia Amanda Miguel and Jéssica Odoni
Technical support
ecletica@ctrlk.com.br



SUMMARY

EDITORIAL BOARD.....	3
EDITORIAL.....	4
EDITOR'S NOTE.....	7
DATABASE.....	8
INSTRUCTIONS FOR AUTHORS.....	9

ORIGINAL ARTICLES

High photocatalytic activity of Ag/Ag ₃ PO ₄ :W heterostructure formed by femtosecond laser irradiation	20
<i>Aline Barrios Trench, Vinícius Teodoro, Letícia Guerreiro da Trindade, Thales Rafael Machado, Gladys Minguez-Vega, Eloisa Cordoncillo, Carlos Doñate-Buendía, Juan Andrés, Elson Longo</i>	
Catalytic potential of titanium oxide and gold doped titanium oxide nanoparticles in the selectivity benzyl alcohol oxidation.....	28
<i>Arthur Martins Gabriel, Karla da Silva Malaquias, Fernando Henrique Cristovan, Tatiane Moraes Arantes</i>	
YVO ₄ :RE (RE = Eu, Tm, and Yb/Er) nanoparticles synthesized by the microwave-assisted hydrothermal method for photoluminescence application	39
<i>Ivo Mateus Pinatti, Camila Cristina de Foggi, Marcio Daldin Teodoro, Elson Longo, Alexandre Zirpoli Simões, Ieda Lúcia Viana Rosa</i>	
Comparative study of benznidazole encapsulation in boron nitride and carbon nanotubes: A quantum chemistry study	50
<i>Jeziel Rodrigues dos Santos, Osmair Vital de Oliveira, Rafael Giordano Viegas, José Divino dos Santos, Elson Longo</i>	
Activated carbon from pumpkin seeds: Production by simultaneous carbonization activation for occupational respiratory protection	63
<i>Walquíria Joseane da Silva, Nivaldo Freire de Andrade Neto, Carlos Alberto Paskocimas, Juan Alberto Chaves Ruiz, Fabíola Correa Carvalho, Elson Longo, Fabiana Villela da Motta, Maurício Roberto Bomio Delmonte</i>	
Surfactant effects in the morphology and the photocatalytic activity of the BaMoO ₄ crystals	80
<i>Amanda Fernandes Gouveia, Gustavo Venancio Bellucci, Lara Kelly Ribeiro, Marcelo Assis, Ieda Lúcia Viana Rosa, Elson Longo, Juan Andrés, Miguel Angel San-Miguel</i>	
Luminescence and structural properties of Ca _{1-x} ZrO ₃ :Eu _x : An experimental and theoretical approach	90
<i>Marcelo Assis, Marisa Carvalho de Oliveira, Amanda Fernandes Gouveia, Lara Kelly Ribeiro, Ieda Lucia Viana Rosa, Renan Augusto Pontes Ribeiro, Juan Manuel Andrés Bort, Elson Longo</i>	
Performance and stability of femtosecond laser-irradiated Fe ₂ O ₃ materials as photocatalysts for methylene blue dye discoloration	105
<i>Josiane Carneiro Souza, Tiago Almeida Martins, Regiane Cristina de Oliveira, Julio Ricardo Sambrano, Cleber Renato Mendonça, Leonardo de Boni, Edson Roberto Leite, Elson Longo</i>	
Influence of Zr-metal-organic framework coupling on the morphology and photoelectrochemical properties of SnO ₂	120
<i>Letícia Guerreiro da Trindade, Letícia Zanchet, Bianca Lins Zambon da Silva, Elson Longo, Tatiana Martelli Mazzo</i>	
Influence of Cu-doped TiO ₂ on its structural and photocatalytic properties.....	130
<i>Vinícius Teodoro, Elson Longo, Maria Aparecida Zaghete, Leinig Antonio Perazolli</i>	

High photocatalytic activity of Ag/Ag₃PO₄:W heterostructure formed by femtosecond laser irradiation

Aline Barrios Trench¹, Vinícius Teodoro¹, Letícia Guerreiro da Trindade², Thales Rafael Machado¹, Gladys Minguez-Vega³, Eloisa Cordoncillo⁴, Carlos Doñate-Buendía^{3,5}, Juan Andrés⁶, Elson Longo¹⁺

1. Federal University of Sao Carlos, Center for the Development of Functional Materials, São Carlos, Brazil.
2. University of São Paulo, São Carlos Institute of Chemistry, São Carlos, Brazil.
3. University Jaume I, Institut de Noves Tecnologies de la Imatge, Castelló, Spain.
4. University Jaume I, Department of Inorganic and Organic Chemistry, Castelló, Spain.
5. University of Wuppertal, Materials Science and Additive Manufacturing, Wuppertal, Germany.
6. University Jaume I, Department of Analytical and Physical Chemistry, Castelló, Spain.

+Corresponding author: Elson Longo, **Phone:** +55 16 33519588, **Email address:** elson.liec@gmail.com

ARTICLE INFO

Article history:

Received: July 22, 2021

Accepted: September 01, 2021

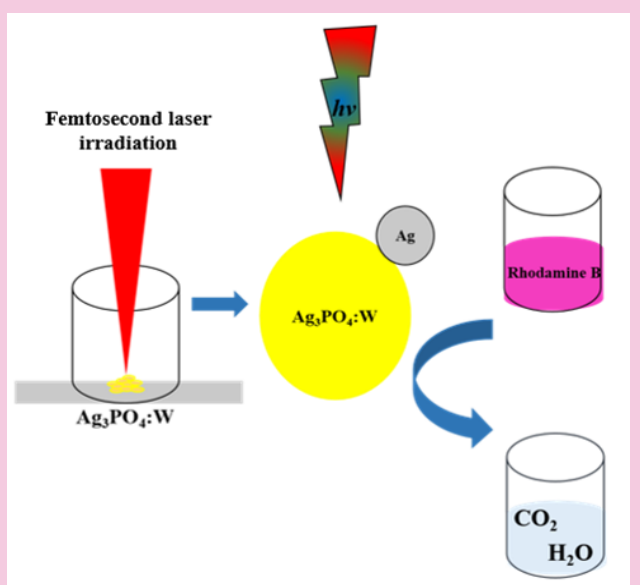
Published: April 11, 2022

Keywords:

1. Ag₃PO₄
2. doping
3. heterostructure
4. photocatalytic property

Section Editors: Elson Longo and Juan Manuel Andrés Bort

ABSTRACT: In this work, the W-doped Ag₃PO₄ was prepared by the chemical coprecipitation method and irradiated with a femtosecond laser (FL). The successful formation of the Ag/Ag₃PO₄:W heterostructure was confirmed by XRD analysis. A higher structural disorder in the [PO₄] clusters was observed for the FL irradiated sample (Ag₃PO₄:W-FL), indicating the formation of Ag metallic from the Ag₃PO₄ structure. The photocatalytic activity of the samples was studied by photodegradation of rhodamine B under visible light irradiation. The formation of Ag nanoparticles on the surface of Ag₃PO₄:W led to a degradation rate constant 3.54 times higher than the nonirradiated sample. This higher photocatalytic activity was related to the surface plasmon resonance effect of the Ag metallic, which acts by capturing photoexcited electrons from the Ag₃PO₄:W, avoiding the recombination of electron-hole pairs, and thus improving the photocatalytic activity.



1. Introduction

Water sources contain various types of contaminants (Sousa *et al.*, 2018), with industrial waste being the contaminants that draw the major attention in environmental pollution, thus requiring a suitable treatment (Karimi-Maleh *et al.*, 2020). Among industrial wastes, organic dyes are the main concern due to their high generated content and toxicity, being of fundamental importance the proper treatment. Rhodamine B (RhB) is an organic dye that can cause damage to humans, leading to skin and eye irritations and respiratory problems (Aljerf, 2018; Dong *et al.*, 2010). Several treatment methods have been studied, such as heterogeneous photocatalysis, which has been considered promising for the treatment of organic dyes because of its green and clean aspects, simplicity and low cost (Zangeneh *et al.*, 2015). Silver phosphate (Ag_3PO_4) has been receiving attention from researchers since its discovery for presenting photocatalytic properties such as the extremely high photooxidative capacity for the evolution of O_2 from water and the decomposition of efficient organic dyes using sunlight (Chen *et al.*, 2015; He *et al.*, 2019; Trench *et al.*, 2018; Zwara *et al.*, 2018). Furthermore, Ag_3PO_4 presents advantages in relation to other well-known photocatalysts, such as TiO_2 , due to its ability to absorb light in the visible region (Fujishima and Honda, 1972). However, Ag_3PO_4 has the disadvantage of photocorrosion and fast recombination of electron-hole pairs, decreasing its stability as a photocatalyst, making its use unfeasible (Chen *et al.*, 2015). Therefore, studies that aim to modify to improve the Ag_3PO_4 photocatalytic activity are of great interest (R. Santos *et al.*, 2020; Shaveisi and Sharafnia, 2020; Shi *et al.*, 2019).

Among the modification methods, the doping process was applied to overcome these disadvantages of Ag_3PO_4 . Our research group has showed a significant improvement of the photocatalytic performance of Mo- and W-doped Ag_3PO_4 (Trench *et al.*, 2018; 2020), while very recently ultra-active Ag_3PO_4 with different W doping rates were successfully synthesized by Trench *et al.*, 2020. Moreover, the deposition of noble nanoparticles, such as Ag, Au, Pt and Pd, onto the surface of Ag_3PO_4 is an important approach to produce a metal semiconductor composite with enhanced photocatalytic performance (Y. Liu *et al.*, 2012; Yan *et al.*, 2014; Z. Liu *et al.*, 2017). This behavior mainly stems from the surface plasmon resonance (SPR) effect of metal nanoparticles, which are related to the collective oscillations of free electrons that can lead to improved visible light absorption, the superior

separation of electron-hole pairs in the composite material, and by the inhibition of photocorrosion mechanisms due to the accumulation of electrons in the Ag nanoparticles instead of Ag_3PO_4 surface (Li *et al.*, 2019).

The decoration of semiconductors with metal nanoparticles is mainly conducted by the adsorption of metal precursors on their surface followed by the chemical reduction in solution (Kochuveedu *et al.*, 2013). Alternatively, the femtosecond laser (FL) irradiation is attracting attention as a cost-effective, fast and clean method for the fabrication of metal-semiconductor heterostructure in which the requirement of organic solvents or chemical reducing agents are minimized (Tan *et al.*, 2013; Vorobyev and Guo, 2013). The short pulses of the laser can induce the nanoparticles formation from distinct bulk targets, as the migration of Ag atoms to the surface of complex oxides followed by their reduction into metallic species (Machado *et al.*, 2018). Our research group reported the formation of Ag nanoparticles on $\alpha\text{-Ag}_2\text{WO}_4$ with superior bactericidal activity (Assis *et al.*, 2018), the laser-induced formation of Ag/Cr particles on AgCrO_4 (Lemos *et al.*, 2019), and the synthesis of Ag-Bi nanoalloys from Ag_2WO_4 and NaBiO_3 targets (Machado *et al.*, 2018). In special, we reported the nucleation and growth of Ag nanoparticles on Ag_3PO_4 surface mediated by FL irradiation (C. Santos *et al.*, 2019). As a step forward, in the present study we demonstrate the formation of $\text{Ag}/\text{Ag}_3\text{PO}_4\text{:W}$ heterostructure by FL irradiation and its superior photocatalytic activity in compare to $\text{Ag}_3\text{PO}_4\text{:W}$, as evidenced by RhB visible light-driven photodegradation process.

2. Materials and methods

2.1 Synthesis of $\text{Ag}_3\text{PO}_4\text{:W}$ and preparation of $\text{Ag}_3\text{PO}_4\text{:W-FL}$ samples

The $\text{Ag}_3\text{PO}_4\text{:W}$ sample was synthesized using the coprecipitation method and doped with 1% mol $\text{Na}_2\text{WO}_4 \cdot 2\text{H}_2\text{O}$, as previously reported by Trench *et al.* (2020).

$\text{Ag}_3\text{PO}_4\text{:W}$ was irradiated with a Ti:sapphire laser (Femtopower Compact Pro, Femto Lasers) using 30 fs full width at half maximum (FWHM) pulses at the central wavelength of 800 nm, and a repetition rate of 1 kHz. A laser beam of 6 mm diameter and mean power of 185 mW was focused onto the surface of $\text{Ag}_3\text{PO}_4\text{:W}$ with a 75 mm lens. To obtain the $\text{Ag}_3\text{PO}_4\text{:W-FL}$ heterostructure, the $\text{Ag}_3\text{PO}_4\text{:W}$ was placed at the bottom of a quartz cuvette attached to a two-dimensional

motion-controlled stage moving in a raster scanning at a constant speed of 0.5 mm s^{-1} in the focus plane perpendicular to the laser beam.

2.2 Characterization techniques

The structural features at long-range of the samples were investigated by X-ray diffraction (XRD) performed in a D/Max-2500PC diffractometer (Rigaku, Japan) using $\text{Cu K}\alpha$ radiation ($\lambda = 1.54056 \text{ \AA}$), at a scan rate of $0.5^\circ \text{ min}^{-1}$. The structural features at short-range of the samples were investigated by micro-Raman scattering spectroscopy measurements performed in a LabRAM iHR550 Horiba Jobin Yvon spectrometer coupled with a charge-coupled device (CCD, Synapse) as a signal detector, and an ion argon laser with 514.5 nm of wavelength (Melles Griot). The optical absorption spectroscopy measurements in the ultraviolet and visible region were performed in the diffuse reflectance mode in a Varian spectrophotometer model Cary 5G (USA) in the range of 250–800 nm. Field emission scanning electron microscopy (FE-SEM) was performed using a FEI microscope (Model Inspect F50) operating at 5 kV.

2.3 Photocatalytic experiments

The photocatalytic activity of $\text{Ag}_3\text{PO}_4\text{:W}$ and $\text{Ag}_3\text{PO}_4\text{:W-FL}$ samples were tested for degradation of RhB (95%, Aldrich) under visible light irradiation. For this experiment, 50 mg of each sample and 50 mL of RhB (10 mg L^{-1}) were used, which were submitted to an ultrasonic bath (Branson, model 1510; frequency 42 kHz) for 5 min and 30 min of constant agitation, in order to reach the adsorption-desorption balance and later exposed to irradiation of six lamps (Philips TL-D, 15 W). Aliquots were taken at 1 min intervals, centrifuged and their degradation monitored by measuring the peak of maximum RhB absorption ($\lambda_{\text{max}} = 554 \text{ nm}$) using an ultraviolet-visible (UV-Vis) spectrophotometer (V-660, JASCO). A test under the same conditions without the presence of catalysts was also carried out.

3. Results and discussion

Figure 1a shows the XRD patterns of $\text{Ag}_3\text{PO}_4\text{:W}$ and $\text{Ag}_3\text{PO}_4\text{:W-FL}$ samples. The diffraction peaks for both samples indicated the cubic phase of Ag_3PO_4 with $P-43n$ space group, according to the Inorganic Crystal Structure Database (ICSD) code 14000 (Masse *et al.*, 1976). No secondary or any dopant related phases were observed for $\text{Ag}_3\text{PO}_4\text{:W}$ sample, indicating the successfully of insertion of W as dopant into the Ag_3PO_4

structure. However, for the sample irradiated with the FL, it was observed the emergence of a peak at approximately 37.8° (2θ), as can be seen in Fig. 1b. The as-mentioned peak is assigned to the (111) diffraction plane of cubic phase of Ag with $Fm-3m$ space group, which is the most intense diffraction peak for this structure, according to the ICSD code 604630 (Jette and Foote, 1935). It is well-known that the FL irradiation in Ag-containing materials, such as Ag_3PO_4 , induces the reduction of Ag^+ cations in the structure for the formation of Ag nanoparticles on the semiconductor surface (Assis *et al.*, 2018; 2019; C. Santos *et al.*, 2019). Herewith, the FL irradiation effectively allowed the formation of $\text{Ag}/\text{Ag}_3\text{PO}_4\text{:W}$ heterostructure in the $\text{Ag}_3\text{PO}_4\text{:W-FL}$ samples.

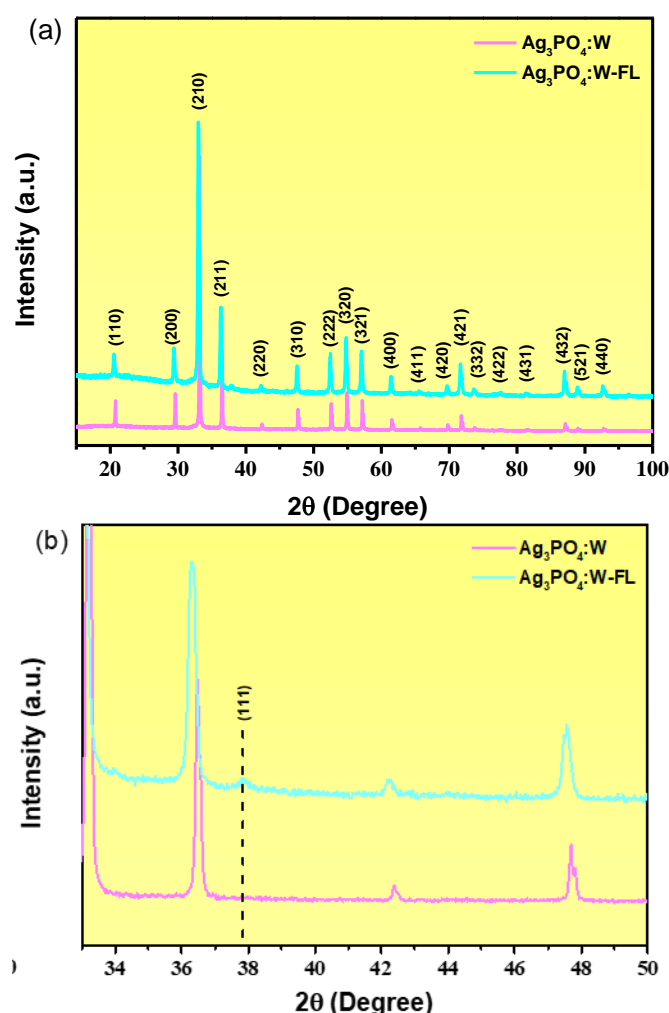


Figure 1. XRD patterns of $\text{Ag}_3\text{PO}_4\text{:W}$ and $\text{Ag}_3\text{PO}_4\text{:W-FL}$ samples in the range of $10\text{--}100^\circ$ (a) and in the range of $33\text{--}50^\circ$ (b).

Figure 2 shows the Raman spectra of $\text{Ag}_3\text{PO}_4\text{:W}$ and $\text{Ag}_3\text{PO}_4\text{:W-FL}$ samples. According to the group theory analysis, the cubic phase of Ag_3PO_4 structure presents

18 Raman active modes ($\Gamma = 2 A_1 + 4 E + 12 T_2$) (Trench *et al.*, 2018; Botelho *et al.*, 2015). The observed Raman bands for the prepared samples are located at approximately 100, 237, 539, 700, 904, and 997 cm^{-1} . All these modes are related to the cubic phase of Ag_3PO_4 and no Raman bands related to any secondary or W dopant phases were observed. The bands located at 100 and 237 cm^{-1} have been assigned to the translational and/or rotational modes with T_2 symmetry of $[\text{PO}_4]$ clusters. The band located at 539 cm^{-1} is assigned to the bending mode with T_2 symmetry of $[\text{PO}_4]$ clusters. The band located at 700 cm^{-1} is attributed to the symmetric stretching mode of the $[\text{PO}_4]$ clusters. The most intense band located at 904 cm^{-1} is related to the symmetric stretching (A_1) mode, whereas the band located at 997 cm^{-1} is related to the asymmetric stretching mode (T_2) mode of $[\text{PO}_4]$ clusters.

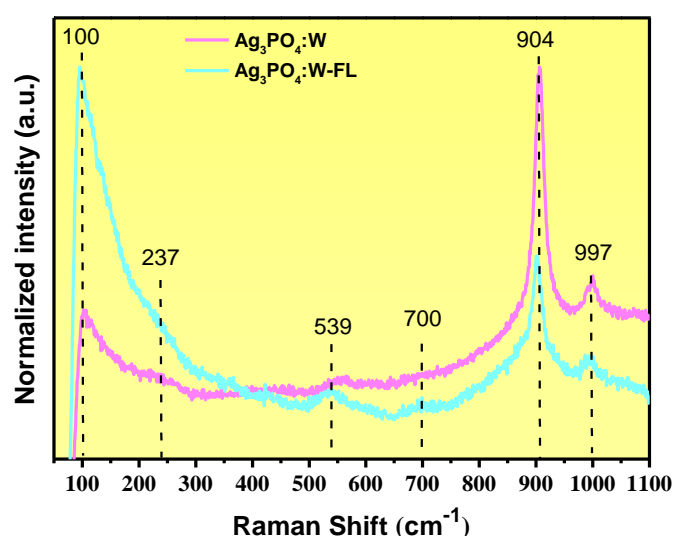


Figure 2. Raman spectra of $\text{Ag}_3\text{PO}_4:\text{W}$ and $\text{Ag}_3\text{PO}_4:\text{W-FL}$ samples.

It can be observed that the $\text{Ag}_3\text{PO}_4:\text{W-FL}$ sample presented a remarkable decrease of the relative intensity of the band at 904 cm^{-1} compared to the $\text{Ag}_3\text{PO}_4:\text{W}$ sample. As observed in XRD results, the FL irradiation in $\text{Ag}_3\text{PO}_4:\text{W}$ sample induced the formation of metallic Ag that arises from the reduction of Ag^+ cations in the Ag_3PO_4 structure. This process generates Ag vacancies in the structure, which induce a local structural rearrangement of the adjacent $[\text{PO}_4]$ clusters. This rearrangement causes variations in the coordination parameters of the clusters, *i.e.*, bond angles and lengths, thus increasing the structural disorder in the $[\text{PO}_4]$ clusters. The structural disorder in the clusters leads to a break of local symmetry that decreases the freedom degree of vibrational modes the $[\text{PO}_4]$ clusters, hence decreasing the intensity of Raman scattering.

UV-Vis diffuse reflectance measurements were employed to determine the optical band gap energies of the prepared samples. Considering that the absorption spectrum of the Ag_3PO_4 is governed by indirect electronic transitions (Botelho *et al.*, 2016), Fig. 3a and b show the Tauc plot (Wood and Tauc, 1972) for the $\text{Ag}_3\text{PO}_4:\text{W}$ and $\text{Ag}_3\text{PO}_4:\text{W-FL}$ samples, respectively. It can be observed a slight decrease in the band gap energy for the $\text{Ag}_3\text{PO}_4:\text{W-FL}$ compared to the $\text{Ag}_3\text{PO}_4:\text{W}$ sample, being the values of 2.53 and 2.43 eV, respectively. As previous mentioned in Raman analysis, the FL irradiation in the $\text{Ag}_3\text{PO}_4:\text{W}$ sample induced structural disorder in the $[\text{PO}_4]$ clusters due to the formation of Ag vacancies in the Ag_3PO_4 structure. These structural distortions induce the formation of intermediate energy levels within the band gap, which can act as electron traps, thus decreasing the band gap energy of the FL irradiated sample.

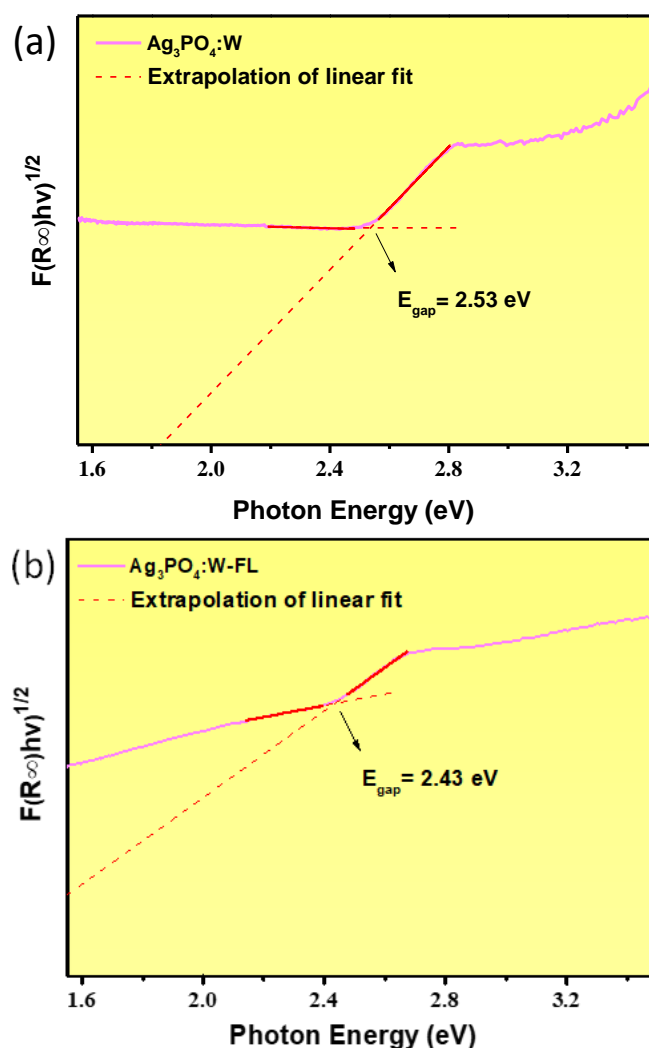


Figure 3. Tauc plot for the $\text{Ag}_3\text{PO}_4:\text{W}$ (a) and $\text{Ag}_3\text{PO}_4:\text{W-FL}$ (b) samples.

The morphological aspects of the $\text{Ag}_3\text{PO}_4\text{:W}$ and $\text{Ag}_3\text{PO}_4\text{:W-FL}$ samples were investigated by FE-SEM analysis. Figure 4a and b shows the FE-SEM images of the $\text{Ag}_3\text{PO}_4\text{:W}$ and $\text{Ag}_3\text{PO}_4\text{:W-FL}$ samples, respectively, with their corresponding insets with magnified regions of the images. For the $\text{Ag}_3\text{PO}_4\text{:W}$ sample, it can be observed nano- and microparticles with quasi-spherical shape. These morphologies are similar to those previously reported (Trench *et al.*, 2018; 2020). However, the FE-SEM image of the $\text{Ag}_3\text{PO}_4\text{:W-FL}$ sample presents smaller and agglomerated particles compared to the $\text{Ag}_3\text{PO}_4\text{:W}$ sample. These aspects arise from the high local energy of the pulsed FL in the sample, thus inducing the fragmentation and coalescence of the particles. Moreover, according to reported works (Assis *et al.*, 2018; C. Santos *et al.*, 2019) and the XRD results, the presence of nanoparticles on the surface of larger particles can be assigned to the Ag metallic nanoparticles.

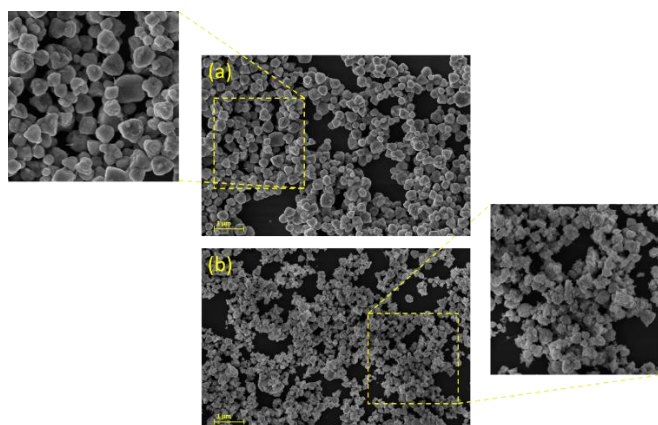


Figure 4. FE-SEM images of $\text{Ag}_3\text{PO}_4\text{:W}$ (a) and $\text{Ag}_3\text{PO}_4\text{:W-FL}$ (b) samples.

The photocatalytic activity of the $\text{Ag}_3\text{PO}_4\text{:W}$ and $\text{Ag}_3\text{PO}_4\text{:W-FL}$ samples were investigated by the degradation of RhB under visible light irradiation. Figure 5a shows the degradation efficiency of both prepared samples and the control experiment without photocatalyst. As can be seen, no significant degradation was observed in the absence of photocatalyst. As previously reported, the $\text{Ag}_3\text{PO}_4\text{:W}$ sample presents a highly photocatalytic activity for RhB degradation under visible light irradiation, allowing approximately 82.5% of RhB degradation in only 3 min of reaction (Trench *et al.*, 2020). However, it was observed a remarkable improvement of the photocatalytic activity of the FL irradiated sample, allowing 100% of RhB degradation in 3 min of reaction. To further compare, the $\text{Ag}_3\text{PO}_4\text{:W}$ and $\text{Ag}_3\text{PO}_4\text{:W-FL}$ samples promoted 60.5% and 97.2% of RhB in only 2

min of reaction. Figure 5b shows the Langmuir-Hinshelwood plot for the pseudo first-order kinetics model (B. Liu *et al.*, 2014) for both prepared samples and the control experiment. It was observed that the $\text{Ag}_3\text{PO}_4\text{:W-FL}$ sample presented a rate constant (k) 3.54 times higher than the $\text{Ag}_3\text{PO}_4\text{:W}$ sample.

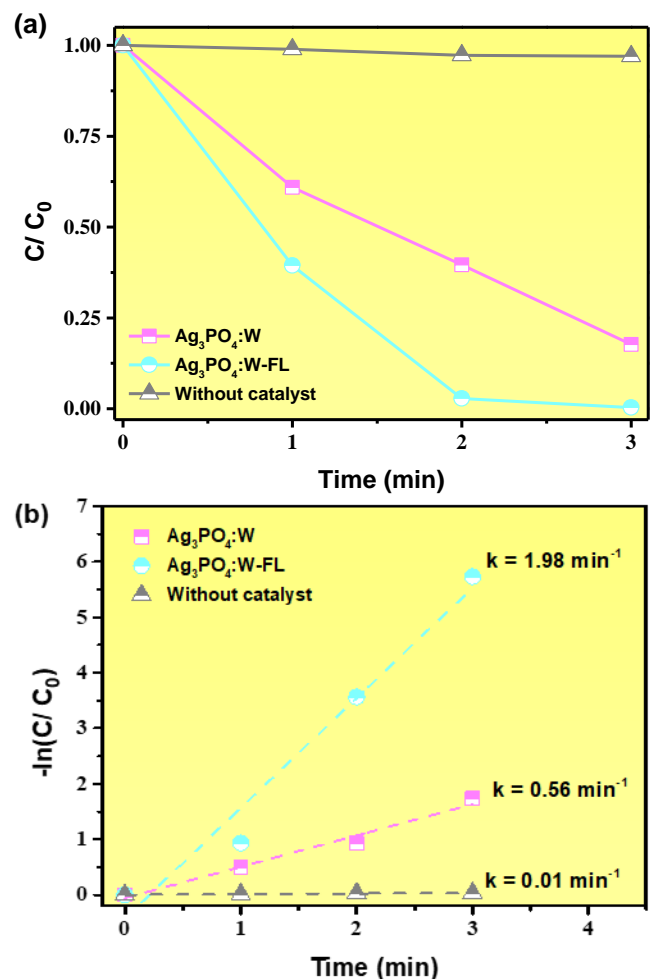


Figure 5. Relative concentration of RhB against reaction time in photocatalytic experiments (a) and pseudo first-order kinetics plot (b) of $\text{Ag}_3\text{PO}_4\text{:W}$ and $\text{Ag}_3\text{PO}_4\text{:W-FL}$ samples.

It has been demonstrated that the FL irradiation in Ag-containing materials induces the formation of Ag nanoparticles, as observed by XRD results and inferred by FE-SEM analysis. The formation of Ag nanoparticles on the surface of Ag_3PO_4 particles results in a semiconductor/metal interface. This interface has an important role in the photocatalytic performance of the $\text{Ag}_3\text{PO}_4\text{:W-FL}$ sample due to the charge carrier transport (Koyappayil *et al.*, 2020; Nubla and Sandhyarani, 2020; Silva *et al.*, 2019; Sofi and Majid, 2019). The visible light irradiation photoexcites electrons from the valence band to the conduction band. The photoexcited electrons

can participate in reduction reactions with the reaction media, but also recombine with the holes in the valence band. The presence of the Ag nanoparticles on the Ag_3PO_4 surface under visible light irradiation can act as electron traps due to the SPR effect. Thus, the photoexcited electrons in the conduction band of AgPO_4 can be transferred to the Ag nanoparticles. These electrons in the Ag nanoparticles can perform the reduction reactions with the reaction media, whereas the holes in the valence band of Ag_3PO_4 can perform the oxidation reactions. Herewith, the electron transfer from the conduction band of Ag_3PO_4 to Ag nanoparticles decreases the recombination rate of the electron-hole pairs, hence increasing their availability to perform the redox reactions. These reactions can be performed directly with the RhB adsorbed on the particle surface and also indirectly by the formation of radical species.

Moreover, as observed by Raman and UV-Vis results, the FL irradiation in $\text{Ag}_3\text{PO}_4\text{:W}$ induced structural disorder in the $[\text{PO}_4]$ clusters, which generated intermediate energy levels within the band gap. These energy levels can also act as traps for photoexcited electrons in the recombination process, thus decreasing the recombination rate of the electron-hole pairs. Therefore, the FL irradiation in $\text{Ag}_3\text{PO}_4\text{:W}$ sample induced the formation of Ag nanoparticles and intermediate energy levels that can act as electron traps, promoting a significant improvement of the photocatalytic performance of the $\text{Ag}_3\text{PO}_4\text{:W}$.

4. Conclusions

The FL irradiation in $\text{Ag}_3\text{PO}_4\text{:W}$ sample induced the formation of metallic Ag and also structural disorder in $[\text{PO}_4]$ clusters, as observed by XRD and Raman results. The FE-SEM indicated the fragmentation and agglomeration of Ag_3PO_4 particles due to the high local energy of the pulsed laser. Further, it was observed the emergence of nanoparticles in the Ag_3PO_4 surface, which can be assigned to the Ag nanoparticles. The structural disorder in the $[\text{PO}_4]$ clusters induced the formation of intermediate energy levels within band gap, as observed by the decrease in its energy. The FL irradiation promoted a significant improvement of the photocatalytic activity of the $\text{Ag}_3\text{PO}_4\text{:W}$ sample, being 3.54 times higher than the non-irradiated sample. This improvement can be attributed to the SPR effect by the formation of Ag nanoparticles and the intermediate energy levels. Both can act as traps for the photoexcited electrons, which increase the availability of the electron-hole pairs to perform the redox reactions with the reaction medium. Therefore, the FL irradiation has proved to be an effective method for the development of

metal-semiconductor heterostructure and for the enhancement of photocatalytic properties.

Authors' contribution

Conceptualization: Trench, A. B.; Longo, E.

Data curation: Trench, A. B.; Teodoro, V.; Trindade, L. G.; Machado, T. R.

Formal Analysis: Trench, A. B.; Teodoro, V.; Trindade, L. G.; Machado, T. R.

Funding acquisition: Not applicable.

Investigation: Trench, A. B.

Methodology: Trench, A. B.; Longo, E.; Minguéz-Veja, G.; Cordoncillo, E.; Doñate-Buendía, C.; Andrés, J.

Project administration: Trench, A. B.; Longo, E.

Resources: Longo, E.

Software: Not applicable.

Supervision: Longo, E.

Validation: Trench, A. B.

Visualization: Trench, A. B.

Writing – original draft: Trench, A. B.; Teodoro, V.; Trindade, L. G.; Machado, T. R.; Longo, E.

Writing – review & editing: Trench, A. B.; Longo, E.; Minguéz-Veja, G.; Cordoncillo, E.; Doñate-Buendía, C.; Andrés, J.

Data availability statement

All data sets were generated or analyzed in the current study.

Funding

Fundação de Amparo à Pesquisa do Estado de São Paulo (FAPESP). Grant No: 2013/07296-2.

Coordenação de Aperfeiçoamento de Pessoal de Nível Superior - Brasil (CAPES). Finance Code: 001.

Conselho Nacional de Desenvolvimento Científico e Tecnológico (CNPq). Grant No: 142035/2017-3.

Universitat Jaume I. Project: UJI-B2019-30; UJI-B2019-37; UJI-B2019-41.

Ministerio de Ciencia, Innovación y Universidades (Spain). Project: PGC2018094417-B-I00.

Ministerio de Ciencia e Innovación. PID2019-110927RB-I00.

Generalitat Valenciana. PROMETEO/2020/029.

Acknowledgments

The authors are very grateful to the “Serveis Centrals d’Instrumentación Científica” (SCIC) of the University Jaume I for the use of the femtosecond laser.

References

Aljerf, L. High-efficiency extraction of bromocresol purple dye and heavy metals as chromium from industrial effluent by adsorption onto a modified surface of zeolite: Kinetics and equilibrium study. *J. Environ. Manage.* **2018**, *225*, 120–132. <https://doi.org/10.1016/j.jenvman.2018.07.048>

Assis, M.; Cordoncillo, E.; Torres-Mendieta, R.; Beltran-Mir, H.; Mínguez-Vega, G.; Oliveira, R.; Leite, E. R.; Foggi, C. C.; Vergani, C. E.; Longo, E.; Andres, J. Towards the scale-up of the formation of nanoparticles on alpha-Ag₂WO₄ with bactericidal properties by femtosecond laser irradiation. *Sci. Rep.* **2018**, *8* (1), 1884. <https://doi.org/10.1038/s41598-018-19270-9>

Assis, M.; Robeldo, T.; Foggi, C. C.; Kubo, A. M.; Mínguez-Vega, G.; Condoncillo, E.; Beltran-Mir, H.; Torres-Mendieta, R.; Andres, J.; Oliva, M.; Vergani, C. E.; Barbugli, P. A.; Camargo, E. R.; Borra, R. C.; Longo, E. Ag Nanoparticles/alpha-Ag₂WO₄ Composite Formed by Electron Beam and Femtosecond Irradiation as Potent Antifungal and Antitumor Agents. *Sci. Rep.* **2019**, *9*, 9927. <https://doi.org/10.1038/s41598-019-46159-y>

Botelho, G.; Sczancoski, J. C.; Andres, J.; Gracia, L.; Longo, E. Experimental and Theoretical Study on the Structure, Optical Properties, and Growth of Metallic Silver Nanostructures in Ag₃PO₄. *J. Phys. Chem. C* **2015**, *119* (11), 6293–6306. <https://doi.org/10.1021/jp512111v>

Botelho, G.; Andres, J.; Gracia, L.; Matos, L. S.; Longo, E. Photoluminescence and Photocatalytic Properties of Ag₃PO₄ Microcrystals: An Experimental and Theoretical Investigation. *ChemPlusChem* **2016**, *81* (2), 202–212. <https://doi.org/10.1002/cplu.201500485>

Chen, X.; Dai, Y.; Wang, X. Methods and mechanism for improvement of photocatalytic activity and stability of Ag₃PO₄: A review. *J. Alloys Compound* **2015**, *649*, 910–932. <https://doi.org/10.1016/j.jallcom.2015.07.174>

Dong, W.; Lee, C. W.; Lu, X.; Sun, Y.; Hua, W.; Zhuang, G.; Zhang, S.; Chen, J.; Hou, H.; Zhao, D. Synchronous role of coupled adsorption and photocatalytic oxidation on ordered mesoporous anatase TiO₂-SiO₂ nanocomposites generating excellent degradation activity of RhB dye. *Appl. Catal. B* **2010**, *95* (3-4), 197–207. <https://doi.org/10.1016/j.apcatb.2009.12.025>

Fujishima, A.; Honda, K. Electrochemical photolysis of water at a semiconductor electrode. *Nature* **1972**, *238*, 37–38. <https://doi.org/10.1038/238037a0>

He, G.; Yang, W.; Zheng, W.; Gong, L.; Wang, X.; An, Y.; Tian, M. Facile controlled synthesis of Ag₃PO₄ with various morphologies for enhanced photocatalytic oxygen evolution from water splitting. *RSC Advances* **2019**, *9* (32), 18222–18231. <https://doi.org/10.1039/C9RA01306G>

Jette, E. R.; Foote, F. Precision Determination of Lattice Constants. *J. Chem. Phys.* **1935**, *3* (10), 605–616. <https://doi.org/10.1063/1.1749562>

Karimi-Maleh, H.; Kumar, B. G.; Rajendran, S.; Qin, J.; Vadivel, S.; Durgalakshmi, D.; Gracia, F.; Soto-Moscoso, M.; Orooji, Y.; Karimi, F. Tuning of metal oxides photocatalytic performance using Ag nanoparticles integration. *J. Mol. Liq.* **2020**, *314*, 113588. <https://doi.org/10.1016/j.molliq.2020.113588>

Kochuveedu, S. T.; Jang, Y. H.; Kim, D. H. A study on the mechanism for the interaction of light with noble metal-metal oxide semiconductor nanostructures for various photophysical applications. *Chem. Soc. Rev.* **2013**, *42* (21), 8467–8493. <https://doi.org/10.1039/c3cs60043b>

Koyappayil, A.; Berchmans, S.; Lee, M.-H. Dual enzyme-like properties of silver nanoparticles decorated Ag₂WO₄ nanorods and its application for H₂O₂ and glucose sensing. *Colloids Surf. B Biointerfaces* **2020**, *189*, 110840. <https://doi.org/10.1016/j.colsurfb.2020.110840>

Lemos, P. S.; Silva, G. S.; Roca, R. A.; Assis, M.; Torres-Mendieta, R.; Beltrán-Mir, H.; Mínguez-Vega, G.; Andrés, J.; and Longo, E. Laser and electron beam-induced formation of Ag/Cr structures on Ag₂CrO₄. *Phys. Chem. Chem. Phys.* **2019**, *21* (11), 6101–6111. <https://doi.org/10.1039/c8cp07263a>

Li, X.; Xu, P.; Chen, M.; Zeng, G.; Wang, D.; Chen, F.; Tang, W.; Chen, C.; Zhang, C.; Tan, X. Application of silver phosphate-based photocatalysts: Barriers and solutions. *Chem. Eng. J.* **2019**, *366*, 339–357. <https://doi.org/10.1016/j.cej.2019.02.083>


Liu, Y.; Fang, L.; Lu, H.; Liu, L.; Wang, H.; Hu, C. Highly efficient and stable Ag/Ag₃PO₄ plasmonic photocatalyst in visible light. *Catal. Commun.* **2012**, *17*, 200–204. <https://doi.org/10.1016/j.catcom.2011.11.001>

Liu, B.; Zhao, X.; Terashima, C.; Fujishima, A.; Nakata, K. Thermodynamic and kinetic analysis of heterogeneous photocatalysis for semiconductor systems. *Phys. Chem. Chem. Phys.* **2014**, *16* (19), 8751–8760. <https://doi.org/10.1039/c3cp55317e>

Liu, Z.; Liu, Y.; Xu, P.; Ma, Z.; Wang, J.; Yuan, H. Rational Design of Wide Spectral-Responsive Heterostructures of Au Nanorod Coupled Ag₃PO₄ with Enhanced Photocatalytic Performance. *ACS Appl. Mater. Interfaces* **2017**, *9* (24), 20620–20629.

- Machado, T. R.; Macedo, N. G.; Assis, M.; Doñate-Buendia, C.; Mínguez-Vega, G.; Teixeira, M. M.; Foggi, C. C.; Vergani, C. E.; Beltran-Mir, H.; Andres, J.; Cordoncillo, E.; Longo, E. From Complex Inorganic Oxides to Ag-Bi Nanoalloy: Synthesis by Femtosecond Laser Irradiation. *ACS omega* **2018**, *3* (8), 9880–9887. <https://doi.org/10.1021/acsomega.8b01264>
- Masse, R.; Torjman, I.; Durif, A. Refinement of Crystal-Structure of Silver Monophosphate, Ag_3PO_4 -Existence of High-Temperature Form. *Zeitschrift Fur Kristallographie* **1976**, *144*, 76–81. <https://doi.org/10.1524/zkri.1976.144.1-6.76>
- Nubla, K.; Sandhyarani, N. Ag nanoparticles anchored Ag_2WO_4 nanorods: An efficient methanol tolerant and durable Pt free electro-catalyst toward oxygen reduction reaction. *Electrochim. Acta* **2020**, *340*, 135942. <https://doi.org/10.1016/j.electacta.2020.135942>
- Santos, C. C.; Assis, M.; Machado, T. R.; Pereira, P. F. S.; Mínguez-Vega, G.; Cordoncillo, E.; Beltran-Mir, H.; Doñate-Buendía, C.; Andrés, J.; Longo, E. Proof-of-concept studies directed toward the formation of metallic Ag nanostructures from Ag_3PO_4 induced by electron beam and femtosecond laser. *Part. Part. Syst. Charact.* **2019**, *36* (6), 1800533. <https://doi.org/10.1002/ppsc.201800533>
- Santos, R. K.; Martins, T. A.; Silva, G. N.; Conceição, M. V. S.; Nogueira, I. C.; Longo, E.; Botelho, G. $\text{Ag}_3\text{PO}_4/\text{NiO}$ Composites with Enhanced Photocatalytic Activity under Visible Light. *ACS omega* **2020**, *5* (34), 21651–21661. <https://doi.org/10.1021/acsomega.0c02456>
- Shaveisi, Y.; Sharifnia, S. Deriving $\text{Ag}_3\text{PO}_4/\text{CaO}$ composite as a stable and solar light photocatalyst for efficient ammonia degradation from wastewater. *J. Energy Chem.* **2018**, *27* (1), 290–299. <https://doi.org/10.1016/j.jechem.2017.06.012>
- Shi, H.; Yang, S.; Han, C.; Niu, Z.; Li, H.; Huang, X.; Ma, J. Fabrication of $\text{Ag}/\text{Ag}_3\text{PO}_4/\text{WO}_3$ ternary nanoparticles as superior photocatalyst for phenol degradation under visible light irradiation. *Solid State Sci.* **2019**, *96*, 105967. <https://doi.org/10.1016/j.solidstatesciences.2019.105967>
- Silva, E. Z.; Faccin, G. M.; Machado, T. R.; Macedo, N. G.; Assis, M.; Maya-Johnson, S.; Sczancoski, J. C.; Andrés, J.; Longo, E.; San-Miguel, M. A. Connecting Theory with Experiment to Understand the Sintering Processes of Ag Nanoparticles. *J. Phys. Chem. C* **2019**, *123* (17), 11310–11318. <https://doi.org/10.1021/acs.jpcc.9b02107>
- Sofi, F. A.; Majid, K. Plasmon induced interfacial charge transfer across Zr-based metal-organic framework coupled Ag_2WO_4 heterojunction functionalized by Ag NPs: Efficient visible light photocatalyst. *Chem. Phys. Lett.* **2019**, *720*, 7–14. <https://doi.org/10.1016/j.cplett.2019.02.005>
- Sousa, J. C. G.; Ribeiro, A. R.; Barbosa, M. O.; Pereira, M. F. R.; Silva, A. M. T. A review on environmental monitoring of water organic pollutants identified by EU guidelines. *J. Hazard. Mater.* **2018**, *344*, 146–162. <https://doi.org/10.1016/j.jhazmat.2017.09.058>
- Tan, D.; Zhou, S.; Qiu, J.; Khusro, N. Preparation of functional nanomaterials with femtosecond laser ablation in solution. *J. Photochem. Photobiol. C Photochem. Rev.* **2013**, *17*, 50–68. <https://doi.org/10.1016/j.jphotochemrev.2013.08.002>
- Trench, A. B.; Machado, T. R.; Gouveia, A. F.; Assis, M.; Trindade, L. G.; Santos, C.; Perrin, A.; Perrin, C.; Oliva, M.; Andrés, J.; Longo, E. Connecting structural, optical, and electronic properties and photocatalytic activity of $\text{Ag}_3\text{PO}_4:\text{Mo}$ complemented by DFT calculations. *Appl. Catal. B* **2018**, *238*, 198–211. <https://doi.org/10.1016/j.apcatb.2018.07.019>
- Trench, A. B.; Machado, T. R.; Gouveia, A. F.; Foggi, C. C.; Teodoro, V.; Sánchez-Montes, I.; Teixeira, M. M.; Trindade, L. G.; Jacomaci, N.; Perrin, A.; Perrin, C.; Aquino, J. M.; Andrés, J.; Longo, E. Rational Design of W-Doped Ag_3PO_4 as an Efficient Antibacterial Agent and Photocatalyst for Organic Pollutant Degradation. *ACS omega* **2020**, *5* (37), 23808–23821. <https://doi.org/10.1021/acsomega.0c03019>
- Vorobyev, A. Y.; Guo, C. Direct femtosecond laser surface nano/microstructuring and its applications. *Laser Photonics Rev.* **2013**, *7* (3), 385–407. <https://doi.org/10.1002/lpor.201200017>
- Wood, D. L.; Tauc, J. Weak Absorption Tails in Amorphous Semiconductors. *Phys. Rev. B* **1972**, *5* (8), 3144–3151. <https://doi.org/10.1103/PhysRevB.5.3144>
- Yan, T.; Zhang, H.; Liu, Y.; Guan, W.; Long, J.; Li, W.; You, J. Fabrication of robust $\text{M}/\text{Ag}_3\text{PO}_4$ ($\text{M} = \text{Pt}, \text{Pd}, \text{Au}$) Schottky-type heterostructures for improved visible-light photocatalysis. *RSC Adv.* **2014**, *4* (70), 37220. <https://doi.org/10.1039/C4RA06254J>
- Zangeneh, H.; Zinatizadeh, A. A. L.; Habibi, M.; Akia, M.; Isa, M. H. Photocatalytic oxidation of organic dyes and pollutants in wastewater using different modified titanium dioxides: A comparative review. *J. Ind. Eng. Chem.* **2015**, *26*, 1–36. <https://doi.org/10.1016/j.jiec.2014.10.043>
- Zwara, J.; Grabowska, E.; Klimczuk, T.; Lisowski, W.; Zaleska-Medynska, A. Shape-dependent enhanced photocatalytic effect under visible light of Ag_3PO_4 particles. *J. Photochem. Photobiol. A Chem.* **2018**, *367*, 240–252. <https://doi.org/10.1016/j.jphotochem.2018.08.006>

Catalytic potential of titanium oxide and gold doped titanium oxide nanoparticles in the selectivity benzyl alcohol oxidation

Arthur Martins Gabriel¹, Karla da Silva Malaquias¹, Fernando Henrique Cristovan¹, Tatiane Moraes Arantes¹⁺

1. Federal University of Jataí, Chemistry Department, Jataí, Brazil.

+Corresponding author: Tatiane Moraes Arantes, **Phone:** +556436068214, **Email address:** tmarantes@ufj.edu.br

ARTICLE INFO

Article history:

Received: July 21, 2021

Accepted: October 11, 2021

Published: April 11, 2022

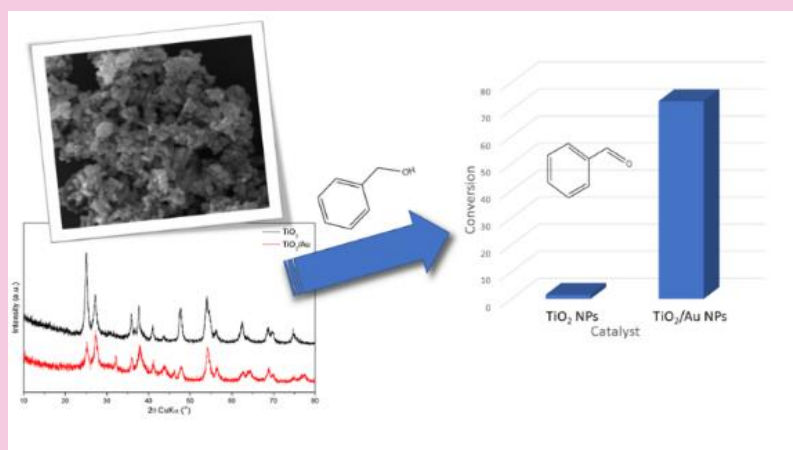
Keywords:

1. organic catalysis
2. oxide nanoparticles
3. hydrothermal method

Section Editors: Elson Longo and Juan Manuel Andrés Bort

ABSTRACT: Titanium oxide (TiO_2) nanoparticles have been widely used and researched in recent years due to their wide application in several areas such as solar cells, catalysis and their chemical, non-toxic and electrical properties. Thus, this work aimed to study the catalytic potential of these nanomaterials through the oxidation of benzyl alcohol, for which TiO_2 nanoparticles synthesized by the hydrothermal method and decorated with gold nanoparticles obtained by the Turkevich method (TiO_2/Au) were used. The catalyst proved to be active for the catalysis of

benzyl alcohol oxidation, with a yield of about 73% for the TiO_2/Au catalyst and 1.4% for the TiO_2 catalyst. Additionally, it was observed that the catalyst was selective, since the GC-MS and FTIR spectra showed only benzaldehyde as the final reaction product. The selective oxidation of alcohols is one of the most significant transformations in organic chemistry, as it is essential for the production of industrial intermediates.



1. Introduction

Nanotechnology field has found great application in many areas, including medicine, pharmacology and industry, and is considered to be one of the most active areas in modern material research (Chen and Mao, 2007). The increase in surface area, changes in the size and morphology of nanoparticles give them different properties, which are considered improvements when compared to the raw material. New properties, increased reactivity and potential applications in many areas of research such as antibacterial, antiviral, diagnostics, anticancer and directed to the controlled release of drugs, have led to a wide exploration of metallic nanoparticles (Bavanilatha *et al.*, 2019).

An important point regarding the synthesis of these nanostructures is the precise control of size and shape, since some properties are specifically linked to these structural characteristics (Li *et al.*, 2021). The control of these characteristics, in a hydrothermal processing, can be obtained in the nucleation and growth processes. Controlling synthesis variables, such as temperature, concentration and time, ensures greater control over the characteristics of the product to be synthesized (Arantes, 2009).

Titanium oxide is a white solid inorganic substance (Abisharani *et al.*, 2019). This semiconductor ceramic material has three main crystallographic structures: anatase, rutile and brookite, where the first two being most used because they are more thermodynamically stable (Montalvo-Quiros and Luque-Garcia, 2019). Furthermore, TiO₂ has been applied in supercapacitors, replacing ruthenium oxide due to its thermal stability, potential oxidation strength and chemical stability. This material becomes even more attractive due to its high relative abundance, low cost and safety of use (Ali *et al.*, 2020; Haider *et al.*, 2017; Kaneta *et al.*, 2019; Reddy *et al.*, 2019; Tayel *et al.*, 2018).

TiO₂ nanoparticles maintain the macroscopic material characteristics such as low cost, nontoxicity and resistance to chemical erosion, in addition to presenting catalytic and photocatalytic properties that do not exist in the macroscopic material (Cao *et al.*, 2015; S. Gupta and Tripathi, 2011; Radetić, 2013; W. Zhao *et al.*, 2021). Additionally, when associated with noble metals such as Au, Ag and Pt, it is possible to obtain excellent magnetic, optical and electrical properties (Li *et al.*, 2021; Srinivasan *et al.*, 2019; Sun *et al.*, 2017; Wang *et al.*, 2021). TiO₂ nanoparticles have wide applications in cosmetics, pharmaceuticals, skin care products, toothpastes, primarily to protect the skin from UV rays, and as a food coloring and inks (Abisharani *et*

al., 2019; Ali *et al.*, 2020; Bavanilatha *et al.*, 2019; Messaddeq *et al.*, 2019).

Surface modification is used to provide a wide range of functionality to nanoparticles, in addition to improving their specific properties (Ozidal *et al.*, 2019; Tomovska *et al.*, 2011). Thus, the photocatalytic and biological properties can be improved. One of the methodologies for functionalization of TiO₂ nanoparticles is the use of silane coupling agents. Methoxy and ethoxysilanes are the most widely used because they are easy to handle and the by-products are alcohols are noncorrosive and volatile (Dalod *et al.*, 2017; Tomovska *et al.*, 2011).

In addition, another technique that allows the modification of the properties of a nanomaterial is the synthesis of other metallic nanoparticles on top of other nanoparticles, such as the Turkevich method, a technique used to produce spherical silver nanoparticles (Gorup *et al.*, 2011).

The functionalization of nanoparticles allows the creation of hybrid nanostructures, which offer distinct advantages compared to the individual components and can also display new properties and functions for practical applications. These enhanced properties arise from the synergy between the different components due to increased interactions between them. The components of a hybrid nanostructure may be selected from a wide range of materials such as fibers, enzymes, quantum dots, conductive polymers, organometallic structures, magnetic nanomaterials. These hybrid nanostructures have enhanced active surface area, excellent adsorption capacity, easy biomolecular conjugation, improved conductivity and electrocatalytic activity. Hybrid nanostructures have been used as nanocarriers, immunological probes for the detection of biomarkers, bioanalysis, catalytical, tissue growth and healing and energy management (Borah *et al.*, 2021; Choi *et al.*, 2021; Diez-Castellnou *et al.*, 2021; Y. Gupta and Ghrera, 2021; Mitra *et al.*, 2021; Mourdikoudis *et al.*, 2021; Yang *et al.*, 2021; Zare and Sarkati, 2021; Zheng *et al.*, 2021).

The TiO₂ nanoparticles use of TiO₂ nanoparticles in several areas of science has grown a lot in recent years. It is noteworthy their use in the medical area solar cells and photocatalysis (Ananthakumar *et al.*, 2016; Kafshgari and Goldman, 2020; McNamara and Tofail, 2017; Wu *et al.*, 2020). In recent studies, X.-F. Zhang *et al.* (2019) concluded that TiO₂ nanoparticles have their photocatalytic activity improved by modifying nano-TiO₂ with noble metals, obtaining conversion rates higher than 60% in the conversion of benzyl alcohol into benzaldehyde. Lin *et al.* (2018) also observed a high photocatalytic activity in lanthanide-doped TiO₂

nanoparticles in dye degradation. Although TiO₂ nanoparticles and composite nanomaterials present high photocatalytic activity as explained, there is still a challenge regarding the use of TiO₂ nanoparticles in the field of catalysis, especially with regard to organic and/or specific catalysis.

In the present work, TiO₂ nanoparticles were synthesized and had their surface modified with gold nanoparticles in order to obtain a nanomaterial with high catalytic activity, which was measured in benzyl alcohol oxidation tests, as described in this manuscript.

2. Experimental

2.1 TiO₂ nanoparticles synthesis

Titanium oxide nanoparticles were synthesized by the hydrothermal method through the hydrolysis of titanium peroxocomplex gel. This gel was synthesized by the reaction between titanium isopropoxide IV (Ti[OCH(CH₃)₂]₄) and a solution of hydrogen peroxide (H₂O₂) 30% by volume, in a molar ratio of 1:10 Ti:H₂O₂, with the volume adjusted to 100 mL using deionized water and the solution refluxed at 80 °C for 15 minutes, obtaining a yellow gel. A 10 g aliquot of this gel was added to 45 mL of deionized water and placed in the aluminum hydrothermal reaction, containing an internal Teflon beaker, placed in an oven at 140 °C for 24 hours. After this period, the solution was oven dried, obtaining a pale powder.

2.2 TiO₂ nanoparticle surface modification with Au nanoparticles

Gold doped TiO₂ nanoparticles were obtained from the surface modification of TiO₂ nanoparticles with gold nanoparticles. Therefore, the reduction of gold in the presence of metal oxide nanoparticles was performed by the adapted Turkevich method (Gorup *et al.*, 2011). In a beaker, 98 mL of deionized water and 0.1 g of TiO₂ nanoparticles were added, heated under magnetic stirring to a temperature of 90 °C. Then, 1.0 mL of HAuCl₄ solution (0.1 mol L⁻¹) and 1.0 mL of sodium citrate solution (0.3 mol L⁻¹) were added. The mixture was kept under stirring and at a controlled temperature of 90 °C for 10 minutes. The solution was cooled to room temperature and the product was centrifuged and washed with deionized water and then dried in an oven.

2.3 Benzyl alcohol oxidation tests

To test the catalytic potential of the nanomaterials, catalytic tests were carried out in the oxidation reaction

of benzyl alcohol in its derivatives in the presence of nanoparticles. One mL of benzyl alcohol was added with 0.3 g of potassium carbonate in the aluminum reactor with 0.005 g of TiO₂/Au nanoparticles which was closed and left for 24 h at 160 °C in the oven. For comparison, the same test was performed under the same conditions using TiO₂ nanoparticles and no catalyst.

2.4 Characterizations

Titanium oxide nanoparticles and gold doped titanium oxide nanoparticles were characterized by X-ray diffraction (XRD), UV-visible spectroscopy and infrared spectroscopy (UV-Vis). All nanoparticles' catalytic activity was investigated in the benzyl alcohol oxidation reaction and followed by infrared spectroscopy and gas chromatography coupled to mass spectrometer (GC-MS).

3. Results

It was possible to perform the synthesis of TiO₂ nanoparticles by the proposed method. X-ray analysis is shown in Fig. 1. The anatase peaks found at 2θ values of 25.28, 36.94, 48.04, 53.89, 55.06, 62.11, 68.76 and 70.30 correspond to the crystallographic planes (101), (103), (200), (105), (211), (213), (116) and (220), respectively. Rutile peaks appear at 2θ values of 27.44, 36.08, 41.22, 44.05, 62.74, 74.40 and 76.50 correspond to the crystallographic planes (110), (101), (111), (210), (002), (320) and (202), respectively. It was determined that the nanostructures had 71% of the anatase crystallographic phase (PDF 00-021-1272) and 29% of the rutile crystallographic phase (PDF 00-021-1276). The crystallite size measured by Scherrer equation was 15 and 27 nm for rutile phase (110 and 310) showing rod shape particles and 9 nm for anatase phase shown spherical shape (101 and 200).

Recently, TiO₂ nanomaterials have been prepared by different methodologies, where liquid phase processing stands out. The characteristics of the material are closely linked to the synthesis methodology (S. Gupta and Tripathi, 2011). It is verified in the literature the possibility of obtaining nanomaterials with different size, morphology and crystallographic phase, as it has been reported the obtention of 60 nm size TiO₂-anatase nanoparticles (J. Zhang *et al.*, 2017), 5.7 nm sized nanorods (Dalod *et al.*, 2017) and even TiO₂-rutile nanotubes sizing 20 nm in diameter (Yan *et al.*, 2010).

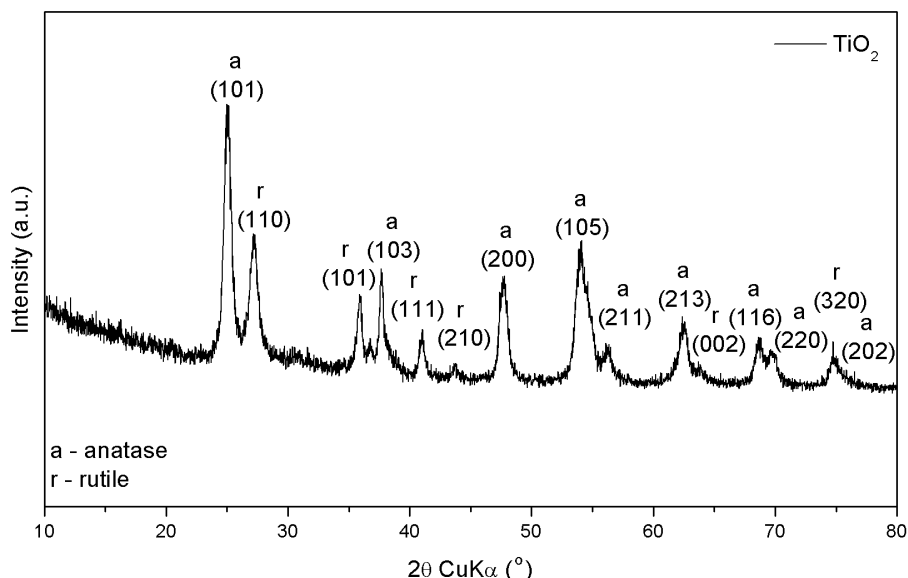


Figure 1. TiO₂ nanoparticles XRD patterns.

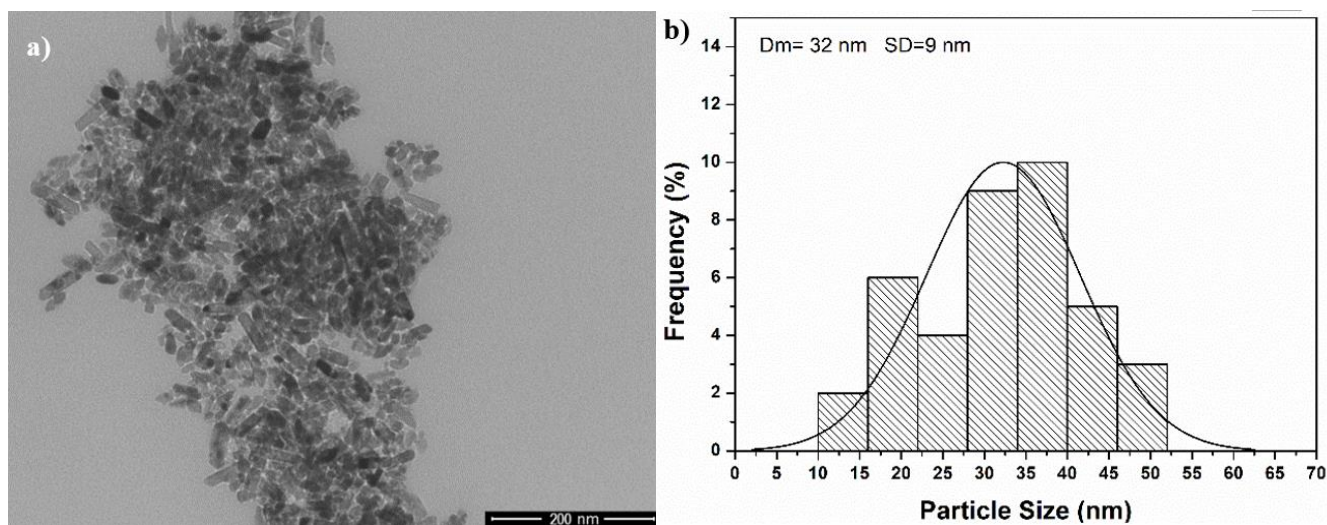


Figure 2. TEM images (a) and size distribution histogram (b) for TiO₂ nanoparticles.

Transmission electron microscopy (TEM) images were able to confirm the average size 32 nm at length and show rod shape morphology, as seen in the Fig. 2. Figure 3 shows a scanning electron microscopy (SEM) image of the TiO₂ nanoparticles, which shows a uniform distribution of the nanomaterial.

TiO₂ nanoparticles modified with gold (TiO₂/Au) were also analyzed by XRD, whose diffractogram is shown in Fig. 4. The presence of Au nanoparticles on the surface of TiO₂ nanoparticles is confirmed by the presence of peaks found at 2θ values of 32.19 and 46.12, corresponding to the crystallographic planes (111) and (200) (Beck *et al.*, 2008; C. Zhao *et al.*, 2006).

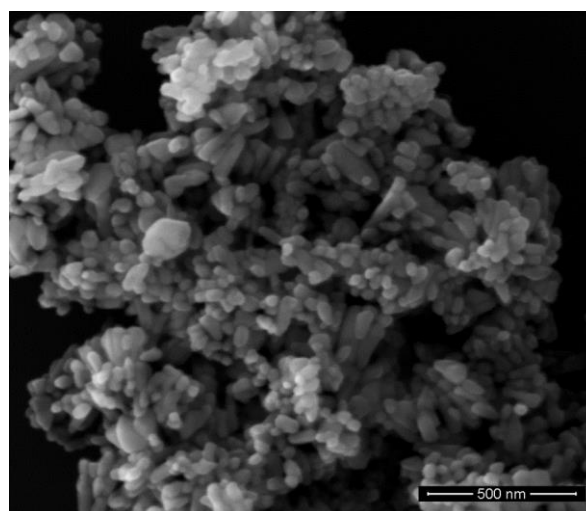


Figure 3. SEM image of TiO₂ nanoparticles.

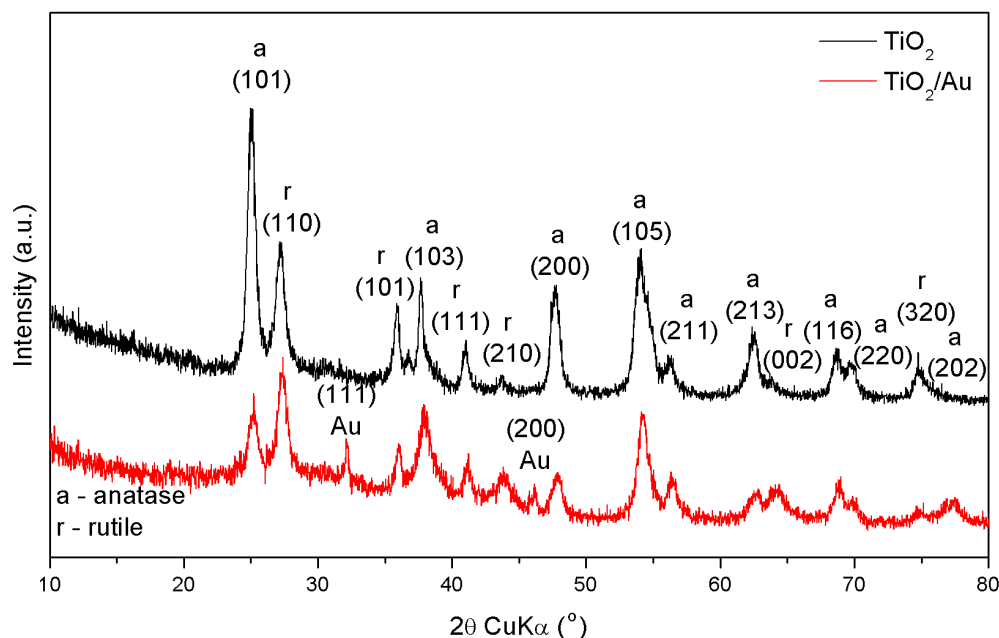


Figure 4. TiO₂/Au nanoparticles XRD patterns.

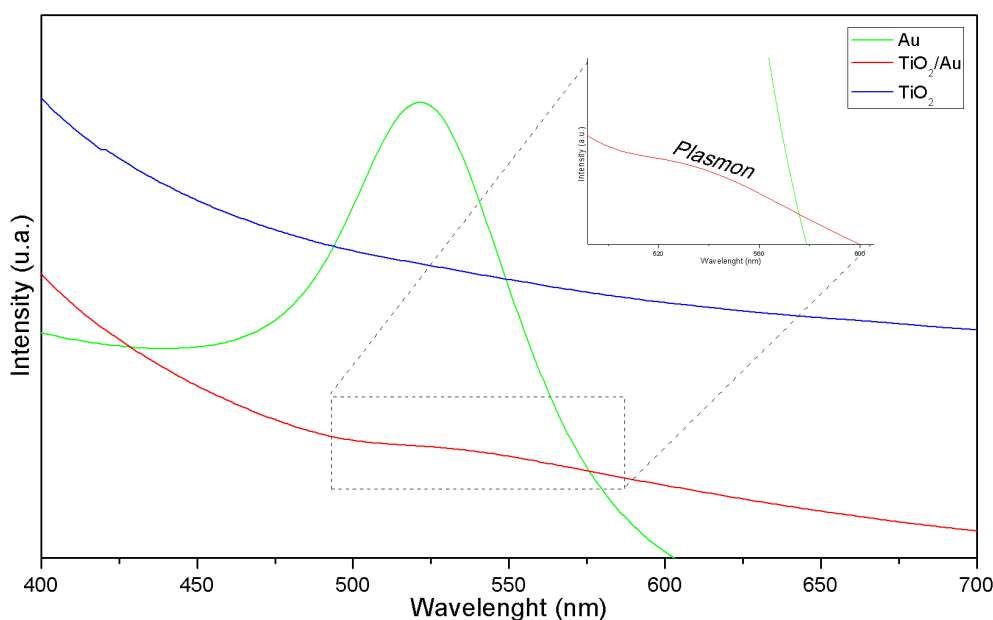


Figure 5. TiO₂/Au, TiO₂ and Au nanoparticles UV-Vis spectra.

The presence of gold nanoparticles coating the surface of titanium oxide nanoparticles was also verified by UV-Vis spectroscopy showing the Au nanoparticles the plasmon band at 550 nm. The presence of the plasmon band characteristic of gold in TiO₂/Au nanoparticles contributes to the characterization of the material (Verma *et al.*, 2020). This band formation can be seen in Fig. 5.

Figure 6 shows FEG-SEM images of TiO₂/Au nanoparticles. Although it is possible to observe the TiO₂ nanoparticles, the spherical gold nanoparticles are

not visible. It is believed that this was due to image resolution or even the low concentration or size of the nanoparticles. However, it is noteworthy that the other characterization techniques proved their presence.

TiO₂ nanoparticles were shown to be active for catalyzing the oxidation of benzyl alcohol, showing significant yield, even more so for titanium oxide nanoparticles coated with gold nanoparticles. Uncoated TiO₂ nanoparticles showed a catalytic yield of 1.4% and gold doped TiO₂ nanoparticles showed a catalytic yield of 73% and this catalyst showed to be selective (> 98%),

converting benzyl alcohol only to benzaldehyde. **Figure 7** shows the chromatogram of the tests' product. An analysis of the precursor was also carried out under the same conditions to identify and determine the level of purity of the alcohol, since it is naturally oxidized by air over time.

In addition, the mass spectrum of the species was also analyzed. **Figure 8a** shows the mass spectra of benzyl alcohol, as well as its characteristic fragmentation, showing peaks in m/z 108, 107, 91, 79, 77 and 51, which, according to the literature and the equipment's database, characterize the benzyl alcohol. **Figure 8b** shows the mass spectrum and characteristic fragmentation of benzaldehyde, the peaks at m/z 106, 105, 77, 51 and 50 are also in accordance with the literature and characterize benzaldehyde. **Figure 8c** shows the mass spectrum and characteristic fragmentation of benzyl benzoate, whose peaks at 212, 105, 91 and 77 characterize benzyl benzoate.

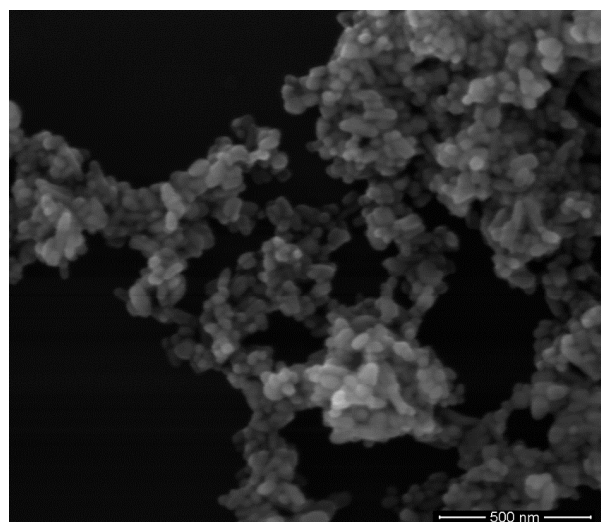


Figure 6. FEG-SEM image of TiO₂/Au nanoparticles.

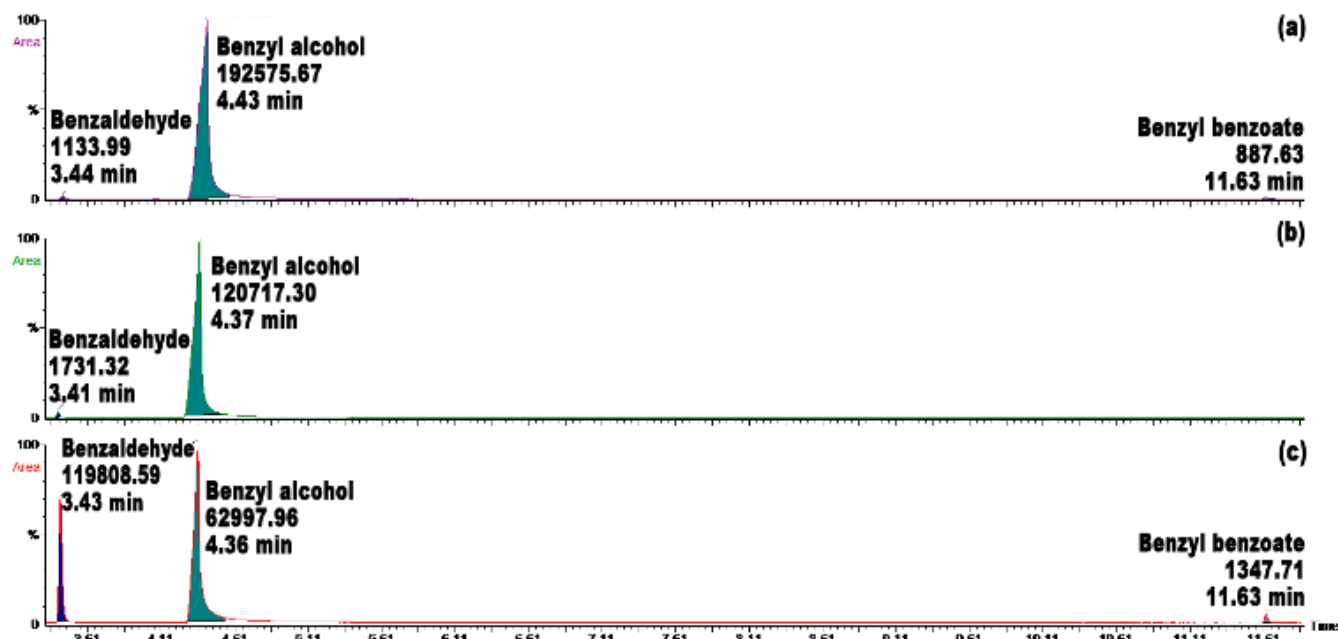
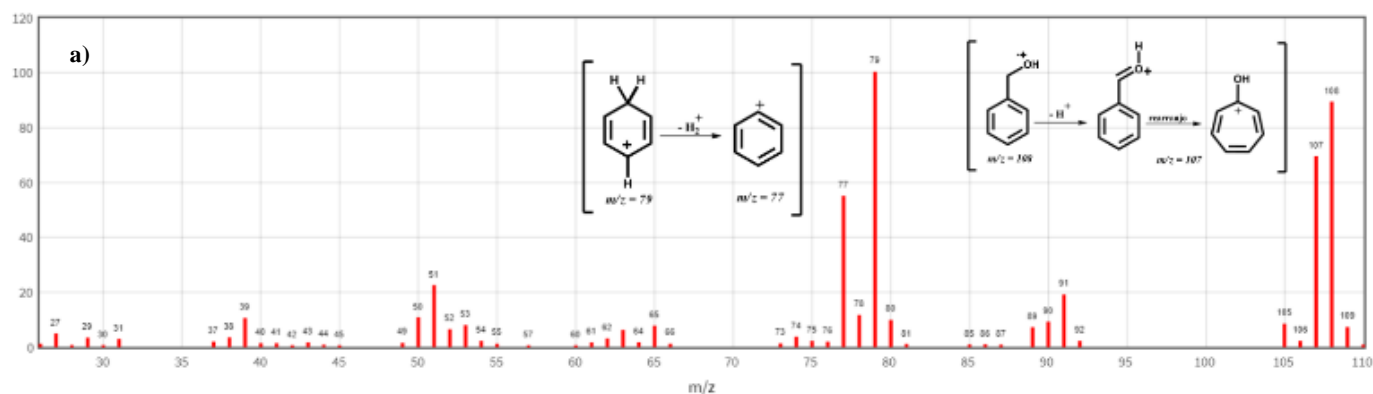


Figure 7. Chromatogram of (a) benzyl alcohol, (b) TiO₂ NPs catalyzed product and (c) TiO₂/Au NPs catalyzed product.



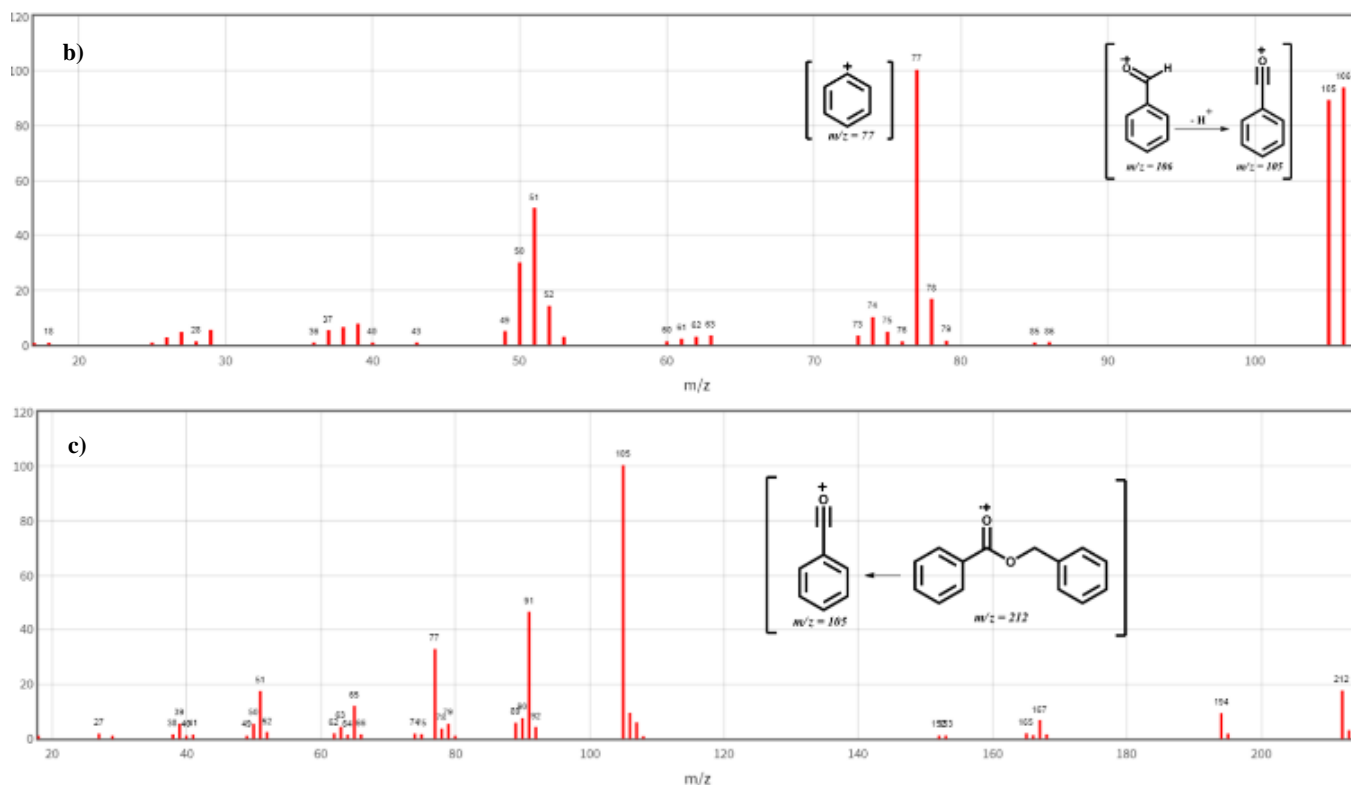


Figure 8. Mass spectra and characteristic fragmentations: (a) Benzyl alcohol; (b) Benzaldehyde and (c) Benzyl benzoate.

Figure 9 shows the Fourier transform infrared spectroscopy (FTIR) spectra of the tests' products, where the appearance of a characteristic band by the C=O stretch can be noticed, which also shows the formation of benzaldehyde.

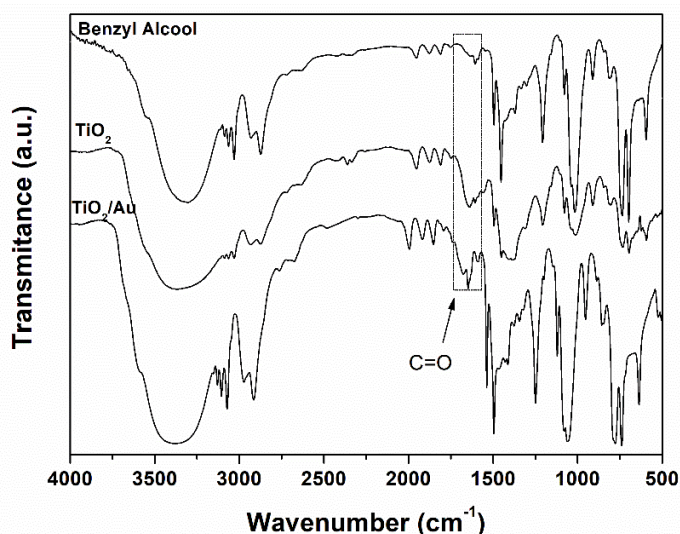


Figure 9. FTIR spectra for TiO₂/Au NPs, TiO₂ NPs oxidated product and pure benzyl alcohol.

The Gas chromatography–mass spectrometry (CG-MS) and FTIR spectra showed that the nanoparticles

showed selectivity, where only the presence of benzaldehyde was observed as a reaction product. Selective oxidation of alcohols is one of the most significant transformations of organic chemistry since it is essential for industrial intermediates production, such as ketones, epoxides, aldehydes and acids. Previous reports (Conte *et al.*, 2010; Fristrup *et al.*, 2008), that supported that Au nanoparticles catalyze the oxidation of benzaldehyde by enhancing the formation of the intermediate acyl radicals, rule out the possibility that the supported gold–palladium catalyst used in our earlier work on benzyl alcohol oxidation is responsible for the inhibition of benzaldehyde oxidation. The only other component, which could prevent the further oxidation of benzaldehyde, is the remaining benzyl alcohol. In recent study, Sankar *et al.* (2014) demonstrate by chromatographic analyses of reaction mixtures during the initial stages of oxidation of benzyl alcohol; the analysis revealed that no other products were formed and confirm Partenheimer's observations that in benzyl alcohol oxidation catalyzed by Co (III), benzoic acid production only begins to accelerate when the benzyl alcohol level in the reaction mixture falls below ~10%. That a very small amount of benzyl alcohol, present in benzaldehyde, is evidently involved in preventing the oxidation of benzaldehyde to benzoic

acid forms the premise for the more detailed studies presented below. The authors showed that benzyl alcohol was probably acting to quench free radicals involved in autoxidation of benzaldehyde and that related molecules should act similarly.

Comparing with other authors giving in Tab. 1, it is noted that TiO₂ nanoparticles are used for developing several nanostructured catalysts, mainly using them with noble metals. The nanomaterial synthesized in this work presented a conversion rate and selectivity superior to other works.

Table 1. Catalytic performance of nanoparticles in benzyl alcohol oxidation.

Type	Catalyst	Conversion (%)	Selectivity ^a (%)	Reference
Catalysis	Pd/TiO ₂	4.5	85.9	Sun <i>et al.</i> (2017)
	Au@Pd/TiO ₂	14.3	91.6	
	Au/TiO ₂ nanotube	23.2	> 99.0	Verma <i>et al.</i> (2020)
	Au/TiO ₂ nanorod	32.5	> 99.0	
	Au/TiO ₂ microporous	9.6	> 99.0	
	Pd/TiO ₂	57.6	74.1	Weerachawanasak <i>et al.</i> (2015)
	Pt/TiO ₂ (anatase)	76.7	> 99.0	Liu <i>et al.</i> (2017)
	Pt/TiO ₂ (rutile)	34.3	> 99.0	
	TiO ₂	1.6	79.3	Du <i>et al.</i> (2020)
	Pd/TiO ₂	39.1	70.3	
	TiO ₂	3.0	88.0	Nowicka <i>et al.</i> (2019)
	Pd/Zn/TiO ₂	52.0	67.0	
Photocatalysis	TiO ₂	3.4	> 98.0	X.-F. Zhang <i>et al.</i> (2019)
	Au/TiO ₂	16.3	> 98.0	
	Pt/TiO ₂	32.2	> 98.0	

^a Selectivity to benzaldehyde.

4. Conclusions

We presented herein the synthesis of a heterogeneous catalyst comprised of TiO₂ and TiO₂/Au NPs, with a controlled rod shape morphology and average size 32 nm. The catalyst exhibited remarkable and efficient activity for the benzyl alcohol oxidation. The CG-MS and FTIR spectra showed that the nanoparticles showed selectivity, where only the presence of benzaldehyde was observed as a reaction product. This work provides great potential for the selective oxidation of alcohols with high activity.

Authors' contribution

Conceptualization: Gabriel, A. M.; Malaquias, K. S.; Cristovan, F. H.; Arantes, T. M.

Data curation: Gabriel, A. M.; Malaquias, K. S.

Formal Analysis: Gabriel, A. M.; Malaquias, K. S.; Arantes, T. M.

Funding acquisition: Arantes, T. M.

Investigation: Gabriel, A. M.; Malaquias, K. S.; Cristovan, F. H.; Arantes, T. M.

Methodology: Gabriel, A. M.; Malaquias, K. S.; Cristovan, F. H.; Arantes, T. M.

Project administration: Cristovan, F. H.; Arantes, T. M.

Resources: Malaquias, K. S.; Cristovan, F. H.; Arantes, T. M.

Software: Not applicable.

Supervision: Arantes, T. M.

Validation: Malaquias, K. S.; Cristovan, F. H.; Arantes, T. M.

Visualization: Gabriel, A. M.; Arantes, T. M.

Writing – original draft: Gabriel, A. M.

Writing – review & editing: Gabriel, A. M.; Cristovan, F. H.; Arantes, T. M.

Data availability statement

All data sets were generated or analyzed in the current study.

Funding

Not applicable.

Acknowledgments

Not applicable.

References

- Abisharani, J. M.; Devikala, S.; Kumar, R. D.; Arthanareeswari, M.; Kamaraj, P. Green synthesis of TiO₂ nanoparticles using *Cucurbita pepo* seeds extract. *Mater. Today Proc.* **2019**, *14*, 302–307. <https://doi.org/10.1016/j.matpr.2019.04.151>
- Ali, N.; Ali, F.; Khurshid, R.; Ikramullah; Ali, Z.; Afzal, A.; Bilal, M.; Iqbal, H. M. N.; Ahmad, I. TiO₂ nanoparticles and epoxy-TiO₂ nanocomposites: A review of synthesis, modification strategies, and photocatalytic potentialities. *J. Inorg. Organomet. Polym. Mater.* **2020**, *30*, 4829–4846. <https://doi.org/10.1007/s10904-020-01668-6>
- Ananthakumar, S.; Ramkumar, J.; Babu, S. M. Semiconductor nanoparticles sensitized TiO₂ nanotubes for high efficiency solar cell devices. *Renew. Sustain. Energy Rev.* **2016**, *57*, 1307–1321. <https://doi.org/10.1016/j.rser.2015.12.129>
- Arantes, T. M. Incorporação por via coloidal de nanopartículas sintéticas em polímeros comerciais. Master thesis, Universidade Federal de São Carlos, São Carlos, SP, 2009.
- Bavanilatha, M.; Yoshitha, L.; Nivedhitha, S.; Sahithya, S. Bioactive studies of TiO₂ nanoparticles synthesized using *Glycyrrhiza glabra*. *Biocatal. Agric. Biotechnol.* **2019**, *19*, 101131. <https://doi.org/10.1016/j.bcab.2019.101131>
- Beck, A.; Horváth, A.; Stefler, G.; Katona, R.; Geszti, O.; Tolnai, G.; Liotta, L. F.; Guzzi, L. Formation and structure of Au/TiO₂ and Au/CeO₂ nanostructures in mesoporous SBA-15. *Catal. Today* **2008**, *139* (3), 180–187. <https://doi.org/10.1016/j.cattod.2008.05.039>
- Borah, R.; Ninakanti, R.; Nuyts, G.; Peeters, H.; Pedrazo-Tardajos, A.; Nuti, S.; Velde, C. V.; De Wael, K.; Lenaerts, S.; Bals, S.; Verbruggen, S. W. Selectivity in the Ligand Functionalization of Photocatalytic Metal Oxide Nanoparticles for Phase Transfer and Self-Assembly Applications. *Chem. Eur. J.* **2021**, *27* (35), 9011–9021. <https://doi.org/10.1002/chem.202100029>
- Cao, Z.; Yang, L.; Chen, H.; Xu, C.; Qi, D.; Zhu, S.; Ziener, U. Preparation of Au/TiO₂ nanocomposite particles with high visible-light photocatalytic activity in inverse miniemulsions. *Colloid Polym. Sci.* **2015**, *293*, 277–288. <https://doi.org/10.1007/s00396-014-3412-8>
- Chen, X.; Mao, S. S. Titanium dioxide nanomaterials: synthesis, properties, modifications and applications. *Chem. Rev.* **2007**, *107* (7), 2891–2959. <https://doi.org/10.1021/cr0500535>
- Choi, D.; Kim, J. H.; Kwon, D. C.; Shin, C. H.; Ryu, H.; Yoon, E.; Lee, H.-C. Crystalline silicon nanoparticle formation by tailored plasma irradiation: Self-structurization, nucleation and growth acceleration, and size control. *Nanoscale* **2021**, *13* (23), 10356–10364. <https://doi.org/10.1039/D1NR00628B>
- Conte, M.; Miyamura, H.; Kobayashi, S.; Chechik, V. Enhanced acyl radical formation in the Au nanoparticle-catalysed aldehydeoxidation. *Chem. Commun.* **2010**, *46* (1), 145–147. <https://doi.org/10.1039/B918200D>
- Dalod, A. R. M.; Henriksen, L.; Grande, T.; Einarsrud, M.-A. Functionalized TiO₂ nanoparticles by single-step hydrothermal synthesis: The role of the silane coupling agents. *Beilstein J. Nanotechnol.* **2017**, *8* (1), 304–312. <https://doi.org/10.3762/bjnano.8.33>
- Diez-Castellnou, M.; Suo, R.; Marro, N.; Matthew, S. A. L.; Kay, E. R. Rapidly adaptive all-covalent nanoparticle surface engineering. *Chem. Eur. J.* **2021**, *27* (38), 9948–9953. <https://doi.org/10.1002/chem.202101042>
- Du, M.; Zeng, G.; Ye, C.; Jin, H.; Huang, J.; Sun, D.; Li, Q.; Chen, B.; Li, X. Solvent-free photo-thermocatalytic oxidation of benzyl alcohol on Pd/TiO₂ (B) nanowires. *Mol. Catal.* **2020**, *483*, 110771. <https://doi.org/10.1016/j.mcat.2020.110771>
- Fristrup, P.; Johansen, L. B.; Christensen, C. H. Mechanistic investigation of the gold-catalyzed aerobic oxidation of aldehydes: added insight from Hammett studies and isotopic labelling experiments. *Chem. Commun.* **2008**, 7345 (24), 2750–2752. <https://doi.org/10.1039/b803270j>
- Gorup, L. F.; Longo, E.; Leite, E. R.; Camargo, E. R. Moderating effect of ammonia on particle growth and stability of quasi-monodisperse silver nanoparticles synthesized by the Turkevich method. *J. Colloid Interface Sci.* **2011**, *360* (2), 355–358. <https://doi.org/10.1016/j.jcis.2011.04.099>
- Gupta, S. M.; Tripathi, M. A review of TiO₂ nanoparticles. *Chin. Sci. Bull.* **2011**, *56*, 1639. <https://doi.org/10.1007/s11434-011-4476-1>
- Gupta, Y.; Ghrera, A. S. Recent advances in gold nanoparticle-based lateral flow immunoassay for the detection of bacterial infection. *Arch. Microbiol.* **2021**, *203*, 3767–3784. <https://doi.org/10.1007/s00203-021-02357-9>
- Haider, A. J.; Al-Anbari, R. H.; Kadhim, G. R.; Salame, C. T. Exploring potential environmental applications of TiO₂ nanoparticles. *Energy Procedia* **2017**, *119*, 332–345. <https://doi.org/10.1016/j.egypro.2017.07.117>
- Kafshgari, M. H.; Goldmann, W. H. Insights into theranostic properties of titanium dioxide for nanomedicine. *Nano-Micro Lett.* **2020**, *12*, 22. <https://doi.org/10.1007/s40820-019-0362-1>
- Kaneta, K.; Tahara, S.; Idota, N.; Sugahara, Y. Preparation of inorganic-organic hybrid gels by radical exchange reaction

- using TiO₂ nanoparticles modified with organophosphonic acid bearing C-ON bonds. *Mater. Today Proc.* **2019**, *16* (Part. 1), 180–186. <https://doi.org/10.1016/j.matpr.2019.05.291>
- Li, J.; Wu, X.; Liu, S. W. Fluorinated TiO₂ Hollow Photocatalysts for Photocatalytic Applications. *Wuli Huaxue Xuebao/ Acta Phys. - Chim. Sin.* **2021**, *37* (6), 2009038. <https://doi.org/10.3866/PKU.WHXB202009038>.
- Lin, X.; Chen, H.; Hu, Z.; Hou, Y.; Dai, W. Enhanced visible light photocatalysis of TiO₂ by Co-modification with Eu and Au nanoparticles. *Solid State Sci.* **2018**, *83*, 181–187. <https://doi.org/10.1016/j.solidstatesciences.2018.07.007>
- Liu, J.; Zou, S.; Lu, L.; Zhao, H.; Xiao, L.; Fan, J. Room temperature selective oxidation of benzyl alcohol under base-free aqueous conditions on Pt/TiO₂. *Catal. Commun.* **2017**, *99*, 6–9. <https://doi.org/10.1016/j.catcom.2017.05.015>
- McNamara, K.; Tofail, S. A. M. Nanoparticles in biomedical applications. *Adv. Phys. X* **2017**, *2* (1), 54–88. <https://doi.org/10.1080/23746149.2016.1254570>
- Messaddeq, S. H.; Bonnet, A.-S.; Santagnelli, S. H.; Salek, G.; Colmenares, Y. N.; Messaddeq, Y. Photopolymerized hybrids containing TiO₂ nanoparticles for gradient-index lens. *Mater. Chem. Phys.* **2019**, *236*, 121793. <https://doi.org/10.1016/j.matchemphys.2019.121793>
- Mitra, A.; Trifkovic, M.; Ponnurangam, S. Surface functionalization-induced effects on nanoparticle dispersion and associated changes in the thermophysical properties of polymer nanocomposites. *Macromolecules* **2021**, *54* (9), 3962–3971. <https://doi.org/10.1021/acs.macromol.1c00184>
- Montalvo-Quiros, S.; Luque-Garcia, J. L. Combination of bioanalytical approaches and quantitative proteomics for the elucidation of the toxicity mechanisms associated to TiO₂ nanoparticles exposure in human keratinocytes. *Food Chem. Toxicol.* **2019**, *127*, 197–205. <https://doi.org/10.1016/j.fct.2019.03.036>
- Mourdikoudis, S.; Kostopoulou, A.; LaGrow, A. P. Magnetic nanoparticle composites: Synergistic effects and applications. *Adv. Sci.* **2021**, *8* (12), 2004951. <https://doi.org/10.1002/advs.202004951>
- Nowicka, E.; Althahban, S.; Leah, T. D.; Shaw, G.; Morgan, D.; Kiely, C. J.; Roldan, A.; Hutchings, G. J. Benzyl alcohol oxidation with Pd-Zn/TiO₂: Computational and experimental studies. *Sci. Technol. Adv. Mater.* **2019**, *20* (1), 367–378. <https://doi.org/10.1080/14686996.2019.1598237>
- Ozdamar, Z. D.; Sahmetlioglu, E.; Narin, I.; Cumaoglu, A. Synthesis of gold and silver nanoparticles using flavonoid quercetin and their effects on lipopolysaccharide induced inflammatory response in microglial cells. *3 Biotech* **2019**, *9* (6), 212. <https://doi.org/10.1007/s13205-019-1739-z>
- Radetić, M. Functionalization of textile materials with TiO₂ nanoparticles. *J. Photochem. Photobiol. C: Photochem. Rev.* **2013**, *16*, 62–76. <https://doi.org/10.1016/j.jphotochemrev.2013.04.002>
- Reddy, P. N. K.; Shaik, D. P. M. D.; Ganesh, V.; Nagamalleswari, D.; Thyagarajan, K.; Prasanth, P. V. Structural, optical and electrochemical properties of TiO₂ nanoparticles synthesized using medicinal plant leaf extract. *Ceram. Int.* **2019**, *45* (13), 16251–16260. <https://doi.org/10.1016/j.ceramint.2019.05.147>
- Sankar, M.; Nowicka, E.; Carter, E.; Murphy, D. M.; Knight, D. W.; Bethell, D.; Hutchings, G. J. The benzaldehyde oxidation paradox explained by the interception of peroxy radical by benzyl alcohol. *Nat. Commun.* **2014**, *5*, 3332. <https://doi.org/10.1038/ncomms4332>
- Srinivasan, M.; Venkatesan, M.; Arumugam, V.; Natesan, G. Green synthesis and characterization of titanium dioxide nanoparticles (TiO₂ NPs) using *Sesbania grandiflora* and evaluation of toxicity in zebra fish embryos. *Process Biochem.* **2019**, *80*, 197–202. <https://doi.org/10.1016/j.procbio.2019.02.010>
- Sun, J.; Han, Y.; Fu, H.; Qu, X.; Xu, Z.; Zheng, S. Au@Pd/TiO₂ with atomically dispersed Pd as highly active catalyst for solvent-free aerobic oxidation of benzyl alcohol. *Chem. Eng. J.* **2017**, *313*, 1–9. <https://doi.org/10.1016/j.cej.2016.12.024>
- Tayel, A.; Ramadan, A. R.; El Seoud, O. A. Titanium dioxide/graphene and titanium dioxide/graphene oxide nanocomposites: synthesis, characterization and photocatalytic applications for water decontamination. *Catalysts* **2018**, *8* (11), 491. <https://doi.org/10.3390/catal8110491>
- Tomovska, R.; Daniloska, V.; Asua, J. M. UV/Vis photocatalytic functionalization of TiO₂ nanoparticle surfaces toward water repellent properties. *J. Mater. Chem.* **2011**, *21* (43), 17492–17497. <https://doi.org/10.1039/c1jm13412d>
- Verma, P.; Mori, K.; Kuwahara, Y.; Cho, S. J.; Yamashita, H. Synthesis of plasmonic gold nanoparticles supported on morphology-controlled TiO₂ for aerobic alcohol oxidation. *Catal. Today* **2020**, *35*, 255–261. <https://doi.org/10.1016/j.cattod.2019.10.014>
- Wang, Z.; Feng, J.; Li, X.; Oh, R.; Shi, D.; Akdim, O.; Xia, M.; Zhao, L.; Huang, X.; Zhang, G. Au-Pd nanoparticles immobilized on TiO₂ nanosheet as an active and durable catalyst for solvent-free selective oxidation of benzyl alcohol. *J. Colloid Interface Sci.* **2021**, *588*, 787–794. <https://doi.org/10.1016/j.jcis.2020.11.112>
- Weerachawanasak, P.; Hutchings, G. J.; Edwards, J. K.; Kondrat, S. A.; Miedziak, P. J.; Prasertham, P.; Panpranot, J. Surface functionalized TiO₂ supported Pd catalysts for

solvent-free selective oxidation of benzyl alcohol. *Catal. Today* **2015**, *250*, 218–225. <https://doi.org/10.1016/j.cattod.2014.06.005>

Wu, Y.; Chen, L.; Chen, F.; Zou, H.; Wang, Z. A key moment for TiO₂: Prenatal exposure to TiO₂ nanoparticles may inhibit the development of offspring. *Ecotoxicol. Environ. Saf.* **2020**, *202*. <https://doi.org/10.1016/j.ecoenv.2020.110911>

Yan, J.; Feng, S.; Lu, H.; Wang, J.; Zheng, J.; Zhao, J.; Li, L.; Zhu, Z. Alcohol induced liquid-phase synthesis of rutile titania nanotubes. *Mater. Sci. Eng. B* **2010**, *172* (2), 114–120. <https://doi.org/10.1016/j.mseb.2010.04.032>

Yang, F.; Liu, X.; Yang, Z. Chiral metal nanoparticle superlattices enabled by porphyrin-based supramolecular structures. *Angew. Chemie Int. Ed.* **2021**, *60* (26), 14671–14678. <https://doi.org/10.1002/anie.202103809>

Zare, M.; Sarkati, M. N. Chitosan-functionalized Fe₃O₄ nanoparticles as an excellent biocompatible nanocarrier for silymarin delivery. *Polym. Adv. Technol.* **2021**, *32* (10), 4094–4100. <https://doi.org/10.1002/pat.5416>

Zhang, J.; Wang, D.; Zhang, H. One-step hydrothermal synthesis of small TiO₂ porous nanoparticles for efficient degradation of organic dyes. *J. Nanosci. Nanotechnol.* **2017**, *18* (5), 3185–3191. <https://doi.org/10.1166/jnn.2018.14663>

Zhang, X.-F.; Wang, Z.; Zhong, Y.; Qiu, J.; Zhang, X.; Gao, Y.; Gu, X.; Yao, J. TiO₂ nanorods loaded with Au–Pt alloy nanoparticles for the photocatalytic oxidation of benzyl alcohol. *J. Phys. Chem. Solids* **2019**, *126*, 27–32. <https://doi.org/10.1016/j.jpcs.2018.10.026>

Zhao, C.; Zhao, Q.; Zhao, Q.; Qiu, J.; Zhu, C. Deposition of Au/TiO₂ film by pulsed laser. *Appl. Surf. Sci.* **2006**, *252* (20), 7415–7421. <https://doi.org/10.1016/j.apsusc.2005.08.086>

Zhao, W.; Li, Y.; Shen, W. Tuning the shape and crystal phase of TiO₂ nanoparticles for catalysis. *Chem. Commun.* **2021**, *57* (56), 6838–6850. <https://doi.org/10.1039/D1CC01523K>

Zheng, G.; Peng, H.; Jiang, J.; Kang, G.; Liu, J.; Zheng, J.; Liu, Y. Surface functionalization of PEO nanofibers using a TiO₂ suspension as sheath fluid in a modified coaxial electrospinning process. *Chem. Res. Chin. Univ.* **2021**, *37* (3), 571–577. <https://doi.org/10.1007/s40242-021-1118-2>

YVO₄:RE (RE = Eu, Tm, and Yb/Er) nanoparticles synthesized by the microwave-assisted hydrothermal method for photoluminescence application

Ivo Mateus Pinatti¹⁺, Camila Cristina de Foggi², Marcio Daldin Teodoro³, Elson Longo⁴, Alexandre Zirpoli Simões¹, Ieda Lúcia Viana Rosa⁴

1. São Paulo State University, Faculty of Engineering, Guaratinguetá, Brazil.
2. Federal University of Rio Grande do Sul, School of Dentistry, Porto Alegre, Brazil.
3. Federal University of São Carlos, Department of Physics, São Carlos, Brazil.
4. Federal University of São Carlos, Center for the Development of Functional Materials, São Carlos, Brazil.

+Corresponding author: Ivo Mateus Pinatti, **Phone:** +55 16 33518214, **Email address:** ivopinatti@hotmail.com

ARTICLE INFO

Article history:

Received: July 29, 2021

Accepted: October 11, 2021

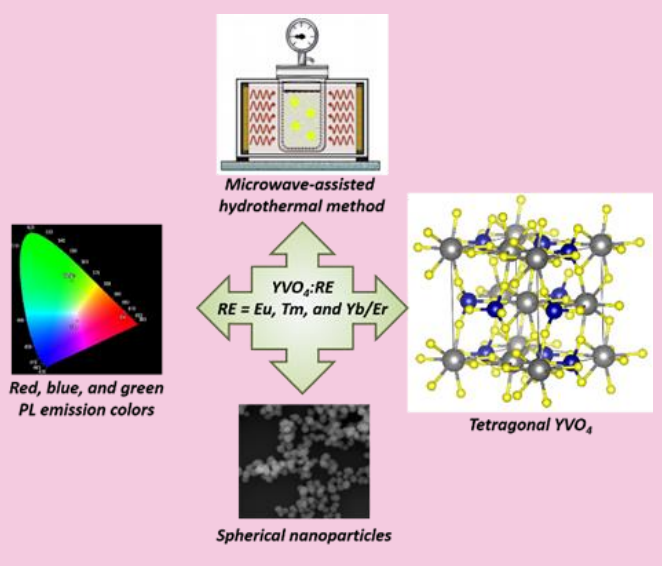
Published: April 11, 2022

Keywords:

1. yttrium vanadate
2. rare earth
3. photoluminescence
4. semiconductor

Section Editors: Elson Longo and Juan Manuel Andrés Bort

ABSTRACT: Here, an experimental study is presented on the YVO₄:RE (RE = Eu, Tm, and Yb/Er) nanoparticles synthesized by means of the microwave-assisted hydrothermal method. Different characterization techniques (X-ray diffraction, Raman and ultraviolet-visible spectroscopy, field emission scanning electron microscopy, transmission electron microscopy, and photoluminescence emissions) have been employed to examine the structural, optical, as well as its morphology and photoluminescent properties. The as-synthesized samples present different emission colors due to RE³⁺ ions, as well as nanosized spherical morphology because of synthesis method. These materials can be considered efficient materials for optical devices.



1. Introduction

Photoluminescent (PL) materials with high quantum efficiency present practical applications in many research areas, such as optoelectronics, medicine, biolabels, physics, among others (Ferreira *et al.*, 2018; Panayiotakis *et al.*, 1996; Shen *et al.*, 2010). Consequently, several inorganic matrices are studied, in which its PL property was deeply explored due to its host lattice composition, structure, morphology as well as doping and others crystal modifications (Li *et al.*, 2021). Ideally, these materials may present well-defined characteristics such as size, optical properties, and a wide range of emission colors (Liu *et al.*, 2016).

Moreover, visible-emitting phosphors can be achieved by doping different kinds of rare earth (RE) ions into lanthanide orthovanadates. The orthovanadate matrix absorbs in the ultraviolet region of electromagnetic spectrum due to ligand-metal charge transfer (LMCT) from the 2p orbital in O^{2-} to the 3d orbital in vanadate. The YVO_4 nanoparticles, as an example, are an ideal transparent host lattice for PL activators and present low toxicity in biological medium (Rivera-Enríquez and Fernández-Osorio, 2021). YVO_4 also presents relative low phonon energy, excellent thermal, mechanical, and chemical stability and high optical performance. Furthermore, the D_{2d} local point symmetry of the eight-coordinated Y^{3+} ion in the tetragonal crystal structure (space group D_{4h}) is an ideal doping site for RE^{3+} ions (Liu *et al.*, 2015). For instance, controlled fabrication of $YVO_4:Eu^{3+}$ nanoparticles and nanowires were achieved by microwave assisted chemical synthesis (Huong *et al.*, 2016).

Several works related the doping of RE^{3+} ions into different types of inorganic matrices (Pinatti *et al.*, 2015; 2016; 2019a; 2019b; Yang *et al.*, 2018). The RE emissions arise from the 4f–4f or 5d–4f transitions from the UV to near-IR range of electromagnetic spectrum. Also, upconverting (UC) materials are an unprecedented technology which consists of absorption of two or more lower-energy photons and subsequently emission of one higher-energy photon. This strategy is specially used for solar energy materials, bioimaging, among other applications. Materials composed of Yb^{3+}/Er^{3+} as activator ions can be efficiently excited using NIR (near-infrared) laser radiation to generate visible emission. For example, photostable and small $YVO_4:Yb/Er$

upconversion nanoparticles in water were obtained and presented intense upconversion emission (Alkahtani *et al.*, 2021). However, many of these materials present poor luminescence efficiency and/or complicated synthesis procedure, which results in no defined or irregular sizes particles (Ji *et al.*, 2021; Kshetri *et al.*, 2018; Sousa Filho *et al.*, 2019; Woźny *et al.*, 2019).

Accordingly, in this work, we report the synthesis of $YVO_4:RE$ (RE = Eu, Tm, and Yb/Er) nanoparticles by the microwave-assisted hydrothermal (MAH) method. These nanoparticles were structurally characterized and potentially studied in terms of its PL properties. In addition, the structure, vibrational frequency and morphology are compared to rationalize the structure, morphology, and PL emissions.

2. Experimental

2.1 Synthesis

One mmol of NH_4VO_3 (99%, Sigma-Aldrich) was dissolved in 40 mL of distilled water at room temperature under magnetic stirring until the reagent was completely dissolved. Additionally, 2 mmol of $Y(NO_3)_3 \cdot 4H_2O$ (99.999%, Sigma-Aldrich) was dissolved in 40 mL of distilled water at room temperature. $RE(NO_3)_3$ (RE = Eu, Tm, Yb, and Er) solutions were prepared by dissolving RE_2O_3 in aqueous hot solution of HNO_3 and evaporating the excess of acid. Stoichiometric volume of RE solutions were mixed together with the Y solution. The amount of 5 mol% of Eu^{3+} , and Tm^{3+} ; and 5 mol% $Yb^{3+}/2$ mol% Er^{3+} were chosen due to previous works related to maximum PL emission intensity achieved. After complete dissolution of the reactants, the V solution was mixed with the Y solution to obtain YVO_4 and with the Y/RE solution to obtain $YVO_4:RE$ nanoparticles. Subsequently, the mixture was stirred for 10 min, and, thereafter, it was transferred to the MAH system at 160 °C for 32 min, as it was the ideal conditions for many materials obtained by this methodology. The precipitates formed were collected at room temperature, washed with distilled water until the pH was neutralized, and dried in a conventional furnace at 60 °C for 12 h. Figure 1 shows a representation of the synthesis procedure herein described.

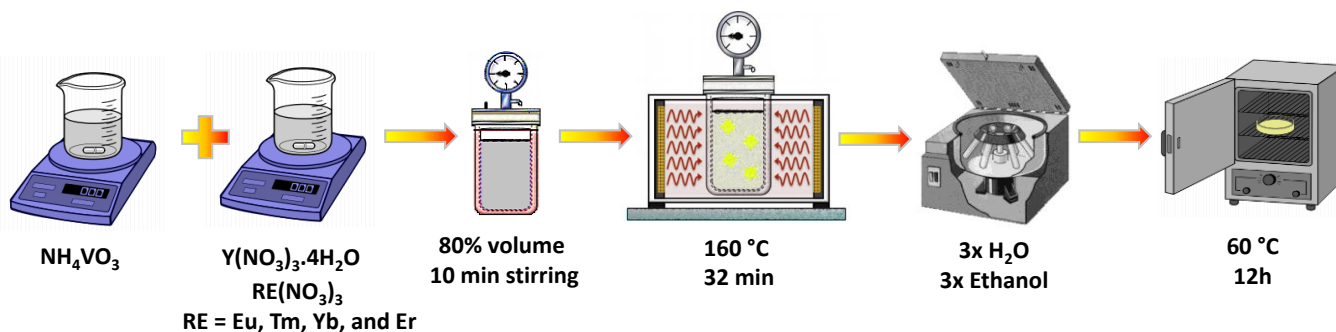


Figure 1. Schematic representation of synthesis procedure of the nanoparticles.

2.2 Characterizations

The nanoparticles were structurally characterized by X-ray diffraction (XRD) patterns using a D/Max-2000PC diffractometer Rigaku (Japan) with $\text{Cu K}\alpha$ radiation ($\lambda = 1.5406 \text{ \AA}$) in the 2θ range from 10° to 80° in the normal routine, with a scanning velocity of 2° min^{-1} . This unit cell was modelled using the visualization for electronic and structural analysis (VESTA) program (Momma and Izumi, 2008; 2011), version 3. Micro-Raman spectroscopy was conducted on a Horiba Jobin-Yvon (Japan) spectrometer charge-coupled device detector and argon-ion laser (Melles Griot, United States) operating at 532 nm with a maximum power of 200 mW. The ultraviolet-visible spectrophotometry (UV-vis) spectra were taken using a spectrophotometer (model Cary 5G) (Varian, USA) in diffuse-reflectance mode. Morphological analysis of the particles was recorded via field-emission scanning electron microscopy (FE-SEM) using a Carl Zeiss microscope (model Supra 35) operated at an accelerating voltage of 30 kV and a working distance of 3.7 mm. Transmission electron microscopy (TEM) and high-resolution transmission electron microscopy (HRTEM) analysis was performed using a Jeol JEM-2100F with a field-emission gun (FEG) operating at 200 kV. For the micrographs, the samples (approximately 1 mg) were dispersed in 3 mL of distilled water and kept 15 min in the ultrasound bath. Then, one drop of the suspension was deposited on a silicon wafer, dried at room temperature and finally attached to a sample stub using carbon tape for FE-SEM analysis; and one drop of the suspension was deposited on the copper grid and dried at room temperature for TEM analysis. Photoluminescence (PL) measurements were performed by two distinct equipment. In the first one, the samples were excited by a 355 nm laser (Cobolt/Zouk) focused on a $20 \mu\text{m}$ spot, $50 \mu\text{W}$ of power. The backscattered luminescence was dispersed by a 20 cm spectrometer with the signal detected by a charged coupled device

detector (Andor technologies). In the second one, the PL spectra were carried out with 325 nm excitation source of a krypton ion laser (Coherent Innova) and 200 mW laser output, at monochromator Thermal Jarrel-Ash Monospec and a Hamamatsu R446 photomultiplier. All measurements were performed at room temperature.

3. Results and discussion

3.1 X-ray diffraction patterns

Figure 2 shows the XRD patterns of $\text{YVO}_4:\text{RE}$, and all the diffraction peaks can be readily indexed to the pure tetragonal YVO_4 phase (PDF No. 17-0341) (Rivera-Enrez and Fernandez-Osorio, 2021; Yu *et al.*, 2002). The intense and sharp peaks confirm the samples are pure and present high crystallinity, as well as structural long-range order. Also, Y^{3+} site is an ideal environment with a D_{2d} point symmetry for RE emitter. So, effectively Y-by-RE substitution occurs in the host lattice because RE^{3+} and Y^{3+} have similar ionic radius, as widely reported by many works (Matos *et al.*, 2016; Rivera-Enrez and Fernandez-Osorio, 2021). This substitution was not perceived on the XRD patterns due to the limitation of detection of the XRD instrument.

A representation of the unit cell for the orthorhombic $\text{YVO}_4:\text{RE}$ nanoparticles are presented in Fig. 3. This unit cell was modelled using the lattice parameters and atomic positions, as well as the possible RE-by-Y substitution. The Y/RE coordination environment is a distorted dodecahedral $[\text{YO}_8]/[\text{REO}_8]$ clusters, while V is a distorted tetrahedral $[\text{VO}_4]$ cluster.

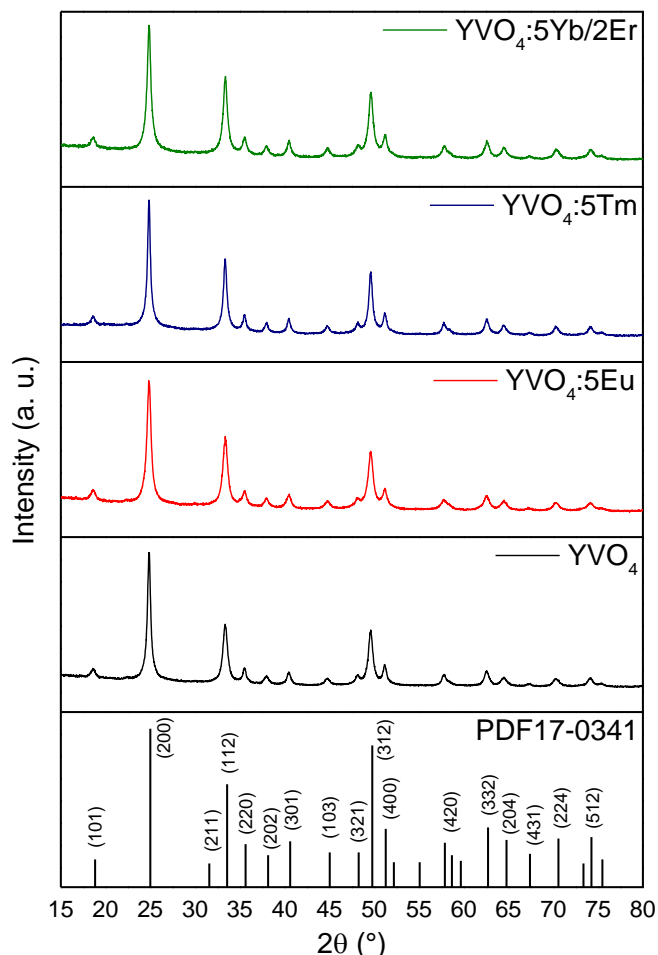


Figure 2. X-ray diffraction patterns of the $\text{YVO}_4:\text{RE}$ nanoparticles.

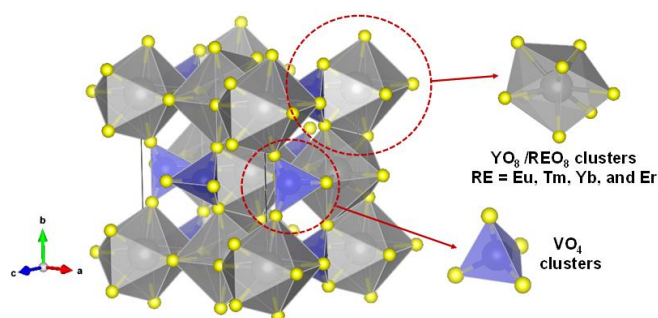


Figure 3. Unit cell representation of $\text{YVO}_4:\text{RE}$ nanoparticles. Gray, blue, and yellow balls are Y/RE, V and O atoms, respectively.

3.2 Raman spectroscopy

Figure 4 shows the room temperature Raman spectra of $\text{YVO}_4:\text{RE}$ nanoparticles excited by a green laser. Experimentally, seven active Raman modes were observed at 155, 260, 367, 482, 796, 820, and 874 cm^{-1} for the YVO_4 , $\text{YVO}_4:\text{5Eu}$, and $\text{YVO}_4:\text{5Tm}$ samples. For the $\text{YVO}_4:\text{5Yb/2Er}$, six active Raman modes were

observed at 328, 402, 638, 796, 818, and 871 cm^{-1} . Also, the $\text{YVO}_4:\text{5Yb/2Er}$ nanoparticle present a broad PL emission, as observed in the Raman spectra, due to the Yb/Er ions. These results confirm the structural short-range order of all samples (Jayaraman *et al.*, 1987).

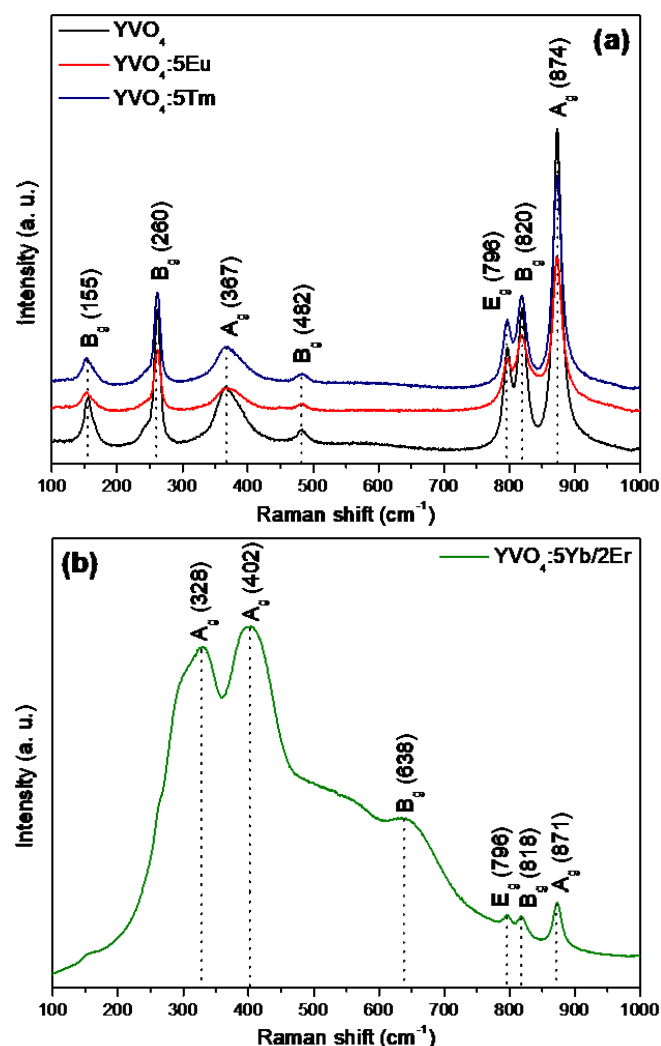


Figure 4. Raman spectra of the (a) $\text{YVO}_4:\text{RE}$ (RE = Eu and Tm), and (b) $\text{YVO}_4:\text{5Yb/2Er}$ nanoparticles.

3.3 UV-vis spectroscopy

Figure 5 illustrates the UV-vis diffuse reflectance spectra of the $\text{YVO}_4:\text{RE}$ nanoparticles in the range of 275–750 nm. The samples showed absorption in the ultraviolet region at approximately 450 nm. The absorption is a result of electronic transition between the valence band (VB) formed predominantly by O 2p state, and the conduction band (CB) composed mainly by V 3d states (Yang *et al.*, 2018). Also, the $\text{YVO}_4:\text{5Tm}$ sample present the ${}^3\text{H}_6 \rightarrow {}^3\text{F}_3$ transition, and the $\text{YVO}_4:\text{5Yb/2Er}$ present the ${}^4\text{I}_{15/2} \rightarrow {}^2\text{H}_J$ ($J = 11/2$ and $9/2$) transitions.

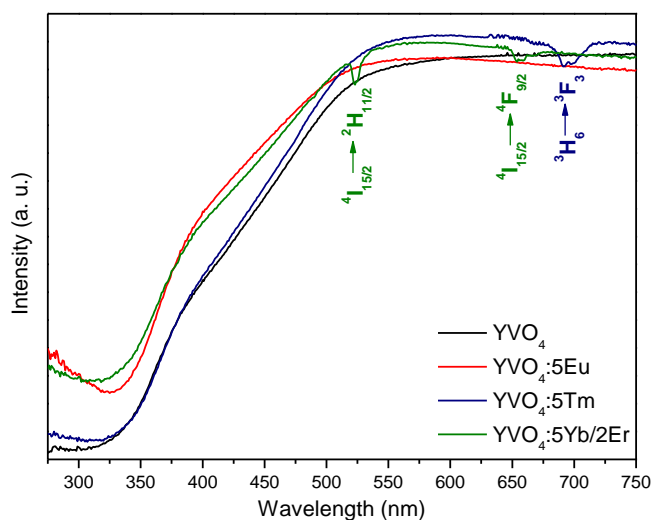
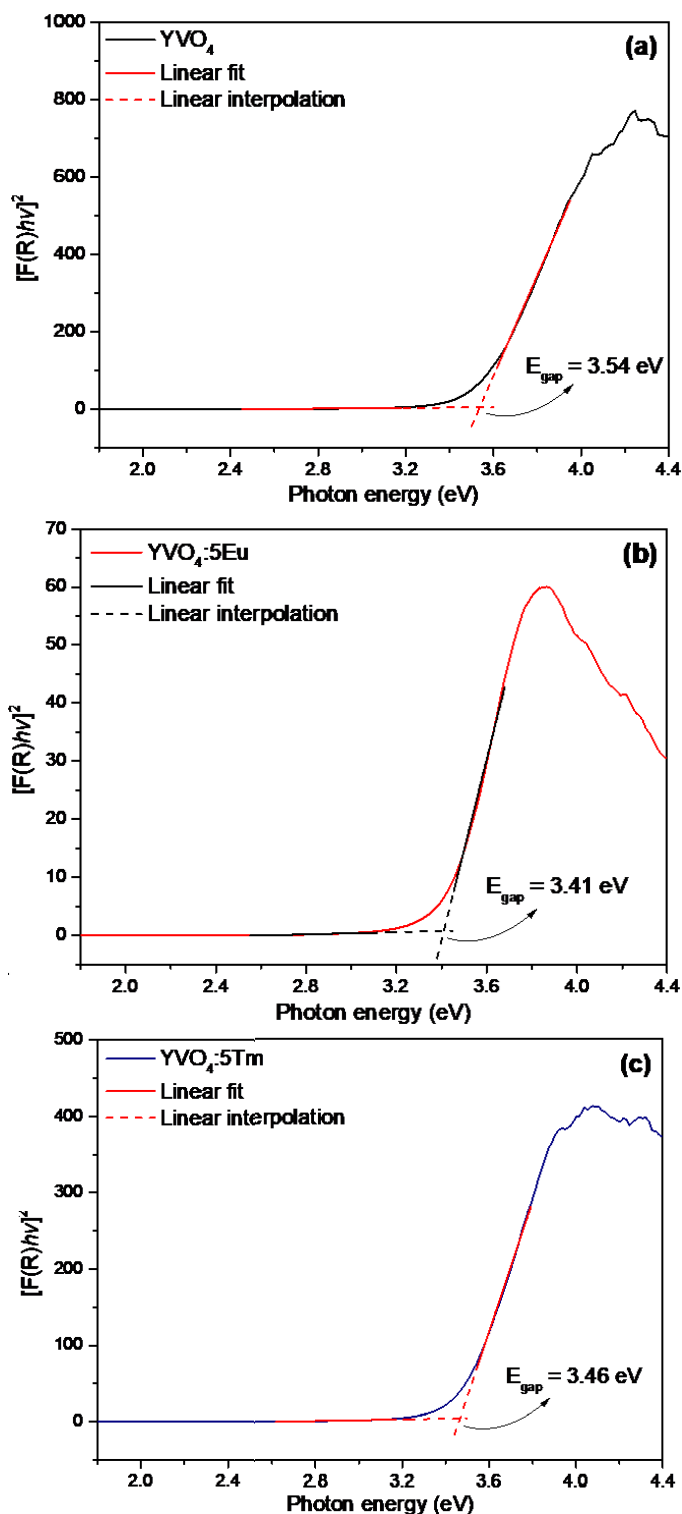


Figure 5. The UV-vis diffuse reflectance spectra of the $\text{YVO}_4\text{:RE}$ nanoparticles.

The band gap energy (E_{gap}) values were calculated using the relation of the Kubelka–Munk and Wood Tauc function, as previously reported (Pinatti *et al.*, 2019a), and it was obtained by linear extrapolation of the UV-vis curve in the $[\text{F}(\text{R}_\infty)h\nu]^n$ versus $h\nu$ graph. $\text{F}(\text{R}_\infty)$ is the Kubelka–Munk function, $h\nu$ is the photon energy, and n is a constant related to the type of electronic transition of a semiconductor ($n = 0.5$ for direct allowed, $n = 2$ for indirect allowed, $n = 1.5$ for direct forbidden, and $n = 3$ for indirect forbidden). The theoretical calculation predicts a direct allowed transition for YVO_4 . Thus, the E_{gap} values obtained were 3.54, 3.41, 3.46, and 3.39 eV for the YVO_4 , $\text{YVO}_4\text{:5Eu}$, $\text{YVO}_4\text{:5Tm}$, and $\text{YVO}_4\text{:5Yb/2Er}$ samples, respectively (Fig. 6). These results show that the E_{gap} values decrease due to insertion of the RE ions, indicating that the degree of order-disorder at electronic level were affected due to Y-by-RE substitution. This behavior was previously observed in other RE doped materials and is attributed mainly by the contribution of $4f^n$ electrons of RE^{3+} ions either to the VB or CB, which can increase the covalent bonding of V–O and reduce the E_{gap} . This happens because the energy level of RE^{3+} ions matches the energy level of VO_4^{3-} , contributing to an effective energy transfer from the VO_4^{3-} to the excited states of RE^{3+} ions (Yang *et al.*, 2018).



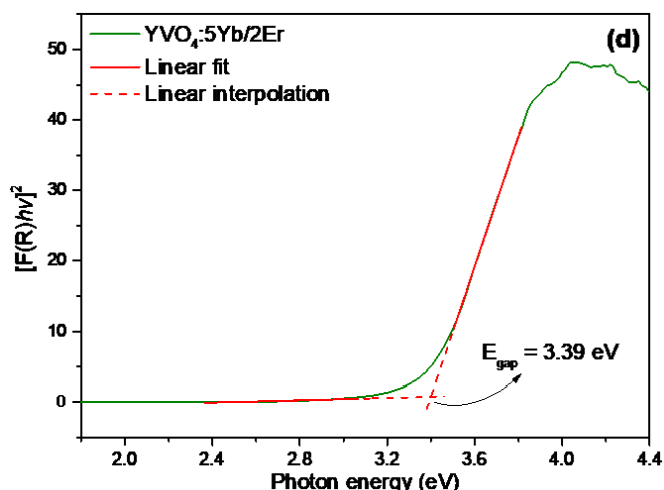


Figure 6. Band gap energy (E_{gap}) for the $YVO_4:RE$ nanoparticles.

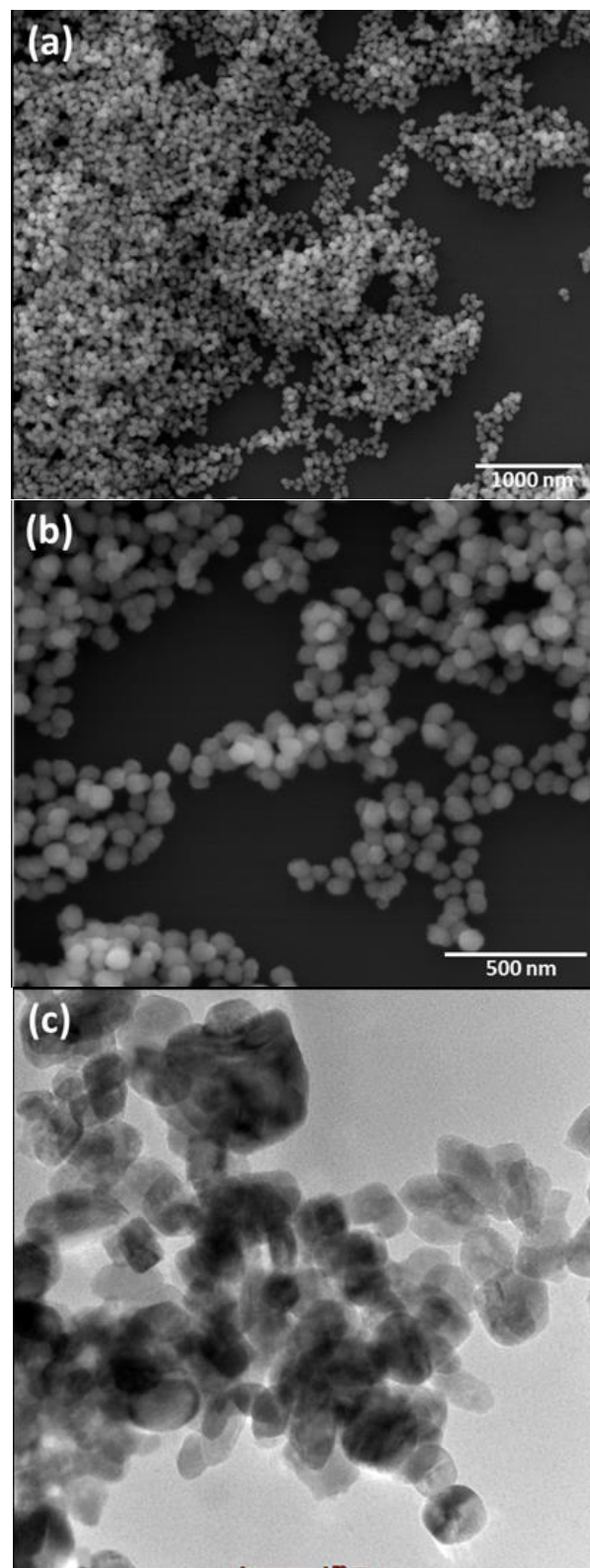
3.4 Field-emission scanning electron microscopy and TEM

The detailed morphology and particle size of YVO_4 nanoparticles were assessed by FE-SEM, and the nanostructures were further characterized by TEM and HRTEM. Field emission scanning electron microscopy micrographs of the YVO_4 nanoparticles are shown in Fig. 7a and b. It is clearly seen spherical nanoparticles which exhibit a high degree of homogeneity in the shape and size. As shown in Fig. 7a and b, the particles present smooth surface, well-defined shape, and are mainly aggregated with a monodisperse size distribution.

Figure 7c shows the TEM image of YVO_4 nanoparticles. It was mainly observed spherical-like particles of sizes ranging from 20 to 50 nm. Most of them have perfect circular morphology, while other present small deformations. Figure 7d shows the HRTEM image of YVO_4 nanoparticles. The YVO_4 nanoparticles presented a single crystalline nature and the lattice spacing was calculated to be 0.363 nm between two adjacent lattice fringes, which could be indexed to 200 planes of zircon-type YVO_4 . This is in agreement with the XRD results (Shen *et al.*, 2010). Moreover, the other $YVO_4:RE$ samples also showed similar morphology and as single-crystalline and this can be attributed to the similar preparative conditions and the low dopant concentration of RE^{3+} ions (data not shown).

These results confirm that nanosized YVO_4 of spherical morphology can be obtained by the MAH method at short reactional time and low temperature. Moreover, this morphology, as well as the size, are effectively acquired without the use of surfactants, templates, organic solvents, or adjustment of pH value

of the medium, which is usually required to obtain homogeneous and nanosized particles.



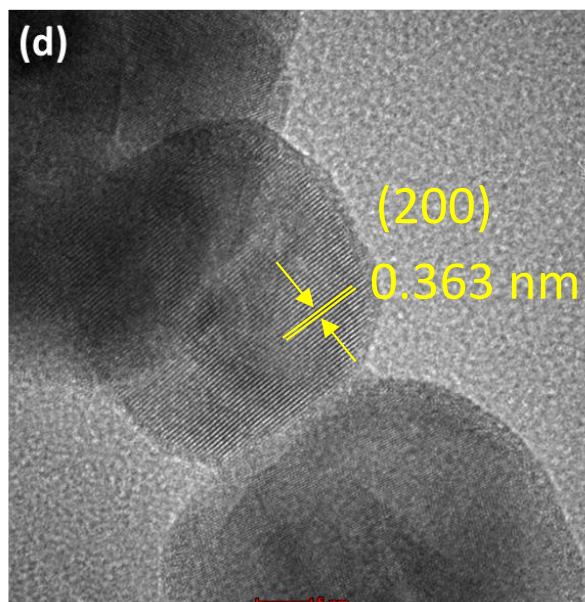


Figure 7. (a, b) FE-SEM images, (c) TEM image, and (d) HRTEM image of YVO_4 nanoparticles.

3.5 Photoluminescence spectroscopy

Figure 8 shows the PL emission spectra at room temperature of $\text{YVO}_4:\text{RE}$ nanoparticles under the excitation wavelength of 355 nm. **Figure 8a** shows the PL emission spectra of $\text{YVO}_4:\text{RE}$ (RE = Tm, and Yb/Er) nanoparticles, presenting an intense band at 540 nm due to VO_4^{3-} clusters (Jin *et al.*, 2011), and the $\text{YVO}_4:5\text{Tm}$ nanoparticles also present the $^3\text{H}_4 \rightarrow ^3\text{H}_6$ transition at 806 nm. Particularly, the $\text{YVO}_4:\text{Eu}$ nanoparticles present intense $^5\text{D}_1 \rightarrow ^7\text{F}_J$ ($J = 1$ and 2) and $^5\text{D}_0 \rightarrow ^7\text{F}_J$ ($J = 1-4$) transitions, which arises due to the efficient energy transfer from VO_4^{3-} clusters to the Eu^{3+} ions (see Fig. 8b) (Matos *et al.*, 2016; Pinatti *et al.*, 2019a; Saltarelli *et al.*, 2014).

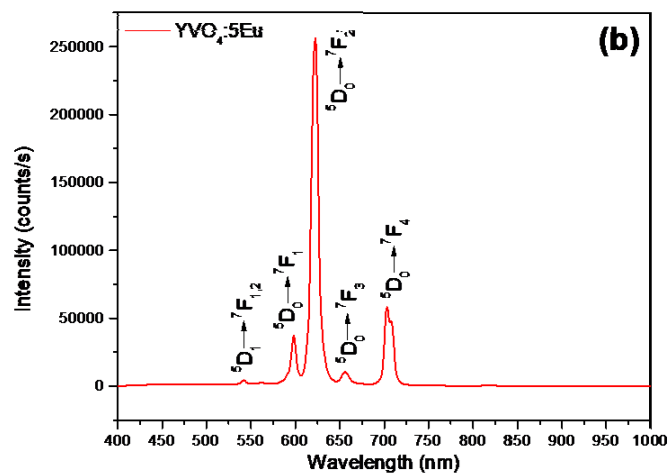
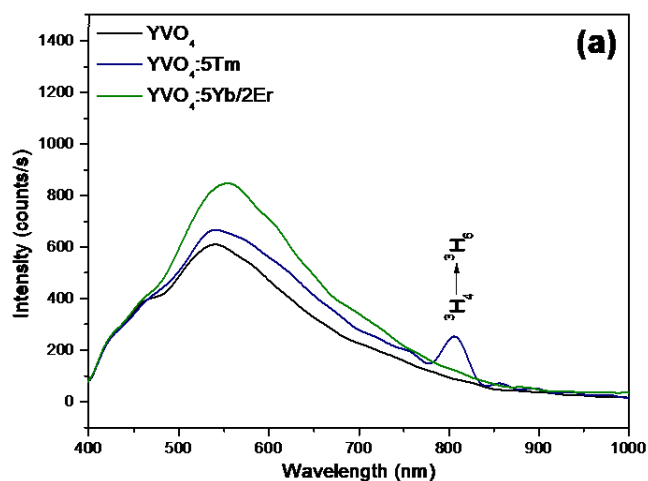


Figure 8. Photoluminescent emission spectra of (a) $\text{YVO}_4:\text{RE}$ (RE = Tm and Yb/Er), and (b) $\text{YVO}_4:5\text{Eu}$ nanoparticles.

Figure 9 shows the PL emission spectra at room temperature of $\text{YVO}_4:\text{RE}$ nanoparticles under the excitation wavelength of 325 nm, as well as the CIE chromatic diagram. **Figure 9a** shows the PL emission spectra of the $\text{YVO}_4:5\text{Eu}$ nanoparticles, which presents characteristic Eu^{3+} peaks at 543, 564, 595, 622, 655, and 705 nm ascribed to the $^5\text{D}_1 \rightarrow ^7\text{F}_J$ ($J = 1$ and 2), and $^5\text{D}_0 \rightarrow ^7\text{F}_J$ ($J = 1-4$) transitions, respectively (Almeida *et al.*, 2021; Pinatti *et al.*, 2015). **Figure 9b** shows the PL emission spectra of the $\text{YVO}_4:5\text{Tm}$ nanoparticles, which present characteristic Tm^{3+} peaks at 480, 548, 650, and 795 nm related to the $^1\text{D}_2 \rightarrow ^3\text{F}_J$ ($J = 4$ and 5), $^1\text{G}_4 \rightarrow ^3\text{F}_4$, and $^3\text{H}_4 \rightarrow ^3\text{H}_6$ transitions, respectively (Pinatti *et al.*, 2019a). **Figure 9c** shows the PL emission spectra of the $\text{YVO}_4:5\text{Yb}/2\text{Er}$ nanoparticles, which present characteristic Er^{3+} peaks at 530, 555, and 671 nm attributed to the $^2\text{H}_{11/2} \rightarrow ^4\text{I}_{15/2}$, $^4\text{S}_{3/2} \rightarrow ^4\text{I}_{15/2}$, and $^4\text{F}_{9/2} \rightarrow ^4\text{I}_{15/2}$ transitions, respectively (Alkahtani *et al.*, 2021; Mahata *et al.*, 2015; Sun *et al.*, 2006; Woźny *et al.*, 2018; Zhang *et al.*, 2010). **Figure 9d** shows the CIE chromatic diagram and the respective positions of x, and y coordinates of the $\text{YVO}_4:\text{RE}$ (RE = Eu, Tm, and Yb/Er) nanoparticles obtained through the PL emission spectra. The (x,y) chromatic coordinates positions are listed in Tab. 1. The $\text{YVO}_4:5\text{Eu}$, $\text{YVO}_4:5\text{Tm}$, and $\text{YVO}_4:5\text{Yb}/2\text{Er}$ nanoparticles present intense emitting color in the red, blue, and green region of the diagram, respectively. These results confirm the pureness and brightness of the samples and can be considered as optimum materials for optical devices.

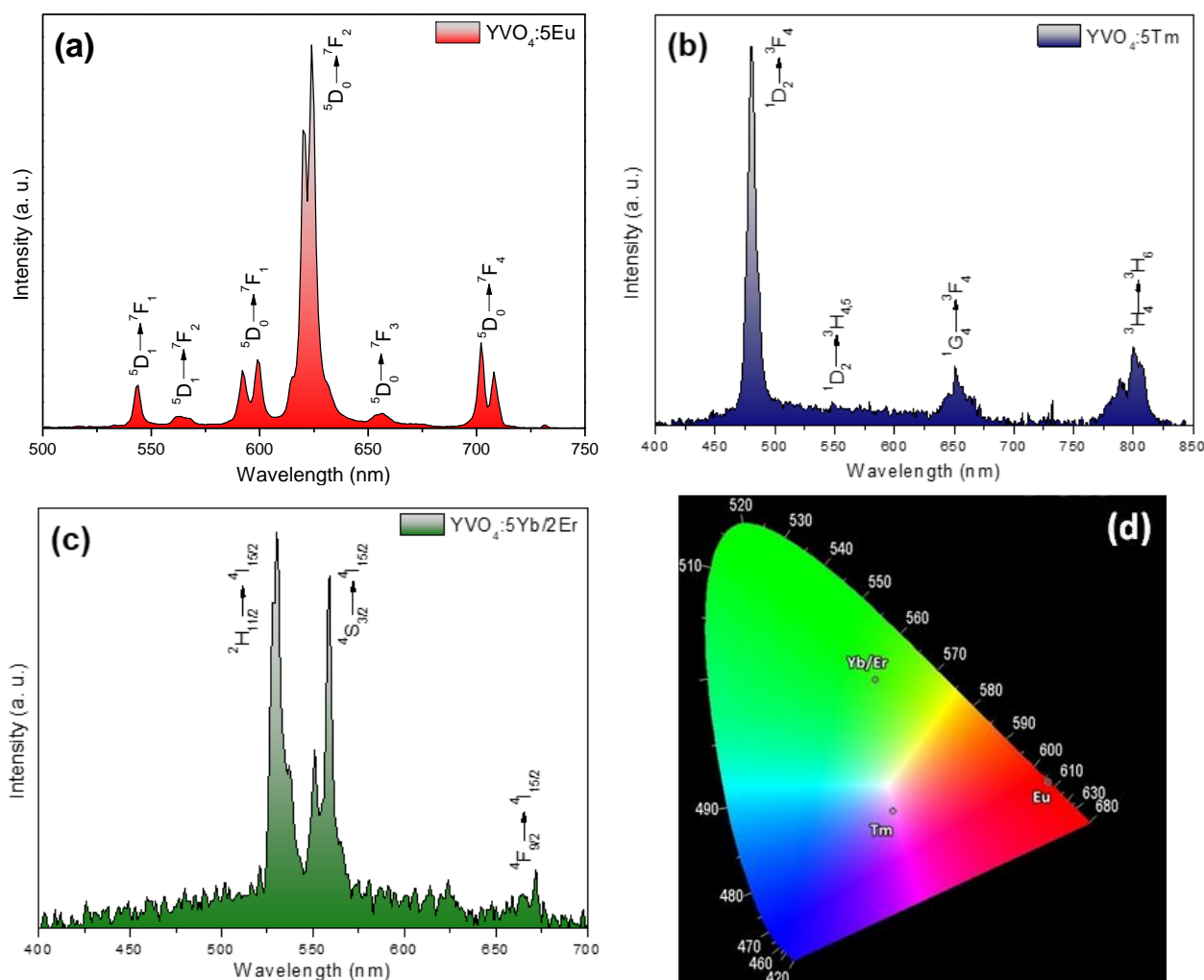


Figure 9. Photoluminescent emission spectra of (a) $\text{YVO}_4:5\text{Eu}$, (b) $\text{YVO}_4:5\text{Tm}$, (c) $\text{YVO}_4:5\text{Yb}/2\text{Er}$ nanoparticles, and (d) CIE chromatic diagram.

Table 1. Chromatic coordinates values obtained by the PL emission spectra of the $\text{YVO}_4:\text{RE}$ nanoparticles.

Samples	Chromatic coordinates	
	x	y
$\text{YVO}_4:5\text{Eu}$	0.65	0.34
$\text{YVO}_4:5\text{Tm}$	0.36	0.29
$\text{YVO}_4:5\text{Yb}/2\text{Er}$	0.33	0.53

Figure 10 shows a schematic energy level diagram and a proposed energy transfer mechanism for the $\text{YVO}_4:\text{RE}$ nanoparticles. For the $\text{YVO}_4:5\text{Eu}$ nanoparticles, it is observed that, under excitation at 325 nm, electrons are excited from VB into the charge transfer state (CTS) of the VO_4^{3-} clusters. Then, the excitation energy is transferred from the VO_4^{3-} group to the $^5\text{D}_4$ level of Eu^{3+} cations. Afterwards, Eu^{3+} cations in the populated $^5\text{D}_4$ level undergo multiphonon relaxation to the $^5\text{D}_1$ level that radiatively decay to the $^7\text{F}_j$ ($J = 1$ and 2) levels; and to the $^5\text{D}_0$ level that radiatively decay

to the $^7\text{F}_j$ ($J = 1-4$) levels. For the $\text{YVO}_4:5\text{Tm}$ nanoparticles, the excitation energy is transferred from the VO_4^{3-} group to the $^3\text{P}_2$ level of Tm^{3+} cations. Then, Tm^{3+} cations in the populated $^3\text{P}_2$ level undergo multiphonon relaxation to the $^1\text{D}_2$ level that radiatively decay to the $^7\text{F}_4$ and $^3\text{H}_4$ levels; and to the $^1\text{G}_4$ level that radiatively decay to the $^7\text{F}_4$ and $^3\text{H}_6$ levels. Finally, for the $\text{YVO}_4:5\text{Yb}/2\text{Er}$ nanoparticles, the excitation energy is transferred from the VO_4^{3-} group to the $^4\text{F}_{7/2}$ level of Er^{3+} cations. Then, Er^{3+} cations in the populated $^4\text{F}_{7/2}$ level undergo multiphonon relaxation to the $^2\text{H}_{11/2}$ and $^4\text{S}_{3/2}$ levels that radiatively decay to the $^4\text{I}_{15/2}$ level; and to the $^4\text{F}_{9/2}$ level that radiatively decay to the $^4\text{I}_{15/2}$ level. Alternatively, according to the energy conservation law, a two-photon process can occur and populate the green and red UC emissions of Er^{3+} ions. The successive energy transfers are: $^4\text{I}_{15/2}(\text{Er}^{3+}) + ^2\text{F}_{5/2}(\text{Yb}^{3+}) \rightarrow ^4\text{I}_{11/2}(\text{Er}^{3+}) + ^2\text{F}_{7/2}(\text{Yb}^{3+})$ and $^4\text{I}_{11/2}(\text{Er}^{3+}) + ^2\text{F}_{5/2}(\text{Yb}^{3+}) \rightarrow ^4\text{F}_{7/2}(\text{Er}^{3+}) + ^2\text{F}_{7/2}(\text{Yb}^{3+})$ excite Er^{3+} ions to the $^4\text{F}_{7/2}$ state. Er^{3+}

ions at the $^2H_{11/2}/^4S_{3/2}$ states, arising from the nonradiative relaxation (NR) process of the $^4F_{7/2}$ state, radiatively decay to the $^4I_{15/2}$ state, resulting the green UC emissions. The $^4F_{9/2}$ red emitting state is populated

by the process: $^4I_{13/2}(\text{Er}^{3+}) + ^2F_{5/2}(\text{Yb}^{3+}) \rightarrow ^4F_{9/2}(\text{Er}^{3+}) + ^2F_{7/2}(\text{Yb}^{3+})$, where the $^4I_{13/2}$ state is populated by NR process of the $^4I_{11/2}$ state (Ji *et al.*, 2021).

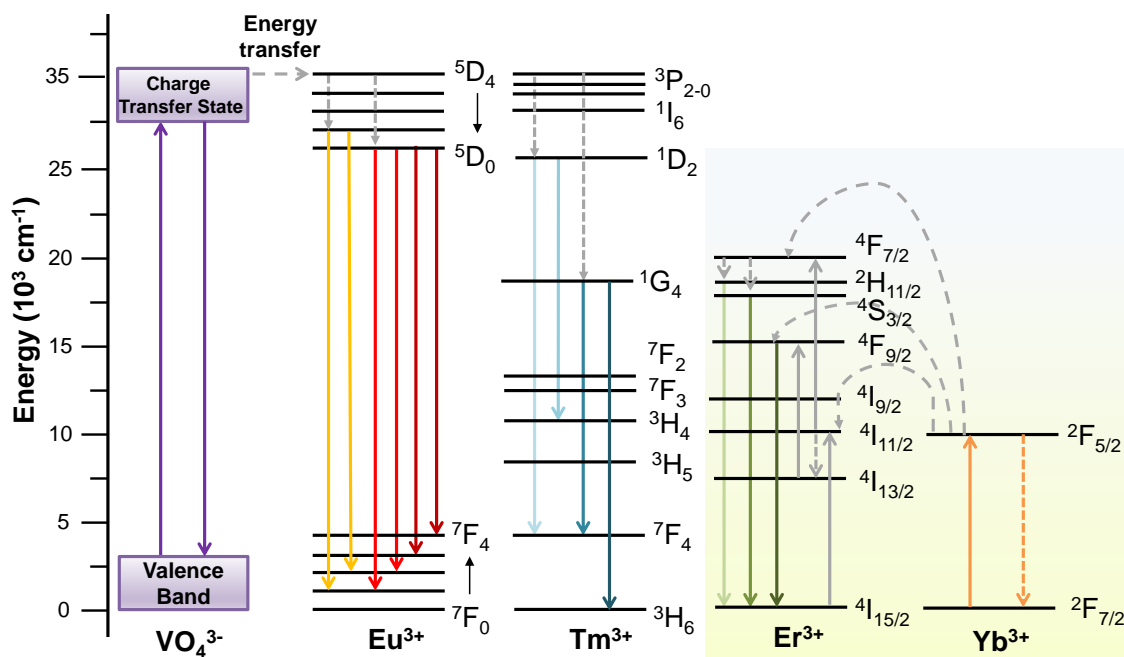


Figure 10. Schematic energy level diagram and a proposed energy transfer mechanism for the YVO₄:RE nanoparticles. Solid arrows = radiative transition, dashed arrows = energy transfer, and dotted arrows = nonradiative transition.

4. Conclusions

In summary, we reported the efficient synthesis of YVO₄:RE nanoparticles by the microwave-assisted hydrothermal method. Long-range order was confirmed by XRD patterns, which showed sharp and well-defined peaks with no segregated materials. Vibrational Raman modes observed represent a signature of the structural organization in the short-range. The UV-vis spectra indicate that the band gap value decreases due to RE doping attesting structural order-disorder of the materials. The FE-SEM, TEM, and HRTEM images prove that the materials are spherical and in the nanoscale size. Photoluminescent emission spectra present transitions in the red, blue, and green regions, attesting these materials as good phosphors in the visible region. Also, the YVO₄:5Yb/2Er is a good candidate as promising material for UC phosphor.

Authors' contribution

Conceptualization: Pinatti, I. M.; Foggi, C. C.; Teodoro, M. D.; Longo, E.; Simões, A. Z.; Rosa, I. L. V.

Data curation: Pinatti, I. M.; Foggi, C. C.; Teodoro, M. D.; Longo, E.; Simões, A. Z.; Rosa, I. L. V.

Formal Analysis: Pinatti, I. M.; Foggi, C. C.; Teodoro, M. D.; Longo, E.; Simões, A. Z.; Rosa, I. L. V.

Funding acquisition: Pinatti, I. M.; Foggi, C. C.; Teodoro, M. D.; Longo, E.; Simões, A. Z.; Rosa, I. L. V.

Investigation: Pinatti, I. M.; Foggi, C. C.; Teodoro, M. D.; Longo, E.; Simões, A. Z.; Rosa, I. L. V.

Methodology: Pinatti, I. M.; Foggi, C. C.; Teodoro, M. D.; Longo, E.; Simões, A. Z.; Rosa, I. L. V.

Project administration: Pinatti, I. M.; Foggi, C. C.; Teodoro, M. D.; Longo, E.; Simões, A. Z.; Rosa, I. L. V.

Resources: Pinatti, I. M.; Foggi, C. C.; Teodoro, M. D.; Longo, E.; Simões, A. Z.; Rosa, I. L. V.

Software: Not applicable.

Supervision: Longo, E.; Simões, A. Z.; Rosa, I. L. V.

Validation: Pinatti, I. M.; Foggi, C. C.; Teodoro, M. D.; Longo, E.; Simões, A. Z.; Rosa, I. L. V.

Visualization: Pinatti, I. M.; Foggi, C. C.; Teodoro, M. D.; Longo, E.; Simões, A. Z.; Rosa, I. L. V.

Writing – original draft: Pinatti, I. M.; Foggi, C. C.; Teodoro, M. D.; Longo, E.; Simões, A. Z.; Rosa, I. L. V.

Writing – review & editing: Pinatti, I. M.; Foggi, C. C.; Teodoro, M. D.; Longo, E.; Simões, A. Z.; Rosa, I. L. V.

Data availability statement

The data will be available upon request.

Funding

Fundação de Amparo à Pesquisa do Estado de São Paulo (FAPESP). Grant No.: 13/07296-2; 17/12594-3; 19/03722-3; 19/25944-8.

Acknowledgments

The authors would like to acknowledge Maximo Siu Li (IFSC-USP), Rorivaldo Camargo (CDMF-UFSCar), and Sandra Maria Terenzi Bellini (CDMF-UFSCar) for technical and scientific contributions.

This manuscript is dedicated to the memory of Professor Dr. José Arana Varela, pioneer with notable achievements in the fields of materials science, physics and chemistry. He was one of the founders of the Interdisciplinary Laboratory of Electrochemistry and Ceramics (LIEC), Brazil. Dr. Varela contributed significantly to the development of Brazilian science, and had an outstanding international reputation as an educator and researcher.

References

- Alkahtani, M.; Alfahd, A.; Alsofyani, N.; Almuqhim, A. A.; Qassem, H.; Alshehri, A. A.; Almughen, F. A.; Hemmer, P. Photostable and small $\text{YVO}_4:\text{Yb},\text{Er}$ upconversion nanoparticles in water. *Nanomaterials* **2021**, *11* (6), 1535. <https://doi.org/10.3390/nano11061535>
- Almeida, P. B.; Pinatti, I. M.; Oliveira, R. C.; Teixeira, M. M.; Santos, C. C.; Machado, T. R.; Longo, E.; Rosa, I. L. V. Structural, morphological and photoluminescence properties of $\beta\text{-Ag}_2\text{MoO}_4$ doped with Eu^{3+} . *Chem. Pap.* **2021**, *75*, 1869–1882. <https://doi.org/10.1007/s11696-020-01489-4>
- Ferreira, N. H.; Furtado, R. A.; Ribeiro, A. B.; Oliveira, P. F.; Ozelin, S. D.; Souza, L. D. R.; Rinaldi Neto, F.; Miura, B. A.; Magalhães, G. M.; Nassar, E. J.; Tavares, D. C. Europium(III)-doped yttrium vanadate nanoparticles reduce the toxicity of cisplatin. *J. Inorg. Biochem.* **2018**, *182*, 9–17. <https://doi.org/10.1016/j.jinorgbio.2018.01.014>
- Huong, T. T.; Vinh, L. T.; Phuong, H. T.; Khuyen, H. T.; Anh, T. K.; Tu, V. D.; Minh, L. Q. Controlled fabrication of the strong emission $\text{YVO}_4:\text{Eu}^{3+}$ nanoparticles and nanowires by microwave assisted chemical synthesis. *J. Lumin.* **2016**, *173*, 89–93. <https://doi.org/10.1016/j.jlumin.2016.01.003>
- Jayaraman, A.; Kourouklis, G. A.; Espinosa, G. P.; Cooper, A. S.; Van Uitert, L. G. A high-pressure Raman study of yttrium vanadate (YVO_4) and the pressure-induced transition from the zircon-type to the scheelite-type structure. *J. Phys. Chem. Solids* **1987**, *48* (8), 755–759. [https://doi.org/10.1016/0022-3697\(87\)90072-2](https://doi.org/10.1016/0022-3697(87)90072-2)
- Ji, H.; Tang, J.; Tang, X.; Yang, Z.; Zhang, H.; Qian, Y. Enhanced upconversion emissions of $\text{NaNbO}_3:\text{Er}^{3+}/\text{Yb}^{3+}$ nanocrystals via Mg^{2+} ions doping. *Mater. Lett.* **2021**, *302*, 130348. <https://doi.org/10.1016/j.matlet.2021.130348>
- Jin, Y.; Li, C.; Xu, Z.; Cheng, Z.; Wang, W.; Li, G.; Lin, J. Microwave-assisted hydrothermal synthesis and multicolor tuning luminescence of $\text{Y}_x\text{V}_{1-x}\text{O}_4:\text{Ln}^{3+}$ ($\text{Ln} = \text{Eu}, \text{Dy}, \text{Sm}$) nanoparticles. *Mater. Chem. Phys.* **2011**, *129* (1–2), 418–423. <https://doi.org/10.1016/j.matchemphys.2011.04.035>
- Kshetri, Y. K.; Regmi, C.; Kim, H.-S.; Lee, S. W.; Kim, T. H. Microwave hydrothermal synthesis and upconversion properties of $\text{Yb}^{3+}/\text{Er}^{3+}$ doped YVO_4 nanoparticles. *Nanotechnology* **2018**, *29* (20), 204004. <https://doi.org/10.1088/1361-6528/aab2bf>
- Li, K.; Chen, T.; Mao, H.; Chen, Y.; Wang, J. Preparation and Upconversion Emission Investigation of the $\text{YVO}_4:\text{Yb}^{3+}:\text{Er}^{3+}$ Nanomaterials and Their Coupling with the Au Nanoparticles. *J. Electron. Mater.* **2021**, *50*, 1189–1195. <https://doi.org/10.1007/s11664-020-08636-3>
- Liu, Y.; Xiong, H.; Zhang, N.; Leng, Z.; Li, R.; Gan, S. Microwave synthesis and luminescent properties of $\text{YVO}_4:\text{Ln}^{3+}$ ($\text{Ln} = \text{Eu}, \text{Dy}$ and Sm) phosphors with different morphologies. *J. Alloys Compd.* **2015**, *653*, 126–134. <https://doi.org/10.1016/j.jallcom.2015.09.015>
- Liu, Y.; Yang, C.; Xiong, H.; Zhang, N.; Leng, Z.; Li, R.; Gan, S. Surfactant assisted synthesis of the $\text{YVO}_4:\text{Ln}^{3+}$ ($\text{Ln} = \text{Eu}, \text{Dy}, \text{Sm}$) phosphors and shape-dependent luminescence properties. *Colloids Surf. A Physicochem. Eng. Asp.* **2016**, *502*, 139–146. <https://doi.org/10.1016/j.colsurfa.2016.05.006>
- Mahata, M. K.; Kumar, K.; Rai, V. K. $\text{Er}^{3+}-\text{Yb}^{3+}$ doped vanadate nanocrystals: A highly sensitive thermographic phosphor and its optical nanoheater behavior. *Sens. Actuators B Chem.* **2015**, *209*, 775–780. <https://doi.org/10.1016/j.snb.2014.12.039>
- Matos, M. G.; Rocha, L. A.; Nassar, E. J.; Verelst, M. Influence of Bi^{3+} ions on the excitation wavelength of the $\text{YVO}_4:\text{Eu}^{3+}$ matrix. *Opt. Mater.* **2016**, *62*, 12–18. <https://doi.org/10.1016/j.optmat.2016.09.035>

- Momma, K.; Izumi, F. VESTA: a three-dimensional visualization system for electronic and structural analysis. *J. Appl. Cryst.* **2008**, *41*, 653–658. <https://doi.org/10.1107/S0021889808012016>
- Momma, K.; Izumi, F. VESTA 3 for three-dimensional visualization of crystal, volumetric and morphology data. *J. Appl. Cryst.* **2011**, *44*, 1272–1276. <https://doi.org/10.1107/S0021889811038970>
- Panayiotakis, G.; Cavouras, D.; Kandarakis, I.; Nomicos, C. A study of X-ray luminescence and spectral compatibility of europium-activated yttrium-vanadate (YVO₄:Eu) screens for medical imaging applications. *Appl. Phys. A* **1996**, *62*, 483–486. <https://doi.org/10.1007/BF01567121>
- Pinatti, I. M.; Nogueira, I. C.; Pereira, W. S.; Pereira, P. F. S.; Gonçalves, R. F.; Varela, J. A.; Longo, E.; Rosa, I. L. V. Structural and photoluminescence properties of Eu³⁺ doped α -Ag₂WO₄ synthesized by the green coprecipitation methodology. *Dalton Trans.* **2015**, *44* (40), 17673–17685. <https://doi.org/10.1039/C5DT01997D>
- Pinatti, I. M.; Mazzo, T. M.; Gonçalves, R. F.; Varela, J. A.; Longo, E.; Rosa, I. L. V. CaTiO₃ and Ca_{1-3x}Sm_xTiO₃: Photoluminescence and morphology as a result of Hydrothermal Microwave Methodology. *Ceram. Int.* **2016**, *42* (1) (Part B), 1352–1360. <https://doi.org/10.1016/j.ceramint.2015.09.074>
- Pinatti, I. M.; Fern, G. R.; Longo, E.; Ireland, T. G.; Pereira, P. F. S.; Rosa, I. L. V.; Silver, J. Luminescence properties of α -Ag₂WO₄ nanorods co-doped with Li⁺ and Eu³⁺ cations and their effects on its structure. *J. Lumin.* **2019a**, *206*, 442–454. <https://doi.org/10.1016/j.jlumin.2018.10.104>
- Pinatti, I. M.; Pereira, P. F. S.; Assis, M.; Longo, E.; Rosa, I. L. V. Rare earth doped silver tungstate for photoluminescent applications. *J. Alloys Compd.* **2019b**, *771*, 433–447. <https://doi.org/10.1016/j.jallcom.2018.08.302>
- Rivera-Enríquez, C. E.; Fernández-Osorio, A. L. Synthesis of YVO₄:Eu³⁺ nanophosphors by the chemical coprecipitation method at room temperature. *J. Lumin.* **2021**, *236*, 118110. <https://doi.org/10.1016/j.jlumin.2021.118110>
- Saltarelli, M.; Matos, M. G.; Faria, E. H.; Ciuffi, K. J.; Rocha, L. A.; Nassar, E. J. Preparation of YVO₄:Eu³⁺ at low temperature by the hydrolytic sol-gel methodology. *J. Sol-Gel Sci. Technol.* **2014**, *73*, 283–292. <https://doi.org/10.1007/s10971-014-3525-z>
- Shen, J.; Sun, L. D.; Zhu, J. D.; Wei, L. H.; Sun, H. F.; Yan, C. H. Biocompatible bright YVO₄:Eu nanoparticles as versatile optical bioprobes. *Adv. Funct. Mater.* **2010**, *20* (21), 3708–3714. <https://doi.org/10.1002/adfm.201001264>
- Sousa Filho, P. C.; Alain, J.; Leménager, G.; Larquet, E.; Fick, J.; Serra, O. A.; Gacoin, T. Colloidal Rare Earth Vanadate Single Crystalline Particles as Ratiometric Luminescent Thermometers. *J. Phys. Chem. C* **2019**, *123* (4), 2441–2450. <https://doi.org/10.1021/acs.jpcc.8b12251>
- Sun, Y.; Liu, H.; Wang, X.; Kong, X.; Zhang, H. Optical spectroscopy and visible upconversion studies of YVO₄:Er³⁺ nanocrystals synthesized by a hydrothermal process. *Chem. Mater.* **2006**, *18*, 2726–2732. <https://doi.org/10.1021/cm051971m>
- Woźny, P.; Szczeszak, A.; Lis, S. Effect of various surfactants on changes in the emission color chromaticity in upconversion YVO₄: Yb³⁺, Er³⁺ nanoparticles. *Opt. Mater.* **2018**, *76*, 400–406. <https://doi.org/10.1016/j.optmat.2018.01.009>
- Woźny, P.; Runowski, M.; Lis, S. Emission color tuning and phase transition determination based on high-pressure up-conversion luminescence in YVO₄: Yb³⁺, Er³⁺ nanoparticles. *J. Lumin.* **2019**, *209*, 321–327. <https://doi.org/10.1016/j.jlumin.2019.02.008>
- Yang, L.; Peng, S.; Zhao, M.; Yu, L. New synthetic strategies for luminescent YVO₄:Ln³⁺ (Ln = Pr, Sm, Eu, Tb, Dy, Ho, Er) with mesoporous cell-like nanostructure. *Opt. Mater. Express* **2018**, *8*, 3805–3819. <https://doi.org/10.1364/OME.8.003805>
- Yu, M.; Lin, J.; Wang, Z.; Fu, J.; Wang, S.; Zhang, H. J.; Han, Y. C. Fabrication, patterning, and optical properties of nanocrystalline YVO₄:A (A = Eu³⁺, Dy³⁺, Sm³⁺, Er³⁺) phosphor films via sol-gel soft lithography. *Chem. Mater.* **2002**, *14*, 2224–2231. <https://doi.org/10.1021/cm011663y>
- Zhang, Y.-m.; Li, Y.-h.; Li, P.; Hong, G.-y.; Yu, Y.n. Preparation and upconversion luminescence of YVO₄:Er³⁺, Yb³⁺. *Int. J. Miner. Metall. Mater.* **2010**, *17*, 225–228. <https://doi.org/10.1007/s12613-010-0218-7>

Comparative study of benzimidazole encapsulation in boron nitride and carbon nanotubes: A quantum chemistry study

Jeziel Rodrigues dos Santos¹⁺, Osmair Vital de Oliveira², Rafael Giordano Viegas², José Divino dos Santos³, Elson Longo¹

1. Federal University of Sao Carlos, Department of Chemistry, São Carlos, Brazil.
2. Federal Institute of Education Science and Technology of São Paulo, Catanduva, Brazil.
3. Goiás State University, Department of Chemistry, Anápolis, Brazil.

+Corresponding author: Jeziel Rodrigues dos Santos, **Phone:** +5562981791374, **Email address:** prof.jeziel@gmail.com

ARTICLE INFO

Article history:

Received: July 19, 2021

Accepted: October 19, 2021

Published: April 11, 2022

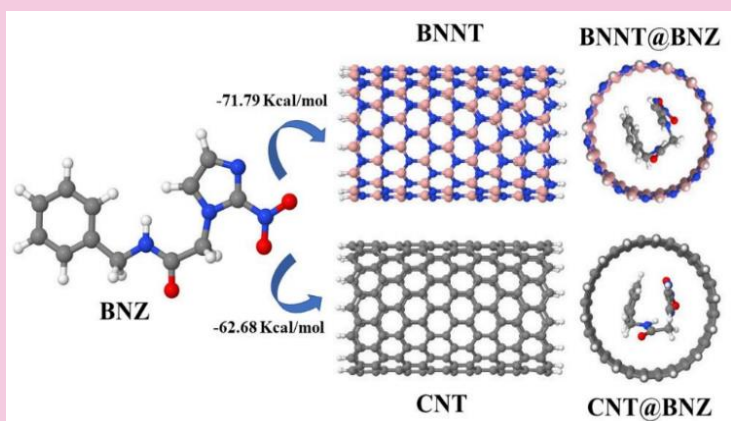
Keywords:

1. BNNT
2. CNT
3. benzimidazole
4. encapsulation
5. chagas disease
6. DFT

Section Editors: Elson Longo and Juan Manuel Andrés Bort

ABSTRACT: Quantum chemistry methods were used to study boron nitride and carbon nanotubes as possible carriers of antichagasic benzimidazole to improve their water solubility and bioavailability. Structurally, no significant changes were observed in both nanotubes throughout the encapsulation process. For the BNZ@BNNT complex, it was possible to notice short interactions, at 0.215 nm, between the hydrogen atoms of the BNZ and the nitrogen atoms of the BNNT. The binding energy reveals that both nanotubes are capable of encapsulating BNZ in an aqueous medium, with values of -71.79 and -62.68

kcal/mol for the BNZ@BNNT and BNZ@CNT complexes. The enthalpy of solvation indicates that the complexes are soluble in water with values of -32.35 and -28.76 kcal mol⁻¹ for the BNZ@BNNT and BNZ@CNT complexes. Regarding chemical stability, E_g and η show that BNZ@BNNT has greater stability (E_g/η of 3.35/1.68 eV) than BNZ@CNT (0.16/0.08 eV). Overall, our results demonstrate that BNNT is a better candidate to be used as a carrier of BNZ than CNT due to its greater structural and chemical stability.



1. Introduction

Chagas disease is caused by the protozoan *Trypanosoma cruzi*, which is transmitted mainly by the hematophagous vector insect popularly known as kissing bug. This insect belongs to the order *Hemiptera* and family *Reduviidae* and it is usually found around rock and wood piles and in cracks and gaps of walls and roofs, for instance. This disease is mainly transmitted by the bite of the kissing bug, but it can also be transmitted by blood transfusion and congenital transmission. Some of the efficient ways that have been widely used to control Chagas disease are environmental control and application of insecticides.

Although this disease was discovered in 1909 by the sanitary physician Carlos Chagas, until nowadays there are only two drugs that can treat it: benznidazole and nifurtimox. However, both drugs have low efficiency and strong side effects (Coura and Castro, 2002) presenting an inhibitory activity only in the acute phase of the disease. Additionally, in Brazil, the commercialization of the drug nifurtimox is prohibited (Fairlamb, 1999). It must be emphasized that, according to data obtained from the World Health Organization (WHO), Chagas disease still causes approximately 10,000 deaths per year. Although benznidazole is still in use, it has some limitations such as low water solubility and low permeability. Therefore, high doses of this drug are required to achieve therapeutic efficacy, which consequently increases its toxicity and side effects. A strategy commonly adopted in the literature to overcome these limitations is the use of encapsulating agents, which has been used as drug carriers of antichagasic drugs, such as nanoemulsions (E. Oliveira *et al.*, 2017; Streck *et al.*, 2019; Vermelho *et al.*, 2018), polymeric nanoparticles (Seremeta *et al.*, 2019; Silva *et al.*, 2019), liposomes (Morilla *et al.*, 2002; Vinuesa *et al.*, 2017) and cyclodextrins (Lyra *et al.*, 2012; Melo *et al.*, 2013; Soares Sobrinho *et al.*, 2011) among others.

Even though carrier agents are efficient, the elaboration and development of new nanocarriers have a high experimental cost. Computational chemistry then emerges as a relatively low-cost tool to assist researchers in the optimization of experiments, reducing operating costs. In this sense, O. Oliveira and Viegas (2020), recently used computational chemistry methods to show that cucurbit[7]uril is a possible new carrier agent of benznidazole. Carbon nanotube (CNT) is another class of nanocarriers that have been extensively studied over the past two decades. In addition to their electrical and optical properties (Rathod *et al.*, 2019), CNTs are also inert and chemically stable (Anzar *et al.*, 2020), which increases their potential application in

drug delivery. For such reasons, CNTs have been used as drug carriers in the treatment of different diseases (Wang and Moriyam, 2011). Another nanotube of great interest is the boron nitride nanotube (BNNT). Despite having similar properties, CNTs are metallic or semiconductor, while BNNTs are electrically insulating (Kim *et al.*, 2018). Like CNTs, BNNTs have also been widely used in drug delivery (Ciofani, 2010). Regarding the toxicity, the BNNTs are nontoxic and biocompatible, while possible cytotoxicity of CNTs have been observed (Dehaghani *et al.*, 2020).

From a theoretical point of view, quantum chemistry methods have been adopted to study the encapsulation of different drugs in these nanotubes. For example, both CNT and BNNT have been used to encapsulate anticancer (Azarakhshi *et al.*, 2021; Mahdaviyar and Moridzadeh, 2014; Shayan and Nowroozi, 2018; Zaboli *et al.*, 2020) and anti-HIV (Xu *et al.*, 2018) drugs, among others. Recently, CNT (10,10) was used to encapsulate 1,4-dihydropyridine derivatives (Dutra *et al.*, 2017) using the density functional theory. In another study, pure and silicon-doped BNNT (12,0) were employed to adsorb sarin (Santos *et al.*, 2020). In the present work, we propose the use of quantum chemistry methods to study the encapsulation of benznidazole in CNT and BNNT nanotubes in zigzag form (14,0) aiming to improve its bioavailability in the body. It should be noted that until the present moment the use of these nanotubes for the encapsulation of such antichagasic agent has not been reported in the literature.

2. Materials and Methods

The BNNT and CNT zigzag models (14,0) with diameters of 11.78 and 11.06 Å, respectively, were used as a model vehicle to study the BNZ@BNNT and BNZ@CNT complexes. The BNNT and CNT structures were generated using a script (see [Supplementary Material S1](#)) with chiral vectors m (18) and n (0) and length of 18.06 and 17.83 Å, respectively. To avoid the effects caused by the ends of the nanotubes, both ends of each nanotube were hydrogenated (Fig. 1). In order to construct the molecular geometry of the BNZ@BNNT and BNZ@CNT complexes, a translational script was used to center the BNZ inside the nanotubes ([Supplementary Material S2](#)). The molecular geometry of the BNZ was built through its internal coordinates, considering bond length, bond angle and twist angle. This information was later converted into Cartesian coordinates with the aid of the Molden (Schaffenaar and Noordik, 2000), which is a free code package for structural visualization.

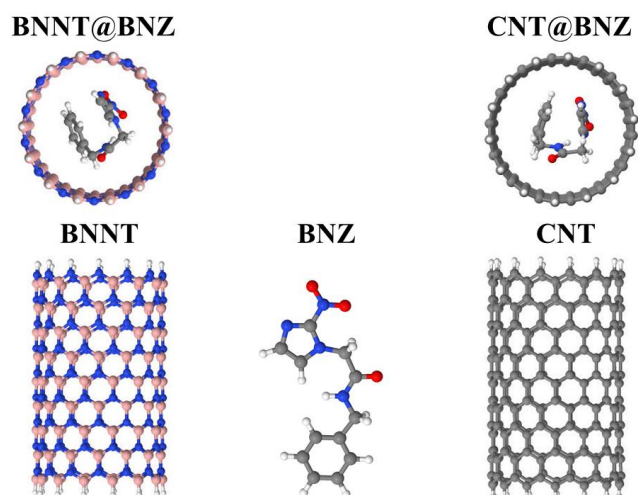


Figure 1. Optimized structures with the DFT-GD3//B3LYP/6-31G(d) method. Oxygen in red, carbon in grey, hydrogen in white, nitrogen in blue, and boron in salmon.

The models (BNNT, CNT and BNZ) and the complexes (BNZ@BNNT and BNZ@CNT) were initially optimized with the PM7 Hamiltonian using the MOPAC2016 program (Stewart, 2016). Subsequently, the structures with minimum energies were reoptimized through DFT, with B3LYP hybrid functional and 6-31G(d) basis function (Rassolov *et al.*, 2001). This theory level was chosen to balance the computational cost and quality of results. The dispersion interaction correction was taken into account by employing the Grimme method (GD3) (Grimme *et al.*, 2010). The stationary points were characterized as a minimum point of energy through harmonic vibrational states, whose imaginary frequencies were not observed. DFT calculations were performed in vacuum and in solvent medium (H₂O) using the PCM method (Scalmani and Frisch, 2010) for the dielectric constant of H₂O and the Gaussian 09 computational package. The natural orbital bonding (NBO) method (Reed *et al.*, 1985) was used to calculate atomic charges. The binding energy (E_{bind}) and the enthalpy of solvation (H_{solv}) of the complexes in vacuum and in solvent medium were calculated using Eqs. 1 and 2, respectively.

$$E_{\text{bind}} = E_{\text{NT-BNZ}} - (E_{\text{NT}} + E_{\text{BNZ}}) \quad (1)$$

$$H_{\text{solv}} = E_{\text{NT-BNZ-solv}} - E_{\text{NT-BNZ-vacuum}} \quad (2)$$

where $E_{\text{NT-BNZ}}$ is the total energy of the complexes (BNZ@BNNT and BNZ@CNT), considering the calculations for the vacuum and the solvent medium, E_{NT} is the total energy of the studied nanotubes (BNNT and CNT), E_{BNZ} is the total energy of the BNZ molecule

and $E_{\text{NT-BNZ-solv}}$ are the total energies of the complexes obtained in the solvent and gas phases, respectively.

3. Results and discussion

The encapsulation of BNZ in the BNNT (14.0) and CNT (14.0) was investigated herein using theoretical methods to obtain a new drug delivery system to be used in Chagas disease. Figure 1 presents the most stable geometries obtained for the studied models in aqueous media, using the dielectric constant of water for taking into account the solvent medium.

As it can be seen in Fig. 1, no significant structural change was observed in the BNNT and CNT after the encapsulation process. The main structural differences found in the BNZ molecule are in agreement with the lower root mean square deviation values (RMSD) (< 0.765 nm), which were calculated from the superposition between the unencapsulated and encapsulated BNZ molecule. For the formed complexes, it was possible to observe hydrogen interactions of the order of 0.215 nm between the hydrogen atoms present in the BNZ molecule and the nitrogen atoms from the BNNT nanotube. These interactions provided great stability to the BNZ@BNNT complex when compared to the BNZ@CNT, which is in accordance with the results in Tab. 1, that were calculated from Eq. 1.

To better understand the energetic processes involved in the encapsulation process, the electronic structures for the model vehicles, as well as for the formed complexes, are presented and discussed. The electronic properties were used to clarify the interaction between the BNZ molecule and the inner surface of the BNNT and the CNT model vehicles. The reactivity parameters were based on the energies of molecular orbitals occupied with the highest energy (HOMO, E_{HOMO}) and those unoccupied with the lowest energy (LUMO, E_{LUMO}). According to the Koopmans' theorem (Koopmans, 1934), the ionization potential (IP) is the negative of the HOMO energy ($-E_{\text{HOMO}}$), while the electron affinity (EA) can be approximated by the negative of the LUMO energy ($-E_{\text{LUMO}}$). The energy gap is another property obtained from the energies of E_{HOMO} and E_{LUMO} , being defined as the absolute difference ($|E_{\text{HOMO}} - E_{\text{LUMO}}|$). Table 1 summarizes the electronic properties obtained in our calculations.

Table 1. Electronic properties obtained from DFT-GD3//B3LYP/6-31G(d) calculations.

Compounds	E _{bind} kcal/mol	H _{solv} kcal/mol	E _{HOMO} eV	E _{LUMO} eV	E _g eV	IP eV	EA eV	Dipole Debye
BNZ/(vacuum)	-	-12.72	-7.04	-2.52	4.52	7.04	2.52	7.81
BNZ/(solvent)	-		-6.72	-2.71	4.01	6.72	2.71	9.98
BNNT/(vacuum)	-	-28.19	-6.37	-0.29	6.08	6.37	0.29	23.81
BNNT/(solvent)	-		-6.28	-0.37	5.91	6.28	0.37	31.99
CNT/(vacuum)	-	-10.41	-3.80	-3.64	0.16	3.80	3.64	0.09
CNT/(solvent)	-		-3.82	-3.66	0.16	3.82	3.66	0.10
BNZ@BNNT/(vacuum)	-80.36	-32.35	-6.29	-2.96	3.33	6.29	2.96	19.38
BNZ@BNNT/(solvent)	-71.79		-6.26	-2.91	3.35	6.26	2.91	23.44
BNZ@CNT/(vacuum)	-69.05	-28.76	-3.80	-3.64	0.16	3.80	3.64	0.16
BNZ@CNT/(solvent)	-62.68		-3.83	-3.67	0.16	3.83	3.67	7.10

Table 2. Quantum molecular descriptors were obtained through the reactivity parameters E_{HOMO} and E_{LUMO} using DFT-GD3//B3LYP/6-31G(d) calculations.

Compounds	μ eV	χ eV	η eV	ω eV	S eV
BNZ (vacuum)	-7.48	7.48	2.26	4.84	0.22
BNZ (solvent)	-4.72	4.72	2.01	1.82	0.25
BNNT (vacuum)	-3.33	3.33	3.04	0.89	0.16
BNNT (solvent)	-3.33	3.33	2.96	0.91	0.17
CNT (vacuum)	-3.72	3.72	0.08	3.49	6.25
CNT (solvent)	-3.74	3.74	0.08	3.51	6.25
BNZ@BNNT (vacuum)	-4.63	4.63	1.67	2.23	0.25
BNZ@BNNT (solvent)	-4.59	4.59	1.68	2.19	0.30
BNZ@CNT (vacuum)	-3.72	3.72	0.08	3.49	6.25
BNZ@CNT (solvent)	-3.75	3.75	0.08	3.52	6.25

In addition, quantum molecular descriptors can be used to better understand the interactions between BNZ and the model vehicles. For this, the global hardness (η), electronegativity (χ), electronic chemical potential (μ), electrophilicity index (ω) and softness chemistry (S) were calculated from Eqs. 3–7, respectively (Koopmans, 1934; Lobo *et al.*, 2020; Serhan *et al.*, 2020; Sheikhi *et al.*, 2018). For instance, μ measures the evasion affinity of a molecule from chemical equilibrium, η measures the charge transfer and the chemical reactivity of a molecule, χ is the capacity of a molecule to attract electrons, and ω is the electrophilic power of a molecule. Furthermore, the stability of molecular systems is related to hardness (η), which is a tool to understand chemical reactivity (Khaleghian and Azarakhshi, 2019). All these quantum descriptors are displayed in Tab. 2.

$$\eta = \frac{I-EA}{2} \quad (3)$$

$$\chi = \frac{I+EA}{2} \quad (4)$$

$$\mu = \frac{-I+EA}{2} \quad (5)$$

$$\omega = \frac{\mu^2}{2} \quad (6)$$

$$S = \frac{1}{2\eta} \quad (7)$$

As shown in Tab. 2, the global hardness value (η) for the BNNT is 3.04 eV in vacuum and 2.96 eV in solvent medium. However, after the formation of the BNZ@BNNT complex, these values change to 1.67 eV in vacuum and 1.68 eV in solvent medium, i.e., the η value of the BNNT decreases as it interacts with the BNZ molecule. These values are greater than those for the BNZ@CNT system, where the η value is practically unchanged (Tab. 2). This is in agreement with the energy of formation of the complexes, as shown in Tab. 1. The electrophilicity index (ω) calculation reveals that the BNZ@BNNT has higher values than the BNZ and isolated BNNT in the solvent phase, thus implying that this complex has a better electrophilic characteristic. Nevertheless, when comparing both complexes, it is possible to observe that, in aqueous media, the BNZ@CNT (3.52 eV) acts as an electrophile due to its high ω value in comparison with the BNZ@BNNT (2.19 eV). In contrast, the lower value of electronegativity (χ) of the BNZ@CNT (3.75 eV)

compared to the BNZ@BNNT (4.59 eV) shows that it acts as a nucleophile in solvent phase. The same conclusion can be reached using the μ and η descriptors, being the electrophile characterized by a high value of μ and a low value of η , whereas the opposite is true for the nucleophile.

The dipole moment values of the model vehicles are altered according to the interaction between the BNZ molecule and their internal surfaces (Tab. 1). The change in dipole moment after interaction indicates a charge transference between the BNZ molecule and the BNNT and CNT model vehicles. For better visualization of this process, Fig. 2 illustrates the molecular electrostatic potential (MEP) for the studied compounds.

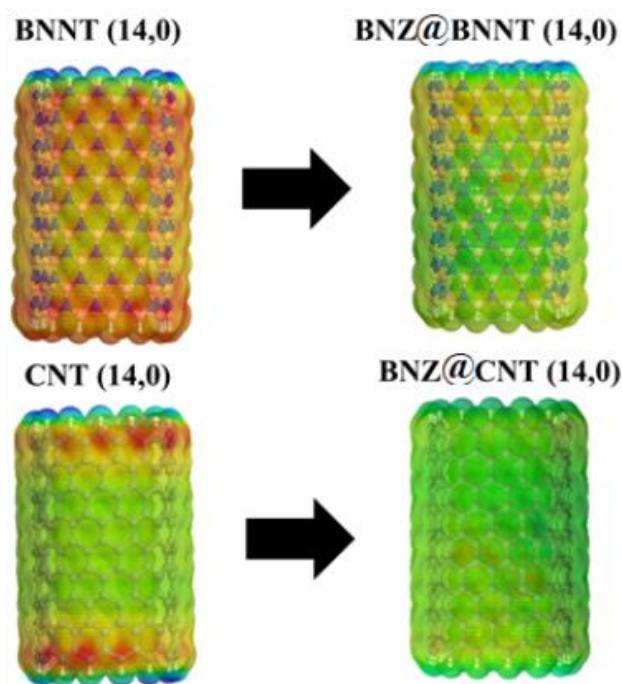


Figure 2. Representation of the molecular electrostatic potential (MEP, in eV) of the BNNT and CNT model vehicles, and the BNZ molecule. For MPE, the negative and positive charges range from red to blue, respectively (for interpretation of the color references in this legend, please refer to the web version of this article).

As it can be seen in Fig. 2, charge transfers can be evidenced by the modification in the MEP after the formation of the BNZ@BNNT and BNZ@CNT complexes. Therefore, according to Tabs. 1 and 2, this transfer process is very important to improve the electronic properties of the studied nanotubes.

4. Conclusions

Chagas disease, caused by the protozoan *Trypanosoma cruzi*, was discovered in 1909 by Carlos Chagas. Although this disease is responsible for nearly 10.000 deaths per year worldwide, there is only one effective drug against it: benznidazole (BNZ). However, it has low water solubility and low bioavailability in the organism. Therefore, herein we used quantum chemistry methods to characterize two nanotubes (BNNT and CNT) to be used as carrier agents for the BNZ. The optimized structures of the complexes showed that the presence of BNZ inside the nanotubes did not alter their structural form, which is desired in drug delivery. The binding energy (E_{bind}) revealed that the BNNT and CNT are able to encapsulate BNZ with E_{bind} values of -71.79 and -62.68 kcal mol $^{-1}$ for the BNZ@BNNT and BNZ@CNT complexes, respectively, in aqueous media. The solvation enthalpy of -32.35 and -28.76 kcal mol $^{-1}$ for the BNZ@BNNT and BNZ@CNT complexes, respectively, indicated that they are soluble in water. Additionally, the energy gap (E_g) and global hardness (η) showed that the BNZ@BNNT presents higher stability, with (E_g/η) value of 3.35/1.68 eV against 0.16/0.08 eV for the BNZ@CNT. The electrophilicity index (ω) and electronegativity (χ) values indicated that the BNZ@BNNT and BNZ@CNT act as nucleophile and electrophile, respectively, in aqueous media. Finally, the present results demonstrate that the BNNT is a better candidate to be used as a carrier agent for BNZ than the CNT due to its higher chemical stability, lower binding energy and lower solvation enthalpy.

Authors' contribution

Conceptualization: Santos, J. R.; Oliveira, O. V.; Viegas, R. G.

Data curation: Santos, J. R.; Santos, J. D.

Formal Analysis: Santos, J. R.; Santos, J. D.; Oliveira, O. V.; Viegas, R. G.; Longo, E.

Funding acquisition: Not applicable.

Investigation: Santos, J. R.; Santos, J. D.; Oliveira, O. V.; Viegas, R. G.; Longo, E.

Methodology: Santos, J. R.; Santos, J. D.

Project administration: Oliveira, O. V.; Longo, E.; Santos, J. D.

Resources: Longo, E.; Santos, J. D.

Software: Santos, J. R.; Santos, J. D.

Supervision: Longo, E.

Validation: Santos, J. R.; Santos, J. D.; Oliveira, O. V.; Viegas, R. G.; Longo, E.

Visualization: Santos, J. R.; Santos, J. D.; Oliveira, O. V.; Viegas, R. G.; Longo, E.

Writing – original draft: Santos, J. R.; Oliveira, O. V.; Viegas, R. G.

Writing – review & editing: Santos, J. R.; Oliveira, O. V.; Viegas, R. G.

Data availability statement

The data will be available upon request.

Funding

Not applicable.

Acknowledgments

This research was carried out with the support of the Center for High Performance Computing at the State University of Goiás. Jeziel Rodrigues dos Santos thanks CAPES for providing a research grant.

References

- Anzar, N.; Hasan, R.; Tyagi, M.; Yadav, N.; Narang, J. Carbon nanotube: A review on synthesis, properties and plethora of applications in the field of biomedical science. *Sensors Int.* **2020**, *1*, 100003. <https://doi.org/10.1016/j.sintl.2020.100003>
- Azarakhshi, F.; Sheikhi, M.; Shahab, S.; Khaleghian, M.; Sirotsina, K.; Yurlevich, H.; Novik, D. Investigation of encapsulation of Talzenna drug into carbon and boron-nitride nanotubes [CNT(8,8-7) and BNNT(8,8-7)]: A DFT study. *Chem. Pap.* **2021**, *75*, 1521–1533. <https://doi.org/10.1007/s11696-020-01407-8>
- Ciofani, G. Potential applications of boron nitride nanotubes as drug delivery systems. *Expert Opin. Drug Deliv.* **2010**, *7* (8), 889–893. <https://doi.org/10.1517/17425247.2010.499897>
- Coura, J. R.; Castro, S. L. A critical review on Chagas disease chemotherapy. *Mem. Inst. Oswaldo Cruz* **2002**, *97* (1), 3–24. <https://doi.org/10.1590/S0074-02762002000100001>
- Dehaghani, M. Z.; Bagheri, B.; Nasiriasayesh, A.; Mashhadzadeh, A. H.; Zarrintaj, P.; Rabiee, N.; Bagherzadeh, M.; Habibzadeh, S.; Abida, O.; Saeb, M. R.; Jang, H. W.; Shokouhimehr, M. Insight into the self-insertion of a protein inside the boron nitride nanotube. *ACS Omega* **2020**, *5* (49), 32051–32058. <https://doi.org/10.1021/acsomega.0c05080>
- Dutra, L. M.; Oliveira, O. V.; Santos, J. D. Computational studies on the encapsulation of 1,4-dihydropyridine derivatives into CNT(10,10). *Aust. J. Chem.* **2017**, *70* (3), 252–257. <https://doi.org/10.1071/CH16165>
- Fairlamb, A. H. Future prospects for the chemotherapy of Chagas' disease. *Medicina (B. Aires)* **1999**, *59* (Suppl. 2), 179–187.
- Grimme, S.; Antony, J.; Ehrlich, S.; Krieg, H. A consistent and accurate *ab initio* parametrization of density functional dispersion correction (DFT-D) for the 94 elements H-Pu. *J. Chem. Phys.* **2010**, *132* (15), 154104. <https://doi.org/10.1063/1.3382344>
- Khaleghian, M.; Azarakhshi, F. Theoretical modelling of encapsulation of the Altretamine drug into BN(9,9-5) and AlN(9,9-5) nano rings: A DFT study. *Mol. Phys.* **2019**, *117* (18), 2559–2569. <https://doi.org/10.1080/00268976.2019.1574987>
- Kim, J. H.; Pham, T. V.; Hwang, J. H.; Kim, C. S.; Kim, M. J. Boron nitride nanotubes: Synthesis and applications. *Nano Convergence* **2018**, *5*, 17. <https://doi.org/10.1186/s40580-018-0149-y>
- Koopmans, T. Über Die Zuordnung von Wellenfunktionen Und Eigenwerten Zu Den Einzelnen Elektronen Eines Atoms. *Physica* **1934**, *1* (1–6), 104–113. [https://doi.org/10.1016/S0031-8914\(34\)90011-2](https://doi.org/10.1016/S0031-8914(34)90011-2)
- Lobo, J. A. P.; Santos, J. R.; Oliveira, O. V.; Silva, E. L.; Santos, J. D. Theoretical study of greenhouse gases on the zirconium oxide nanotube surface. *Chem. Phys. Lett.* **2020**, *745*, 137236. <https://doi.org/10.1016/j.cplett.2020.137236>
- Lyra, M. A. M.; Soares-Sobrinho, J. L.; Figueiredo, R. C. B. Q.; Sandes, J. M.; Lima, Á. A. N.; Tenório, R. P.; Fontes, D. A. F.; Santos, F. L. A.; Rolim, L. A.; Rolim-Neto, P. J. Study of benzimidazole-cyclodextrin inclusion complexes, cytotoxicity and trypanocidal activity. *J. Incl. Phenom. Macrocycl. Chem.* **2012**, *73*, 397–404. <https://doi.org/10.1007/s10847-011-0077-5>
- Mahdaviifar, Z.; Moridzadeh, R. Theoretical prediction of encapsulation and adsorption of platinum-anticancer drugs into single walled boron nitride and carbon nanotubes. *J. Incl. Phenom. Macrocycl. Chem.* **2014**, *79*, 443–457. <https://doi.org/10.1007/s10847-013-0367-1>
- Melo, P. N.; Barbosa, E. G.; De Caland, L. B.; Carpegiani, H.; Garnerio, C.; Longhi, M.; Fernandes-Pedrosa, M. F.; Silva-Júnior, A. A. Host-guest interactions between benzimidazole and beta-cyclodextrin in multicomponent complex systems involving hydrophilic polymers and triethanolamine in aqueous solution. *J. Mol. Liq.* **2013**, *186*, 147–156. <https://doi.org/10.1016/j.molliq.2013.07.004>
- Morilla, M. J.; Benavidez, P.; Lopez, M. O.; Bakas, L.; Romero, E. L. Development and *in vitro* characterisation of a benzimidazole liposomal formulation. *Int. J. Pharm.* **2002**, *249* (1–2), 89–99. [https://doi.org/10.1016/S0378-5173\(02\)00453-2](https://doi.org/10.1016/S0378-5173(02)00453-2)
- Oliveira, E. C. V.; Carneiro, Z. A.; Albuquerque, S.; Marchetti, J. M. Development and evaluation of a nanoemulsion containing Ursolic acid: A promising trypanocidal agent: Nanoemulsion with ursolic acid against *T. Cruzi*. *AAPS PharmSciTech* **2017**, *18*, 2551–2560. <https://doi.org/10.1208/s12249-017-0736-y>

- Oliveira, O. V.; Viegas, R. G. Cucurbit[7]uril as a possible nanocarrier for the antichagasic benzimidazole: A computational approach. *J. Incl. Phenom. Macrocycl. Chem.* **2020**, *98* (1–2), 93–103. <https://doi.org/10.1007/s10847-020-01014-w>
- Rassolov, V. A.; Ratner, M. A.; Pople, J. A.; Redfern, P. C.; Curtiss, L. A. 6-31G* basis set for third-row atoms. *J. Comput. Chem.* **2001**, *22* (9), 976–984. <https://doi.org/10.1002/jcc.1058>
- Rathod, V.; Tripathi, R.; Joshi, P.; Jha, P. K.; Bahadur, P.; Tiwari, S. Paclitaxel encapsulation into dual-functionalized multi-walled carbon nanotubes. *AAPS PharmSciTech* **2019**, *20*, 51. <https://doi.org/10.1208/s12249-018-1218-6>
- Reed, A. E.; Weinstock, R. B.; Weinhold, F. Natural Population Analysis. *J. Chem. Phys.* **1985**, *83* (2), 735. <https://doi.org/10.1063/1.449486>
- Santos, J. R.; Silva, E. L.; Oliveira, O. V.; Santos, J. D. Theoretical study of sarin adsorption on (12,0) boron nitride nanotube doped with silicon atoms. *Chem. Phys. Lett.* **2020**, *738*, 136816. <https://doi.org/10.1016/j.cplett.2019.136816>
- Scalmani, G.; Frisch, M. J. Continuous surface charge polarizable continuum models of solvation. I. General formalism. *J. Chem. Phys.* **2010**, *132* (11), 114110. <https://doi.org/10.1063/1.3359469>
- Schaftenaar, G.; Noordik, J. H. Molden: A pre- and post-processing program for molecular and electronic structures. *J. Comput. Aided. Mol. Des.* **2000**, *14*, 123–134. <https://doi.org/10.1023/A:1008193805436>
- Seremeta, K. P.; Arrúa, E. C.; Okulik, N. B.; Salomon, C. J. Development and characterization of benzimidazole nano- and microparticles: A new tool for pediatric treatment of Chagas disease? *Colloids Surf. B Biointerfaces* **2019**, *177*, 169–177. <https://doi.org/10.1016/j.colsurfb.2019.01.039>
- Serhan, M.; Abusini, M.; Almahmoud, E.; Omari, R.; Al-Khaza'leh, K.; Abu-Farsakh, H.; Ghozlan, A.; Talla, J. The electronic properties of different chiralities of defected boron nitride nanotubes: Theoretical study. *Comput. Condens. Matter* **2020**, *22*, e00439. <https://doi.org/10.1016/j.cocom.2019.e00439>
- Shayan, K.; Nowroozi, A. Boron nitride nanotubes for delivery of 5-fluorouracil as anticancer drug: A theoretical study. *Appl. Surf. Sci.* **2018**, *428*, 500–513. <https://doi.org/10.1016/j.apsusc.2017.09.121>
- Sheikhi, M.; Shahab, S.; Khaleghian, M.; Hajikolaee, F. H.; Balakhanava, I.; Alnajjar, R. Adsorption properties of the molecule resveratrol on CNT(8,0-10) nanotube: Geometry optimization, molecular structure, spectroscopic (NMR, UV/Vis, excited state), FMO, MEP and HOMO-LUMO investigations. *J. Mol. Struct.* **2018**, *1160*, 479–487. <https://doi.org/10.1016/j.molstruc.2018.01.005>
- Silva, A. M. S.; Caland, L. B.; Doro, P. N.M; Oliveira, A. L. C. S. L.; de Araújo-Júnior, R. F.; Fernandes-Pedrosa, M. F.; do Egito, E. S. T.; da Silva-Junior, A. A. Hydrophilic and Hydrophobic Polymeric Benzimidazole-Loaded Nanoparticles: Physicochemical Properties and in Vitro Antitumor Efficacy. *J. Drug Deliv. Sci. Technol.* **2019**, *51*, 700–707. <https://doi.org/10.1016/j.jddst.2019.04.005>
- Soares Sobrinho, J. L.; Soares, M. F. de L. R.; Torres Labandeira, J. J.; Alves, L. D. S.; Rolim Neto, P. J. Improving the solubility of the antichagasic drug benzimidazole through formation of inclusion complexes with cyclodextrins. *Quim. Nova* **2011**, *34* (9), 1534–1538. <https://doi.org/10.1590/S0100-40422011000900010>
- Stewart Computational Chemistry*; Stewart, J. J. P.: Colorado Springs, 2016. <http://openmopac.net/> (accessed 2021-04-14)
- Streck, L.; Sarmiento, V. H. V.; Menezes, R. P. R. P. B. de; Fernandes-Pedrosa, M. F.; Martins, A. M. C.; da Silva-Júnior, A. A. Tailoring microstructural, drug release properties, and antichagasic efficacy of biocompatible oil-in-water benzimidazole-loaded nanoemulsions. *Int. J. Pharm.* **2019**, *555*, 36–48. <https://doi.org/10.1016/j.ijpharm.2018.11.041>
- Vermelho, A. B.; Cardoso, V. S.; Ricci Junior, E.; Santos, E. P. dos; Supuran, C. T. Nanoemulsions of sulfonamide carbonic anhydrase inhibitors strongly inhibit the growth of *Trypanosoma cruzi*. *J. Enzyme Inhib. Med. Chem.* **2018**, *33* (1), 139–146. <https://doi.org/10.1080/14756366.2017.1405264>
- Vinuesa, T.; Herráez, R.; Oliver, L.; Elizondo, E.; Acarregui, A.; Esquisabel, A.; Pedraz, J. L.; Ventosa, N.; Veciana, J.; Viñas, M. Benzimidazole nanoformulates: A chance to improve therapeutics for chagas disease. *Am. J. Trop. Med. Hyg.* **2017**, *97* (5), 1469–1476. <https://doi.org/10.4269/ajtmh.17-0044>
- Wang, Q.; Moriyam, H. Carbon nanotube-based thin films: Synthesis and properties. In *Carbon Nanotubes - Synthesis, Characterization, Applications*; IntechOpen, 2011; pp 487–514. <https://doi.org/10.5772/22021>
- Xu, H.; Li, L.; Fan, G.; Chu, X. DFT study of nanotubes as the drug delivery vehicles of Efavirenz. *Comput. Theor. Chem.* **2018**, *1131*, 57–68. <https://doi.org/10.1016/j.comptc.2018.03.032>
- Zaboli, M.; Raissi, H.; Zaboli, M. Investigation of nanotubes as the smart carriers for targeted delivery of mercaptopurine anticancer drug. *J. Biomol. Struct. Dyn.* **2020**, 1–14. <https://doi.org/10.1080/07391102.2020.1860823>

Comparative study of benznidazole encapsulation in boron nitride and carbon nanotubes: A quantum chemistry study

Jeziel Rodrigues dos Santos¹⁺, Osmair Vital de Oliveira², Rafael Giordano Viegas², José Divino dos Santos³, Elson Longo¹

1. Federal University of Sao Carlos, Department of Chemistry, São Carlos, Brazil.
2. Federal Institute of Education Science and Technology of São Paulo, Catanduva, Brazil.
3. Goiás State University, Department of Chemistry, Anápolis, Brazil.

+Corresponding author: Jeziel Rodrigues dos Santos, **Phone:** +5562981791374, **Email address:** prof.jeziel@gmail.com

ARTICLE INFO

Article history:

Received: July 19, 2021

Accepted: October 19, 2021

Published: April 11, 2022

Keywords:

1. BNNT
2. CNT
3. benznidazole
4. encapsulation
5. chagas disease
6. DFT

Section Editors: Elson Longo and Juan Manuel Andrés Bort

S1. Script to generate cartesian coordinates for BNNT and CNT models.

```
#!/bin/bash
#UEG - UnUCET - Nanotubos das formas [(XY)n]m, com n e m PARES E IMPARES
#FORMA ZIG-ZAG ou BARCO - v.08
#Dr. José Divino dos Santos e MsC.Jeziel Rodrigues
#como executar: ./shell-nano-otim-xy-par-impar.sh $1 $2 $3 $4 $5 $6 $7 $8 $9
$10 $11 $12 $13 $14

pi=` echo "scale=10;4*a(1)"|bc -l `
n0=$1 #Numero de atomos na base GaAs, ZnO, C, BN ...
m=$2 #Numero de niveis do nanotubo
d=$3 #distancia X-X
tipo=$4 #tipo de crescimento - zig ou bar
atomo1=$5 #Simbolo atomico 1
atomo2=$6 #Simbolo atomico 2
metodo=$7 #Metodo semiempirico - MNDO, AM1, PM3
multi=$8 #Multiplicidades - SINGLET, DOUBLET, TRIPLET, QUARTET ...
carga=$9 #Cargas - +2, +1, 0, -1, -2 ...
shift;shift;shift;shift;shift;shift;shift;shift;shift;
metodoAb=$1 #Metodo Ab-inicio: HF, RHF, UHF, DFT, ...
baseAb=$2 #Base Ab-inicio: 3-21G, 6-31G, lanl2dz, GEN, ...
multiAb=$3 #Multiplicidades abinitio: 1, 2, 3, 4 ...
cargaAb=$4 #Cargas - +2, +1, 0, -1, -2 ...
grad=$5 #Gradiente procurado
fatd1=1.0 #fator de D1=fatd1*D1
fatd2=1.0 #fator de D2=fatd2*D2
fatd3=1.0 #fator de D3=fatd3*D3
```



```

otimd=1.0 #otimizador de distancia
otima=1.0 #otimizador de angulo
otimt=1.0 #otimizador de torsao
#Exemplos:
if [ "${tipo}" = "zig" ]
then
  #Crescimento ZIG-ZAG
  n=` echo "${n0}"|bc -l ` #numero de atomos X na base
  nome=nano${tipo}-${atomo1}${atomo2}-n${n}-m${m}-${metodo}-${multi}-
c${carga}
  te=` echo "scale=10;(0.0000*2*${pi}/${n})"|bc -l ` #angulo inicial; zero
grau
  dte=` echo "scale=10;(2*${pi}/${n})"|bc -l ` #incremento do angulo
  D1=`echo "scale=10;${fatd1}*(2*${d}*c(${pi}/6))"|bc -l ` # distancia basica
X-X
  ra=`echo "scale=10;(${D1})/(sqrt(2 - 2*c(2*${pi}/${n})))"|bc -l ` #raio
ZIG-ZAG
  #curv=`echo "scale=10;1/${ra}"|bc -l ` # distancia basica do ZIG-ZAG
  incl=0.00000
  inc2=` echo "scale=10;1.0000*(${pi}/${n})"|bc -l ` #angulo inicial de Y
  incte=` echo "scale=10;1.0000*(${pi}/${n})"|bc -l ` #incremento do angulo
no nivel
  D2=`echo "scale=10;${fatd2}*(${d}*s(${pi}/6))"|bc -l ` # incr D2*fat2
  D3=`echo "scale=10;${fatd3}*(${d} + ${d}*s(${pi}/6))"|bc -l ` # incr
D3*fat3
  tx=`echo "scale=10;-${ra}*c(${te} + ${incl})"|bc -l ` #translacao em x
  ty=`echo "scale=10;-${ra}*s(${te} + ${incl})"|bc -l ` #translacao em y
  z2=`echo "scale=10;0.0000*s(${pi}/6)"|bc -l ` #coord z2
# echo " ${metodo} PREC SHIFT1000 DEBUG LET T=1999999 + " > ${nome}.dat
# echo " DUMP=250000 XYZ PL GEO-OK ${multi} CHARGE=${carga} " >>
${nome}.dat
echo " ${metodo} UHF CYCLES=30000 PREC SHIFT1000 DEBUG LET T=19999999 + "
> ${nome}.dat
echo " DUMP=250000 AUX GNORM=0.01 PL GEO-OK ${multi} CHARGE=${carga} " >>
${nome}.dat
echo " ${nome}" >> ${nome}.dat
echo " " >> ${nome}.dat
j=1
while [ ${j} -le ${m} ]
do

  i=1
  while [ ${i} -le ${n} ]
  do
    x1=`echo "scale=10;${tx} + ${ra}*c(${te} + ${incl})"|bc -l ` #coord
x1
    y1=`echo "scale=10;${ty} + ${ra}*s(${te} + ${incl})"|bc -l ` #coord y1
    x2=`echo "scale=10;${tx} + ${ra}*c(${te} + ${inc2})"|bc -l ` #coord
x2
    y2=`echo "scale=10;${ty} + ${ra}*s(${te} + ${inc2})"|bc -l ` #coord y2
    echo "${atomo1} ${x1} 1 ${y1} 1 ${z2} 1 " >> ${nome}.dat
    echo "${atomo2} ${x2} 1 ${y2} 1 ${D2} 1 " >> ${nome}.dat
    te=` echo "scale=10;${te} + ${dte}"|bc -l `
  done
done

```

```

i=` expr ${i} + 1 `
done
z2=` echo "scale=10;${z2} + ${D3}"|bc -l `
D2=` echo "scale=10;${D2} + ${D3}"|bc -l `
inc1=` echo "scale=10;${inc1} + ((-1)^(${j}-1))*${inc1}"|bc -l `
inc2=` echo "scale=10;${inc2} + ((-1)^(${j}-1))*${inc2}"|bc -l `
j=` expr ${j} + 1 `

done
#rodar-mopac2016.sh ${nome}.dat
#/opt/mopac/MOPAC2016.exe ${nome}.dat
conv-xyz-dat-gjf-supercomputador.sh ${nome} ${metodoAb} ${baseAb}
${cargaAb} ${multiAb} 14 24
# conv-arc-dat-gjf.sh ${nome} ${metodoAb} ${baseAb} ${cargaAb} ${multiAb}
# echo "batg03-vulc ${nome} " >> fila-abinitio-varredor.sh
# batg03-vulc ${nome}
# grep -H "SCF Done" ${nome}.log >> energias-abi-varredor.sh
else
#Crescimento BARCO
n=` echo "${n0}"|bc -l ` #numero de carbono vezes quatro
nome=nano${tipo}-${atomo1}${atomo2}-n${n}-m${m}-${metodo}-${multi}-
c${carga}

te=` echo "scale=10;0.0000*(2*${pi}/${n})"|bc -l ` # angulo
te0=` echo "scale=10;2*${pi}/${n}"|bc -l ` # angulo
inc1=` echo "scale=10;${pi}/${n}"|bc -l ` #incremento do angulo de nivel
dte=` echo "scale=10;(2*${pi}/${n})"|bc -l ` #incremento do angulo maior -
Zn-Zn
D1=`echo "scale=10;${fatd1}*(2*(${d} + ${d}*c(2*${pi}/${n})))"|bc -l ` #
distancia basica do BARCO
ra=`echo "scale=10;(${D1})/(sqrt(2 - 2*c(2*${pi}/${n})))"|bc -l ` #raio
BARCO
#curv=`echo "scale=10;1/${ra}"|bc -l ` # curvatura BARCO
#echo "curv=${curv}"
inc=0.00000
dte1=` echo "scale=10;${fatd2}*(${te0}/3)"|bc -l ` #incremento do angulo
menor - Zn-O
D3=`echo "scale=10;${fatd3}*(${d}*s(${pi}/3))"|bc -l ` # incr em z2*fatdz2
dz1=`echo "scale=10;${d}*s(${pi}/3)"|bc -l ` # incremento em z1
#dz2=`echo "scale=10;${fatdz2}*(2*${d}*s(${pi}/3))"|bc -l ` # incr em
z2*fatdz2
tx=`echo "scale=10;-${ra}*c(${te} + ${inc})"|bc -l ` #translacao em x
ty=`echo "scale=10;-${ra}*s(${te} + ${inc})"|bc -l ` #translacao em y
z1=`echo "scale=10;0.0000*s(${pi}/6)"|bc -l ` #coord z1
# echo " ${metodo} PREC SHIFT1000 DEBUG LET T=1999999 + " > ${nome}.dat
# echo " DUMP=250000 XYZ PL GEO-OK ${multi} CHARGE=${carga} " >>
${nome}.dat
echo " ${metodo} UHF CYCLES=30000 PREC SHIFT1000 DEBUG LET T=19999999 + "
> ${nome}.dat
echo " DUMP=250000 AUX GNORM=0.01 PL GEO-OK ${multi} CHARGE=${carga} " >>
${nome}.dat
echo " ${nome}" >> ${nome}.dat
echo " " >> ${nome}.dat

```

```

j=1
while [ ${j} -le ${m} ]
do

    i=1
    while [ ${i} -le ${n} ]
    do
        x1=`echo "scale=10;${tx} + ${ra}*c(${te} + ${inc})"|bc -l `      #coord
        y1=`echo "scale=10;${ty} + ${ra}*s(${te} + ${inc})"|bc -l `      #coord
        x2=`echo "scale=10;${tx} + ${ra}*c(${te} + ${dte1} + ${inc})"|bc -l `
        #coord x2
        y2=`echo "scale=10;${ty} + ${ra}*s(${te} + ${dte1} + ${inc})"|bc -l `
        #coord y2
        echo "${atomo1}  ${x1}  1  ${y1}  1  ${z1}  1 " >> ${nome}.dat
        echo "${atomo2}  ${x2}  1  ${y2}  1  ${z1}  1 " >> ${nome}.dat
        te=` echo "scale=10;${te} + ${dte}"|bc -l `
        #z1=` echo "scale=10;${z1} + ((-1)^${i})*${dz1}"|bc -l `
        i=` expr ${i} + 1 `
    done
    z1=` echo "scale=10;${z1} + ${D3}"|bc -l `
    inc=` echo "scale=10;${inc} + ((-1)^(${j}))*${incte}"|bc -l `

    j=` expr ${j} + 1 `

done

#!/bin/bash
#adição de hidrogenio nas pontas de nanobar
#Msc.Jeziel e Dr.José Divino dos Santos          v.01          23/08/2018
nome=$1          #nomes dos arquivos bar.mol (sem .mol)
tipo=$2          #tipo de nanotubos: 1-armchair 2-zigzag
if [ ${tipo} -eq 1 ]
then
    ###Armchair
    echo > temp1; rm temp1; echo > temp2; rm temp2; n=` echo ${nome}.mol|cut -
d- -f3|cut -dn -f2 `; m=` echo ${nome}.mol|cut -d- -f4|cut -dm -f2 `; nat=`
echo "2*${n}*${m}"|bc `; nf=` echo "2*${n}*(${m} - 1) + 2"|bc `; nu=` echo
"2*${n} + 2"|bc `; nl=` expr ${nat} + 2 `; i=3; while [ ${i} -le ${nl} ];do
v=(` head -${i} ${nome}.mol|tail -1|awk '{printf("%s  %6.6f  %6.6f  %6.6f
\n",  $1, $2, $3, $4 )}'`); if [ ${i} -le ${nu} ]; then echo "${v[0]}
${v[1]}  ${v[2]}  ${v[3]}" >> temp1 ; awk -v vx="${v[1]}" -v vy="${v[2]}"
-v vz="${v[3]}" 'BEGIN{printf("%s  %6.6f  %6.6f  %6.6f  \n", "H", vx,
vy, vz - 1.0)}' >> temp2 ; fi ; if [ ${i} -gt ${nu} ] && [ ${i} -le ${nf} ];
then echo "${v[0]}  ${v[1]}  ${v[2]}  ${v[3]}" >> temp1 ; fi; if [ ${i}
-gt ${nf} ]; then echo "${v[0]}  ${v[1]}  ${v[2]}  ${v[3]}" >> temp1 ; awk
-v vx="${v[1]}" -v vy="${v[2]}" -v vz="${v[3]}" 'BEGIN{printf("%s  %6.6f
%6.6f  %6.6f  \n", "H", vx, vy, vz + 1.0)}' >> temp2 ; fi ; i=` expr ${i}
+ 1 ` ; done ; natH=` echo "4*${n}"|bc ` ; natotal=` echo "2*${n}*${m} +
${natH}"|bc `; echo "  ${natotal}  " > ${nome}-${natH}H.mol ; echo "

```

```









">> ${nome}-${natH}H.mol; cat temp1 temp2 >> ${nome}-${natH}H.mol; molder
${nome}-${natH}H.mol
else
###Zigzag
#rm temp1; echo > temp2; rm temp2; n=` echo ${nome}.mol|cut -d- -f3|cut -
dn -f2 `; m=` echo ${nome}.mol|cut -d- -f4|cut -dm -f2 `; nat=` echo
"2*${n}*${m}"|bc `; nf=` echo "2*${n}*($m - 1) + 2"|bc `; nu=` echo "2*${n}
+ 2"|bc `; nl=` expr ${nat} + 2 `; i=3; while [ ${i} -le ${nl} ];do v=(` head
-${i} ${nome}.mol|tail -1|awk '{printf("%s %6.6f %6.6f %6.6f \n",
$1, $2, $3, $4 )}'`); if [ ${i} -le ${nu} ]; then echo "${v[0]} ${v[1]}
${v[2]} ${v[3]}" >> temp1 ; awk -v vx="${v[1]}" -v vy="${v[2]}" -v
vz="${v[3]}" -v i0="${i}" 'BEGIN{ip=(-1)^(i0); if(ip==-1){ printf("%s
%6.6f %6.6f %6.6f \n", "H", vx, vy, vz - 1.0); }; }' >> temp2 ; fi ;
if [ ${i} -gt ${nu} ] && [ ${i} -le ${nf} ]; then echo "${v[0]} ${v[1]}
${v[2]} ${v[3]}" >> temp1 ; fi; if [ ${i} -gt ${nf} ]; then echo
"${v[0]} ${v[1]} ${v[2]} ${v[3]}" >> temp1 ; awk -v vx="${v[1]}" -v
vy="${v[2]}" -v vz="${v[3]}" -v i0="${i}" 'BEGIN{ ip=(-1)^(i0);
if(ip==1){ printf("%s %6.6f %6.6f %6.6f \n", "H", vx, vy, vz + 1.0);
}; }' >> temp2 ; fi ; i=` expr ${i} + 1 ` ; done ; natH=` echo "2*${n}"|bc `
; natotal=` echo "2*${n}*${m} + ${natH}"|bc `; echo " ${natotal} " >
${nome}-${natH}H.mol ; echo " >> ${nome}-${natH}H.mol; cat temp1
temp2 >> ${nome}-${natH}H.mol; molder ${nome}-${natH}H.mol
echo > temp1; rm temp1; echo > temp2; rm temp2; echo > temp3; rm temp3;
n=` echo ${nome}.mol|cut -d- -f3|cut -dn -f2 `; m=` echo ${nome}.mol|cut -d-
-f4|cut -dm -f2 `; nat=` echo "2*${n}*${m}"|bc `; meio=` echo "${n}*${m}"|bc
`; nf=` echo "2*${n}*($m - 1) + 2"|bc `; nu=` echo "2*${n} + 2"|bc `; nl=`
expr ${nat} + 2 `; i=3; while [ ${i} -le ${nl} ];do v=(` head -${i}
${nome}.mol|tail -1|awk '{printf("%s %6.6f %6.6f %6.6f \n", $1, $2,
$3, $4 )}'`); if [ ${i} -le ${nu} ]; then echo "${v[0]} ${v[1]} ${v[2]}
${v[3]}" >> temp1 ; awk -v vx="${v[1]}" -v vy="${v[2]}" -v vz="${v[3]}" -v
i0="${i}" 'BEGIN{ip=(-1)^(i0); if(ip==-1){ printf("%s %6.6f %6.6f
%6.6f \n", "H", vx, vy, vz - 1.0); }; }' >> temp2 ; fi ; if [ ${i} -gt
${nu} ] && [ ${i} -le ${nf} ]; then echo "${v[0]} ${v[1]} ${v[2]}
${v[3]}" >> temp1 ; fi; if [ ${i} -gt ${nf} ]; then echo "${v[0]}
${v[1]} ${v[2]} ${v[3]}" >> temp1 ; awk -v vx="${v[1]}" -v vy="${v[2]}"
-v vz="${v[3]}" -v i0="${i}" 'BEGIN{ ip=(-1)^(i0); if(ip==1){ printf("%s
%6.6f %6.6f %6.6f \n", "H", vx, vy, vz + 1.0); }; }' >> temp2 ; fi ;
if [ ${i} -eq ${meio} ]; then awk -v vx="${v[1]}" -v vy="${v[2]}" -v
vz="${v[3]}" 'BEGIN{ printf("%s %6.6f %6.6f %6.6f \n", "C", vx +
1.70 , vy , vz ); }' >> temp3 ; fi ; i=` expr ${i} + 1 ` ; done ; natH=`
echo "2*${n}"|bc `; natotal=` echo "2*${n}*${m} + ${natH} + 1"|bc `; echo "
${natotal} " > ${nome}-${natH}H.mol ; echo " >> ${nome}-${natH}H.mol;
cat temp1 temp2 temp3 >> ${nome}-${natH}H.mol; molder ${nome}-${natH}H.mol
fi

```


S2. script to encapsulate the BNZ in the geometric center of the BNNT and CNT models.

```
#!/bin/bash
#Ponto geométrico
#MsC. Jeziel Rodrigues dos Santos      28/03/2019      v.01
nome=$1                                #nome do arquivo.mol (sem .mol)
nl=` wc -l ${nome}.mol|awk '{print $1}' `
nat=` wc -l ${nome}.mol|awk '{print $1 - 2}' `
#####ponto médio coordenada x
i=3; sx=0.000000; while [ ${i} -le ${nat} ]
do
at=` head -${i} ${nome}.mol|tail -1|awk '{print $1}' `
x=` head -${i} ${nome}.mol|tail -1|awk '{print $2}' `
sx=` echo "scale=6;${sx} + ${x}"|bc -l `
#echo "${at}    ${x}    ${sx}"
i=` expr ${i} + 1 `
done
mx=` echo "scale=6;${sx}/${nat}"|bc -l `
#echo [ mediax=${mx} ]
#####ponto médio coordenada y
i=3; sy=0.000000; while [ ${i} -le ${nat} ]
do
at=` head -${i} ${nome}.mol|tail -1|awk '{print $1}' `
y=` head -${i} ${nome}.mol|tail -1|awk '{print $3}' `
sy=` echo "scale=6;${sy} + ${y}"|bc -l `
#echo "${at}    ${y}    ${sy}"
i=` expr ${i} + 1 `
done
my=` echo "scale=6;${sy}/${nat}"|bc -l `
#echo [ mediay=${my} ]
#####ponto médio coordenada z
i=3; sz=0.000000; while [ ${i} -le ${nat} ]
do
at=` head -${i} ${nome}.mol|tail -1|awk '{print $1}' `
z=` head -${i} ${nome}.mol|tail -1|awk '{print $3}' `
sz=` echo "scale=6;${sz} + ${z}"|bc -l `
#echo "${at}    ${z}    ${sz}"
i=` expr ${i} + 1 `
done
mz=` echo "scale=6;${sz}/${nat}"|bc -l `
echo [${mx}    ${my}    ${mz} ] > ponto-medio-${nome}.mol
```

Activated carbon from pumpkin seeds: Production by simultaneous carbonization activation for occupational respiratory protection

Walquíria Joseane da Silva¹, Nivaldo Freire de Andrade Neto¹⁺, Carlos Alberto Paskocimas¹, Juan Alberto Chaves Ruiz², Fábíola Correa Carvalho², Elson Longo³, Fabiana Villela da Motta¹, Maurício Roberto Bomio Delmonte¹

1. Federal University of Rio Grande do Norte, Department of Materials Engineering, Natal, Brazil.
2. SENAI Institute for Renewable Energy Innovation, Natal, Brazil.
3. Federal University of São Carlos, Center for the Development of Functional Materials, São Carlos, Brazil.

+Corresponding author: Nivaldo Freire Andrade Neto, **Phone:** +55 84 33422406, **Email address:** nfandraden@gmail.com

ARTICLE INFO

Article history:

Received: July 21, 2021

Accepted: October 26, 2021

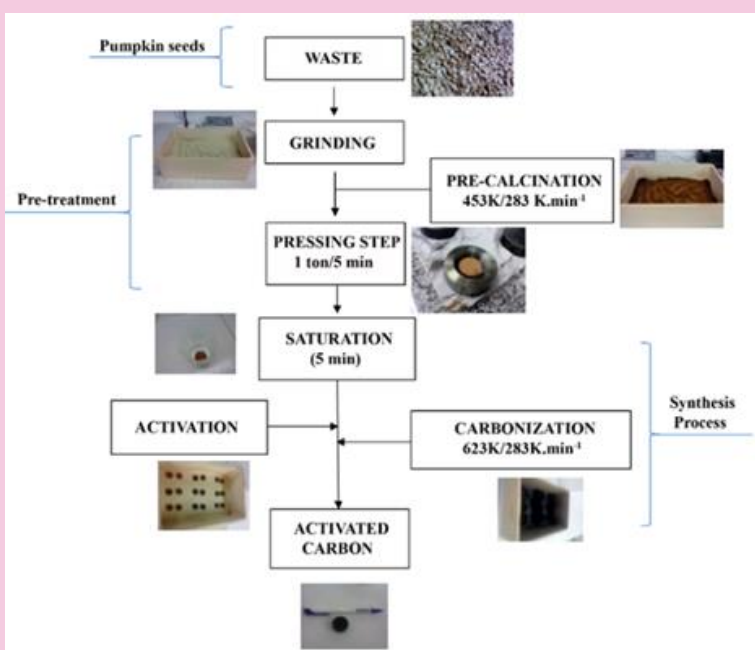
Published: April 11, 2022

Keywords:

1. activated carbon
2. pumpkin seeds
3. simultaneous carbonization-activation
4. high adsorption capacity

Section Editors: Elson Longo and Juan Manuel Andrés Bort

ABSTRACT: Activated carbon materials are derived from carbonaceous sources and used as a technological element for various industrial purposes. These materials are present in most filters (cartridges) in personal respiratory protective equipment. Due to this context and to enhance sustainability concepts and human health in the production of materials, this study aimed to produce activated carbon from an abundant agricultural waste in the northeast Brazil through a route that not only favors its simultaneous carbonization and activation but also its thermal neutralization. The precursor biomass was characterized by particle size analysis, a standard testing method for moisture and ash content which were characterized by FRX, CHN, and thermal analysis. The produced activated carbon was characterized by potential of hydrogen (pH), XRD, BET, SEM, TPD by ammonia and UV-Vis analysis. The activated carbons showed yields between 73 and 78%. The morphology varied in function of the biomass interaction with the type and concentration of acid used. The produced samples showed adsorption capacity and selectivity to ammonia gas.



1. Introduction

Occupational respiratory protection (ORP) is often a legal requirement in some countries to guarantee the health and safety of thousands of workers who are exposed to harmful substances which may cause occupational diseases by inhaling contaminated air in the workplace. Appropriate respirators shall be used when engineering control measures are not feasible, are being implemented, evaluated, or in emergency cases (Connor *et al.*, 2016). Respirators are specific personal protective equipment designed to provide respiratory protection (MacIntyre *et al.*, 2014). Protection of some respirators occurs by removing contaminants from the air: respirators of this type include particulate respirators, which filter out airborne particles (Connor *et al.*, 2016). They have activated carbon inside their filters (cartridges) and their classification type can vary according to the risk agent to be absorbed.

Activated carbon is any carbonaceous material with favorable characteristics for adsorption reactions: well-developed internal surface area, pore structure, and superficial functional groups (Pezoti *et al.*, 2016; Poinern *et al.*, 2011) used as an adsorbent, catalyst, catalyst support, and energy storage (Shen *et al.*, 2014). On the other hand, activated carbon can also be used as an active surface to be doped or combined with other elements in a wide possibility for industrial applications (Shen *et al.*, 2014). Easy operation, large-scale production, high efficiency, sensitivity to toxic substances, and the possibility of reuse favors using activated carbon in the adsorption process (Shen *et al.*, 2014).

Activated carbons produced from biomass residues have been an important research area. Agricultural biomass and industrial waste have been used as raw material in the preparation of activated carbon (Pezoti Junior *et al.*, 2014) to find abundant, renewable, and low-cost precursors in contrast to the high production costs on an industrial scale and because of the use of nonrenewable sources of activated commercial carbons (Nunes *et al.*, 2015). Various types of waste and biomass have recently been processed to obtain activated carbon for several industrial purposes such as coconut shells (Nunes *et al.*, 2015), macadamia nuts shells (Martins *et al.*, 2014), bamboo (Shengsen Wang *et al.*, 2015), peach and olive pits (Tsyntarski *et al.*, 2015), pineapple (Mahamad *et al.*, 2015), peanut shells (Zhang and Lu, 2015), rice husks (Dalai *et al.*, 2015), sugarcane bagasse (Dalai *et al.*, 2015; Gonzaga *et al.*, 2018), sewage sludge (Huang *et al.*, 2017; Wu *et al.*, 2014), waste from palm tree stems (AIOthman *et al.*, 2014), seeds from *Platanus*

orientalis biomass (Dodevski *et al.*, 2017), and banana peel (Van Thuan *et al.*, 2017), among others.

Pumpkin is a typical fruit in northeastern Brazil. Oil extraction from its seeds does not have any significant productive or technological relevance in the region. Therefore, when these seeds are not reused for planting, they are either intended for human and animal consumption just because of the beneficial nutrients they contain (Carvalho *et al.*, 2012) or are discarded (Joshi *et al.*, 1993). Thus, it is a by-product of the agricultural segment with low technological and commercial impact. Traditional methods to produce activated carbon propose the carbonization of biomass followed by the use of activators (whether chemical or physical or a combination of both) in two asynchronous different steps (Gonçalves *et al.*, 2016; Solís-Domínguez *et al.*, 2011). An improvement in the production process has recently been considered so that these steps occur simultaneously. This process is classified as a synchronous one-step process. As a result, the characteristics of the obtained material vary according to these production steps.

Thus, this paper aimed to synthesize activated carbon from pumpkin seeds using the carbonization route and chemical activation by thermal neutralization. The relationship among the synthesis methodology, reagents, and starting materials used with the characteristics shown by the activated carbon was investigated. Adsorption experiments with TPD were carried out with ammonia in the presence of moisture. It became an agent which carried risks caused by accidental inhalation, which is harmful to people's health in working conditions in all industries where it is employed. Moreover, the adsorption potential of aqueous solutions of methylene blue dye was investigated following the ultraviolet-visible (UV-Vis) measurements in the absorbance model. Furthermore, this investigation may demonstrate the effectiveness of the produced material for environmental applications, human health, and removing pollutants from wastewater.

2. Experimental

2.1 Characteristics

The plant which originates pumpkin belongs to the *Cucurbita* genus (Cucurbitaceae family) (Hameed *et al.*, 2008) and comprises various wild and domesticated species native to the Americas. The plant grows well in hot and dry climates (Ferreira *et al.*, 2017). Pumpkin has flat edible seeds (Njoku *et al.*, 2014).

2.2 Characterization of the biomass

The pumpkin seeds were fragmented into a food commercial crusher for 7 min at 400 W of power and (55 ± 5) Hz. The material was deagglomerated using a 200-mesh sieve. The fragmented seeds were then characterized by particle size analysis using laser diffraction, the standard testing method for moisture and ash content, X-ray fluorescence (FRX), elementary chemical analysis (CHN), and thermal analysis. The distribution curve of the particle size analysis by laser diffraction carried out in the waste was obtained by granulometry in a CILAS 1180 device in an aqueous liquid dispersant, and then subjected to the effects of ultrasonic agitation for 60 s. The standard testing method for moisture and ash content was performed according to ASTM E1755 and E1756, respectively.

Chemical composition was obtained by FRX spectroscopy using an EDX-720 Shimadzu in a vacuum atmosphere. Elementary chemical analysis was performed with 2.7 mg in a Pekin Elmer analyzer 2400 Series II model connected to a microbalance model AutoBalance controller. Helium gas (18 psi – 900 mL min⁻¹– 913 K) and oxygen (15 psi – 50 mL min⁻¹ – 1198 K) were used.

A thermal analysis was performed in a Netzsch STA Model 449F3 device at a heating rate of 283 K min⁻¹ and a temperature range of 303–1023 K using 10 mg of the sample under synthetic airflow (100 mL min⁻¹).

2.3 Pretreatment

The precalcination of biomass was performed at 453 K with an isotherm of 1 h and a heating rate of 283 K min⁻¹ in a Linn Elektro Therm furnace. Next, the material was pressed into pellets in a stainless-steel matrix in a ratio of 0.3:1 of binder/raw material using 1 Ton for 5 min. Pellets were fabricated in a cylindrical shape of approximately 25 mm in diameter by 5 mm high.

2.4 Synthesis

The samples were produced by the carbonization reaction and concomitant to chemical activation. Three different acids were used in this process: hydrochloric (CLO), sulfuric (SUL), and nitric (NIT) acids in different concentrations (10%, 30%, 50% in acid:water volume, respectively) for chemical activation. This method was applied according to the following procedure: each pellet obtained (after the pretreatment) was put in an acid solution for 5 min until complete

saturation and placed directly into a mullite-cordierite box. The pellets were covered with precalcined raw biomass. The box was immediately closed and heated to 623 K at a heating rate of 283 K min⁻¹ in an air atmosphere for 10 min. The method is illustrated in the flow chart demonstrating the experimental procedure as shown in Fig. 1. Thermal neutralization was applied to the obtained activated carbons: the samples were heated between 573–673 K for 144 h and then cooled at room temperature. The pellets were deagglomerated in an agate mortar.

The nomenclature used to identify the samples were PS (pumpkin seeds) plus the abbreviation of the employed acid + amount (%) of activator used. This nomenclature was used for different amounts of acids and concentrations.

2.5 Characterization of activated carbons

The following techniques were used to characterize active carbons: potential of hydrogen (pH), X-ray diffraction (XRD), specific surface area using BET (Brunauer-Emmett-Teller), and scanning electron microscopy (SEM), temperature-programmed desorption (TPD) by ammonia and UV-vis spectrometer. The pH measures were performed in a diluted aqueous solution with deagglomerated powders of activated carbon produced in a mass ratio of 1:1 (water:sample) under stirring for 10 min at room temperature (298K). The solution was filtered and measured by the electrometric method using a Hanna PH21 digital meter with a measuring range of 0–14, resolution of 0.01, an accuracy of ± 0.02 , and HI 1110 electrode type. XRD diffractograms were performed by a Shimadzu XRD-7000 diffractometer, CuK α monochromatic radiation, with an angular range of 2 θ range from 10 to 80°, scanning speed of 1° min⁻¹, a step of 0.02°, a voltage of 40 kV and a current of 30 mA. The specific surface area measurements were obtained by a Quanta Chrome Corporation NOVA model-2000 using the BET method. The samples were previously degassed at 473K for 1 h. The SEM micrographs were obtained using a Hitachi High-TM3000 microscope. The samples were directly deposited into a metallic holder coated with carbon to fix them.

TPD by ammonia was performed in the automated analyzer Micromeritics AutoChem II 2029. TPD runs occurred with approximately 0.100 g of material at a flow of 50 mL min⁻¹ of helium gas at ambient temperature up to 383 K (heating rate of 283 K min⁻¹), and then up to 573 K. It was then cooled down to 323 K. After 1 min, a gaseous mixture of ammonia and helium

(5% NH_3/He) with a flow rate of 50 mL min^{-1} was introduced for 30 min under the same heating rate. Thereafter, the inert gas recirculated in the system at the same flow rate, and the sequence of the described process was repeated by heating at 373 K (283 K min^{-1} ,

15 min) and 573 K (283 K min^{-1} , 20 min). The UV-vis spectrometer was performed using a Shimadzu UV-2600 spectrophotometer at a wavelength range between 400 and 800 nm .

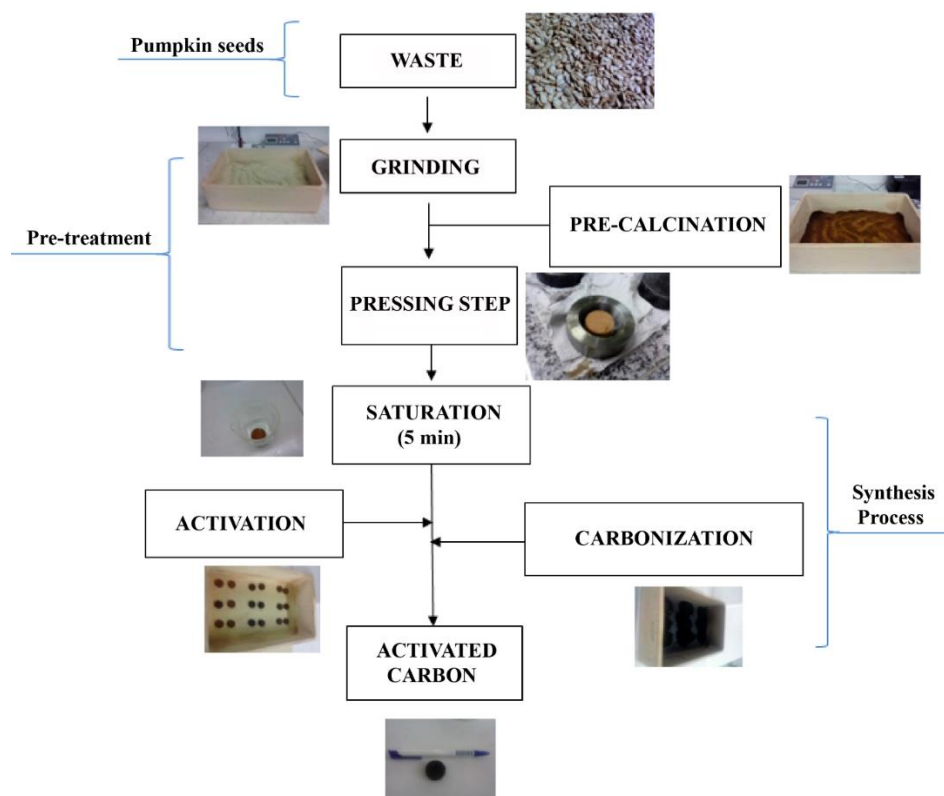


Figure 1. Flowchart of the experimental production procedure for the activated carbon.

3. Results and Discussion

3.1 Characterization of the precursor biomass

Waste processing in the fragmentation and burning processes was achieved by reducing the particle size through grinding, which provided a more homogenous and uniform characteristic to the raw material. The intrinsic characteristics of the raw material determined the type of grinding used, and therefore conditioned its grinding evolution. The oleaginous nature of the seeds which are sensitive to high temperatures made the traditional use of fragmentation equipment unfeasible. This justified the use of commercial crushers as described in the methodology.

The result of particle sizes of the powder obtained after waste fragmentation in natura is shown in the granulometric distribution curve in Fig. S1 (Supplementary Information). The sample shows a wide variation in the particle size, irregular visual appearance,

and wide distribution range between 2.5 to 550 mm . The average particle size measured is about 59.75 mm . Enlargement in the size distribution technique suggests the presence of rough particles with an irregular shape that is not perfectly spherical, according to the principle of the technique and the Fraunhofer Theory (Beuselinck *et al.*, 1998).

After the grinding process, the in natura samples have a level of humidity and ash of 0.10% and 10.44% , respectively. It is known that the presence of moisture in biomass is related to the intrinsic characteristics of the waste such as aspects of cultivation, storage, and production steps, or their combination with each one of the factors. The presence of inorganic impurities is relatively higher than the humidity (only 0.1%), which can indicate a waste that is less saturated with reduced hydration. This may lead to the mass loss being minimized by humidity.

The gravimetric variation which represented the standard result and was adapted from the ash content is shown in Fig. 2. A reduction in the isotherm time for

preserving the thermal stability of the waste during the test ash content did not significantly affect the results. This was one of the viable ways for the variations which were noted to obtain the constant mass. The residue (0.0922 g) quantities were measured after measuring about 10.44% of the ash content. This percentage represents the amount of the remaining mineral part and impurities after degradation of the organic matter after the test and may have a predominant composition by potassium, phosphorus, sulfur, and sodium as shown in the FRX results of the in natura sample (Tab. 1). The presence of alkali metal oxides, alkaline earth metal, and others with less significant quantities is also observed, which can interact with the activator acid during the carbonization-activation process, thereby causing over-position phases without necessarily exerting a strong influence on the material properties due to the low amounts detected. Evaluating the ash content can represent a measure of minerals and other inorganic materials and possible impurities present in the in natura sample of the pumpkin seeds according to the testing method.

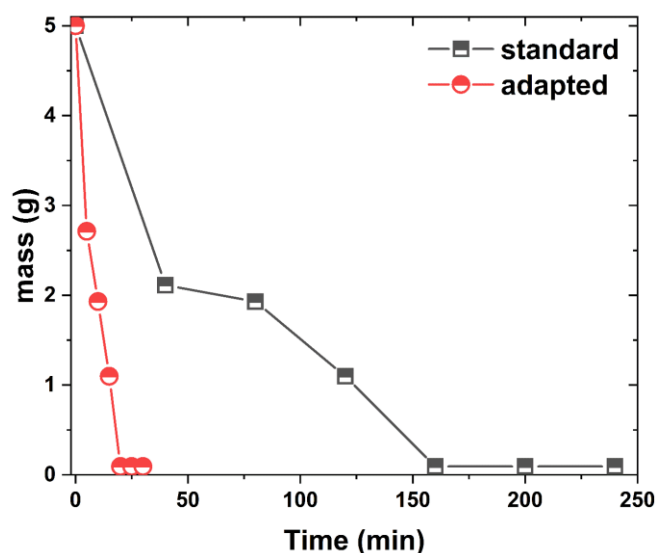


Figure 2. Comparative analysis of the weight loss of in natura ground samples during the ash content test for the standard and adapted samples.

The amount of volatile matter was quantified by elemental chemical analysis in two test runs. The carbon, nitrogen, and oxygen percentages measured in the analyzed samples are shown in Tab. 2. The difference in the carbon percentage between the PS in natura sample and the PS charred sample is very subtle and not significant, which may indicate that all the carbon mass was substantially preserved during the process proposed in this work.

Table 1. Chemical composition of the in natura sample.

Chemical composition	In natura sample (%)
K ₂ O	41.67
P ₂ O ₅	18.61
SO ₃	14.73
Na ₂ O	11.41
CaO	3.07
Fe ₂ O ₃	2.92
SiO ₂	2.46
ZnO	2.21
CuO	1.12
MnO	0.97
Rb ₂ O	0.83

Table 2. Mean values of the CNH composition of PS samples used in this work in comparison with a commercial sample. In which: PS¹ = in natura sample and PS² = sample used in the standard test method for ash content.

Samples	Carbon (%)	Hydrogen (%)	Nitrogen (%)
PS ¹	55.64	9.81	5.88
PS ²	40.64	2.45	9.99

The thermal characterization of in natura PS is shown in Fig. 3. The thermal decomposition occurs in four mass variation steps directly related to the composition of the *Cucurbita* seeds, which are rich in oil, protein, fiber, and micronutrients (Joshi *et al.*, 1993). The mass loss that occurs at approximately 383 K can be attributed to moisture, in turn, related to water removal (Caputi *et al.*, 1991). Next, the second event had a 40.83% weight loss in the range of 415 to 620 K and can be associated with the degradation of the organic matter and with the formation of carbonized material. The third stage occurs quickly at the moment that the temperature reaches a maximum of 653 K with 14.31% weight loss which may be related to the combustion of oils. The fourth decomposition stage occurs between 695–937 K corresponds to 31.66% weight loss which decomposes slowly and may be attributed to protein degradation and thermal decomposition of the other micronutrients. The residue is stable at 923 K and showed a mass change of 7.43%. These results show a reduction of the humidity values and differential thermal stability to the normative parameters applied to biomass in this work. Thus, the standard tests and thermal analysis of biomass were fundamental to achieve a carbonization temperature that was favorable to producing the activated carbon.

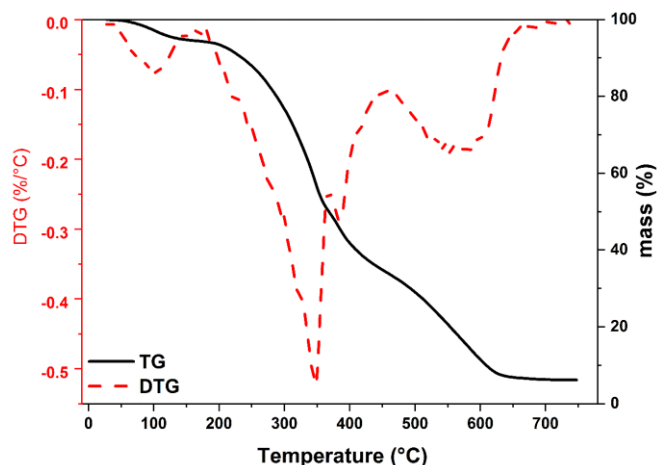


Figure 3. Thermal analysis curves (TG-DTG) of the in natura PS sample.

From the heat treatment applied to obtain the activated carbon, the ignition and activation temperatures are 563~583 and 623 K, respectively. In addition, the gravimetric yield of the powdered and palletized material was 21.93 and 61.41%, respectively. The gravimetric yield in this study was calculated from the ratio of the produced carbon mass and biomass precursor, according to Eq. 1.

$$R (\%) = (\text{produced carbon (mass)}/\text{biomass (mass)}) \times 100 \quad (1)$$

The yield is the determining factor to control the burning and production process. In this sense, it is a variable that indicates the carbonization efficiency in a process given as a percentage. The carbonization temperature and combustion efficiency are also influenced by other factors such as humidification and volatile content which affect the calorific value of the sample. It was also observed that the yields were variable depending on their morphological aspect. The performance was higher when the sample was compressed into a pellet form. Therefore, the processing proposed in this study included the precarbonization together with the pressing procedure. The aim was to minimize the mass loss by moisture and eliminate other components volatilized at 453 K with the precarbonization stage. This was used to increase the carbonization efficiency and enable the process on an industrial scale because the performance in powder form will be low due to the gravimetric yield having little significance when compared with the yields shown in the pellet form.

The percentage value of the burn-off is implicit in the results of the gravimetric yield of activated carbon pellets because the carbonization occurred simultaneously to activation. This understanding

becomes clearer with the yield definition given by Marshall *et al.* (2000), which defines it as the amount of the precursor remaining after pyrolysis and activation. Thus, the total yield of the activated carbon pellet values depends on the activator and proportions used. These results are shown in Tab. 3.

Table 3. Total gravimetric yield of activated carbons according to the activator proportions.

Sample	Total gravimetric yield (%)
PSCLO10	75.94
PSCLO30	80.78
PSCLO50	66.76
PSNIT10	78.00
PSNIT30	78.98
PSNIT50	74.36
PSSUL10	67.82
PSSUL30	76.82
PSSUL50	73.04

Yields vary slightly depending on the activator used. Although it had high and low peaks for the PSCLO30 and PSCLO50 samples, others had yields between 73 and 78%. The analysis of each group demonstrates an increase in the yield in the ratio of 30% activator, and a fall when the activator had a concentration of 50%. However, they are superior to the mean measured in the gravimetric yield of the carbonized pellets (on a dry basis without the activator) in all cases. Another variable observed in this phase was the firing atmosphere, which influences carbonization. As described in the methodology, it was decided to maintain a powder-air bed which provides a reducing atmosphere. This use is also a factor that enables the process on an industrial scale, thereby allowing carbonization in large amounts, avoiding the use of reducing atmospheres, and simplifying the process at a low cost. The powder-air bed can be discarded if the mass ratio is considerably higher than for the available oxygen.

3.2 Characterization of activated carbons

3.2.1 Structural

Literature shows that the typical procedure to produce activated carbon usually involves washing the produced material with water or using a chemical compound, or both, to promote neutralization of the proposed activation, especially when the chemical activation is applied to eliminate the remaining impregnating chemical agent (Hameed *et al.*, 2008; Rovani *et al.*, 2016). The thermal neutralization proposal was an alternative to the commonly reported

traditional neutralization methods. The measured pH values are shown in **Tab. 4**. The pH of the carbonized sample with no activator obtained under the same experimental synthesis conditions was also measured for comparison.

Table 4. pH of activated carbon solutions.

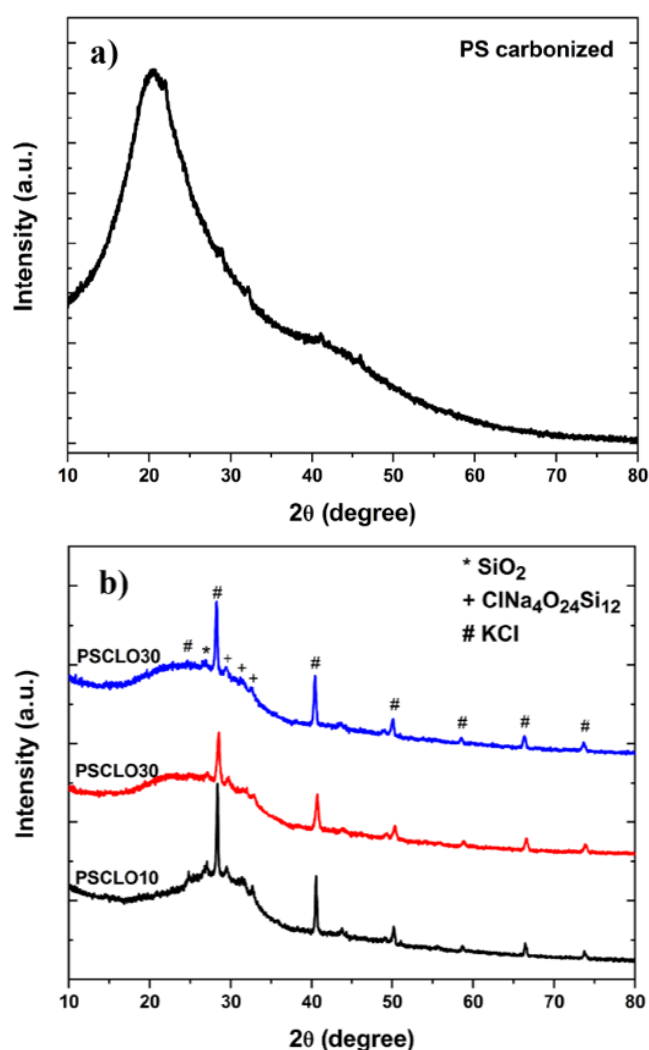
Samples	Colorimetric method	Electrometric method
OS	7	7.02
PSCLO50	6	6.99
PSNIT50	7	7.12
PSSUL50	6	6.36

Samples from the PSCLO group had very moderate acidity, quite close to neutrality. Only samples from the PSSUL group showed a relative acidity of 6.36, probably due to the presence of residual sulfur still present in the carbon structure, making the structure more stable in the proposed neutralization temperature. Therefore, this group was subjected to a new neutralization run at 723 K temperature. After this, the measured pH was around 7.09, with the value approaching neutral given the other samples and a reference sample without an activator which indicates the efficiency of the proposed neutralization. The choice of thermal neutralization over traditional means has the advantage of facilitating the manufacturing process and more viably dealing with the wastes from the process. Washing in the industrial field possibly generates residual effluent, which would constitute another step in the process of burdening deployment, maintenance costs of unit operations, and environmental responsibilities associated with it.

The XRD diffraction of PS carbonized without acid activation is shown in **Fig. 4a**. The PS sample revealed a typical structure of amorphous materials and types of activated carbon with a larger peak at 20.5°. This may be related to the composition of the remaining mineral part after degradation of the organic matter: mineral components are still present in the composition of the waste and/or residual impurities in a very slight amount after the treatment, but not sufficient to promote forming other stable structures with significant crystallinity under the thermal treatment conditions. The XRD of the produced activated carbons is shown in **Fig. 4b**. Compared to **Fig. 4a**, it is noted that an amorphous matrix originally occurs during pyrolysis in overlapping phases when the process is applied in full with the use of the activator simultaneously to carbonization. There was a contour profile presented by the pure carbon plus crystalline phase peaks observed in all groups which varied according to the activator. The identified phases are mixed compounds dispersed in the amorphous

matrix and made up of minerals present in biomass associated with the elements of the employed acid.

Except for PSNIT samples (**Fig. 4c**), which showed a peak at $2\theta = 60^\circ$ of a mixed compound that only exists when a greater amount of activator was used, but without any relative significance. The other groups retained the same profile with each other. It is seen that the activators caused the appearance of different phases in the carbonized material, generating activated carbons with diffraction characteristics depending on the activator used. Sulfuric acid was the agent that caused the greatest change in the activated carbon phases because it generated a greater number of peaks than other activators according to the PSSUL group (**Fig. 4d**). However, the number of dispersed phases of the amorphous base is more discreet in the other group.



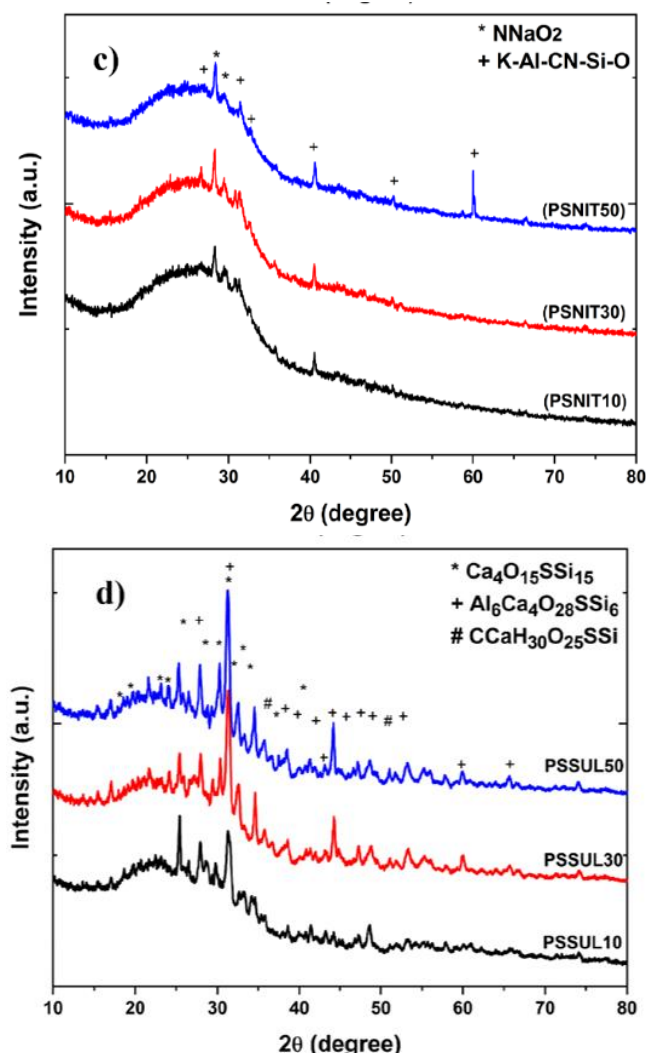


Figure 4 - X-ray diffractogram of the (a) carbonized PS, (b) PSCLO, (c) PSNIT and (d) PSSUL samples.

The XRD analysis showed that the activated carbon characteristics are associated with the composition and waste processing; when subjected to thermal excitation, it tends to eliminate organic and moisture matters, producing pure carbon or forming thermodynamically stable structures related to the presence of inorganic and/or impurities depending on the additives and/or activating elements. Thus, the activated carbon differs from the carbonized sample by the presence of phases resulting from the activator interacting and modifying the structure during processing. This enables us to infer that the activating agent reacted with the biomass during the carbonization process, and carbonization and activation consequently occurred simultaneously as proposed in this work.

The morphology of the samples was analyzed by SEM according to the images in Fig. 5. The in natura waste presented regular, equiaxed, and homogeneous

morphology constituted by blocks and dense plaques with a few scattered spherical corpuscles, which are an intrinsic characteristic of the biomass (Fig. 5a). A sample was collected to check the surface texture and to prove the effects of the proposed alterations concerning the raw material due to the experimental changes applied to the test ash content. The micrograph of this sample (Fig. 5b) shows the permanence of the blocks and characteristic plaques, which in addition to not compromising the test results also caused satisfactory changes in morphology, leaving a matrix with a porous aspect about the initially characterized thick morphology. Thus, the plaques are porous with predominantly well-distributed spherical particles on the surface.

The samples submitted to the simultaneous activation and carbonization process showed different morphologies evidenced by micrographs (Fig. 5c-k). The diameter and pore volume tend to increase in the chemical activation process, and new pores are created due to the reaction between the carbon and activator (Yorgun and Yıldız, 2015). Furthermore, the presence of pores among the plaques was also favored by the simultaneous carbonization, making the biomass pyrolysis occur simultaneously to the activation. It is possible to note an increase in spaces produced by the effects of activating agents in the dense and compact matrix of the in natura waste with varying morphology depending on the activator.

The results of specific surface area (S_{BET}), medium pore diameter (D_{pm}), and the total pore volume (V_{p}) are shown in Tab. 5. The surface area and pore volume values for each group tended to be directly proportional to the concentration of the activator, except for the PSCLO50 and PSSUL50 samples. All the activated carbon samples produced have the same order of magnitude considering all the physical parameters measured in this test; however, the chemical activation with hydrochloric acid showed the best results.

Table 5. Typical parameters determined by BET.

Samples	Physical parameters		
	S_{BET} ($\text{m}^2 \text{g}^{-1}$)	V_{p} ($\text{cm}^3 \text{g}^{-1}$)	D_{pm} (\AA)
PSCLO10	6.77	0.0035	20.68
PSCLO30	8.93	0.0045	20.58
PSCLO50	6.42	0.0033	20.77
PSNIT10	5.08	0.0025	20.35
PSNIT30	5.48	0.0028	20.44
PSNIT50	5.60	0.0028	20.09
PSSUL10	3.68	0.0016	18.43
PSSUL30	5.29	0.0027	20.59
PSSUL50	4.45	0.0022	20.50

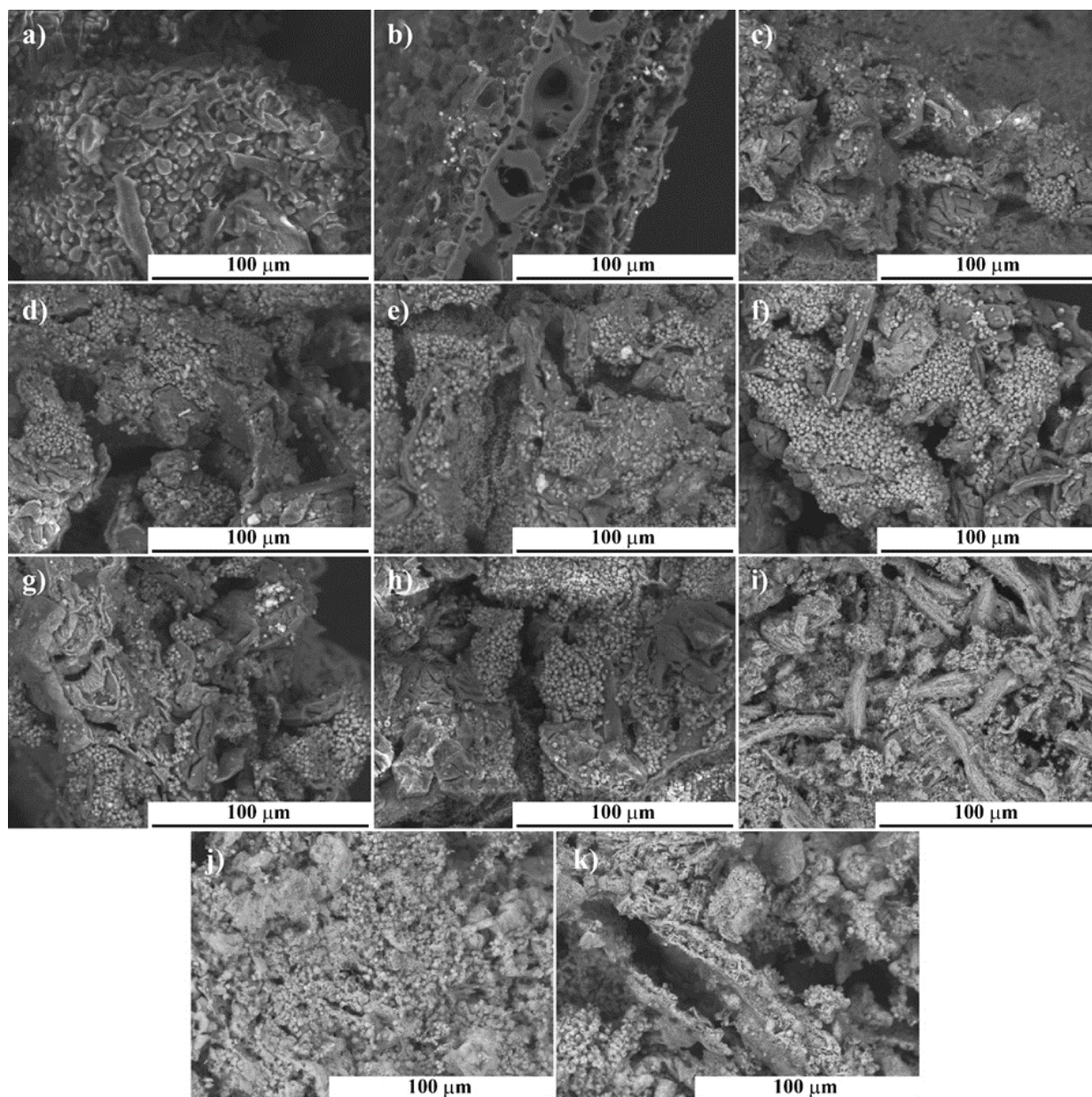


Figure 5. SEM micrographs for the (a) biomass, (b) carbonized PS, (c–e) PSCLO (10, 30 and 50%), (f–h) PSNIT (10, 30 and 50%) and (i–k) PSSUL (10, 30 and 50%) samples.

The specific area values are not only dependent on the processing applied but also influence the intrinsic characteristics of the raw material and the adsorbate. Marshall *et al.* (2000) explained that low burn-off values can lead to a low adsorption capacity by reducing the surface area. As the surface area is not related only to textural properties, it is possible that the adsorption capacity is not impaired, but also to the physical and chemical properties exhibited during adsorption.

The potential of the activated carbon adsorption is not only determined by its total surface area, but also by its inner porous structure, presence of functional groups on the pore surface, and an electrostatic charge of the

adsorbent and adsorbate (Alam *et al.*, 2007). Bansal *et al.* (1989) explained that the adsorption on activated carbon is influenced by three factors: pore size, chemical structure, and active sites. The pore size determines the adsorption capacity, the chemical structure influences the interaction with polar and nonpolar adsorbates (acidic or basic surface groups), and the active sites determine the type of chemical reactions with other molecules. This may also evidence the reasons why the potential for adsorption of these samples was not compromised, as the TPD results and the UV-Vis analysis showed.

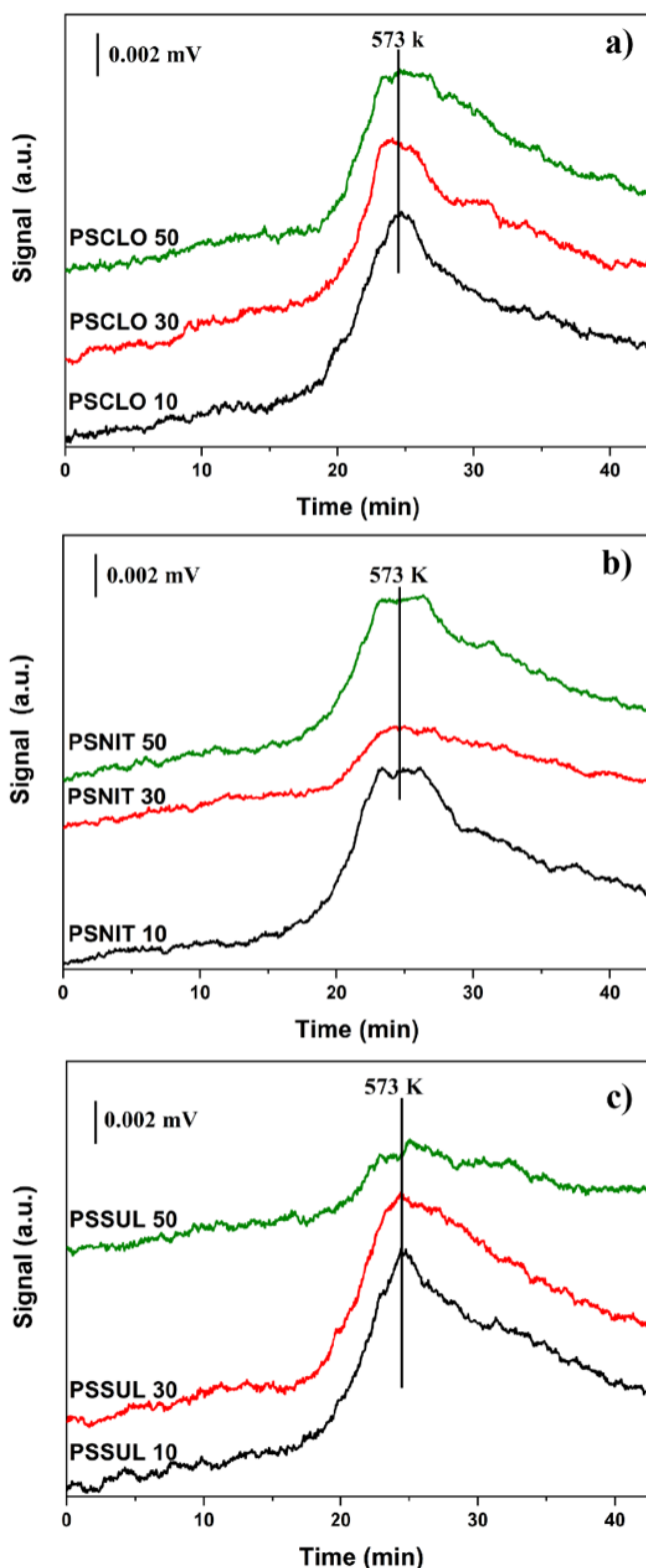
3.2.2 Application

The TPD test results show that the sample groups have profiles with only one desorption region, constituting a peak at 573 K (Fig. 6a–c). This value corresponds to the regeneration temperature of saturated activated carbon; in this case, the test with ammonia gas is appropriate to ensure that this gas is not inhaled by the user during their work as they are using respiratory personal protective equipment without saturation. A filter change is always advisable when saturation occurs from active sites, i.e., when the pores (where adsorption occurs) are completely saturated by the filtrate, reducing the potential of activated carbon and consequently compromising the adsorption capacity. This can vary due to the agent, the concentration, and exposure time of the supposedly contaminated workplace to the risk of contamination by the gaseous chemical agent.

In the case of the PSCLO group sample (Fig. 6a), the desorption profile was similar regardless of the amount of activator used in the preparation of activated carbon. The PSNIT (Fig. 6b) and PSSUL groups (Fig. 6c) showed a variation in the desorption profiles for quantities of 30 and 50%, respectively. This behavior should be directly related to the type of interaction between the acid activator and activated carbon which caused changes with increasing concentration. The amount of desorbed ammonia relative to the acid and its concentration is shown in Fig. 6d. The PSCLO group does not have any significant variations in desorption in function for the activator concentration when compared to the other groups. The adsorption had maximum and minimum peaks of 0.20 and 0.16 mol g⁻¹ of ammonia in the PSCLO10 and PSCLO30 samples, respectively. The sample produced with 50% hydrochloric acid presented an intermediate value. Thus, the similarity of the TPD profiles (Fig. 6a) and desorbed volumes in this group (Fig. 6d) showed that the percentage of activator, in this case, had little influence on the number of acidic sites on the solid surface.

The interaction of activators in the PSNIT and PSSUL groups with the biomass is different and opposite to the increasing amount of acid used in the preparation of the activated carbon. It is more convenient to conduct the treatment using only 10% of the activators in all cases. The samples that showed greater amounts of desorbed NH₃ were PSNIT50 (0.24 mol g⁻¹), PSNIT10, and PSSUL30 (both 0.21 mol g⁻¹), which may indicate a greater number of acid sites, and therefore higher adsorption capacity and selectivity for ammonia gas. The UV-vis spectroscopy results are shown in the [Supplementary Information](#) in

this paper. The spectra show the liquid phase adsorption potential of each material tested with methylene blue dye.



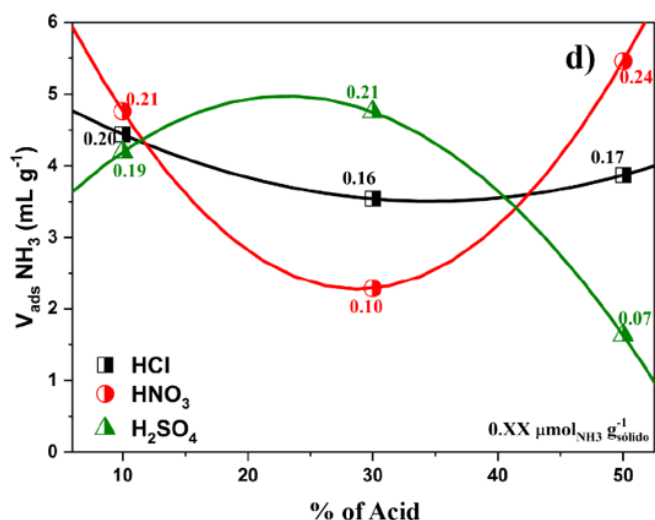


Figure 6. TPD-NH₃ profile curve for the (a) PSCLO, (b) PSNIT and (c) PSSUL samples and (d) total volumes of ammonia desorbed by the activated carbon samples.

The PSCLO and PSNIT groups had adsorption times measured every 2 min and 30 s. The adsorption reaction in the samples from the PSSUL group occurred slightly slower and was therefore measured every 5 min. After the beginning of adsorption, the spectral intervals were measured (at known time intervals) until the maximum adsorption time between the adsorbate (dye) and the adsorbent (activated carbon). There was only pure methylene blue solution at a concentration of 10^{-5} ppm at the initial time (t_0). Thus, the decrease in the characteristic absorption band of methylene blue demonstrated the reactivity of the material.

In Fig. S2 (Supplementary Information), the PSCLO30 sample showed the same reaction time as PSCLO50, but PSCLO50 showed a 100% absorbance reduction with the total color reduction of the solution. Both PSCLO10 and PSCLO30 presented 97% of adsorbed dye, but PSCLO10 was consumed slightly faster. The PSCLO50 sample stood out slightly about the total degradation of the dye. The measurement of reaction time intervals was also made every 2 min and 30 s in the activated carbon samples for the PSNIT group at Fig. S3 (Supplementary Information). The highlight in this group was the PSNIT30 sample whose performance was better than the others: the dye was degraded by 95% in only 2 min and 30 s. The PSNIT10 and PSNIT50 groups showed equal reaction times (17 min and 30 s) and practically the same percentage of adsorbed dye. The total reaction time varied with the acid percentage of the activator used in the synthesis process.

The adsorption reaction times of the PSSUL group were more extensive and variable with the acid synthesis concentration, as can be seen in Fig. S4 (Supplementary Information). The best performance of this group was from the PSSUL10 sample with 99% dye degradation at 25 min, followed by the PSSUL30 with 94% at 55 min. The PSSUL50 sample reached a 50 min reaction time to degrade 89% of methylene blue dye. It was observed that acid concentration in this group was inversely proportional to the degradation performance of the dye for this group.

The adsorption reactions in the liquid phase of the PSSUL showed some instability in the concentration of the methylene blue bands along with the degradation, indicating a possible oscillation of the absorbance dye. It was observed that the dye concentration in the spectra was higher than the initial solution at some moments. The tests were repeated and the results converged at this point, probably caused by some instability in the equipment during the performed readings. Such a situation may also indicate a reversible reaction character by the kinetics and thermodynamics of the reaction with this material in the initial moments, but which tends to stabilize over time and adsorb the dye. The pore structure morphology for this group may also have influenced these results because this acid can carry more hydroxide groups on the surface of the waste during the synthesis process to the other acids, and this may have reduced the interactions between the methylene blue molecules and the adsorbent. This possibility of acid treatment influencing the adsorption of methylene blue in activated carbon was reported by Shaobin Wang *et al.* (2005).

In general, the behavior of the samples from this same group varied little in terms of reactivity among them. Such performance may be associated with hydroxide groups and micropores in similar amounts on the material surface. But the lowest adsorption of methylene blue in PSSUL samples may also have been charged on the surface of the material during acid treatment, which caused little adsorption of negative ions from H₂SO₄ (SO₄⁻) on the positive sites on the surface, which leads to the material surface being less negatively charged, thus making it difficult to adsorb positive charge molecules of methylene blue.

However, the adsorption in all the samples occurred in very short intervals of degradation when compared to the average time normally evaluated by studies in the literature which generally report the evolution of the material's reaction with the dye being measured according to the reactivity of the material and the total reaction time being given in hours (Matos *et al.*, 2015). This short reaction time indicates the reaction potential

of the activated carbons produced in the dye adsorption and the high reactivity of the material to wastewater treatment.

The liquid phase adsorption performance of a commercial activated carbon for respiratory protection filter was tested for comparative purposes. The spectrum is shown in Fig. S5 (Supplementary Information). The commercial sample degraded 95% in 5 min. The sample which had similar behavior and slightly superior performance to the commercial product in this study was the PSNIT30 sample, although the commercial sample has a much higher surface area. This confirms the hypotheses in the literature that the surface area and total pore volume are not the only limitations for the adsorption capacity of activated carbons, but also the micropore volume, the charge on the material's surface, the chemical surface of the adsorbates, and the pH of the solutions (Goyal *et al.*, 2001). The surface area had little influence in terms of proportionality of the activator concentration to the adsorption presented by the groups of activated carbon produced in this study.

Therefore, it is believed that the differential performance of carbonized and acidified samples with nitric acid may reveal greater microporous volume and the chemical and electrical interaction effects of the acid on the carbon surface, which affects the adsorption reaction of the material with the dye and ammonia.

One of the main advantages of using activated carbon in adsorbent applications is its post-use. As they are normally produced in burning processes, the repetition of this process makes them suitable for being discarded in nature or even reused, without harming the environment.

4. Conclusions

The simultaneous carbonization–activation process was efficient for the activated carbon production from pumpkin seeds. Activated carbon adsorbed the ammonia gas, but the higher adsorption capacity and selectivity performance at a low temperature was the activated carbon sample activated in 50% nitric acid. The results showed their potential to be used as adsorbent material with this gas. The material was also shown to be suitable for dye adsorption in wastewater with the sample activated in 30% nitric acid. The activated carbons produced in this study are promising materials to be used in cartridges of individual protection equipment for ORP by a sustainable technological method with low cost and which is feasible on an industrial scale.

Authors' contribution

Conceptualization: Silva, W. J.; Andrade Neto, N. F.

Data curation: Silva, W. J.; Andrade Neto, N. F.; Motta, F. V.; Bomio, M. R. D.

Formal analysis: Silva, W. J.; Andrade Neto, N. F.; Ruiz, J. A. C.; Carvalho, F. C.

Funding acquisition: Not applicable.

Investigation: Silva, W. J.; Andrade Neto, N. F.; Carvalho, F. C.

Methodology: Silva, W. J.; Andrade Neto, N. F.; Ruiz, J. A. C.

Project administration: Silva, W. J.; Andrade Neto, N. F.; Longo, E.; Motta, F. V.; Bomio, M. R. D.

Resources: Silva, W. J.; Andrade Neto, N. F.; Carvalho, F. C.; Longo, E.; Motta, F. V.; Bomio, M. R. D.

Software: Silva, W. J.; Ruiz, J. A. C.

Supervision: Silva, W. J.; Ruiz, J. A. C.; Longo, E.; Motta, F. V.; Bomio, M. R. D.

Validation: Not applicable.

Visualization: Not applicable.

Writing – original draft: Silva, W. J.; Andrade Neto, N. F.; Motta, F. V.; Bomio, M. R. D.

Writing – review & editing: Silva, W. J.; Andrade Neto, N. F.; Motta, F. V.; Bomio, M. R. D.

Data availability statement

All data sets were generated or analyzed in the current study

Funding

Coordenação de Aperfeiçoamento de Pessoal de Nível Superior (CAPES). Finance Code: 2013/2998/2014.

Conselho Nacional de Desenvolvimento Científico e Tecnológico (CNPq). Grant No: 307546/2014.

Acknowledgments

Not applicable.

References

Alam, M. Z.; Muyibi, S. A.; Mansor, M. F.; Wahid, R. Activated carbons derived from oil palm empty-fruit bunches: Application to environmental problems. *J. Environ. Sci.* **2007**, *19* (1), 103–108. [https://doi.org/10.1016/S1001-0742\(07\)60017-5](https://doi.org/10.1016/S1001-0742(07)60017-5)

AlOthman, Z. A.; Habila, M. A.; Ali, R.; Ghafar, A. A.; El-din Hassouna, M. S. Valorization of two waste streams into

- activated carbon and studying its adsorption kinetics, equilibrium isotherms and thermodynamics for methylene blue removal. *Arab. J. Chem.* **2014**, *7* (6), 1148–1158. <https://doi.org/10.1016/j.arabjc.2013.05.007>
- Bansal, R.; Warrington, A. E.; Gard, A. L.; Ranscht, B.; Pfeiffer, S. E. Multiple and novel specificities of monoclonal antibodies O1, O4, and R-mAb used in the analysis of oligodendrocyte development. *J. Neurosci. Res.* **1989**, *24* (4), 548–557. <https://doi.org/10.1002/jnr.490240413>
- Beuselink, L.; Govers, G.; Poesen, J.; Degraer, G.; Froyen, L. Grain-size analysis by laser diffractometry: Comparison with the sieve-pipette method. *CATENA* **1998**, *32* (3-4), 193–208. [https://doi.org/10.1016/S0341-8162\(98\)00051-4](https://doi.org/10.1016/S0341-8162(98)00051-4)
- Caputi, C. A.; De Carolis, G.; Tomasetti, C. Regional intravenous ketanserin and guanethidine therapy in Raynaud's phenomenon. *Angiology* **1991**, *42* (6), 473–480. <https://doi.org/10.1177/000331979104200607>
- Carvalho, L. M. J.; Gomes, P. B.; Godoy, R. L. O.; Pacheco, S.; Monte, P. H. F.; Carvalho, J. L. V.; Nutti, M. R.; Neves, A. C. L.; Vieira, A. C. R. A.; Ramos, S. R. R. Total carotenoid content, α -carotene and β -carotene, of landrace pumpkins (*Cucurbita moschata* Duch): A preliminary study. *Food Res. Int.* **2012**, *47* (2), 337–340. <https://doi.org/10.1016/j.foodres.2011.07.040>
- Connor, T. H.; MacKenzie, B. A.; DeBord, D. G.; Trout, D. B.; O'Callaghan, J. P. *NIOSH List of Antineoplastic and Other Hazardous Drugs in Healthcare Settings, 2016*; DHHS (NIOSH) Publication No. 2016-161; Department of Health and Human Services, Centers for Disease Control and Prevention, National Institute for Occupational Safety and Health: Washington, DC, 2016. <https://www.cdc.gov/niosh/docs/2016-161/pdfs/2016-161.pdf> (accessed 2022-03-16).
- Dalai, C.; Jha, R.; Desai, V. R. Rice Husk and Sugarcane Baggase Based Activated Carbon for Iron and Manganese Removal. *Aquat. Procedia* **2015**, *4*, 1126–1133. <https://doi.org/10.1016/j.aqpro.2015.02.143>
- Dodevski, V.; Janković, B.; Stojmenović, M.; Krstić, S.; Popović, J.; Pagnacco, M. C.; Popović, M.; Pašalić, S. Plane tree seed biomass used for preparation of activated carbons (AC) derived from pyrolysis. Modeling the activation process. *Colloids Surf. A Physicochem. Eng. Asp.* **2017**, *522*, 83–96. <https://doi.org/10.1016/j.colsurfa.2017.03.003>
- Ferreira, T. A.; Oliveira, C. R.; Chaves, P. P. N.; Milhomens, K. K. B.; Barros, H. B.; Nascimento, I. R. Indução da frutificação paternocárpica de frutos em híbrido de abóbora japonesa com 2, 4-D sob condições de temperatura elevada. *Nucleus* **2017**, *14* (1), 145–152. <https://doi.org/10.3738/1982.2278.1686>
- Gonçalves, A. L.; Rodrigues, C. M.; Pires, J. C. M.; Simões, M. The effect of increasing CO₂ concentrations on its capture, biomass production and wastewater bioremediation by microalgae and cyanobacteria. *Algal Res.* **2016**, *14*, 127–136. <https://doi.org/10.1016/j.algal.2016.01.008>
- Gonzaga, L. C.; Carvalho, J. L. N.; Oliveira, B. G.; Soares, J. R.; Cantarella, H. Crop residue removal and nitrification inhibitor application as strategies to mitigate N₂O emissions in sugarcane fields. *Biomass Bioenergy* **2018**, *119*, 206–216. <https://doi.org/10.1016/j.biombioe.2018.09.015>
- Goyal, M.; Rattan, V. K.; Aggarwal, D.; Bansal, R. C. Removal of copper from aqueous solutions by adsorption on activated carbons. *Colloids Surf. A Physicochem. Eng. Asp.* **2001**, *190* (3), 229–238. [http://doi.org/10.1016/S0927-7757\(01\)00656-2](http://doi.org/10.1016/S0927-7757(01)00656-2)
- Hameed, B. H.; El-Khaiary, M. I. Batch removal of malachite green from aqueous solutions by adsorption on oil palm trunk fibre: Equilibrium isotherms and kinetic studies. *J. Hazard. Mater.* **2008**, *154* (1), 237–244. <https://doi.org/10.1016/j.jhazmat.2007.10.017>
- Huang, H.-j.; Yang, T.; Lai, F.-y.; Wu, G.-q. Co-pyrolysis of sewage sludge and sawdust/rice straw for the production of biochar. *J. Anal. Appl. Pyrolysis* **2017**, *125*, 61–68. <https://doi.org/10.1016/j.jaap.2017.04.018>
- Joshi, D. C.; Das, S. K.; Mukherjee, R. K. Physical properties of pumpkin seeds. *J. Agric. Eng. Res.* **1993**, *54* (3), 219–229. <https://doi.org/10.1006/jaer.1993.1016>
- MacIntyre, C. R.; Chughtai, A. A.; Seale, H.; Richards, G. A.; Davidson, P. M. Respiratory protection for healthcare workers treating Ebola virus disease (EVD): Are facemasks sufficient to meet occupational health and safety obligations? *Int. J. Nurs. Stud.* **2014**, *51* (11), 1421–1426. <https://doi.org/10.1016/j.ijnurstu.2014.09.002>
- Mahamad, M. N.; Zaini, M. A. A.; Zakaria, Z. A. Preparation and characterization of activated carbon from pineapple waste biomass for dye removal. *Int. Biodeterior. Biodegradation* **2015**, *102*, 274–280. <https://doi.org/10.1016/j.ibiod.2015.03.009>
- Marshall, W. E.; Ahmedna, M.; Rao, R. M.; Johns, M. Granular activated carbons from sugarcane bagasse: Production and uses. *Int. Sugar J.* **2000**, *102* (1215), 147–151.
- Martins, U. R.; Santos-Silva, A.; Galileo, M. H. M.; Limeira-de-Oliveira, F. Cerambycidae (Coleoptera) dos estados do Piauí e Ceará, Brasil: espécies conhecidas, nova tribo, nova espécie e novos registros. *Iheringia Sér. Zool.* **2014**, *104* (3), 373–384. <https://doi.org/10.1590/1678-476620141043373384>
- Matos, J.; Montaña, R.; Rivero, E., Influence of activated carbon upon the photocatalytic degradation of methylene blue under UV-vis irradiation. *Environ. Sci. Pollut. Res.* **2015**, *22*

(2), 784–791. <https://doi.org/10.1007/s11356-014-2832-9>

Njoku, K. L.; Akinola, M. O.; Nkemdilim, C. M.; Ibrahim, P. M.; Olatunbosun, A. S. Evaluation of the potentials of three grass plants to remediate crude oil polluted soil. *CAES* **2014**, *2* (4), 131–137.

Nunes, P. H. M. P.; Aquino, L. A.; Santos, L. P. D.; Xavier, F. O.; Dezordi, L. R.; Assunção, N. S. Produtividade do trigo submetido a aplicação de nitrogênio e a inoculação com *Azospirillum brasiliense*. *Ver. Bras. Ci. Solo* **2015**, *39*, 174–182. <https://doi.org/10.1590/01000683rbcsc20150354>

Pezoti Junior, O.; Cazetta, A. L.; Souza, I. P. A. F.; Bedin, K. C.; Martins, A. C.; Silva, T. L.; Almeida, V. C. Adsorption studies of methylene blue onto ZnCl₂-activated carbon produced from buriti shells (*Mauritia flexuosa* L.). *J. Ind. Eng. Chem.* **2014**, *20* (6), 4401–4407. <https://doi.org/10.1016/j.jiec.2014.02.007>

Pezoti, O.; Cazetta, A. L.; Bedin, K. C.; Souza, L. S.; Martins, A. C.; Silva, T. L.; Santos Júnior, O. O.; Visentainer, J. V.; Almeida, V. C. NaOH-activated carbon of high surface area produced from guava seeds as a high-efficiency adsorbent for amoxicillin removal: Kinetic, isotherm and thermodynamic studies. *Chem. Eng. J.* **2016**, *288*, 778–788. <https://doi.org/10.1016/j.cej.2015.12.042>

Poinern, G. E.; Brundavanam, R.; Le, X. T.; Djordjevic, S.; Prokic, M.; Fawcett, D. Thermal and ultrasonic influence in the formation of nanometer scale hydroxyapatite bio-ceramic. *Int. J. Nanomed.* **2011**, *6*, 2083–2095. <https://doi.org/10.2147/IJN.S24790>

Rovani, S.; Rodrigues, A. G.; Medeiros, L. F.; Cataluña, R.; Lima, É. C.; Fernandes, A. N. Synthesis and characterisation of activated carbon from agroindustrial waste—Preliminary study of 17β-estradiol removal from aqueous solution. *J. Environ. Chem. Eng.* **2016**, *4* (2), 2128–2137. <https://doi.org/10.1016/j.jece.2016.03.030>

Shen, L.; Li, Y.; Jiang, L.; Wang, X. Response of *Saccharomyces cerevisiae* to the Stimulation of Lipopolysaccharide. *PLoS ONE* **2014**, *9* (8), e104428. <https://doi.org/10.1371/journal.pone.0104428>

Solís-Domínguez, F. A.; Valentín-Vargas, A.; Chorover, J.; Maier, R. M. Effect of arbuscular mycorrhizal fungi on plant biomass and the rhizosphere microbial community structure of mesquite grown in acidic lead/zinc mine tailings. *Sci. Total Environ.* **2011**, *409* (6), 1009–1016. <https://doi.org/10.1016/j.scitotenv.2010.11.020>

Tsyntsarski, B.; Stoycheva, I.; Tsoncheva, T.; Genova, I.; Dimitrov, M.; Petrova, B.; Paneva, D.; Cherkezova-Zheleva, Z.; Budinova, T.; Kolev, H.; Gomis-Berenguer, A.; Ania, C. O.; Mitov, I.; Petrov, N. Activated carbons from waste biomass and low rank coals as catalyst supports for hydrogen production by methanol decomposition. *Fuel Process. Technol.* **2015**, *137*, 139–147. <https://doi.org/10.1016/j.fuproc.2015.04.016>

Technol. **2015**, *137*, 139–147. <https://doi.org/10.1016/j.fuproc.2015.04.016>

Van Thuan, T.; Quynh, B. T. P.; Nguyen, T. D.; Ho, V. T. T.; Bach, L. G. Response surface methodology approach for optimization of Cu²⁺, Ni²⁺ and Pb²⁺ adsorption using KOH-activated carbon from banana peel. *Surf. Interfaces* **2017**, *6*, 209–217. <https://doi.org/10.1016/j.surfin.2016.10.007>

Wang, S.; Li, L.; Wu, H.; Zhu, Z. H. Unburned carbon as a low-cost adsorbent for treatment of methylene blue-containing wastewater. *J. Colloid Interface Sci.* **2005**, *292* (2), 336–343. <https://doi.org/10.1016/j.jcis.2005.06.014>









Wang, S.; Gao, B.; Li, Y.; Mosa, A.; Zimmerman, A. R.; Ma, L. Q.; Harris, W. G.; Migliaccio, K. W. Manganese oxide-modified biochars: preparation, characterization, and sorption of arsenate and lead. *Bioresour. Technol.* **2015**, *181*, 13–17. <https://doi.org/10.1016/j.biortech.2015.01.044>

Wu, L.; Zhang, X.; Liu, D.; Peng, H.; Long, T. Activated Carbons Derived from Livestock Sewage Sludge and their Adsorption Ability for the Livestock Sewage. *IERI Procedia* **2014**, *9*, 33–42. <https://doi.org/10.1016/j.ieri.2014.09.037>

Yorgun, S.; Yıldız, D. Preparation and characterization of activated carbons from Paulownia wood by chemical activation with H₃PO₄. *J. Taiwan Inst. Chem. Eng.* **2015**, *53*, 122–131. <https://doi.org/10.1016/j.jtice.2015.02.032>

Zhang, S. B.; Lu, Q. Y. Characterizing the structural and surface properties of proteins isolated before and after enzymatic demulsification of the aqueous extract emulsion of peanut seeds. *Food Hydrocoll.* **2015**, *47*, 51–60. <https://doi.org/10.1016/j.foodhyd.2015.01.007>

Activated carbon from pumpkin seeds: Production by simultaneous carbonization activation for occupational respiratory protection

Walquíria Joseane da Silva¹, Nivaldo Freire de Andrade Neto¹⁺, Carlos Alberto Paskocimas¹, Juan Alberto Chaves Ruiz², Fabíola Correa Carvalho², Elson Longo³, Fabiana Villela da Motta¹, Maurício Roberto Bomio Delmonte¹

1. Federal University of Rio Grande do Norte, Department of Materials Engineering, Natal, Brazil.
2. SENAI Institute for Renewable Energy Innovation, Natal, Brazil.
3. Federal University of São Carlos, Center for the Development of Functional Materials, São Carlos, Brazil.

+Corresponding author: Nivaldo Freire Andrade Neto, **Phone:** +55 84 33422406, **Email address:** nfandraden@gmail.com

ARTICLE INFO

Article history:

Received: July 21, 2021

Accepted: October 26, 2021

Published: April 11, 2022

Keywords:

1. activated carbon
2. pumpkin seeds
3. simultaneous carbonization-activation
4. high adsorption capacity

Section Editors: Elson Longo and Juan Manuel Andrés Bort

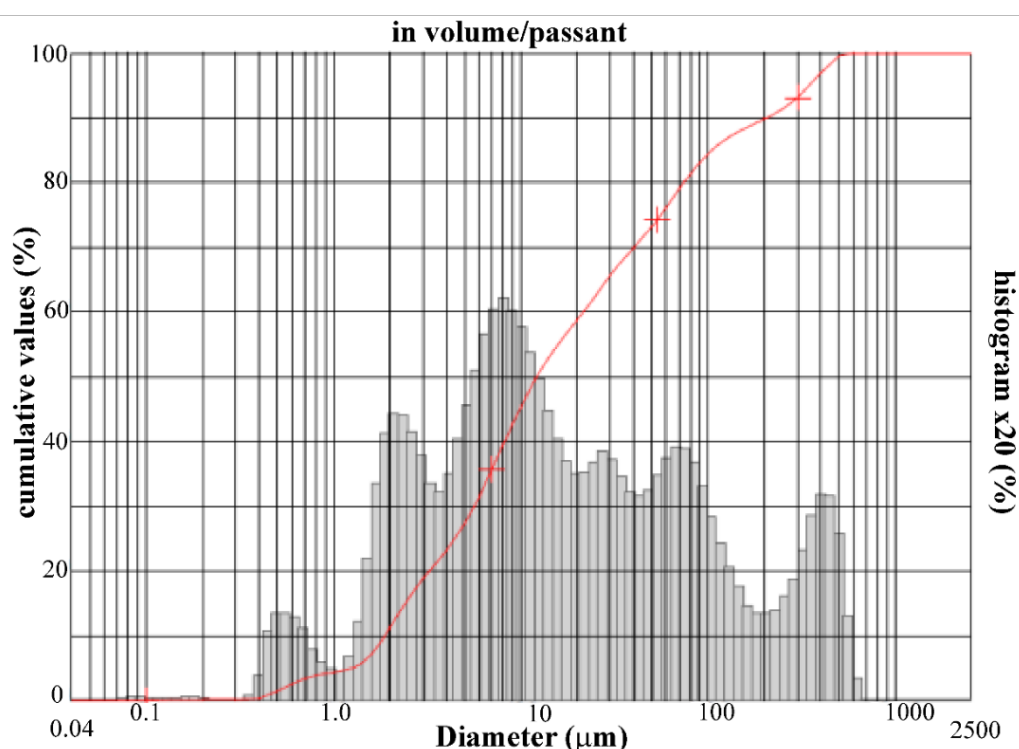


Figure S1. Particle size distribution of the in natura waste after grinding.

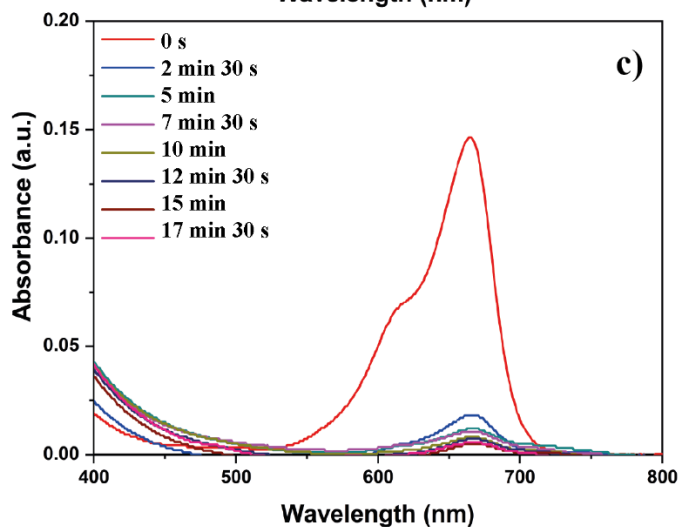
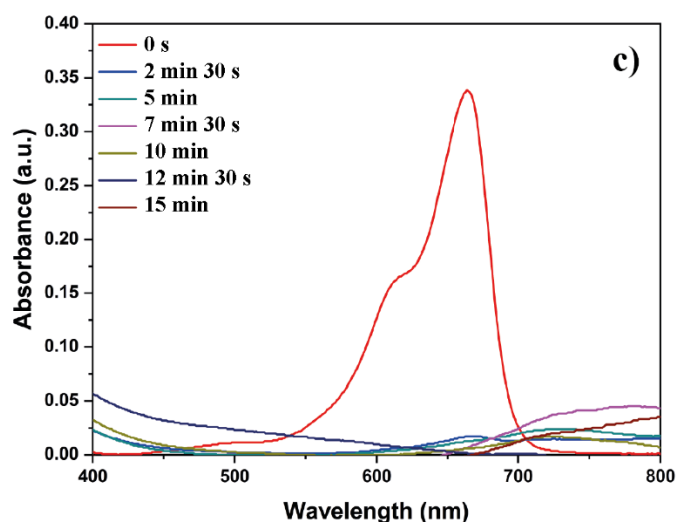
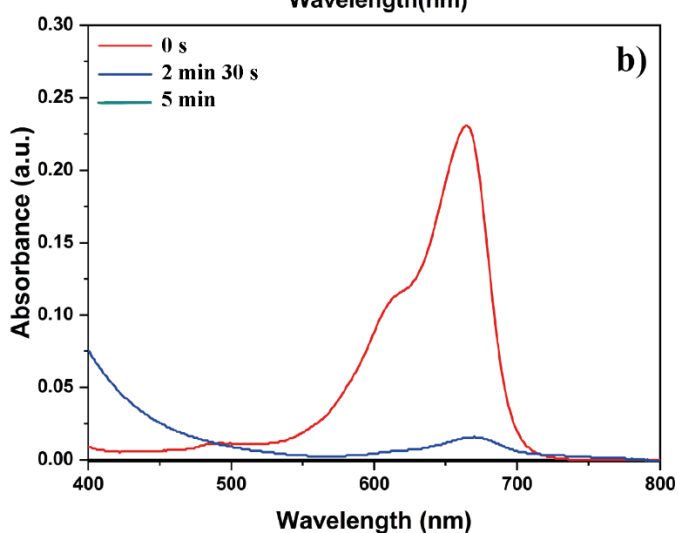
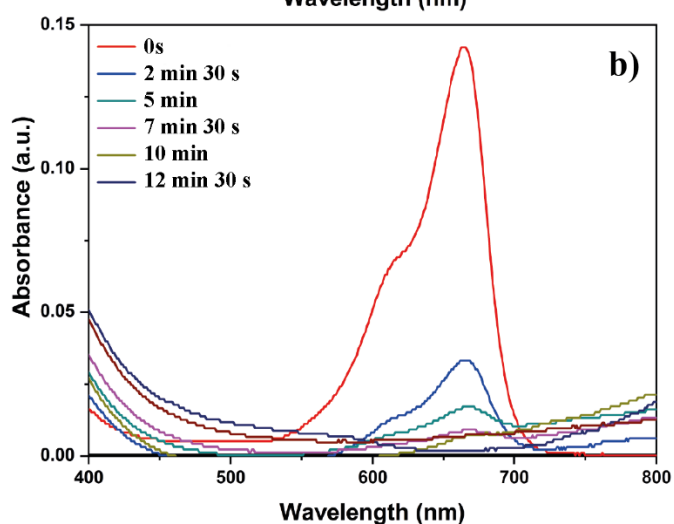
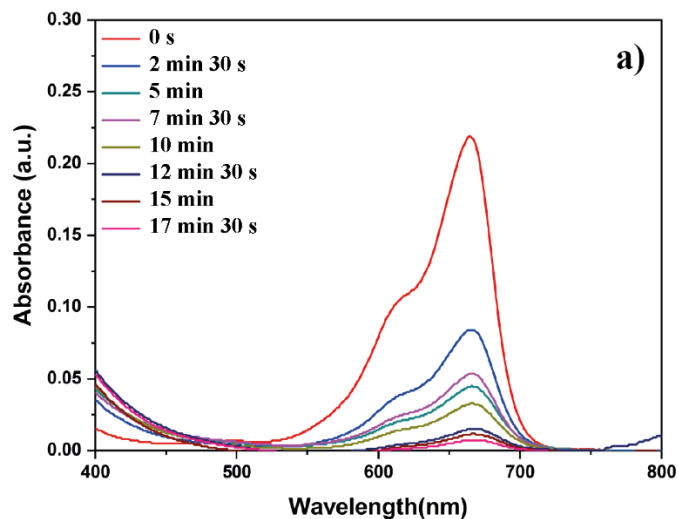
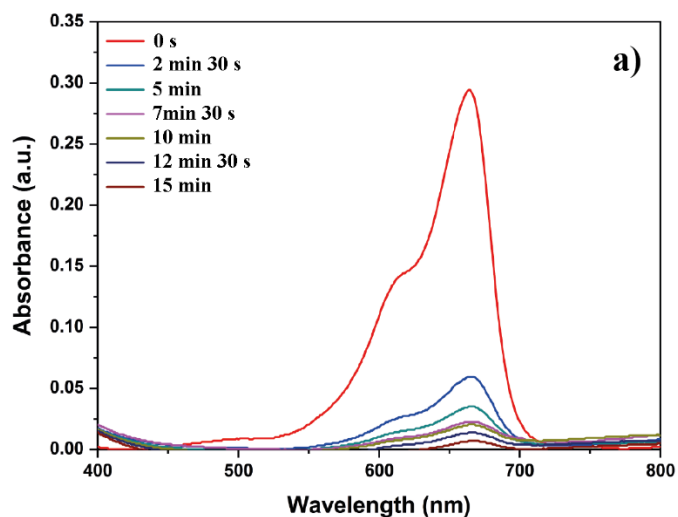


Figure S2. UV-vis absorbance spectrum for the (a) PSCLO10, (b) PSCLO30 and (c) PSCLO50 samples.

Figure S3. UV-vis absorbance spectrum for the (a) PSNIT10, (b) PSNIT30 and (c) PSNIT50 samples.

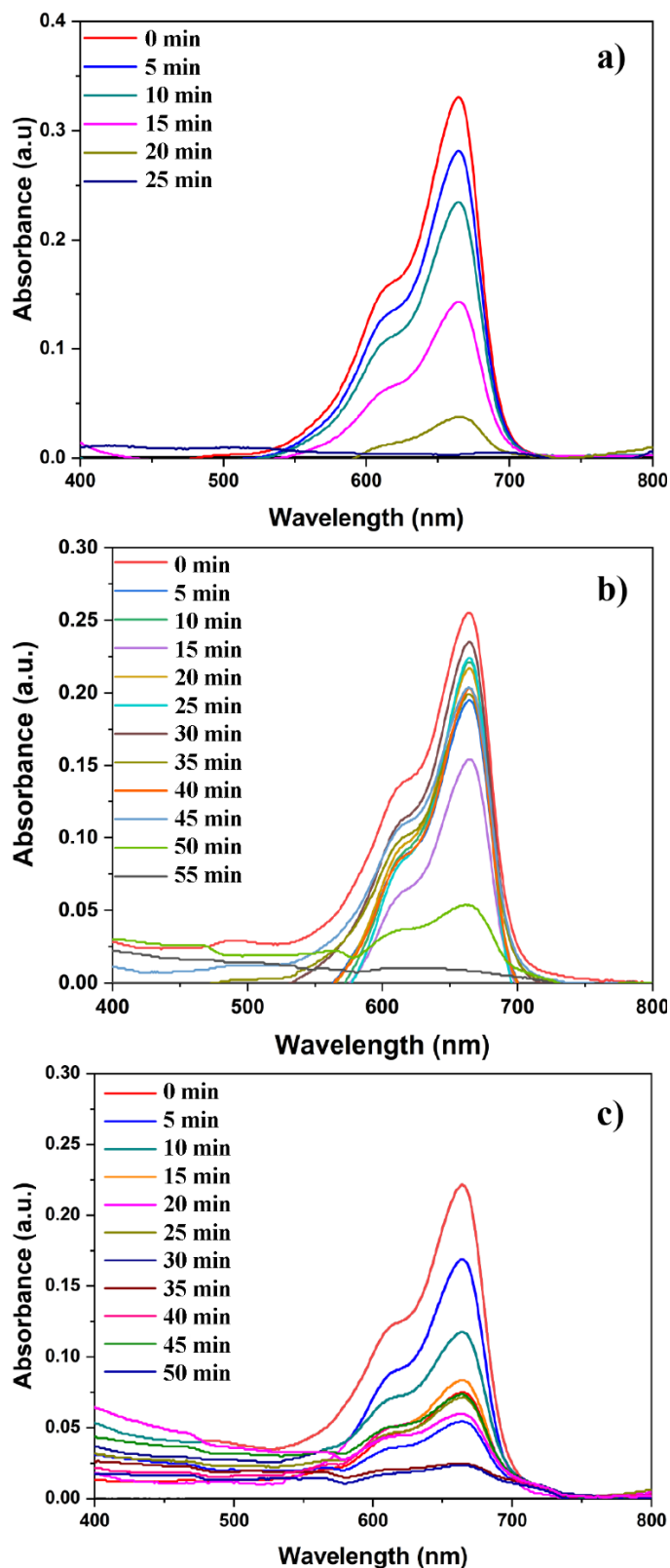


Figure S4. UV-vis absorbance spectrum for the (a) PSSUL10, (b) PSSUL30 and (c) PSSUL50 samples.

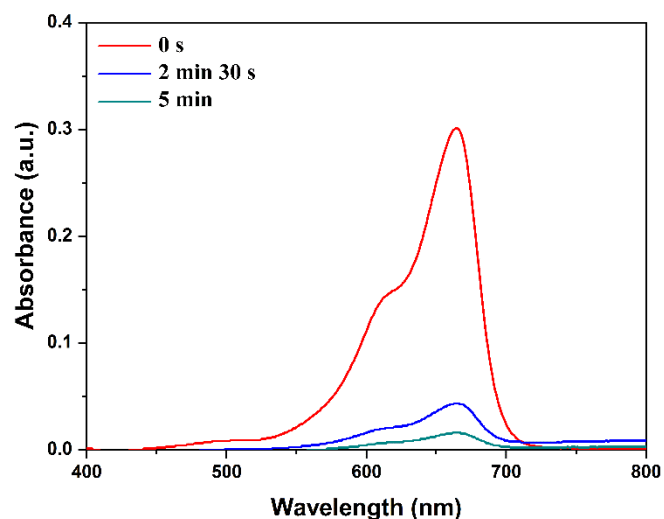


Figure S5. UV-vis absorbance spectrum for the commercial sample.

Surfactant effects in the morphology and the photocatalytic activity of the BaMoO₄ crystals

Amanda Fernandes Gouveia^{1,2+id}, Gustavo Venancio Bellucci^{3id}, Lara Kelly Ribeiro^{3id}, Marcelo Assis^{3id}, Ieda Lúcia Viana Rosa^{3id}, Elson Longo^{3id}, Juan Andrés^{1id}, Miguel Angel San-Miguel^{2id}

1. University Jaume I, Department of Physical and Analytical Chemistry, Castelló, Spain.
2. State University of Campinas, Institute of Chemistry, Campinas, Brazil.
3. Federal University of Sao Carlos, Center for the Development of Functional Materials, São Carlos, Brazil.

+Corresponding author: Amanda Fernandes Gouveia, **Phone:** +34 964728071, **Email address:** gouveiad@uji.es

ARTICLE INFO

Article history:

Received: July 27, 2021

Accepted: November 09, 2021

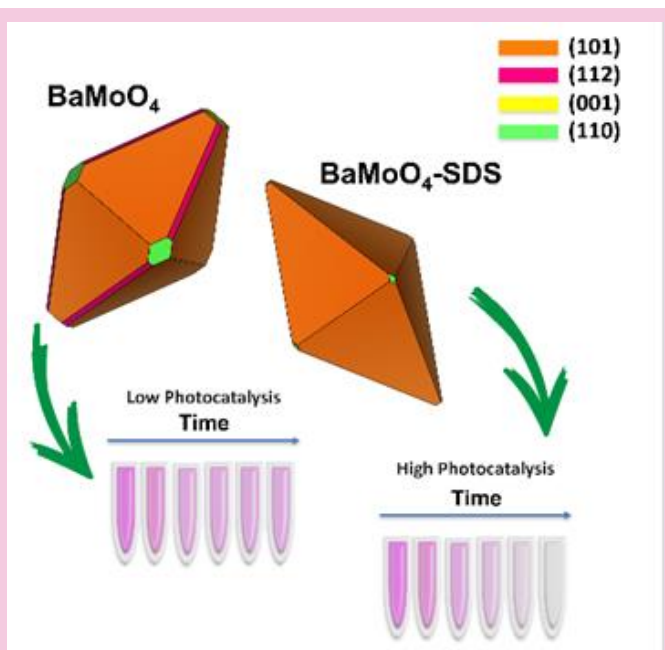
Published: April 11, 2022

Keywords:

1. DFT calculations
2. Rational design of materials
3. Barium molybdate
4. Surfactant-mediated morphology
5. Photocatalytic activity

Section Editors: Elson Longo and Juan Manuel Andrés Bort

ABSTRACT: This paper discloses the effect of the surfactant sodium dodecyl sulfate (SDS) in the morphology and the photocatalytic activity of BaMoO₄ crystals. Experimental techniques were applied to study the order-disorder degree of the samples. First-principles calculations were performed at density functional theory level with the B3LYP hybrid functional. The morphologies were investigated by field emission scanning electron microscopy, and the theoretical crystal shapes were obtained through the Wulff construction. The photocatalytic activity efficiency of the BaMoO₄ crystals was tested against the Rhodamine B (RhB) dye. In this paper, BaMoO₄ synthesized with SDS by the coprecipitation method presented a monophasic crystal with a disordered structure. In addition, the presence of this surfactant generated pores on the surfaces of the material, and those pores were responsible for the appearance of the adsorptive ability enhancing the adsorption process of the RhB dye in the dark, in absence of ultraviolet light.



1. Introduction

In past years, the ceramic's powders and crystals of molybdates were prepared by different methods, such as solid-state reaction (Kumar *et al.*, 2020), precipitation with calcination in high temperatures (Silva *et al.*, 2020), and the crystal growth by the "Czochralski" process (Khan *et al.*, 2020). However, these synthesis methods require high temperatures, long processing times, sophisticated equipment with high maintenance costs and can even lead to the formation of undesirable phases. Therefore, some synthesis methods have been developed and used in the preparation of molybdate crystals (Lakhlifi *et al.*, 2020; Skutina *et al.*, 2021; Tang *et al.*, 2021), such as coprecipitation (Chankhanittha *et al.*, 2021; F. Oliveira *et al.*, 2021), conventional hydrothermal (Farahpour and Arvand, 2021), microwave assisted hydrothermal (Keshari and Dubey, 2021), and sonochemical (Silva Junior *et al.*, 2021). These methods make possible to allay the problems present in older methods and obtain crystals of different sizes and shapes.

In particular, the coprecipitation method, which, according to the literature, is defined as a process for obtaining crystalline materials from the dissolution of reagents or soluble precursors in aqueous solution with or without the presence of a mineralizer (chemical bases) at relatively low temperature, has been used recently in the preparation of different molybdates of different shapes and sizes (Theiss *et al.*, 2016). However, to obtain homogeneous and monophasic molybdate crystals by this method, higher temperatures (> 100 °C) are necessary due to the low reaction kinetics (Kianpour *et al.*, 2013). Studies have been carried out using the coprecipitation method, employing surfactants as stabilizing agents to aid in the kinetics and, thus, reduce the reaction temperature (Kianpour *et al.*, 2016). These surfactants act as reactants during the reaction and stabilize the colloids. The literature also shows the effect of different surfactant ratios in controlling the size of microstructures and improving photocatalytic, photoluminescent, and antibacterial properties (Ji *et al.*, 2020; Keerthana *et al.*, 2021; Ray *et al.*, 2018). Among the used surfactants, the anionic sodium dodecyl sulphate (SDS) acts as a stabilizer protecting the newly formed cation or anion nuclei, which has an intrinsic preference for the growth of their crystals (Kianpour *et al.*, 2013; Luo *et al.*, 2010).

Among molybdates, barium molybdate (BaMoO_4) is relevant material in electro-optics due to its green luminosity production and electro-optic applications, including solid-state lasers and optical fibers. The BaMoO_4 presents a scheelite structure with $I4_1/a$ space

group formed by distorted $[\text{BaO}_8]$ and $[\text{MoO}_4]$ clusters. This material has a high band gap energy (E_{gap}) ~ 4.2 eV (Pereira *et al.*, 2021; Sczancoski *et al.*, 2010; Xia and Chen, 2010). Due to its poor use of light (ultraviolet [UV] light) from the solar spectrum, the photocatalytic efficiency becomes very low. Various techniques have been applied to photogenerate electron-hole pairs in semiconductors to improve photocatalytic performance, such as modeling new crystals through BaMoO_4 synthesis to form new morphologies efficient in enhancing the photocatalytic performance of BaMoO_4 (Hu *et al.*, 2021; Luo *et al.*, 2008; Xia and Chen, 2010). It is possible to correlate the size of materials with different or even new properties; thus, semiconductors designed with different sizes and exposed facets proved to be excellent models to promote, for example, photocatalytic and biocide studies (Macedo *et al.*, 2018).

This paper presents a simple method for the synthesis of uniform and pure BaMoO_4 crystals through the coprecipitation method using the SDS to evaluate the effects on the crystal morphology in the application of Rhodamine B (RhB) degradation. Thus, to endorse the experimental results, first-principles calculations were used to assess the effects of morphology on the degrading processes of the RhB.

2. Experimental sections

2.1 Synthesis

The BaMoO_4 crystals were synthesized by a simple coprecipitation method by using barium nitrate ($\text{Ba}(\text{NO}_3)_2$, Sigma-Aldrich, 99.0%), sodium molybdate dihydrate ($\text{NaMoO}_4 \cdot 2\text{H}_2\text{O}$, Sigma-Aldrich, 99.0%) as precursors, and the sodium dodecyl sulfate (SDS, Synth, 90.0%) as a surfactant. The first step of the synthesis involves the dissolution of 1×10^{-3} mol of the precursor's salts, separately, in 100 mL of deionized water at 70 °C. Then, 1 g of the surfactant SDS was added to the MoO_4^{2-} ions solution. After these steps, the two solutions were mixed under constant stirring. Approximately ten washes with deionized water were carried out at the end, using a centrifugation process (Centrifuge 5804, Eppendorf) to remove the residual Na^+ and organic ions. The synthesized solid was collected and dried in an oven at 65 °C for 24 h. The same procedure described above was repeated to obtain the pure BaMoO_4 crystal by removing the SDS in the precursor solution. The samples were named by BaMoO_4 and BaMoO_4 -SDS for the synthesis without and with SDS, respectively.

2.2 Structural and morphological characterization

The structure of BaMoO₄ crystals was characterized by X-ray diffraction (XRD) with Rietveld and micro-Raman. The morphological change was analyzed through field emission-scanning electron microscopy (FE-SEM), and the electronic modifications were analyzed by UV-visible (UV-vis) spectroscopy.

2.3 Photocatalysis evaluation

To analyze the surfactant's effect in the photocatalytic activity of the BaMoO₄ and BaMoO₄-SDS crystals, it was performed the photodegradation of the RhB (95%, Mallinckrodt) under UV light. The experiment was conducted as follows: 50.0 mL of RhB solution (1×10^{-5} mol L⁻¹) were added to the glass reactor with 50 mg of the sample. The reactor was taken to ultrasound (42 kHz, model 1510) for 5 min in the dark to disperse the BaMoO₄ crystals in the solution and then transferred to the photocatalytic system with 6 UV lamps (TUV Phillips, 15 W, and intensity of 254 nm), in 10 cm from the reactor. Then, to reach the adsorption equilibrium, the system remained in the dark for 40 min (collecting aliquots at -40, -30, -20, -10 and 0 min) at 25 °C and in the next step, the lamps were turned on, and the aliquots were removed at 20, 40, 60, 80, 110 and 140 min. After the reaction, the photocatalytic system was placed in a plastic tube where they were centrifuged at 10,000 rpm for 5 min to remove the catalyst particles from the solution completely. The remaining solution was analyzed by UV-vis absorption spectroscopy in a V-660 spectrophotometer (JASCO). The monitoring of the variation in the RhB absorption band with maximum $\lambda = 554$ nm for photocatalytic tests was investigated.

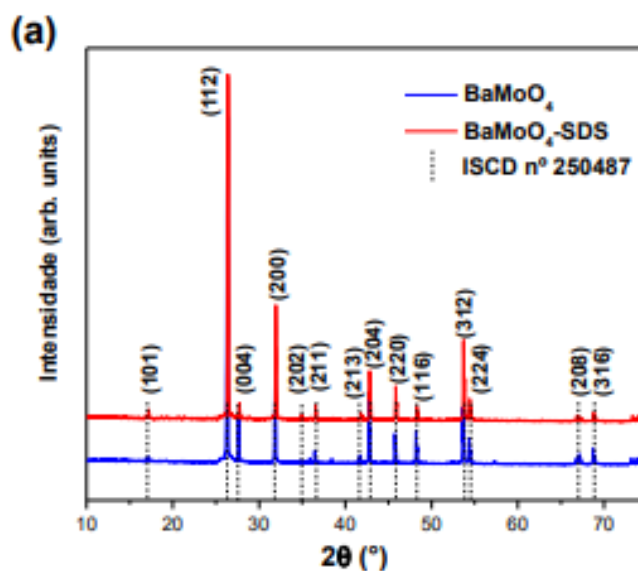
2.4 Theoretical models

First-principles calculations were performed using the CRYSTAL program (Dovesi *et al.*, 2017; 2018) at the DFT level associated with the B3LYP hybrid functional (Becke, 1988; 1993). To study the electronic properties of the BaMoO₄ structure, a unit cell model was created from the refinement data. In the optimization process to obtain the perfect crystal data, without defects, the lattice parameters (a , b , c , and α , β , γ) and the internal coordinates (x , y , z) of each atom were optimized. The electronic band gap energy (E_{gap}) value and the Raman frequencies were computed and compared with the experimental values. From the

calculated surface energy (E_{surf}) values published in the literature (M. Oliveira *et al.*, 2016), associated with the Wulff's construction, it was possible to obtain the ideal theoretical morphology (in vacuum) for the material studied. In addition to this ideal morphology and using the methodology developed by us (Andrés *et al.*, 2015), it was also possible to obtain the experimental morphology in order to compare it with the theoretical one.

3. Results and discussion

The XRD and Rietveld refinement was performed to verify the crystallinity of the material and its phase and structural parameters, as illustrated in Fig. 1. The XRD data allowed an analysis of the material structure at long-distance. It was possible to index and prove that both materials were obtained in their pure phase. As can be seen in Fig. 1a, it was not observed the presence of secondary phases, since the diffraction peaks are in good agreement with those reported for BaMoO₄ in ICSD n° 250487 (Inorganic Crystal Structure Database, ICSD) and the strong and acute peaks indicate that the synthesized crystals have good crystallinity. Structural refinement was performed using the Rietveld method for BaMoO₄ and BaMoO₄-SDS crystals to confirm that the structures belong to the tetragonal structure and obtain the lattice parameters, cell volume, and atomic coordinates (Fig. 1b). The structural refinement's quality was analyzed using the R_{wp} , R_{Bragg} , R_p e χ^2 statics parameters. Minor deviations of these parameters indicate the excellent quality of the structural refinement.



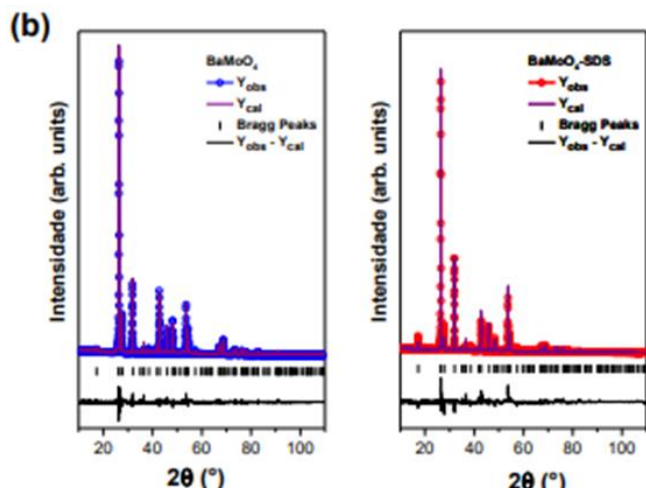


Figure 1. (a) X-ray diffraction patterns and (b) Rietveld refinement for BaMoO₄ crystals in the presence and absence of SDS.

The BaMoO₄ crystals, synthesized by the coprecipitation method with and without SDS, were obtained in their pure tetragonal phase (space group *I4₁/a*). Fig. 2 illustrates the tetragonal BaMoO₄ structure obtained from the refinement data. The crystal lattice of this semiconductor is formed by delta-hedral [BaO₈] and tetrahedral [MoO₄] clusters and contains four formula units per unit cell (*Z* = 4).

The analysis of the structural order/disorder degree of the BaMoO₄ crystals at a short distance was analyzed using the micro-Raman spectra. The results can be found in Fig. 3 and in Tab. 1, compared with the theoretical modes.

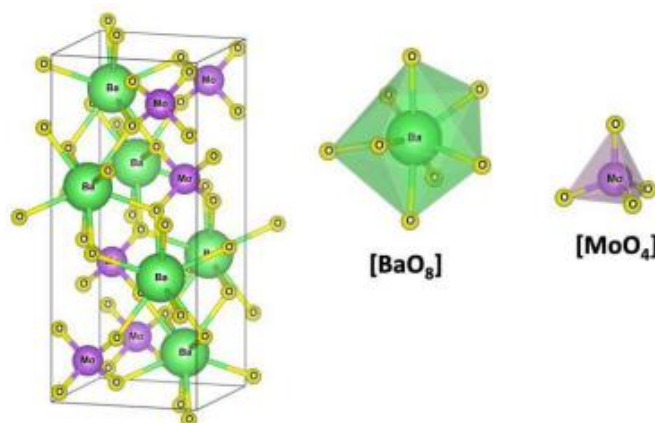


Figure 2. Tetragonal structure of BaMoO₄ and its constituent [BaO₈] and [MoO₄] clusters.

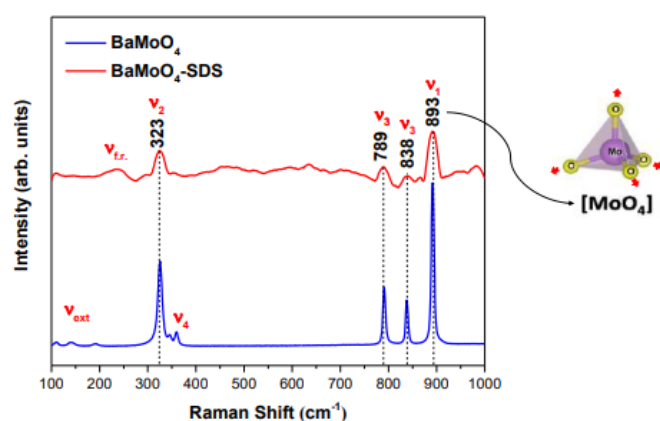


Figure 3. Micro-Raman spectroscopy for BaMoO₄ crystals in the presence and absence of SDS.

Table 1. Vibrational modes and Raman peaks of BaMoO₄ and theoretical values.

Vibrational modes and symmetry		Raman peaks (cm ⁻¹)		
Td	Lattice mode C ⁶ 4h	BaMoO ₄	BaMoO ₄ -SDS	BaMoO ₄ -Theo
ν ₁ (2A ₁)	A _g	893	893	907.95
ν ₃ (2F ₂)	B _g	838	838	853.78
ν ₃ (2F ₂)	E _g	789	789	818.28
ν ₄ (2F ₂)	E _g	360	-	367.90
ν ₄ (2F ₂)	B _g	345	-	366.19
ν ₂ (2E)	B _g , A _g	323	323	332.70
ν _{f,r} * (2F ₁)	E _g	-	238	212.10
ν _{ext} **	B _g	191	-	137.02
ν _{ext} **	E _g	142	-	122.86
ν _{ext} **	B _g , E _g	112	-	80.49

*Free rotation; **external modes.

As can be seen, the Raman bands related to the four active modes were observed. The vibrational modes observed in the Raman spectra are divided into two groups: the internal and external modes. The external

vibrational modes are composed of tetrahedral [MoO₄] clusters with strong covalent bonds between Mo–O and octahedral [BaO₈] clusters (Christofilos *et al.*, 2004; Sczancoski *et al.*, 2010). The internal modes are

composed of tetrahedral $[\text{MoO}_4]$ clusters with a rigid center of mass. The external modes can be considered as reticulated phonons because they result from the movement of $[\text{BaO}_8]$ and $[\text{MoO}_4]$ clusters, in symmetry T_d , in the free space generated (Panchal *et al.*, 2006). The BaMoO_4 samples exhibited all the internal and external modes, corresponding to the material's phase, well defined, indicating that the material is highly crystalline at close range. On the other hand, the Raman spectrum of $\text{BaMoO}_4\text{-SDS}$ showed peaks at 893, 838, 789, and 323 cm^{-1} , showing only the internal modes, demonstrating that this material is partially disordered. In addition, the $\text{BaMoO}_4\text{-SDS}$ has peaks corresponding to the internal modes, with less intensity, which is a characteristic for disordered crystals: the appearance of wide Raman bands reflecting on the density of the phonon states. These Raman results prove that the use of SDS in BaMoO_4 synthesis causes changes in the crystal structure at a short distance and that even with the pure BaMoO_4 phase confirmed by XRD results, these crystals are disordered.

The UV-vis spectra for the BaMoO_4 and $\text{BaMoO}_4\text{-SDS}$ samples made it possible to determine each E_{gap} value, applying the Kubelka–Munk function. This function is generally applied to convert diffuse reflectance into equivalent absorption coefficient and is mainly used to analyze powder samples and is described as (Eq. 1) (Wood and Tauc, 1972):

$$\alpha = F(R) = \frac{(1-R)^2}{2R} \quad (1)$$

where $F(R)$ is Kubelka-Munk function; α is the absorption coefficient, and R is the reflectance. Therefore, the Tauc relation becomes (Eq. 2):

$$F(R) = hv = \alpha(hv - E_{\text{gap}})n \quad (2)$$

where $n = 0.5$ and 2 for direct and indirect transitions, respectively, resulting in direct and indirect band intervals (Spassky *et al.*, 2005). The graphs of $(F(R)hv)^2$ versus hv for all samples are shown in Fig. 4. The extrapolation of linear regions from these graphs to $F(R)hv^2 = 0$ gives the direct band gap values.

The E_{gap} values show a slight variation between the samples. The decrease in the E_{gap} value for the $\text{BaMoO}_4\text{-SDS}$ crystals can be attributed to a reduction in the local order degree, which may have been caused by the creation of new intermediate levels between the valence (VB) and conduction bands (CB). This fact can be attributed to the presence of the SDS surfactant during the synthesis of the material that causes

distortions in the crystal structure, which endorse the experimental Raman spectra.

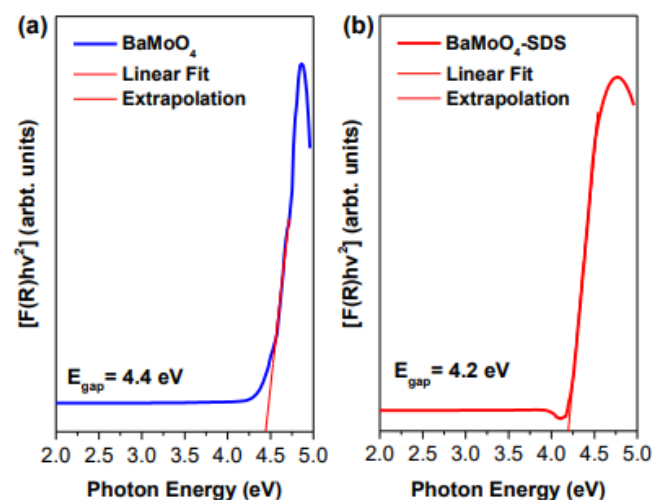
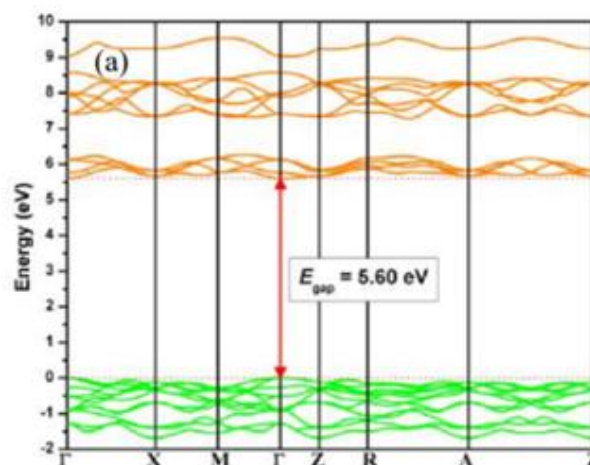


Figure 4. UV-vis spectra for the BaMoO_4 crystals in the presence and absence of SDS.

The theoretical study of the electronic properties corroborates with the UV-vis results. The theoretical model of the BaMoO_4 is seen as a defect-free structure with ideal parameters. This model presented a higher E_{gap} value (Fig. 5a) of 5.60 eV. The observed electronic transition is direct between the Γ -points of the Brillouin zone. The atomic composition of the VB and CB was investigated by analyzing the density of states (DOS) from all atoms in the structure. As shown in Fig. 5b, the VB for BaMoO_4 is mainly formed by the contribution of the orbitals from the O atoms, and these orbitals are mostly antibonding types. On the other hand, the CB is composed primarily by the hybridization of the orbitals from the Mo and O atoms. This region also has a contribution from the Ba atoms. There is the presence of bonding and antibonding orbitals.



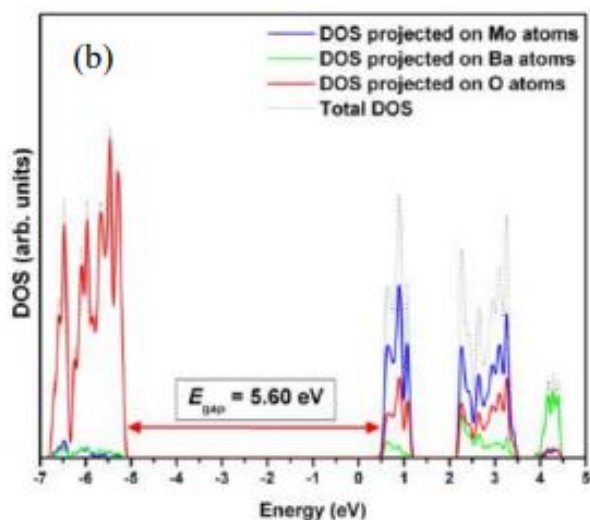


Figure 5. (a) Band structure and (b) Total and projected DOS for the BaMoO₄ structure.

The morphologies of the BaMoO₄ and BaMoO₄-SDS crystals were investigated by microscopy, and the FE-SEM images are illustrated in Fig. 6. The BaMoO₄

crystals synthesized without the surfactant present an octahedron-shaped morphology with a predominance of the (101) surface, with a small contribution of the (112) and (110) surfaces (Fig. 6a). Better visualization of these surfaces can be seen in the theoretical morphology known as Wulff's crystal. To achieve this theoretical morphology, it was employed the methodology developed by Andrés *et al.* (2015), in which used the calculated surface energy (E_{surf}) values associated with the Wulff construction (Wulff, 1901). The E_{surf} of the BaMoO₄ crystals were reported by M. Oliveira *et al.* (2016). The morphology observed for the crystals obtained in the presence of SDS (Fig. 6b) presents the same crystal shape as the sample without SDS (Fig. 6a). However, morphological differences are observed, such as the (112) surface no longer contributes to the morphology of the crystal, and the (110) starts to have a minor contribution. The major difference between the morphologies of BaMoO₄ and BaMoO₄-SDS is in the shape texture. BaMoO₄-SDS crystals have a rugged surface with the presence of pores.

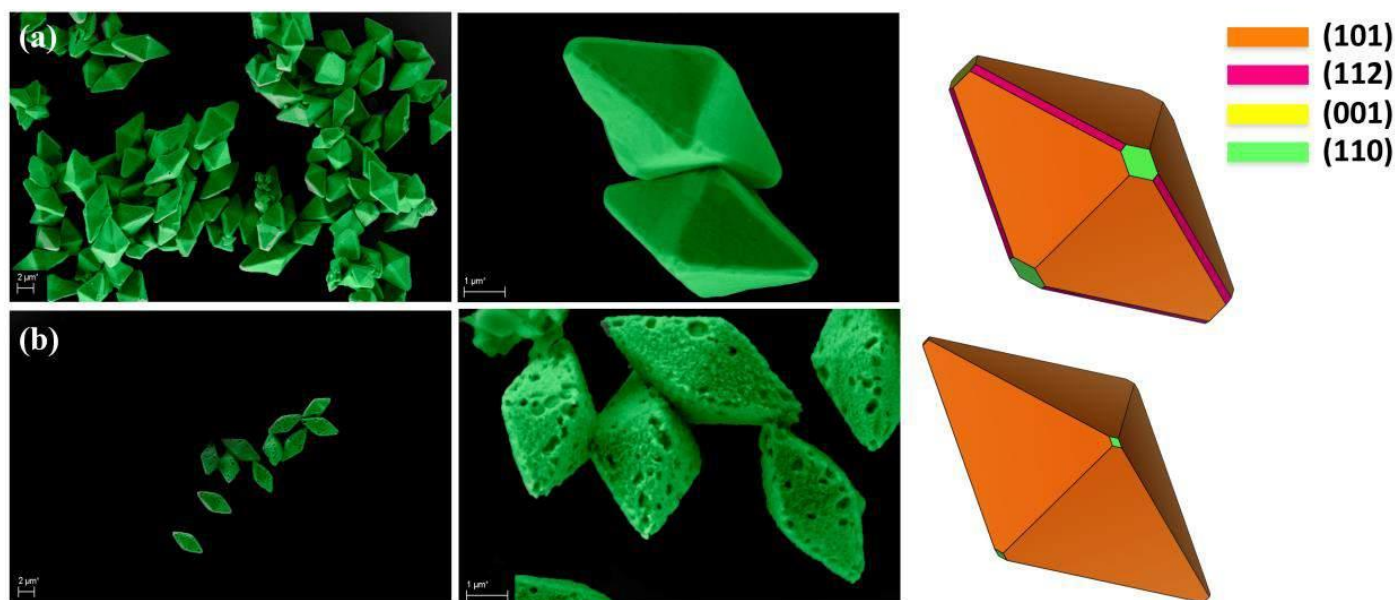


Figure 6. FE-SEM images for the (a) BaMoO₄ e (b) BaMoO₄-SDS crystals. For the comparison, Wulff's crystals are also represented for each sample.

M. Oliveira *et al.* (2016) reported the synthesized of the BaMoO₄ crystals also by the coprecipitation method; however, they used a temperature of 80 °C, at pH 7. They modeled the BaMoO₄ surfaces and calculated the surface energies. The morphology reported by the authors is different from that obtained in this study, with a significant presence of the (100), (112), (110), and (101) surfaces. Through these results, it is possible to

observe that the surfaces of this BaMoO₄ structure present, mainly, different types of clusters for the Ba atom, with several oxygen vacancies.

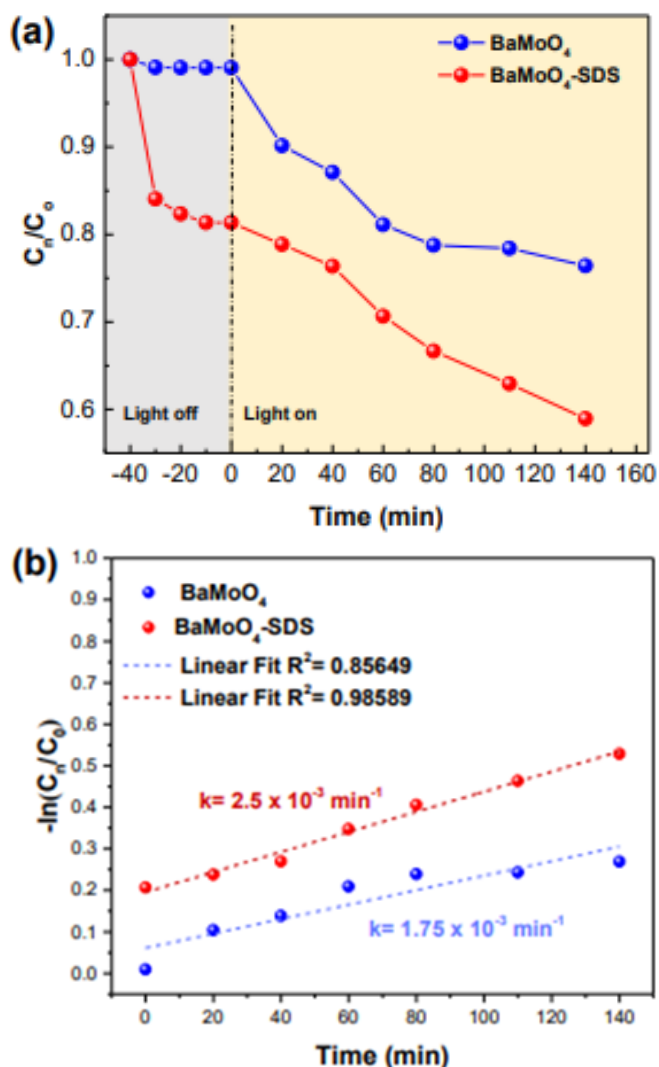


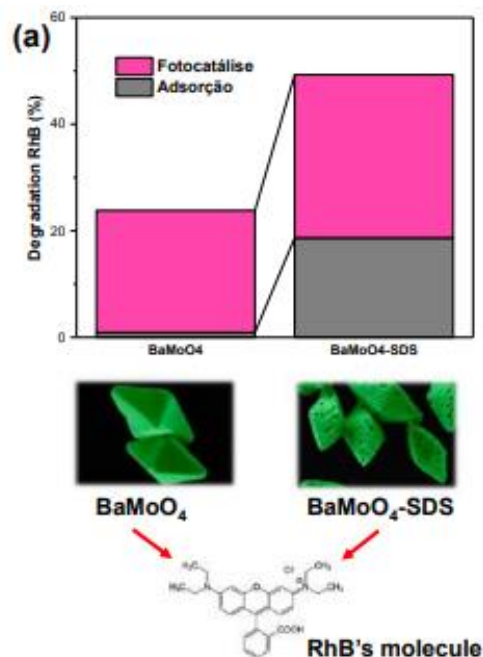
Figure 7. (a) Photocatalysis degradation profile of the RhB dye in 140 min and (b) first-order kinetics for the $BaMoO_4$ crystals in the presence and absence of SDS.

The photocatalytic activity of the $BaMoO_4$ crystals was tested against the RhB dye. The analysis started in the dark (light off) to test the influence of this environment in the photocatalysis process and obtain the adsorptive equilibrium. The equilibrium adsorption-desorption rate of RhB in the dark versus time in the presence of $BaMoO_4$ and $BaMoO_4$ -SDS was shown in Fig. 7a and Fig. 8a. The $BaMoO_4$ -SDS degradation profiles in the dark showed that this material has one more property that has not yet been reported in the literature, the adsorptive capacity. The $BaMoO_4$ -SDS crystals adsorbed about 18% of RhB while $BaMoO_4$ adsorbed about 1% of RhB. This property is acquired by the presence of pores in the crystal surfaces (see FE-SEM images in Fig. 6a), as illustrated in Fig. 8b. The high roughness of this material confers such properties,

and the adsorptive process added to the photocatalytic process certainly makes the material promising in the studies of adsorptive and photocatalysis processes. These two properties were illustrated in Fig. 8b–c. In addition, the $BaMoO_4$ -SDS also has a photocatalytic performance enhancement, as seen in Fig. 7b.

Therefore, by analyzing the degradation profile shown in Fig. 7a, it can be seen that the presence of SDS in the synthesis improved the photocatalytic activity. $BaMoO_4$ crystals degraded about 23% in 140 min, while the degradation of the $BaMoO_4$ -SDS crystals was 45%. The process analysis showed that both degradations occur in first-order kinetics. The calculated velocity constants were $k = 1.75 \times 10^{-3} \text{ min}^{-1}$ and $k = 2.50 \times 10^{-3} \text{ min}^{-1}$ for the $BaMoO_4$ and $BaMoO_4$ -SDS crystals, respectively, as shown in Fig. 7b. So, the increase in reaction kinetics indicates that $BaMoO_4$ synthesis in the presence of SDS is favorable for materials with photocatalytic properties.

Hence, the control of morphology is of fundamental importance because the properties of the materials depend on the kind of surfaces that constitute their morphology. In the case of the $BaMoO_4$ crystal, the use of the SDS favored the increase of the (101) surface and caused deformations on the crystal surfaces, considerably altering the morphology. This change is mainly responsible for creating and improving the main properties of the $BaMoO_4$ crystals studied in this work.



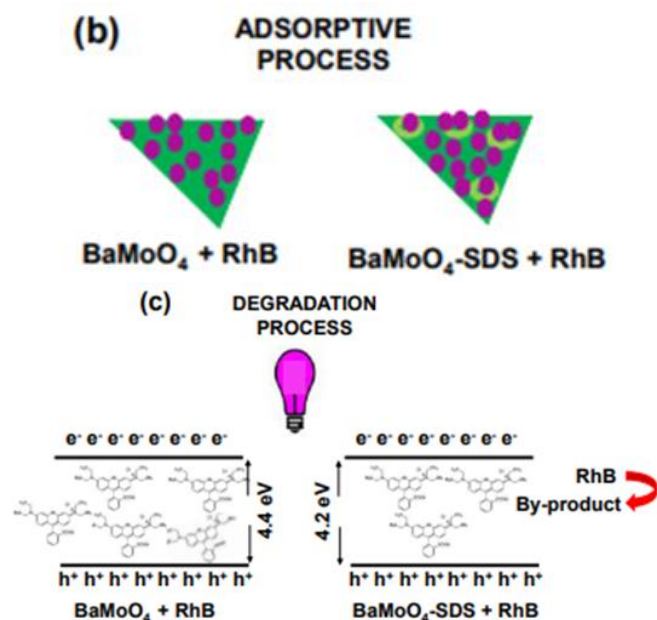


Figure 8. (a) Photocatalysis and adsorptive degradation of the RhB dye. (b) The mechanism proposed for the adsorptive process and (c) degradation process at the BaMoO_4 surfaces on the morphology obtained in the presence and absence of SDS.

4. Conclusions

In this study, it was possible to understand how the presence of a surfactant, in this case, the SDS, can generate changes in the morphology of the BaMoO_4 crystals and how this fact shifts the photocatalytic activity. In the case of BaMoO_4 synthesized with SDS, the presence of this surfactant generated pores on the surface of the material's morphology, and the presence of these pores facilitated the adsorption process of the RhB dye in the dark, without the presence of UV light, and, consequently, a new property for that semiconductor was created, the adsorptive capacity. In addition to the acquired adsorptive ability, BaMoO_4 synthesized with SDS showed a photocatalytic improvement. These results demonstrate that morphology control can influence the creation of new properties, opening a range of opportunities for further studies.

Authors' contribution

Conceptualization: Gouveia, A. F.; Bellucci, G. V.; Ribeiro, L. R.; Assis, M.

Data curation: Gouveia, A. F.; Bellucci, G. V.; Ribeiro, L. R.

Formal Analysis: Gouveia, A. F.; Bellucci, G. V.; Ribeiro, L. R.; Assis, M.

Funding acquisition: Gouveia, A. F.; Bellucci, G. V.; Ribeiro, L. R.; Assis, M.; Rosa, I. L. V.; Longo, E.; Andrés, J.; San-Miguel, M. A.

Investigation: Gouveia, A. F.; Bellucci, G. V.; Ribeiro, L. R.; Assis, M.; Rosa, I. L. V.; Longo, E.; Andrés, J.; San-Miguel, M. A.

Methodology: Gouveia, A. F.; Bellucci, G. V.; Ribeiro, L. R.; Assis, M.

Project administration: Gouveia, A. F.; Ribeiro, L. R.; Longo, E.; Andrés, J.; San-Miguel, M. A.

Resources: Gouveia, A. F.; Longo, E.; Andrés, J.; San-Miguel, M. A.

Software: Gouveia, A. F.; Andrés, J.; San-Miguel, M. A.

Supervision: I. L. V.; Longo, E.; Andrés, J.; San-Miguel, M. A.

Validation: Gouveia, A. F.; Bellucci, G. V.; Ribeiro, L. R.; Assis, M.; Rosa, I. L. V.; Longo, E.; Andrés, J.; San-Miguel, M. A.

Visualization: Gouveia, A. F.; Bellucci, G. V.; Ribeiro, L. R.; Assis, M.; Rosa, I. L. V.; Longo, E.; Andrés, J.; San-Miguel, M. A.

Writing – original draft: Gouveia, A. F.; Ribeiro, L. R.

Writing – review & editing: Gouveia, A. F.; Ribeiro, L. R.; Longo, E.; Andrés, J.; San-Miguel, M. A.

Data availability statement

The data will be available upon request. All data sets were generated or analyzed in the current study.

Funding

Fundação de Amparo à Pesquisa do Estado de São Paulo (FAPESP), <https://doi.org/10.13039/501100001807>. Grant No: 2013/07296-2; 2016/23891-6; 2017/26105-4; 2019/01732-1.

Financiadora de Estudos e Projetos, <https://doi.org/10.13039/501100004809>.

Conselho Nacional de Desenvolvimento Científico e Tecnológico (CNPq), <https://doi.org/10.13039/501100003593>. Grant No: 166281/2017-4; 305792/2020-2.

Generalitat Valenciana, <https://doi.org/10.13039/501100003359>. Grant No: BEST/2021/048.

Acknowledgments

This work used computational resources of the “Centro Nacional de Processamento de Alto Desempenho em São Paulo” (CENAPAD-SP), “Centro de Computação John David Rogers” (CCJDR-UNICAMP), and the CENAPAD-RJ (SDumont) and used experimental resources from Centro de Desenvolvimento de Materiais Funcionais (CDMF). A.F.G acknowledges the Universitat Jaume I for the postdoctoral contract (POSDOC/2019/30), FAPESP for the postdoctoral fellowship and Generalitat Valenciana for the exterior research grant. J.A. acknowledges Universitat Jaume I (project UJI-B2019-30), and the Ministerio de Ciencia, Innovación y Universidades (Spain) (project PGC2018094417-B-I00) for financially supporting this research.

References

- Andrés, J.; Gracia, L.; Gouveia, A. F.; Ferrer, M. M.; Longo, E. Effects of surface stability on the morphological transformation of metals and metal oxides as investigated by first-principles calculations. *Nanotechnology* **2015**, *26* (40), 405703. <https://doi.org/10.1088/0957-4484/26/40/405703>
- Becke, A. D. Density-Functional Exchange-Energy Approximation with Correct Asymptotic-Behavior. *Phys. Rev. A* **1988**, *38*, 3098–3100. <https://doi.org/10.1103/PhysRevA.38.3098>
- Becke, A. D. Density-Functional Thermochemistry .3. The Role of Exact Exchange. *J. Chem. Phys.* **1993**, *98*, 5648–5652. <https://doi.org/10.1063/1.464913>
- Chankhanittha, T.; Somaudon, V.; Watcharakitti, J.; Nanan, S. Solar light-driven photocatalyst based on bismuth molybdate (Bi₄MoO₉) for detoxification of anionic azo dyes in wastewater. *J. Mater. Sci.: Mater. Electron.* **2021**, *32*, 1977–1991. <https://doi.org/10.1007/s10854-020-04965-5>
- Christofilos, D.; Arvanitidis, J.; Kampasakali, E.; Papagelis, K.; Ves, S.; Kourouklis, G. A. High pressure Raman study of BaMoO₄. *Phys. Status Solidi B* **2004**, *241* (14), 3155–3160. <https://doi.org/10.1002/pssb.200405234>
- Dovesi, R.; Saunders, V. R.; Roetti, C.; Orlando, R.; Zicovich-Wilson, C. M.; Pascale, F.; Civalleri, B.; Doll, K.; Harrison, N. M.; Bush, I. J.; D'Arco, P.; Llunel, M.; Causà, M.; Noël, Y.; Maschio, L.; Erba, A.; Rerat, M.; Casassa, S. *CRYSTAL17 User's Manual*; University of Torino, 2017.
- Dovesi, R.; Erba, A.; Orlando, R.; Zicovich-Wilson, C. M.; Civalleri, B.; Maschio, L.; Rerat, M.; Casassa, S.; Baima, J.; Salustro, S.; Kirtman, B. Quantum-mechanical condensed matter simulations with CRYSTAL. *Wiley Interdiscip. Rev. Comput. Mol. Sci.* **2018**, *8* (4), e1360. <https://doi.org/10.1002/wcms.1360>
- Farahpour, M.; Arvand, M. Single-pot hydrothermal synthesis of copper molybdate nanosheet arrays as electrode materials for high areal-capacitance supercapacitor. *J. Energy Storage* **2021**, *40*, 102742. <https://doi.org/10.1016/j.est.2021.102742>
- Hu, X.; Jiang, S.; Fu, S.; Xie, J.; Zhong, L.; Chen, M.; Xiang, G.; Wang, Y.; Li, L.; Zhou, X. Opposite temperature luminescent behaviours of Tb³⁺ and Pr³⁺ co-doped BaMoO₄ glass ceramics for temperature sensing. *J. Lumin.* **2021**, *236*, 118080. <https://doi.org/10.1016/j.jlumin.2021.118080>
- Ji, T.; Ha, E.; Wu, M. Z.; Hu, X.; Wang, J.; Sun, Y. A.; Li, S. J.; Hu, J. Q. Controllable Hydrothermal Synthesis and Photocatalytic Performance of Bi₂MoO₆ Nano/Microstructures. *Catalysts* **2020**, *10*. <https://doi.org/10.3390/catal10101161>
- Keerthana, S. P.; Rani, B. J.; Yuvakkumar, R.; Ravi, G.; Shivatharsiny, Y.; Babu, E. S.; Almoallim, H. S.; Alharbi, S. A.; Velauthapillai, D. Copper molybdate nanoparticles for electrochemical water splitting application. *Int. J. Hydrogen Energy* **2021**, *46* (11), 7701–7711. <https://doi.org/10.1016/j.ijhydene.2020.12.029>
- Keshari, A. S.; Dubey, P. Rapid microwave-assisted vs. hydrothermal synthesis of hierarchical sheet-like NiO/NiMoO₄ hybrid nanostructures for high performance extrinsic pseudocapacitor application. *J. Energy Storage* **2021**, *40*, 102629. <https://doi.org/10.1016/j.est.2021.102629>
- Khan, A.; Daniel, J.; Tyagi, M.; Kim, H. J.; Lee, M. H.; Kim, Y. Czochralski growth, electronic structure, luminescence and scintillation properties of Cs₂Mo₃O₁₀: A new scintillation crystal for 0νββ decay search. *J. Alloys Compd.* **2020**, *821*, 153466. <https://doi.org/10.1016/j.jallcom.2019.153466>
- Kianpour, G.; Salavati-Niasari, M.; Emadi, H. Precipitation synthesis and characterization of cobalt molybdates nanostructures. *Superlattices Microstruct.* **2013**, *58*, 120–129. <https://doi.org/10.1016/j.spmi.2013.01.014>
- Kianpour, G.; Soofivand, F.; Badieli, M.; Salavati-Niasari, M.; Hamadani, M. Facile synthesis and characterization of nickel molybdate nanorods as an effective photocatalyst by co-precipitation method. *J. Mater. Sci.: Mater. Electron.* **2016**, *27*, 10244–10251. <https://doi.org/10.1007/s10854-016-5103-3>
- Kumar, V.; Chen, J.; Li, S.; Matz, S.; Bhavanasi, V.; Parida, K.; Al-Shamery, K.; Lee, P. S. Tri-rutile layered niobium-molybdates for all solid-state symmetric supercapacitors. *J. Mater. Chem. A* **2020**, *8* (38), 20141–20150. <https://doi.org/10.1039/D0TA03678A>
- Lakhlifi, H.; El Jabbar, Y.; El Ouati, R.; Er-Rakho, L.; Durand, B.; Guillemet-Fritsch, S. Synthesis of molybdates

- Zn_{1-x}Co_xMoO₄ (0 ≤ x ≤ 1), by decomposition of the precursors developed by the glycine-nitrate process (GNP), and their characterization. *Mater. Sci. Semicon. Proc.* **2020**, *114*, 105054. <https://doi.org/10.1016/j.mssp.2020.105054>
- Luo, Z.; Li, H.; Shu, H.; Wang, K.; Xia, J.; Yan, Y. Synthesis of BaMoO₄ Nestlike Nanostructures Under a New Growth Mechanism. *Cryst. Growth Des.* **2008**, *8* (7), 2275–2281. <https://doi.org/10.1021/cg700967y>
- Luo, Y.-S.; Dai, X.-J.; Zhang, W.-D.; Yang, Y.; Sun, C. Q.; Fu, S.-Y. Controllable synthesis and luminescent properties of novel erythrocyte-like CaMoO₄ hierarchical nanostructures via a simple surfactant-free hydrothermal route. *Dalton Trans.* **2010**, *39* (9), 2226–2231. <https://doi.org/10.1039/B915099D>
- Macedo, N. G.; Gouveia, A. F.; Roca, R. A.; Assis, M.; Gracia, L.; Andrés, J.; Leite, E. R.; Longo, E. Surfactant-Mediated Morphology and Photocatalytic Activity of α-Ag₂WO₄ Material. *J. Phys. Chem. C* **2018**, *122* (15), 8667–8679. <https://doi.org/10.1021/acs.jpcc.8b01898>
- Oliveira, M. C.; Gracia, L.; Nogueira, I. C.; Gurgel, M. F. C.; Mercury, J. M. R.; Longo, E.; Andres, J. On the morphology of BaMoO₄ crystals: A theoretical and experimental approach. *Cryst. Res. Technol.* **2016**, *51* (10), 634–644. <https://doi.org/10.1002/crat.201600227>
- Oliveira, F. K. F.; Santiago, A. A. G.; Catto, A. C.; Silva, L. F.; Tranquilin, R. L.; Longo, E.; Motta, F. V.; Bomio, M. R. D. Cerium molybdate nanocrystals: Microstructural, optical and gas-sensing properties. *J. Alloys Compd.* **2021**, *857*, 157562. <https://doi.org/10.1016/j.jallcom.2020.157562>
- Panchal, V.; Garg, N.; Sharma, S. M. Raman and x-ray diffraction investigations on BaMoO₄ under high pressures. *J. Phys.: Condens. Matter* **2006**, *18* (16), 3917. <https://doi.org/10.1088/0953-8984/18/16/002>
- Pereira, W. S.; Sczancoski, J. C.; Longo, E. Tailoring the photoluminescence of BaMoO₄ and BaWO₄ hierarchical architectures via precipitation induced by a fast precursor injection. *Mater. Lett.* **2021**, *293*, 129681. <https://doi.org/10.1016/j.matlet.2021.129681>
- Ray, S. K.; Dhakal, D.; Regmi, C.; Yamaguchi, T.; Lee, S. W. Inactivation of *Staphylococcus aureus* in visible light by morphology tuned α-NiMoO₄. *J. Photochem. Photobiol. A* **2018**, *350*, 59–68. <https://doi.org/10.1016/j.jphotochem.2017.09.042>
- Sczancoski, J. C.; Cavalcante, L. S.; Marana, N. L.; Silva, R. O.; Tranquilin, R. L.; Joya, M. R.; Pizani, P. S.; Varela, J. A.; Sambrano, J. R.; Li, M. S.; Longo, E.; Andres, J. *Curr. Appl. Phys.* **2010**, *10* (2), 614–624. <https://doi.org/10.1016/j.cap.2009.08.006>
- Silva Junior, J. L.; Nobre, F. X.; Freitas, F. A.; Carvalho, T. A. F.; Barros, S. S.; Nascimento, M. C.; Manzato, L.; Matos, J. M. E.; Brito, W. R.; Leyet, Y.; Couceiro, P. R. C. Copper molybdate synthesized by sonochemistry route at room temperature as an efficient solid catalyst for esterification of oleic acid. *Ultrason. Sonochem.* **2021**, *73*, 105541. <https://doi.org/10.1016/j.ultsonch.2021.105541>
- Silva, M. V.; Oliveira, D. F. M.; Oliveira, H. S.; Siqueira, K. P. F. Influence of temperature on the structural and color properties of nickel molybdates. *Mater. Res. Bull.* **2020**, *122*, 110665. <https://doi.org/10.1016/j.materresbull.2019.110665>
- Skutina, L.; Filonova, E.; Medvedev, D.; Maignan, A. Undoped Sr₂MMoO₆ Double Perovskite Molybdates (M = Ni, Mg, Fe) as Promising Anode Materials for Solid Oxide Fuel Cells. *Materials* **2021**, *14* (7), 1715. <https://doi.org/10.3390/ma14071715>
- Spassky, D.; Ivanov, S.; Kitaeva, I.; Kolobanov, V.; Mikhailin, V.; Ivleva, L.; Voronina, I. Optical and luminescent properties of a series of molybdate single crystals of scheelite crystal structure. *Phys. Status Solidi C* **2005**, *2* (1), 65–68. <https://doi.org/10.1002/pssc.200460112>
- Tang, C.; Wang, H.; Hong, Y.; Xu, W.; Shi, Q.; Liu, Z. Roughness induced wettability amplification of novel copper molybdate-branched CuO nanorod arrays by non-aqueous solution method. *Mater. Lett.* **2021**, *300*, 130260. <https://doi.org/10.1016/j.matlet.2021.130260>
- Theiss, F. L.; Ayoko, G. A.; Frost, R. L. Synthesis of layered double hydroxides containing Mg²⁺, Zn²⁺, Ca²⁺ and Al³⁺ layer cations by co-precipitation methods—A review. *Appl. Surf. Sci.* **2016**, *383*, 200–213. <https://doi.org/10.1016/j.apsusc.2016.04.150>
- Wood, D. L.; Tauc, J. Weak Absorption Tails in Amorphous Semiconductors. *Phys. Rev. B* **1972**, *5*, 3144. <https://doi.org/10.1103/PhysRevB.5.3144>
- Wulff, G. XXV. Zur Frage der Geschwindigkeit des Wachstums und der Auflösung der Krystallflächen. *Zeitschrift für Kristallographie - Crystalline Materials* **1901**, *34* (1–6). <https://doi.org/10.1524/zkri.1901.34.1.449>
- Xia, Z.; Chen, D. Synthesis and Luminescence Properties of BaMoO₄:Sm³⁺ Phosphors. *J. Am. Ceram. Soc.* **2010**, *93* (5), 1397–1401. <https://doi.org/10.1111/j.1551-2916.2009.03574.x>

Luminescence and structural properties of $\text{Ca}_{1-x}\text{ZrO}_3:\text{Eu}_x$: An experimental and theoretical approach

Marcelo Assis^{1,2+}, Marisa Carvalho de Oliveira¹, Amanda Fernandes Gouveia^{2,3}, Lara Kelly Ribeiro^{1,2}, Ieda Lucia Viana Rosa¹, Renan Augusto Pontes Ribeiro⁴, Juan Manuel Andrés Bort², Elson Longo¹

1. Federal University of São Carlos, Center for the Development of Functional Materials, São Carlos, Brazil.
2. University Jaume I, Department of Physical and Analytical Chemistry, Castelló, Spain.
3. State University of Campinas, Institute of Chemistry, Campinas, Brazil.
4. State University of Minas Gerais, Department of Chemistry, Divinópolis, Brazil.

+Corresponding author: Marcelo Assis, **Phone:** +55 19997347439 **Email address:** marcelostassis@gmail.com

ARTICLE INFO

Article history:

Received: July 29, 2021

Accepted: November 10, 2021

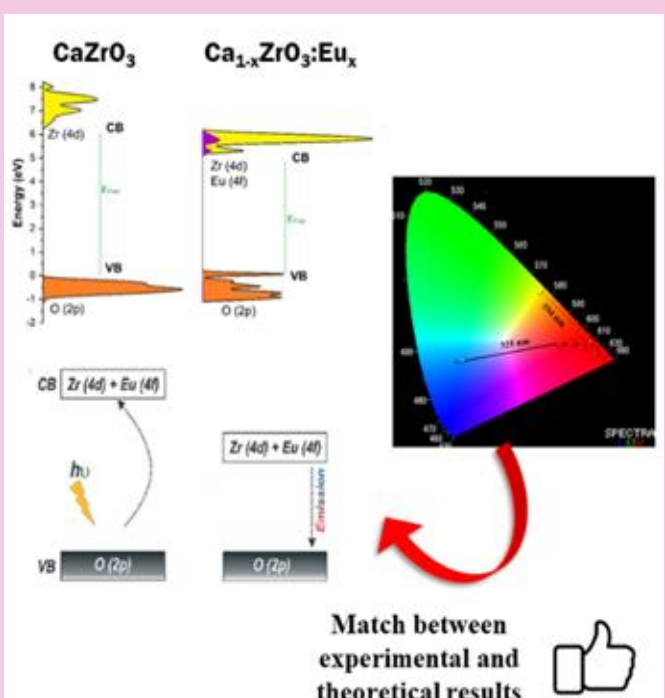
Published: April 11, 2022

Keywords:

1. perovskites
2. europium
3. phosphors
4. DFT

Section Editors: Elson Longo and Juan Manuel Andrés Bort

ABSTRACT: The influence of Eu^{3+} cations in the host matrix of CaZrO_3 was investigated by analyzing its luminescence and structural properties. The $\text{Ca}_{1-x}\text{ZrO}_3:\text{Eu}_x$ crystals ($x = 0.01, 0.02, 0.04,$ and 0.08 mol%) were obtained by a simple sol-gel method followed by a soft thermal treatment without any surfactant. The structural characterization was performed at short-, medium- and long-distance to verify the effect of the dopant in the host matrix. To endorse the experimental results, first-principles calculations were performed by using the CRYSTAL program associated with the density functional theory. The luminescence profile of the sample was investigated by analyzing the excitation and emission spectrum monitoring the emission at 614 nm and excited at 394 nm, noting that the sample Eu-doped with 0.08 mol% has greater emission intensity. The color variations of the characteristic emissions of $\text{Ca}_{1-x}\text{ZrO}_3:\text{Eu}_x$ crystals were evaluated according to the Commission Internationale de L'Éclairage, observing a red shift for all Eu-doped samples. A general luminescence scheme was proposed combining the density of state and the band structure calculations.



1. Introduction

The chemical and thermal stability of materials with perovskites structure (ABO_3), such as $CaZrO_3$ (CZ), have attracted a lot of attention to be used as a host matrix for rare earth cations, thus obtaining efficient phosphors with superior luminescent activity (T. Almeida *et al.*, 2021; Holzapfel *et al.*, 2020; Khan *et al.*, 2020; Kunti *et al.*, 2021; Tian *et al.*, 2020). Their properties were associated to their structural arrangement, electronic structure and the possibility to control the doping sites (A or B) (Fukushima *et al.*, 2020; Navami *et al.*, 2020). The crystalline lattice of the CZ is composed by distorted $[ZrO_6]$ and $[CaO_8]$ clusters, in which the Zr atoms are coordinated by six O atoms in an octahedral symmetry, while the Ca atoms are surrounded by eight O atoms (Eglitis *et al.*, 2020; Zeba *et al.*, 2020).

Rare earth cations can create new defects in the forbidden region of the band gap, modifying the electronic properties that reflect in the charge transfers process and, consequently, in the optical properties (Al Boukhari *et al.*, 2020; Chu *et al.*, 2020). In this way, Eu^{3+} cations have a special role for obtaining efficient red phosphors, luminescent devices and lasers, for example, from the doping of several distinct semiconductor host matrices (P. Kumar *et al.*, 2021; Mazzo *et al.*, 2010; 2014; Ortega *et al.*, 2019; Pinatti *et al.*, 2015). The applications of Eu^{3+} cations are mainly related to its nondegenerate 7F_0 ground state and nonoverlapping ${}^{2S+1}L_J$ multiplets (Targonska *et al.*, 2019). These cations are sensitive to the symmetry of the local doping site and, as a consequence, can be used to identify changes in the chemical environment (Song *et al.*, 2010; J. Zhang *et al.*, 2020). These advantages come from its electronic configuration which also results in a pure and strong luminescence in the red region when excited in the ultraviolet (UV) region of the electromagnetic spectrum (Saif and Abdel-Mottaleb, 2007; Smith *et al.*, 2019; Tymiński *et al.*, 2020). These materials have too several advantages like high Stoke displacement, defined spectrum, long lifetime and high stability (Bai *et al.*, 2013; Lahtinen *et al.*, 2016; van der Ziel and van Uiert, 1969; Zhou *et al.*, 2021).

The $Ca_{1-x}ZrO_3:Eu_x$ (CZE) samples were studied in some previously published papers (Fukushima *et al.*, 2020; Katyayan *et al.*, 2017; S. Kumar *et al.*, 2018; Shimokawa *et al.*, 2015; Tiwari *et al.*, 2015; H. Zhang *et al.*, 2008). The method of obtaining these materials typically employ high-temperature strategies, such as sol-gel combustion method and solid-state reaction, that use temperatures above 1200 °C to not obtain secondary phases with ZrO_2 and nonstoichiometric oxides of Ca

and Zr (Dubey and Tiwari, 2016; Khan *et al.*, 2021; Kunti *et al.*, 2021). These high temperatures also help to form a symmetrical chemical environment for the Eu^{3+} cations, increasing their luminescent emission and their lifetime decay (Fukushima *et al.*, 2020; Shimokawa *et al.*, 2015). Our research group is engaged in the investigation of the doping process with Eu^{3+} cations in different semiconductors (Fernandes *et al.*, 2018; Lovisa *et al.*, 2016; Pinatti *et al.*, 2019), in particular, CZ and CZE samples were previously obtained in another experimental works (André *et al.*, 2014; Oliveira *et al.*, 2017; 2018; Rosa *et al.*, 2015).

As a continuation of this research line, in this joint experimental and theoretical work, we reported the excitation-induced tunable photoluminescence (PL) properties of CZE, at different Eu^{3+} cations concentration (0.01, 0.02, 0.04, and 0.08 mol% named as CZE1, CZE2, CWZ4, and CZE8, respectively). The samples were prepared by a simple sol-gel method followed by a soft thermal treatment (600 °C) without any surfactant. This methodology enabled them to be promising materials in inorganic single-emitting component regions for optical applications. In addition, first-principles quantum-mechanical calculations, at the density functional theory (DFT) level, have been used to study and predict the structure and the PL, which would promote the development of CZE based phosphors.

2. Experimental procedures and computational details

Synthesis: CZ and CZE samples were prepared by the sol-gel method. The starting reagents used were calcium chloride dihydrate ($CaCl_2 \cdot 2H_2O$, 99%, Synth), zirconium oxychloride (IV) octahydrate ($ZrOCl_2 \cdot 8H_2O$, 99.5%, Sigma-Aldrich), europium oxide (Eu_2O_3 , 99%, Sigma-Aldrich), ethylene glycol ($C_2H_6O_2$, 99.9%, J. T. Baker), and citric acid monohydrate ($C_6H_8O_7 \cdot H_2O$, 99.5%, J. T. Baker). The first step of the CZ synthesis consists in the zirconium citrate's preparation. For this, 1×10^{-3} mol of $ZrOCl_2 \cdot 8H_2O$ was added to 25 mL (2.5×10^{-5} mol L^{-1}) of distilled water and add 12×10^{-3} mol of citric acid was added to the solution at 60 °C under stirring. After this process, 1×10^{-3} mol of $CaCl_2 \cdot 2H_2O$ was added to this zirconium citrate. During the previous processes, the solution was kept under N_2 bubbling to avoid the formation of unwanted phases, such as ZrO_2 and nonstoichiometric oxides of Ca and Zr. Then, ethylene glycol (in the proportion 60:40 in relation to the mass of citric acid) was added to the solution and the N_2 bubbling was removed. The temperature of the solution was changed to 80 °C to evaporate the resulting water

and to form a resin. This resin was sent to the oven, undergoing three subsequent thermal processes, 110 °C/1 h, 250 °C/1 h and 400 °C/1 h. The resulting powder was taken to calcination at 600 °C for 1 h, obtaining a final white powder. For CZE samples, an identical process was performed, changing only that an acid solution of Eu^{3+} cations was added to the zirconium citrate before the $\text{CaCl}_2 \cdot 2\text{H}_2\text{O}$. The amount of mass of Eu^{3+} cations to obtain the replacement of Ca^{2+} by Eu^{3+} cations were carried out respecting the purity of the reagents as well as the charge balance.

Characterizations: The CZ and CZE samples were characterized by X-ray diffraction (XRD) with a Rigaku DMax 2500PC ($\text{Cu K}\alpha \lambda = 1.5406 \text{ \AA}$). Element analysis of the samples was performed with a XRF 720 Shimadzu (4 kV and 80 mA). Micro-Raman spectroscopy were performed by the iHR550 spectrometer (Horiba Jobin-Yvon) coupled to a silicon CCD detector and an argon-ion laser (Melles Griot, 514.5 nm, 200 mW). Diffuse reflectance spectroscopy (DRS) measurements were performed using a Varian Cary spectrometer model 5G in the diffuse reflectance mode, with a wavelength range of 300 to 800 nm and a scan speed of 600 nm min^{-1} . Photoluminescence measurements at room temperature were performed using a 500MSpex spectrometer coupled to a GaAs photomultiplier tube (GaAs PMT). A Kimmon He-Cd laser (325 nm laser; 40mW maximum power) was used as the excitation source for PL measurements. The Fluorolog Jobin-Yvon Fluorolog III spectrofluorometer, under excitation of a xenon lamp was used to obtain the emission (394 nm) and excitation (614 nm) spectra as well the decay lifetime.

Computational details: Computational methods and theoretical procedures were utilized to study the bulk properties of CZ and CZE structures. Calculations were carried out using the periodic ab initio CRYSTAL17 package, (Dovesi *et al.*, 2018) based on DFT using the B3LYP hybrid functional (Becke, 1993; Lee *et al.*, 1988). In all calculations, the atomic centers were described by the standard all-electron basis set for the Zr, Ca and O atoms, consisting of (9s)-(7631sp)-(621d), (8s)-(6511sp)-(21d), (8s)-(411sp)-(1d), respectively. Basis sets for Zr, Ca and O were taken from references (De La Pierre *et al.*, 2014; Valenzano *et al.*, 2011), whereas an effective core potential (ECP) pseudopotential, with 11 valence electrons described by (5s5p4d)/[3s3p3d] (VTZ quality) basis sets, was used for the trivalent Eu atom. According to the f-in-core approximation, the electrons of the 4f shell of Eu^{3+} are incorporated in the pseudopotential (Oliveira *et al.*, 2018).

Atomic positions and unit cell parameters were fully relaxed with respect to the total energy of the system for both CZ and CZE models. The convergence criteria for mono- and bielectronic integrals were set to 10^{-8} Hartree, while the RMS gradient, RMS displacement, maximum gradient, and maximum displacement were set to 3.0×10^{-4} , 1.2×10^{-3} , 4.5×10^{-4} , and 1.8×10^{-3} a.u., respectively. Regarding density matrix diagonalization, the reciprocal space net was described by a dense mesh consisting of a shrinking factor set to $4 \times 4 \times 4$ in the Monkhorst-Pack method (Monkhorst and Pack, 1976). The accuracy of the evaluation of the Coulomb and exchange series was controlled by five thresholds, whose adopted values were 10^{-8} , 10^{-8} , 10^{-8} , 10^{-8} (ITOL1 to ITOL4), and 10^{-14} (ITOL5).

Herein, the CZ model was calculated considering the conventional unit cell with orthorhombic symmetry (*Pcmm*) containing 20 atoms. A supercell ($2 \times 1 \times 2$) expansion simulated the crystalline structure of the CZE model, containing 79-atoms, where two Eu^{3+} cations replaced two Ca^{2+} cations leading to the creation of one Ca^{2+} vacancy to neutralize the charges corresponding to a doping concentration of 12.5%. The neutrality in CZE model can be described as $\text{CaZrO}_3 + \text{Eu(III)} \rightarrow \text{Ca}_{0.8125}\text{Eu}_{0.125}\text{ZrO}_3(\text{V}_{\text{Ca}})$, where V_{Ca} represents a calcium vacancy. It is worth to mention that such charge compensation mechanism is commonly used to investigate rare-earth doping in perovskites (Kunti *et al.*, 2021).

A schematic representation in terms of component clusters, the cation replacement and vacancy formation mechanisms associated with the doping process, and the crystalline structure of CZ and CZE models are illustrated in Fig. 1. Here, it is important to point out that Eu-doping configurational tests were carried out to select the most favorable sites for Eu-doping.

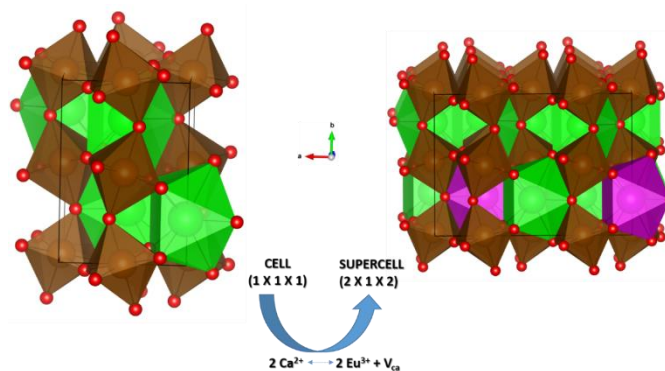


Figure 1. Schematic representation of unit cell expansion and Eu doping in CZ matrix models constructed for DFT calculations. $[\text{ZrO}_6]$, $[\text{CaO}_8]$ and

[EuO₈] clusters in brown, green, and purple colors, respectively.

3. Results and Discussion

In order to understand the modifications generated at long-range in the CZ and CZE samples, XRD diffractograms were performed. XRD shows that all materials have similar profiles linked to the orthorhombic CZ structure (Fig. 2a), according to card

No. 97463 in the *Inorganic Crystal Structure Database* (ICSD) (Levin *et al.*, 2003). The orthorhombic CaZrO₃ structure belongs to the space group *Pcmn*, being formed by distorted [CaO₈] and [ZrO₆] clusters. There was no secondary phase formation, indicating that the Eu³⁺ cations substitution process takes places successfully. For comparison, the theoretical lattice parameters and the unit cell volume calculated at the B3LYP level of theory were listed in Tab. 1.

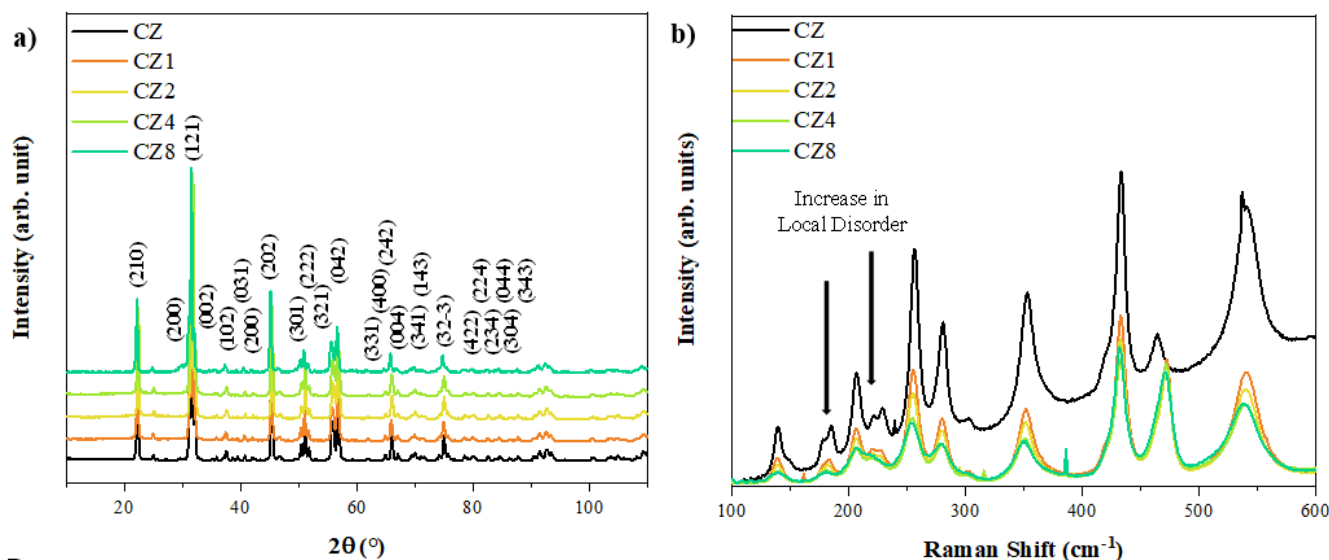


Figure 2. (a) X-ray diffraction and (b) micro-Raman spectra for CZ and CZE samples.

Table 1. Lattice parameters and unit cell volume of CZ and CZE obtained by theoretical simulations and ICSD values.

Sample	Cell Volume	Lattice Parameters		
		$\alpha = \beta = \gamma = 90^\circ$ (<i>Pcmn</i>)		
	Å ³	a (Å)	b (Å)	c (Å)
CZ	258.52	5.594	8.021	5.7611
CZE (12.5%)*	1063.72	11.322	8.069	11.641
ICSD 97463	257.45	5.583	8.007	5.759

*Corresponds to 2×1×2 conventional cells.

An analysis of the results shows that the substitution of Ca²⁺ by Eu³⁺ cations induce variations in the atomic coordinates of the O atoms, indicating the existence of structural and electronic distortions in the [CaO₈], [ZrO₆], and [EuO₈] clusters, as well as changes in the lattice parameters and an expansion of cell parameters of ~2.86% is found in the unit cell volume.

Complementing the XRD analysis, micro-Raman measurements were performed to analyze the short-range modifications caused by the substitution of Eu³⁺ cations in the CZ structure (Fig. 2b). There are 13 active modes in the Raman spectrum, which are related to specific vibrations of the [ZrO₆] clusters (André *et al.*,

2014; Evangeline *et al.*, 2017; Rosa *et al.*, 2015; Zheng *et al.*, 2004). For the CZE samples, it was observed with the increase in the concentration of Eu³⁺ cations, there is a loss of definition in the modes located at 177, 184, 205, 221, and 229 cm⁻¹. This is due to the increase in local disorder caused by the propagation of distortions of [EuO₈] clusters in the CZ structure.

The average crystallite size (D) obtained through the Scherrer's equation (Eqs. 1 and 2) and the lattice strain (ϵ) (Eq. 3) value are shown in Tab. 2.

$$D = \frac{0.89\lambda}{(\beta \cos\theta)} \quad (1)$$

$$\beta = \sqrt{\beta_{obs}^2 - \beta_{st}^2} \quad (2)$$

$$\epsilon = \frac{\beta}{(4 \tan\theta)} \quad (3)$$

where D is the average crystallite size, λ is the X-ray wavelength (0.15406 nm), θ is the Bragg angle, β_{obs} is the experimental full width at half maximum (FWHM)

of the sample, and β_{st} is the FWHM of LaB₆ standard (Muniz *et al.*, 2016). These parameters, D and ε , were also obtained by the Williamson-Hall (WH) plot obtained through Eq. 4:

$$\frac{\beta \cos \theta}{\lambda} = \frac{K}{D} + \frac{4\varepsilon}{\lambda} \sin \theta \quad (4)$$

where β is the FWHM of the peak, D is the crystallite size, λ is the 0.154056 nm, K is 0.89, and ε is the lattice strain (Manohar *et al.*, 2021; Mesquita *et al.*, 2021).

For the CZE samples, a tendency to decrease the D value is observed in reference to the CZ sample. This

behavior is due to the low concentrations of the rare earth that can inhibit the growth of CZ crystallite (El-Bahy *et al.*, 2009; Jayachandriah *et al.*, 2015). In general, the doping process induces a structural and electronic strain in the crystalline lattice, evidenced by the increase in the ε value (W. Liu *et al.*, 2017). To confirm the amount of Eu³⁺ cations in the CZE samples (spectral line La, energy 5.849 keV), X-ray fluorescence (XRF) measurements (S4 Pioneer, Bruker) were performed (Tab. 2). It is observed that the real concentration Eu³⁺ cation is very close to the nominal one, confirming the replacement of Ca²⁺ by Eu³⁺ cations.

Table 2. Crystallite size (D) and lattice strain (ε) obtained by Scherrer's equation and Williamson-Hall model, and Eu concentration obtained by XRF analysis.

Sample	Scherrer		Williamson-Hall		[Eu] (%)	
	D (nm)	ε (10 ⁻³)	D (nm)	ε (10 ⁻³)	Nominal	Real
CZ	31.72	16.98	24.30	18.82	0.0000	0.0000
CZE1	31.58	13.81	20.91	32.53	0.0010	0.0008
CZE2	31.64	30.76	23.76	30.09	0.0020	0.0018
CZE4	31.68	34.93	31.48	16.44	0.0040	0.0041
CZE8	31.42	56.64	17.98	34.07	0.0080	0.0077

The band gap energy (E_{gap}) value was obtained through the Kulbelka-Munk (Yang and Kruse, 2004) calculation for CZ and CZE samples. The E_{gap} values of the samples were 5.75, 5.66, 5.62, 5.60, and 5.35 eV for the samples CZ, CZE1, CZE2, CZE4, and CZE8, respectively. The E_{gap} value obtained for the CZ sample is close to the value obtained in previous works (Maurya

et al., 2016; Yamaguchi *et al.*, 2000; Zeba *et al.*, 2020). This decrease occurs because the incorporation of Eu³⁺ cations in the CZ structure causes new defects and intermediate levels close to the valence (VB) and conduction (CB) bands, which leads to a decrease in E_{gap} (Cyriac *et al.*, 2018; Gupta *et al.*, 2015a).

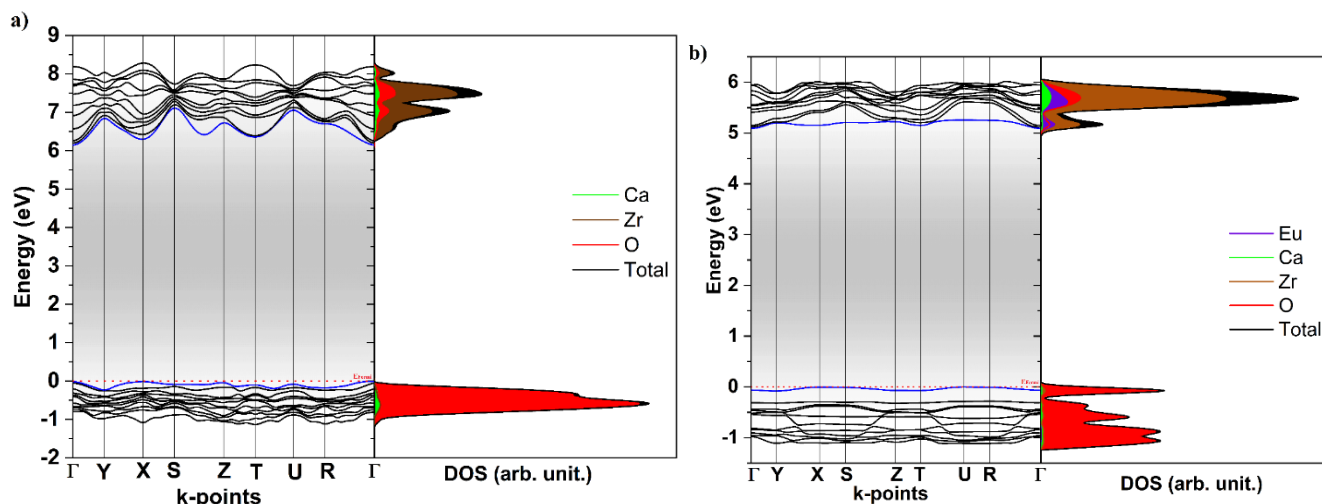


Figure 3. Band structure and DOS profiles for (a) CZ, and (b) CZE materials.

The calculated band structure and density of states (DOS) projected for the atoms and orbitals of CZ and CZE models are displayed in Fig. 3. An analysis of the band structure and projected DOS presented here reveals that the direct transition is produced along the k-

points Γ - Γ (000 to 000) and U- Γ (101 to 000) from the top of the VB to the bottom of the CB of pure and doped models, respectively. The E_{gap} values is 6.23 eV to CZ and 5.09 eV to CZE 12.5% model. As regard the

obtained E_{gap} values, experimental and theoretical values were compared evidencing a good agreement.

An analysis of the DOS, the main contribution to the valence band maximum (VBM) region is due to the $2p$ (p_x , p_y , and p_z), orbitals from the O atoms and a predominance of the $4d$ (d_z^2 , $d_{x^2-y^2}$, d_{xy} , d_{xz} , d_{yz}) and $4f$ (f^8 , f_{xz}^2 , f_{yz}^2 , $f_{z(x^2-y^2)}$, f_{xyz} , $f_{x(x^2-3y^2)}$, $f_{y(3x^2-y^2)}$) states formed by Zr and Eu atoms is found in the conduction band minimum (CBM) region, situated from 6.23 to 9 eV

(CZ) and from 5.09 to 6.5 eV (CZE 12.5%) and with a small contribution from Ca orbitals.

Additionally, the Fig. 4 summarizes the electronic density maps of the CZ and CZE (12.5%) models obtained from the optimized wavefunction, where the electronic density matrix was resolved as isolines that describe the density in an area. These electronic density maps were described along the Ca–O, Zr–O, and Eu–O bonds direction of the models, which corresponds more specifically to the diagonal (110) plane (Fig. 4).

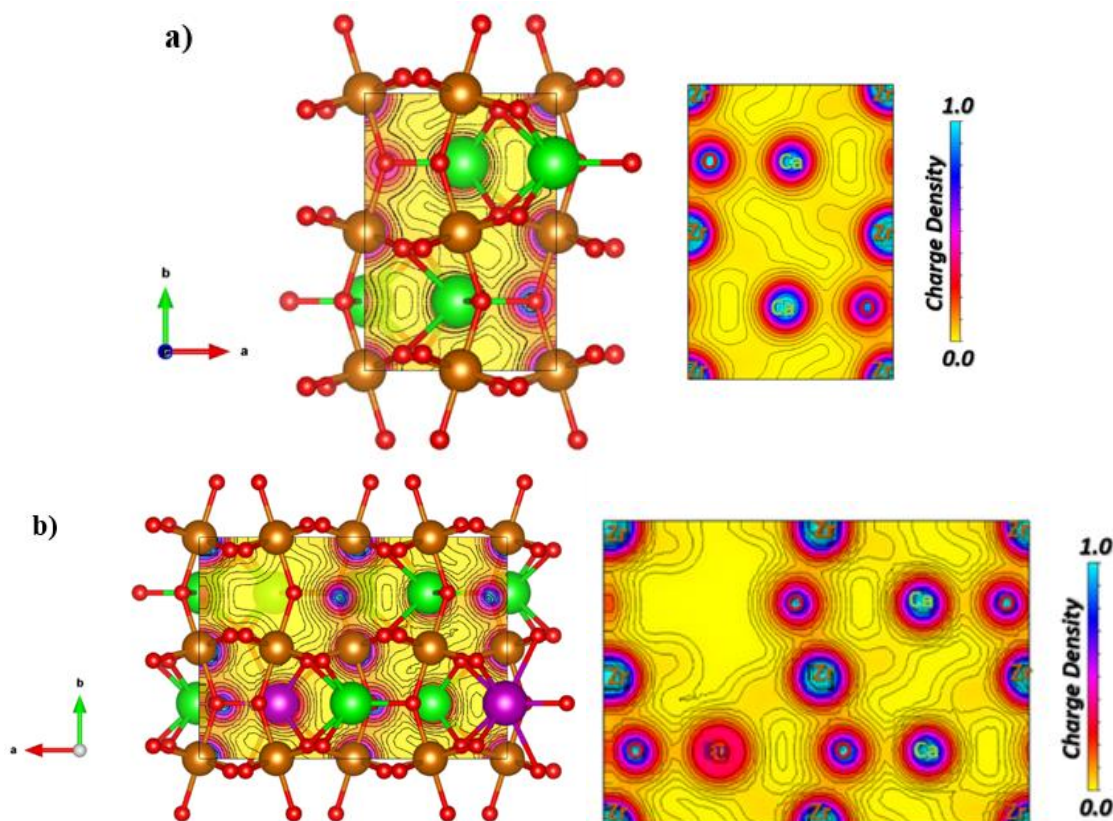


Figure 4. Electron density maps in the diagonal plane (110) for (a) CZ, and (b) CZE materials.

To observe the possible application of CZE samples as a red emitter, the samples were first excited with a laser at 325 nm (Fig. 5). The CZ sample has a broadband emission profile, characteristic of a multiphonic process, involving several intermediate energy states (Gupta *et al.*, 2015b). The maximum emission of the CZ sample is found in approximately 447 nm, in the blue region, which is the result of internal charge transfers of O $2p$ to Zr $4d$ orbitals (Oliveira *et al.*, 2017). For CZE samples, the broadband emission characteristic of the CZ sample is no longer observed, giving space to the specific emission of Eu^{3+} cations. The characteristic emission

bands of the Eu^{3+} cations are located at 584, 596, 615, 659, and 705 nm can be assigned to the transitions $^5\text{D}_0 \rightarrow ^7\text{F}_J$, $J = 0, 1, 2, 3$, and 4, respectively (D'Achille *et al.*, 2021; Gnanam *et al.*, 2021; M. Liu *et al.*, 2021; Riul *et al.* 2021). The intensity of the CZE samples is proportional to the concentration of Eu^{3+} cations, being the CZE1 sample the least intense and CZE8 sample the most intense. The maximum emission of CZE samples was attributed to the $^5\text{D}_0 \rightarrow ^7\text{F}_2$ transitions (615 nm). The appearance of these transitions confirms the CZ structure as a good host matrix for sensitizing the red emission of Eu^{3+} cations.

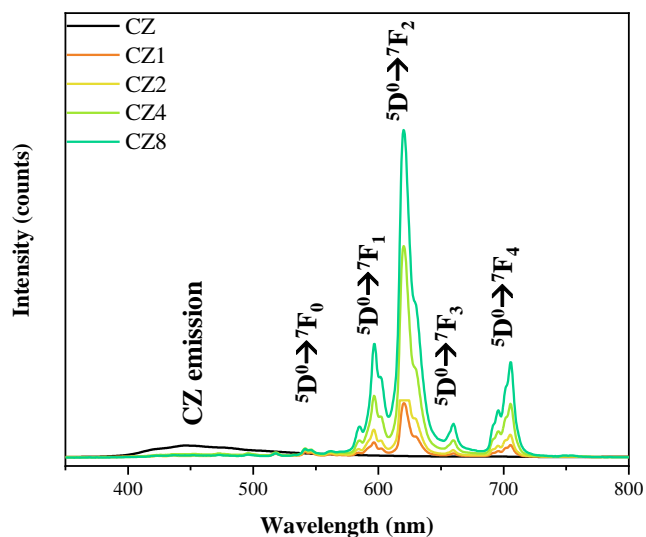


Figure 5. Emission spectra of CZ, and CZE materials excited at 325 nm.

Figure 6a shows the excitation spectra of CZE samples under 614 nm emission band. At 280 nm a broad band related to the CZ matrix is observed. According to Dorenbos (2003), this emission related to the charge transfer band (CTB) of O^{2-} to Eu^{3+} . It is also observed the emissions referring to the transitions of the Eu^{3+} cations for CZE samples. These transitions are ${}^7D_0 \rightarrow {}^5D_J$ ($J = 2, 3$ and 4), ${}^7F_0 \rightarrow {}^5L_J$ ($J = 6, 7$ and 8) and ${}^7F_0 \rightarrow {}^5G_J$ ($J = 4, 5$ and 6) (Vieira *et al.*, 2019). The most intense is located at 394 nm referring to the ${}^7F_0 \rightarrow {}^5L_6$ transition. This transition in specific is useful for applications in near-UV and LEDs (Hou *et al.*, 2012; Singh *et al.*, 2021). The emission spectra of CZE samples excited at 394 nm was shown in Fig. 6b. It is observed that the transitions ${}^5D_0 \rightarrow {}^7F_J$, $J = 0, 1, 2, 3$, and 4 , become more defined, locating at 565, 592, 616, 655, and 703 nm (Chen *et al.*, 2000; X. Liu *et al.*, 2007; Song *et al.*, 2010). The red emission at 616 nm is due to the ${}^5D_0 \rightarrow {}^7F_2$ electric-dipole transition that is parity forbidden and hypersensitive by the crystalline field (Baig *et al.*, 2021; Bharathi *et al.*, 2021; Wu *et al.*, 2021). The ${}^5D_0 \rightarrow {}^7F_1$ magnetic-dipole transition is located at 592 nm it is not affected by the environment (Kalu *et al.*, 2021; Lakde *et al.*, 2021; Peipei *et al.*, 2021). So, the integrated area ratio of the peaks corresponding to ${}^5D_0 \rightarrow {}^7F_2$ and ${}^5D_0 \rightarrow {}^7F_1$ transitions provides information on the changes in the environment around the Eu^{3+} cations (Parchur and Ningthoujam, 2012). The values obtained for the samples are 4.92, 4.91, 4.81, and 4.66 for the samples CZE1, CZE2, CZE4, and CZE8. These values are very close and indicate that the Eu^{3+} environment changes to a higher symmetry site with the increase in the concentration of

Eu^{3+} cations, since the ratio of the relative areas decreases with the increase of the Eu -doping. (P. Almeida *et al.*, 2021; Mazzo *et al.*, 2010; Pinatti *et al.*, 2015).

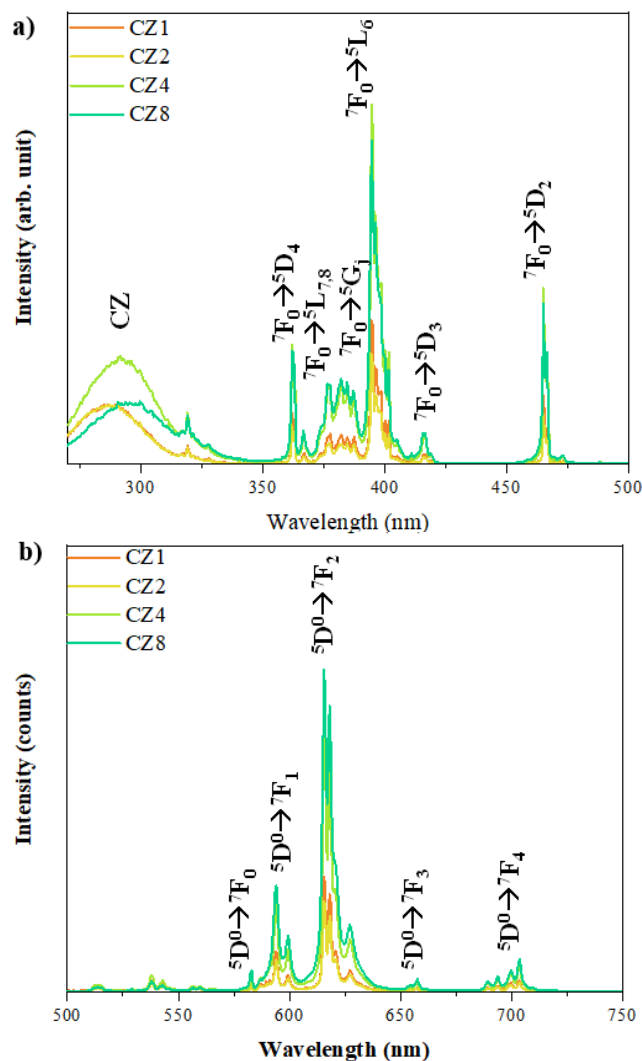


Figure 6. (a) Excitation and (b) emission spectrum of CZE samples monitoring the emission at 614 nm and excited at 394 nm, respectively.

Figure 7a depicts the decay behavior of the ${}^5D_0 \rightarrow {}^7F_2$ transition for Eu^{3+} cations in the CZE samples, using the emission and excitation wavelengths fixed at 614 and 394 nm, respectively (He *et al.*, 2018; Parchur *et al.*, 2011). These life times were fitted using a monoexponential function (Eq. 5):

$$y = y_0 + A_1 \exp\left(-\frac{t}{\tau}\right) \quad (5)$$

where y is the intensity; y_0 is the intensity at the 0 ms; A_1 is the amplitude and τ is the lifetime of the ${}^5D_0 \rightarrow {}^7F_2$ transition (Nyein *et al.*, 2003).

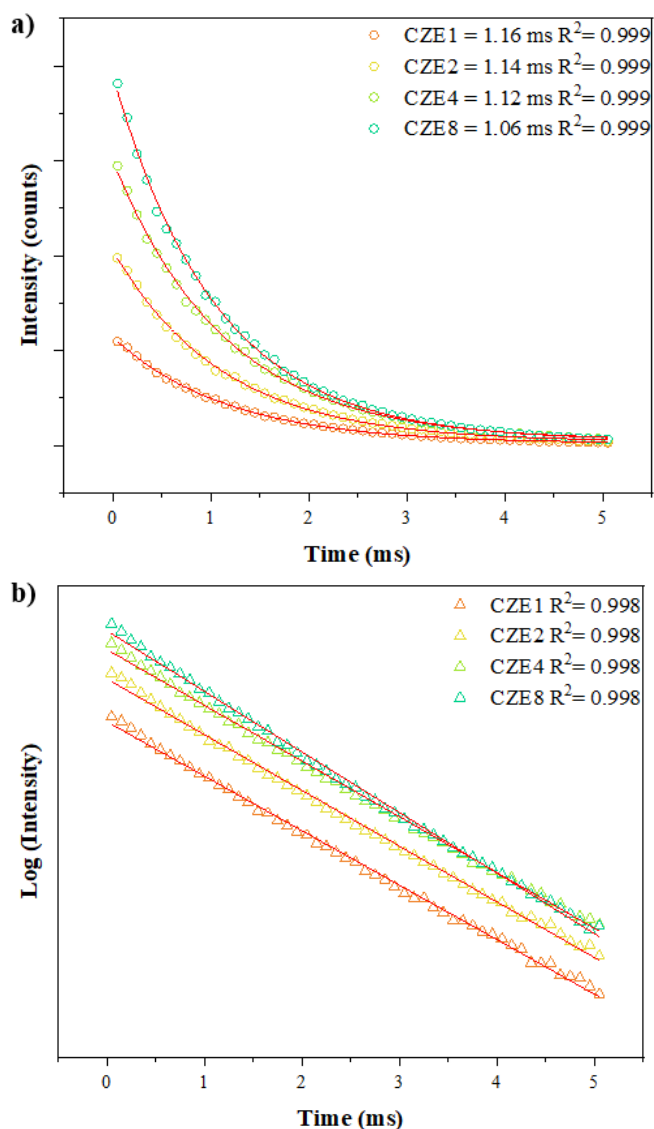


Figure 7. (a) Decay curves and (b) Log of the decay curves ${}^5D_0 \rightarrow {}^7F_2$ transition of CZE samples.

Excited state τ values determined were 1.16, 1.14, 1.12, and 1.06 ms to CZE1, CZE2, CZE4, and CZE8, respectively. The excited state τ values of Eu^{3+} cations decreased with increasing doping concentration due the exchange interactions between activated ions pairs and the higher concentration of the activated ions density around quenching center. Figure 7b shows the monoexponential decay of the samples fitted with an exponential function as the Eq. 5. The energy transfer rate between Eu^{3+} – Eu^{3+} (η_{Eu-Eu}) was calculated by the Eq. 6:

$$\eta_{Eu-Eu} = 1 - \frac{\tau_{CZE}}{\tau_{CZEH}} \quad (6)$$

where τ_{CZE} is the lifetime of CZE samples and τ_{CZEH} is the lifetime of the sample with higher τ (in this case, 1.16 ms to CZE1) (Kunti *et al.*, 2021).

The obtained η_{Eu-Eu} values were 1.72, 3.44 and 8.62, for CZE2, CZE4 and CZE8, respectively. The distance between Eu^{3+} cations decrease with increasing concentration of these cations in the CZ host matrix, causing an energy transfer more efficient and allowing new decay channels (Kunti *et al.*, 2021). These extra channels provide new radiative and nonradiative transition probabilities decreasing the lifetime (İlhan and Keskin, 2018). The efficiency of energy transfer (η_{ET}) (Eq. 7):

$$\eta_{ET} = 1 - \frac{\tau_{CZE}}{\tau_{CZ}} \quad (7)$$

where τ_{CZE} is the lifetime of CZE samples and τ_{CZ} is the lifetime of the CZ sample (2.57 in this case) (Li *et al.*, 2007).

The obtained η_{ET} values were 0.5486, 0.5564, 0.5642, and 0.5875 for the CZE1, CZE2, CZE4, and CZE8, respectively. As expected, the energy transfer efficiency (η_{ET}) goes hand in hand with the increase in the concentration of Eu^{3+} cations.

Figure 8 shows the color variations of the characteristic emissions of the samples according to the Commission Internationale de L'Éclairage (CIE) (Du *et al.*, 2013). As a characteristic emission, for the CZ sample its emission in blue region is observed at 325 and yellow at 394 nm. However, for the CZE samples, with the increase in the amount of Eu^{3+} cations in the CZ host matrix, a displacement towards the red region is observed, reaching almost pure red emission in both excitations.

In addition, theoretical methodology can contribute to an explanation for the optical properties, since a reduction in the band gap value and the PL emissions of CZ and CZE models. In order to clarify the effect of Eu^{3+} cations on the PL emissions of CZ, it was proposed a general scheme combining the DOS and band structure calculations for CZ and CZE models, as shown in Fig. 9.

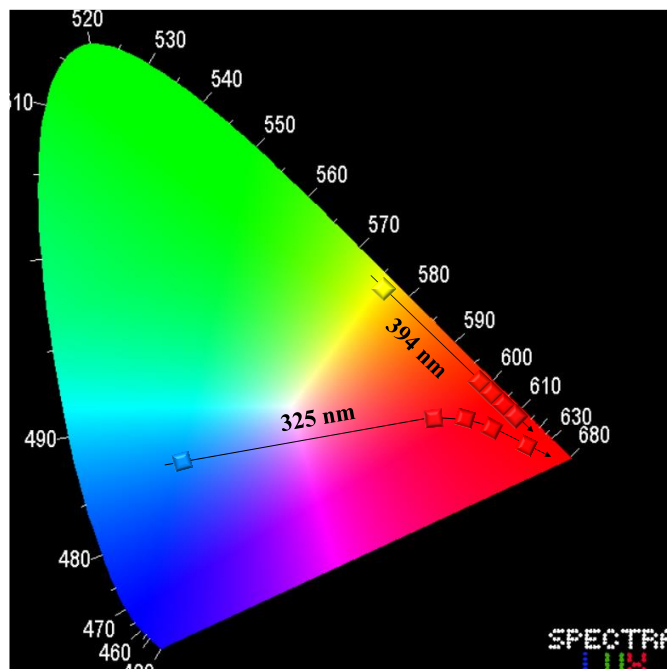


Figure 8. CIE coordinates of CZ and CZE samples excited at 325 and 394 nm.

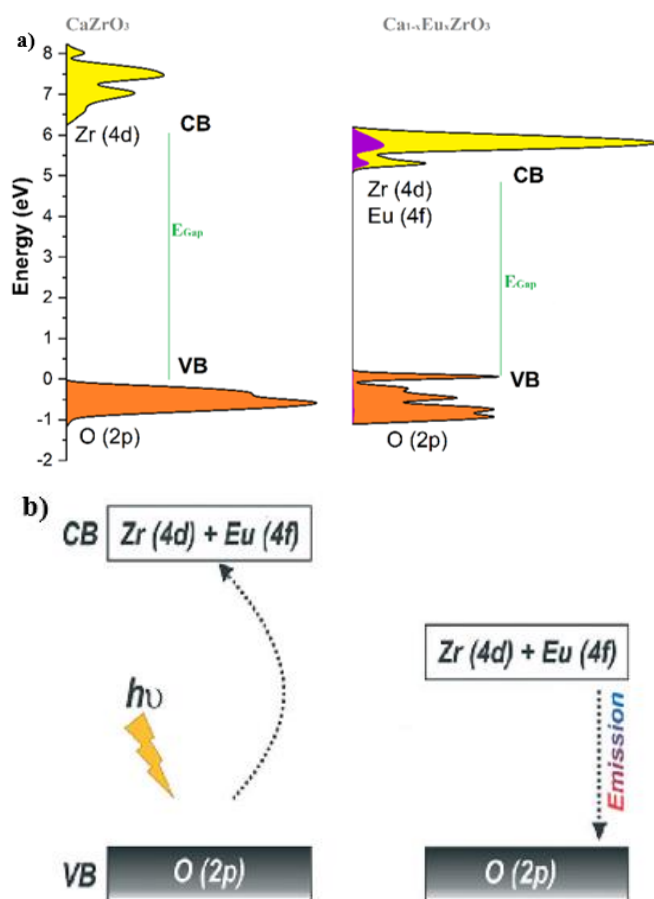


Figure 9. Scheme representing (a) the electronic structure for pure CZ and CZE materials; (b)

photoinduced electron transfer mechanism from the VB to the CB to light emission.

Doping with Eu^{3+} cations generate a new electron density distribution, being located on the oxygen-mediated $[\text{EuO}_8]-[\text{ZrO}_6]$ interaction, to which is trapped in empty Zr (4d) and Eu (4f) orbitals. Initially, the Eu^{3+} cations doping process induces the formation of V_{Ca} sites that perturb the VB energy levels and promotes the insertion of 4f orbitals in the CBM; in other words, intermediate energy levels are introduced in the E_{gap} region, reducing the energy required for electron transfer (Fig. 9a). The next step is the photoinduced electron transfer from the VB to the CB, generating an electron-hole pair within the CZE electronic structure (Fig. 9b). This step is crucial because it offers a new interpretation of the optical properties of a material.

In addition, a deeper insight into the PL emission of pure and Eu-doped structures, based on the effective mass of electrons (m_e^*) and holes (m_h^*), following the procedure reported in a previous study is presented in Tab. 3 (Silva *et al.*, 2020). Such an approach is effective in discussing the photoinduced properties of solid-state materials once the effective mass allows one to ascertain the mobility of the charge carriers.

Table 3. Calculated effective mass of electrons (m_e^*) and holes (m_h^*) of CZ and CZE 12.5%.

Effective mass of electrons and holes CZ		
m_e^*	m_h^*	m_e^*/m_h^*
0.31	2.46	0.126
Effective mass of electrons and holes CZE		
m_e^*	m_h^*	m_e^*/m_h^*
0.49	0.94	0.516

The calculated values reported in Tab. 3 for CZ and CZE indicates that excited electrons are lighter than generated holes. Also, it was observed that Eu-doping induces a heavier (lighter) electron (hole) effective mass in comparison to CZ, increasing the hole mobility that contributes to increase the electron-hole recombination rate, explaining the superior PL properties of CZE. This fact can be associated with the bonding character of Eu-O interactions in comparison to Ca-O summed to the presence of V_{Ca} in the doped crystalline structure due to the electron density redistribution that governs the band gap narrowing for doped samples, as confirmed in Fig. 9. Once the Eu-O bonds are more covalent than Ca-O, the band curvature is affected, and the effective mass of electrons and holes is controlled from doping.

4. Conclusions

In this paper, a simple sol-gel method followed by a soft thermal treatment without any surfactant was applied to investigate the influence of Eu^{3+} cations in the host matrix of CZ. The $\text{Ca}_{1-x}\text{ZrO}_3:\text{Eu}_x$ crystals ($x = 0.01, 0.02, 0.04, \text{ and } 0.08 \text{ mol}\%$) were characterized by XRD and the patterns confirms that the Eu-doped samples present an orthorhombic structure as the CZ pure. However, the results shows that the replacement of Ca^{2+} by Eu^{3+} cations induce local defects in the lattice causing distortions in the $[\text{CaO}_8]$, $[\text{ZrO}_6]$, and $[\text{EuO}_8]$ clusters, as well as changes in the lattice parameters and an expansion of cell parameters. The micro-Raman results disclosure that the presence of Eu^{3+} cations in the host matrix of CZ caused a loss of definition in the modes located at 177, 184, 205, 221, and 229 cm^{-1} due to the increase in local disorder. The real amount of Eu^{3+} cations in the CZE samples was verified by XRF and the results confirms the presence of Eu^{3+} cations in the host matrix. The substitution of Ca^{2+} by Eu^{3+} cations also affected the E_{gap} value in which a decrease with the increase of Eu^{3+} cations amount in the host matrix was observed, and this result was endorsed by the first-principles calculations. According to the DOS analysis, the electronic density in the VBM is due to the O $2p$ orbitals and a predominance of the Zr $4d$ and Eu $4f$ orbitals is observed in the CBM. The luminescence profile of the sample was investigated, and the results show that the intensity of the CZE samples is proportional to the concentration of Eu^{3+} cations, being the CZE1 sample the least intense and CZE8 the most intense. The appearance of the ${}^5\text{D}_0 \rightarrow {}^7\text{F}_2$ transitions (615 nm) confirms that the CaZrO_3 structure is a good host matrix for sensitizing the red emission of Eu^{3+} cations. From the experimental and theoretical results, it was proposed a general luminescence scheme for the CZE samples.

Authors' contribution

Conceptualization: Assis, M.; Oliveira, M. C.; Gouveia, A. F.; Ribeiro, R. A. P.

Data curation: Assis, M.; Ribeiro, R. A. P.; Bort, J. M. A.; Longo, E.

Formal Analysis: Assis, M.; Oliveira, M. C.; Gouveia, A. F.; Ribeiro, L. K.; Ribeiro, R. A. P.

Funding acquisition: Rosa, I. L. V.; Ribeiro, R. A. P.; Bort, J. M. A.; Longo, E.

Investigation: Assis, M.; Oliveira, M. C.; Gouveia, A. F.; Ribeiro, L. K.; Ribeiro, R. A. P.

Methodology: Assis, M.; Oliveira, M. C.

Project administration: Bort, J. M. A.; Longo, E.

Resources: Rosa, I. L. V.; Ribeiro, R. A. P.; Bort, J. M. A.; Longo, E.

Software: Oliveira, M. C.; Gouveia, A. F.; Ribeiro, R. A. P.; Bort, J. M. A.

Supervision: Rosa, I. L. V.; Ribeiro, R. A. P.; Bort, J. M. A.; Longo, E.

Validation: Assis, M.; Oliveira, M. C.; Gouveia, A. F.; Ribeiro, R. A. P.

Visualization: Assis, M.; Oliveira, M. C.; Gouveia, A. F.; Ribeiro, R. A. P.

Writing – original draft: Assis, M.; Oliveira, M. C.; Gouveia, A. F.; Ribeiro, L. K.; Ribeiro, R. A. P.

Writing – review & editing: Assis, M.; Oliveira, M. C.; Gouveia, A. F.; Ribeiro, L. K.; Ribeiro, R. A. P.

Data availability statement

The data will be available upon request.

Funding

Fundação de Amparo à Pesquisa do Estado de São Paulo (FAPESP). Grant No: 2013/07296-2; 2019/01732-1.

Universitat Jaume I. Project: UJI-B2019-30.

Acknowledgments

The authors acknowledge the support of institutes: CDMF (Centro de Desenvolvimento de Materiais Funcionais), Universidade Federal de São Carlos/FAPESP and Universitat Jaume I. M.A. was supported by the Margarita Salas postdoctoral contract MGS/2021/21(UP2021-021) financed by the European Union-NextGenerationEU. J.A. acknowledges Universitat Jaume I (project UJI-B2019-30), the Generalitat Valenciana (Project AICO/2020/329), and the Ministerio de Ciencia, Innovación y Universidades (Spain) (project PGC2018094417-B-I00) for financially supporting this research. A.F.G acknowledges the Universitat Jaume I for the postdoctoral contract (POSDOC/2019/30).

References

Al Boukhari, J.; Khalaf, A.; Hassan, R. S.; Awad, R. Structural, optical and magnetic properties of pure and rare earth-doped NiO nanoparticles. *Appl. Phys. A* **2020**, *126*, 323. <https://doi.org/10.1007/s00339-020-03508-3>

Almeida, P. B.; Pinatti, I. M.; de Oliveira, R. C.; Teixeira, M. M.; Santos, C. C.; Machado, T. R.; Longo, E.; Rosa, I. L. V.

- Structural, morphological and photoluminescence properties of β - Ag_2MoO_4 doped with Eu^{3+} . *Chem. Pap.* **2021**, *75*, 1869–1882. <https://doi.org/10.1007/s11696-020-01489-4>
- Almeida, T. H.; Almeida, D. H.; Gonçalves, D.; Lahr, F. A. R. Color variations in CIELAB coordinates for softwoods and hardwoods under the influence of artificial and natural weathering. *J. Build. Eng.* **2021**, *35* (3), 101965. <https://doi.org/10.1016/j.jobte.2020.101965>
- André, R. S.; Zanetti, S. M.; Varela, J. A.; Longo, E. Synthesis by a chemical method and characterization of CaZrO_3 powders: Potential application as humidity sensors. *Ceram. Int.* **2014**, *40* (10) (Part B), 16627–16634. <https://doi.org/10.1016/j.ceramint.2014.08.023>
- Bai, J.-M.; Zhang, L.; Liang, R.-P.; Qiu, J.-D. Graphene Quantum Dots Combined with Europium Ions as Photoluminescent Probes for Phosphate Sensing. *Chem. – A Eur. J.* **2013**, *19* (12), 3822–3826. <https://doi.org/10.1002/chem.201204295>
- Baig, N.; Kadam, A. R.; Dubey, K.; Dhoble, N. S.; Dhoble, S. J. Wet chemically synthesized $\text{Na}_3\text{Ca}_2(\text{SO}_4)_3\text{Cl:RE}^{3+}$ (RE = Ce, Dy, Eu) phosphors for solid-state lighting. *Radiat. Eff. Defects Solids* **2021**, *176* (5–6), 493–507. <https://doi.org/10.1080/10420150.2021.1871735>
- Becke, A. D. Density-functional thermochemistry. III. The role of exact exchange. *J. Chem. Phys.* **1993**, *98*, 5648. <https://doi.org/10.1063/1.464913>
- Bharathi, N. V.; Jeyakumar, T.; Ramaswamy, S.; Jayabalakrishnan, S. S. Synthesis and characterization of a Eu^{3+} -activated $\text{Ba}_{2-x}\text{V}_2\text{O}_7:x\text{Eu}^{3+}$ phosphor using a hydrothermal method: a potential material for near-UV-WLED applications. *Luminescence* **2021**, *36* (4), 849–859. <https://doi.org/10.1002/bio.4031>
- Chen, W.; Malm, J.-O.; Zwiller, V.; Huang, Y.; Liu, S.; Wallenberg, R.; Bovin, J.-O.; Samuelson, L. Energy structure and fluorescence of Eu^{2+} in ZnS:Eu nanoparticles. *Phys. Rev. B* **2000**, *61*, 11021. <https://doi.org/10.1103/PhysRevB.61.11021>
- Chu, H.; Yao, D.; Chen, J.; Yu, M.; Su, L. Double-Emission Ratiometric Fluorescent Sensors Composed of Rare-Earth-Doped ZnS Quantum Dots for Hg^{2+} Detection. *ACS Omega* **2020**, *5* (16), 9558–9565. <https://doi.org/10.1021/acsomega.0c00861>
- Cyriac, J.; Mathew, S.; Augustine, S.; Nambissan, P. M. G. Defects characterization studies of europium-substituted bismuth ferrite nanocrystals by positron annihilation and other methods. *J. Phys. D: Appl. Phys.* **2018**, *51* (43), 435303. <https://doi.org/10.1088/1361-6463/aadfa7>
- D'Achille, A. E.; Wallace, R. M.; Coffey, J. L. Morphology-dependent fluorescence of europium-doped cerium oxide nanomaterials. *Nanoscale Adv.* **2021**, *3* (12), 3563–3572. <https://doi.org/10.1039/D1NA00096A>
- De La Pierre, M.; Carteret, C.; Maschio, L.; André, E.; Orlando, R.; Dovesi, R. The Raman spectrum of CaCO_3 polymorphs calcite and aragonite: A combined experimental and computational study. *J. Chem. Phys.* **2014**, *140* (16), 164509. <https://doi.org/10.1063/1.4871900>
- Dorenbos, P. Systematic behaviour in trivalent lanthanide charge transfer energies. *J. Phys Condens. Matter* **2003**, *15* (49), 8417. <https://doi.org/10.1088/0953-8984/15/49/018>
- Dovesi, R.; Erba, A.; Orlando, R.; Zicovich-Wilson, C. M.; Civalieri, B.; Maschio, L.; Rérat, M.; Casassa, S.; Baima, J.; Salustro, S.; Kirtman, B. Quantum-mechanical condensed matter simulations with CRYSTAL. *Wiley Interdiscip. Rev. Comput. Mol. Sci.* **2018**, *8* (4), e1360. <https://doi.org/10.1002/wcms.1360>
- Du, Q.; Zhou, G.; Zhou, J.; Zhou, H. Combustion synthesis and photoluminescence properties of $\text{CaZrO}_3:\text{Eu}^{3+}$ with highly enhanced brightness by Li^+ doping. *J. Lumin.* **2013**, *137*, 83–87. <https://doi.org/10.1016/j.jlumin.2012.12.046>
- Dubey, V.; Tiwari, N. Structural and optical analysis on europium doped AZrO_3 (A = Ba, Ca, Sr) phosphor for display devices application. *AIP Conf. Proc.* **2016**, *1728*, 020002. <https://doi.org/10.1063/1.4946052>
- Eglitis, R. I.; Purans, J.; Gabrusenoks, J.; Popov, A. I.; Jia, R. Comparative Ab Initio Calculations of ReO_3 , SrZrO_3 , BaZrO_3 , PbZrO_3 and CaZrO_3 (001) Surfaces. *Crystals* **2020**, *10* (9), 745. <https://doi.org/10.3390/cryst10090745>
- El-Bahy, Z. M.; Ismail, A. A.; Mohamed, R. M. Enhancement of titania by doping rare earth for photodegradation of organic dye (Direct Blue). *J. Hazard. Mater.* **2009**, *166* (1), 138–143. <https://doi.org/10.1016/j.jhazmat.2008.11.022>
- Evangelina, B.; Azeem, P. A.; Prasada Rao, R.; Swati, G.; Haranath, D. Structural and luminescent features of cerium doped CaZrO_3 blue nanophosphors. *J. Alloys Compd.* **2017**, *705*, 618–623. <https://doi.org/10.1016/j.jallcom.2016.11.115>
- Fernandes, S. L.; Gasparotto, G.; Teixeira, G. F.; Cebim, M. A.; Longo, E.; Zaghete, M. A. Lithium lanthanum titanate perovskite ionic conductor: Influence of europium doping on structural and optical properties. *Ceram. Int.* **2018**, *44* (17), 21578–21584. <https://doi.org/10.1016/j.ceramint.2018.08.221>
- Fukushima, H.; Nakauchi, D.; Kato, T.; Kawaguchi, N.; Yanagida, T. Scintillation and luminescence properties of undoped and europium-doped CaZrO_3 crystals. *J. Lumin.* **2020**, *223*, 117231. <https://doi.org/10.1016/j.jlumin.2020.117231>
- Gnanam, S.; Gajendiran, J.; Ramya, J. R.; Ramachandran, K.;

- Raj, S. G. Glycine-assisted hydrothermal synthesis of pure and europium doped CeO₂ nanoparticles and their structural, optical, photoluminescence, photocatalytic and antibacterial properties. *Chem. Phys. Lett.* **2021**, 763, 138217. <https://doi.org/10.1016/j.cplett.2020.138217>
- Gupta, S. K.; Ghosh, P. S.; Sudarshan, K.; Gupta, R.; Pujari, P. K.; Kadam, R. M. Multifunctional pure and Eu³⁺ doped β-Ag₂MoO₄: photoluminescence, energy transfer dynamics and defect induced properties. *Dalton Trans.* **2015a**, 44 (44), 19097–19110. <https://doi.org/10.1039/C5DT03113C>
- Gupta, S. K.; Ghosh, P. S.; Pathak, N.; Tewari, R. Nature of defects in blue light emitting CaZrO₃: Spectroscopic and theoretical study. *RSC Adv.* **2015b**, 5 (70), 56526–56533. <https://doi.org/10.1039/C5RA09637E>
- He, C.; Ji, H.; Huang, Z.; Zhang, X.; Liu, H.; Liu, S.; Liu, Y.; Fang, M.; Wu, X.; Min, X. Preparation and photoluminescence properties of red-emitting phosphor ZnAl₂O₄:Eu³⁺ with an intense ⁵D₀ → ⁷F₀ transition. *Mater. Res. Express* **2018**, 5 (2), 025501. <https://doi.org/10.1088/2053-1591/aaa7c9>
- Holzappel, N. P.; Majher, J. D.; Strom, T. A.; Moore, C. E.; Woodward, P. M. Cs₄Cd_{1-x}Mn_xBi₂Cl₁₂—A Vacancy-Ordered Halide Perovskite Phosphor with High-Efficiency Orange-Red Emission. *Chem. Mater.* **2020**, 32 (8), 3510–3516. <https://doi.org/10.1021/acs.chemmater.0c00454>
- Hou, J.; Yin, X.; Fang, Y.; Huang, F.; Jiang, W. Novel red-emitting perovskite-type phosphor CaLa_{1-x}MgM'O₆: xEu³⁺ (M'=Nb, Ta) for white LED application. *Opt. Mater.* **2012**, 34 (8), 1394–1397. <https://doi.org/10.1016/j.optmat.2012.02.031>
- İlhan, M.; Keskin, İ. Ç. Photoluminescence, radioluminescence and thermoluminescence properties of Eu³⁺ doped cadmium tantalate phosphor. *Dalton Trans.* **2018**, 47 (39), 13939–13948. <https://doi.org/10.1039/C8DT02395F>
- Jayachandriah, C.; Kumar, K. S.; Krishnaiah, G.; Rao, N. M. Influence of Dy dopant on structural and photoluminescence of Dy-doped ZnO nanoparticles. *J. Alloys Compd.* **2015**, 623, 248–254. <https://doi.org/10.1016/j.jallcom.2014.10.067>
- Kalu, O.; Ahemen, I.; Esparza Ponce, H. E.; Moller, J. A. D.; Reyes-Rojas, A. Red-emission analysis, Judd–Ofelt intensity parameters and laser properties of CdMgZnO:xEu³⁺ nanocrystals: the effects of Eu³⁺ concentration. *J. Phys. D: Appl. Phys.* **2021**, 54, 345108. <https://doi.org/10.1088/1361-6463/ac021c>
- Katyayan, S.; Agrawal, S. Synthesis and Investigation of Structural and Optical Properties of Eu³⁺ Doped CaZrO₃ Phosphor. *Mater. Today Proc.* **2017**, 4 (8), 8016–8024. <https://doi.org/10.1016/j.matpr.2017.07.139>
- Khan, A.; Song, F.; Zhou, A.; Gao, X.; Feng, M.; Ikram, M.; Hu, H.; Sang, X.; Liu, L. Tuning white light upconversion emission from Yb³⁺/Er³⁺/Tm³⁺ triply doped CaZrO₃ by altering Tm³⁺ concentration and excitation power. *J. Alloys Compd.* **2020**, 835, 155286. <https://doi.org/10.1016/j.jallcom.2020.155286>
- Khan, A.; Song, F.; Gao, X.; Chen, Z.; Sang, X.; Feng, M.; Liu, L. Introduction of Molybdenum into the lattice of single-host CaZrO₃: Dy³⁺/Eu³⁺ to enhance luminescence intensity of the phosphor for white light emission. *J. Alloys Compd.* **2021**, 881, 160652. <https://doi.org/10.1016/j.jallcom.2021.160652>
- Kumar, S. G. P.; Krishna, R. H.; Kottam, N.; Murthy, P. K.; Manjunatha, C.; Preetham, R.; Shivakumara, C.; Thomas, T. Understanding the photoluminescence behaviour in nano CaZrO₃:Eu³⁺ pigments by Judd-Ofelt intensity parameters. *Dyes Pigm.* **2018**, 150, 306–314. <https://doi.org/10.1016/j.dyepig.2017.12.022>
- Kumar P. R.; Prasad, N.; Veillon, F.; Prellier, W. Raman spectroscopic and magnetic properties of Europium doped nickel oxide nanoparticles prepared by microwave-assisted hydrothermal method. *J. Alloys Compd.* **2021**, 858, 157639. <https://doi.org/10.1016/j.jallcom.2020.157639>
- Kunti, A. K.; Patra, N.; Harris, R. A.; Sharma, S. K.; Bhattacharyya, D.; Jha, S. N.; Swart, H. C. Structural properties and luminescence dynamics of CaZrO₃:Eu³⁺ phosphors. *Inorg. Chem. Front.* **2021**, 8 (3), 821–836. <https://doi.org/10.1039/D0QI01178A>
- Lahtinen, S.; Wang, Q.; Soukka, T. Long-Lifetime Luminescent Europium(III) Complex as an Acceptor in an Upconversion Resonance Energy Transfer Based Homogeneous Assay. *Anal. Chem.* **2016**, 88 (1), 653–658. <https://doi.org/10.1021/acs.analchem.5b02228>
- Lakde, J.; Mehare, C. M.; Pandey, K. K.; Dhoble, N. S.; Dhoble, S. J. Recent development of Eu³⁺-doped phosphor for white LED application: A review. *J. Phys. Conf. Ser.* **2021**, 1913, 012029. <https://doi.org/10.1088/1742-6596/1913/1/012029>
- Lee, C.; Yang, W.; Parr, R.G. Development of the Colle-Salvetti correlation-energy formula into a functional of the electron density. *Phys. Rev. B* **1988**, 37, 785. <https://doi.org/10.1103/PhysRevB.37.785>
- Levin, I.; Amos, T. G.; Bell, S. M.; Farber, L.; Vanderah, T. A.; Roth, R. S.; Toby, B. H. Phase equilibria, crystal structures, and dielectric anomaly in the BaZrO₃–CaZrO₃ system. *J. Solid State Chem.* **2003**, 175 (2), 170–181. [https://doi.org/10.1016/S0022-4596\(03\)00220-2](https://doi.org/10.1016/S0022-4596(03)00220-2)
- Li, Y.-C.; Chang, Y.-H.; Chang, Y.-S.; Lin, Y.-J.; Laing, C.-H. Luminescence and Energy Transfer Properties of Gd³⁺ and Tb³⁺ in LaAlGe₂O₇. *J. Phys. Chem. C* **2007**, 111 (28), 10682–10688. <https://doi.org/10.1021/jp0719107>

- Liu, X.; Lin, C.; Lin, J. White light emission from Eu^{3+} in CaIn_2O_4 host lattices. *Appl. Phys. Lett.* **2007**, *90*, 081904. <https://doi.org/10.1063/1.2539632>
- Liu, W.; Zhang, H.; Wang, H.-g.; Zhang, M.; Guo, M. Titanium mesh supported TiO_2 nanowire arrays/upconversion luminescence Er^{3+} - Yb^{3+} codoped TiO_2 nanoparticles novel composites for flexible dye-sensitized solar cells. *Appl. Surf. Sci.* **2017**, *422*, 304–315. <https://doi.org/10.1016/j.apsusc.2017.06.007>
- Liu, M.; Shu, M.; Yan, J.; Liu, X.; Wang, R.; Hou, Z.; Lin, J. Luminescent net-like inorganic scaffolds with europium-doped hydroxyapatite for enhanced bone reconstruction. *Nanoscale* **2021**, *13* (2), 1181–1194. <https://doi.org/10.1039/D0NR05608A>
- Lovisa, L. X.; Araújo, V. D.; Tranquilin, R. L.; Longo, E.; Li, M. S.; Paskocimas, C. A.; Bomio, M. R. D.; Motta, F. V. White photoluminescence emission from ZrO_2 co-doped with Eu^{3+} , Tb^{3+} and Tm^{3+} . *J. Alloys Compd.* **2016**, *674*, 245–251. <https://doi.org/10.1016/j.jallcom.2016.03.037>
- Manohar, A.; Krishnamoorthi, C.; Pavithra, C.; Thota, N. Magnetic Hyperthermia and Photocatalytic Properties of MnFe_2O_4 Nanoparticles Synthesized by Solvothermal Reflux Method. *J. Supercond. Nov. Magn.* **2021**, *34*, 251–259. <https://doi.org/10.1007/s10948-020-05685-x>
- Maurya, A.; Yadav, R. S.; Yadav, R. V.; Rai, S. B.; Bahadur, A. Enhanced green upconversion photoluminescence from $\text{Ho}^{3+}/\text{Yb}^{3+}$ co-doped CaZrO_3 phosphor via Mg^{2+} doping. *RSC Adv.* **2016**, *6* (114), 113469–113477. <https://doi.org/10.1039/C6RA23835A>
- Mazzo, T. M.; Moreira, M. L.; Pinatti, I. M.; Picon, F. C.; Leite, E. R.; Rosa, I. L. V.; Varela, J. A.; Perazolli, L. A.; Longo, E. $\text{CaTiO}_3:\text{Eu}^{3+}$ obtained by microwave assisted hydrothermal method: A photoluminescent approach. *Opt. Mater.* **2010**, *32*, 990–997. <https://doi.org/10.1016/j.optmat.2010.01.039>
- Mazzo, T. M.; Pinatti, I. M.; Macario, L. R.; Avansi Junior, W.; Moreira, M. L.; Rosa, I. L. V.; Mastelaro, V. R.; Varela, J. A.; Longo, E. Europium-doped calcium titanate: Optical and structural evaluations. *J. Alloys Compd.* **2014**, *585*, 154–162. <https://doi.org/10.1016/j.jallcom.2013.08.174>
- Mesquita, W. D.; Oliveira, M. C.; Assis, M.; Ribeiro, R. A. P.; Eduardo, A. C.; Teodoro, M. D.; Marques, G. E.; Godinho Júnior, M.; Longo, E.; Gurgel, M. F. C. Unraveling the relationship between bulk structure and exposed surfaces and its effect on the electronic structure and photoluminescent properties of $\text{Ba}_{0.5}\text{Sr}_{0.5}\text{TiO}_3$: A joint experimental and theoretical approach. *Mater. Res. Bull.* **2021**, *143*, 111442. <https://doi.org/10.1016/j.materresbull.2021.111442>
- Monkhorst, H. J.; Pack, J. D. Special points fro Brillouin-zone integrations. *Phys. Rev. B* **1976**, *13*, 5188–5192. <https://doi.org/10.1103/PhysRevB.13.5188>
- Muniz, F. T. L.; Miranda, M. A. R.; Santos, C. M.; Sasaki, J. M. The Scherrer equation and the dynamical theory of X-ray diffraction. *Acta Crystallogr.* **2016**, *A72*, 385–390. <https://doi.org/10.1107/S205327331600365X>
- Navami, D.; Darshan, G. P.; Basavaraj, R. B.; Sharma, S. C.; Kavyashree, D.; Venkatachalaiah, K. N.; Nagabhushana, H. Shape controllable ultrasound assisted fabrication of $\text{CaZrO}_3:\text{Dy}^{3+}$ hierarchical structures for display, dosimetry and advanced forensic applications. *J. Photochem. Photobiol. A Chem.* **2020**, *389*, 112248. <https://doi.org/10.1016/j.jphotochem.2019.112248>
- Nyein, E. E.; Hömmerich, U.; Heikenfeld, J.; Lee, D. S.; Steckl, A. J.; Zavada, J. M. Spectral and time-resolved photoluminescence studies of Eu-doped GaN. *Appl. Phys. Lett.* **2003**, *82*, 1655. <https://doi.org/10.1063/1.1560557>
- Oliveira, M. C.; Gracia, L.; Assis, M.; Rosa, I. L. V.; Gurgel, M. F. C.; Longo, E.; Andrés, J. Mechanism of photoluminescence in intrinsically disordered CaZrO_3 crystals: First principles modeling of the excited electronic states. *J. Alloys Compd.* **2017**, *722*, 981–995. <https://doi.org/10.1016/j.jallcom.2017.06.052>
- Oliveira, M. C.; Ribeiro, R. A. P.; Gracia, L.; Lazaro, S. R.; Assis, M.; Oliva, M.; Rosa, I. L. V.; Gurgel, M. F. C.; Longo, E.; Andrés, J. Experimental and theoretical study of the energetic, morphological, and photoluminescence properties of $\text{CaZrO}_3:\text{Eu}^{3+}$. *CrystEngComm* **2018**, *20* (37), 5519–5530. <https://doi.org/10.1039/C8CE00964C>
- Ortega, P. P.; Rocha, L. S. R.; Cortés, J. A.; Ramirez, M. A.; Buono, C.; Ponce, M. A.; Simões, A. Z. Towards carbon monoxide sensors based on europium doped cerium dioxide. *Appl. Surf. Sci.* **2019**, *464*, 692–699. <https://doi.org/10.1016/j.apsusc.2018.09.142>
- Parchur, A. K.; Ningthoujam, R. S.; Rai, S. B.; Okram, G. S.; Singh, R. A.; Tyagi, M.; Gadkari, S. C.; Tewari, R.; Vatsa, R. K. Luminescence properties of Eu^{3+} doped CaMoO_4 nanoparticles. *Dalton Trans.* **2011**, *40* (29), 7595–7601. <https://doi.org/10.1039/c1dt10878f>
- Parchur, A. K.; Ningthoujam, R. S. Behaviour of electric and magnetic dipole transitions of Eu^{3+} , $^5\text{D}_0 \rightarrow ^7\text{F}_0$ and Eu–O charge transfer band in Li^+ co-doped $\text{YPO}_4:\text{Eu}^{3+}$. *RSC Adv.* **2012**, *2* (29), 10859–10868. <https://doi.org/10.1039/C2RA22144F>
- Peipei, D.; Li, G.; Yun, X.; Zhang, Q.; Liu, D.; Lian, H.; Shang, M.; Lin, J. Thermally stable and highly efficient red-emitting Eu^{3+} -doped $\text{Cs}_3\text{GdGe}_3\text{O}_9$ phosphors for WLEDs: non-concentration quenching and negative thermal expansion. *Light Sci. Appl.* **2021**, *10*, 29. <https://doi.org/10.1038/s41377-021-00469-x>

- Pinatti, I. M.; Nogueira, I. C.; Pereira, W. S.; Pereira, P. F. S.; Gonçalves, R. F.; Varela, J. A.; Longo, E.; Rosa, I. L. V. Structural and photoluminescence properties of Eu³⁺ doped α -Ag₂WO₄ synthesized by the green coprecipitation methodology. *Dalton Trans.* **2015**, *44* (40), 17673–17685. <https://doi.org/10.1039/C5DT01997D>
- Pinatti, I. M.; Pereira, P. F. S.; Assis, M.; Longo, E.; Rosa, I. L. V. Rare earth doped silver tungstate for photoluminescent applications. *J. Alloys Compd.* **2019**, *771*, 433–447. <https://doi.org/10.1016/j.jallcom.2018.08.302>
- Riul, A.; Fonseca, F. A. A.; Pugina, R. S.; Caiut, J. M. A. Tuned structure of europium-doped Al₂O₃-yttrium luminescent composites and their spectroscopic behavior. *J. Lumin.* **2021**, *233*, 117925. <https://doi.org/10.1016/j.jlumin.2021.117925>
- Rosa, I. L. V.; Oliveira, M. C.; Assis, M.; Ferrer, M.; André, R. S.; Longo, E.; Gurgel, M. F. C. A theoretical investigation of the structural and electronic properties of orthorhombic CaZrO₃. *Ceram. Int.* **2015**, *41* (2), 3069–3074. <https://doi.org/10.1016/j.ceramint.2014.10.149>
- Saif, M.; Abdel-Mottaleb, M. S. A. Titanium dioxide nanomaterial doped with trivalent lanthanide ions of Tb, Eu and Sm: Preparation, characterization and potential applications. *Inorganica Chim. Acta* **2007**, *360* (9), 2863–2874. <https://doi.org/10.1016/j.ica.2006.12.052>
- Shimokawa, Y.; Sakaida, S.; Iwata, S.; Inoue, K.; Honda, S.; Iwamoto, Y. Synthesis and characterization of Eu³⁺ doped CaZrO₃-based perovskite type phosphors. part II: PL properties related to the two different dominant Eu³⁺ substitution sites. *J. Lumin.* **2015**, *157* (6), 113–118. <https://doi.org/10.1016/j.jlumin.2014.08.042>
- Silva, J. M. P.; Andrade Neto, N. F.; Oliveira, M. C.; Ribeiro, R. A. P.; Lazaro, S. R.; Gomes, Y. F.; Paskocimas, C. A.; Bomio, M. R. D.; Motta, F. V. Recent progress and approaches on the synthesis of Mn-doped zinc oxide nanoparticles: A theoretical and experimental investigation on the photocatalytic performance. *New J. Chem.* **2020**, *44* (21), 8805–8812. <https://doi.org/10.1039/D0NJ01530J>
- Singh, K.; Rajendran, M.; Devi, R.; Vaidyanathan, S. Narrow-band red-emitting phosphor with negligible concentration quenching for hybrid white LEDs and plant growth applications. *Dalton Trans.* **2021**, *50* (14), 4986–5000. <https://doi.org/10.1039/D1DT00449B>
- Smith, M. D.; Connor, B. A.; Karunadasa, H.I. Tuning the Luminescence of Layered Halide Perovskites. *Chem. Rev.* **2019**, *119* (5), 3104–3139. <https://doi.org/10.1021/acs.chemrev.8b00477>
- Song, E.; Zhao, W.; Zhang, W.; Ming, H.; Yi, Y.; Zhou, M. Fluorescence emission spectrum and energy transfer in Eu and Mn co-doped Ba₂Ca(BO₃)₂ phosphors. *J. Lumin.* **2010**, *130* (12), 2495–2499. <https://doi.org/10.1016/j.jlumin.2010.08.021>
- Targonska, S.; Szyszka, K.; Rewak-Soroczynska, J.; Wiglusz, R. J. A new approach to spectroscopic and structural studies of the nano-sized silicate-substituted hydroxyapatite doped with Eu³⁺ ions. *Dalton Trans.* **2019**, *48* (23), 8303–8316. <https://doi.org/10.1039/C9DT01025D>
- Tian, X.; Dou, H.; Wu, L. Bi³⁺-based luminescent thermometry in perovskite-type CaZrO₃ phosphor. *J. Mater. Sci. Mater. Electron.* **2020**, *31*, 3944–3950. <https://doi.org/10.1007/s10854-020-02942-6>
- Tiwari, N.; Kuraria, R. K.; Kuraria, S. R. Optical studies of Eu³⁺ doped CaZrO₃ phosphor for display device applications. *Optik.* **2015**, *126* (23), 3488–3491. <https://doi.org/10.1016/j.ijleo.2015.08.201>
- Tymiński, A.; Śmiechowicz, E.; Martín, I. R.; Grzyb, T. Ultraviolet- and Near-Infrared-Excitable LaPO₄:Yb³⁺/Tm³⁺/Ln³⁺ (Ln = Eu, Tb) Nanoparticles for Luminescent Fibers and Optical Thermometers. *ACS Appl. Nano Mater.* **2020**, *3* (7), 6541–6551. <https://doi.org/10.1021/acsnm.0c01025>
- Valenzano, L.; Civalieri, B.; Chavan, S.; Bordiga, S.; Nilsen, M. H.; Jakobsen, S.; Lillerud, K. P.; Lamberti, C. Disclosing the Complex Structure of UiO-66 Metal Organic Framework: A Synergic Combination of Experiment and Theory. *Chem. Mater.* **2011**, *23* (7), 1700–1718. <https://doi.org/10.1021/cm1022882>
- van der Ziel, J. P.; Van Uitert, L. G. Optical Emission Spectrum of Cr³⁺-Eu³⁺ Pairs in Europium Gallium Garnet. *Phys. Rev.* **1969**, *186*, 332–339. <https://doi.org/10.1103/PhysRev.186.332>
- Vieira, S. A.; Rakov, N.; Araújo, C. B.; Falcão-Filho, E. L. Upconversion luminescence in europium doped Y₂O₃ powder excited by absorption of three, four, and five infrared photons. *Opt. Mater. Express* **2019**, *9* (10), 3952–3961. <https://doi.org/10.1364/OME.9.003952>
- Wu, F.-N.; Yu, H.-J.; Hu, Y.-Y.; Zhang, H.-D.; Zhang, R.; Li, J.; Liu, B.; Wang, X.-P.; Yang, Y.-G.; Wei, L. Effects of slight structural distortion on the luminescence performance in (Ca_{1-x}Eu_x)WO₄ luminescent materials. *Luminescence* **2021**, *36* (1), 237–246. <https://doi.org/10.1002/bio.3941>
- Yamaguchi, S.; Kobayashi, K.; Higuchi, T.; Shin, S.; Iguchi, Y. Electronic transport properties and electronic structure of InO_{1.5}-doped CaZrO₃. *Solid State Ion.* **2000**, *136–137*, 305–311. [https://doi.org/10.1016/S0167-2738\(00\)00408-2](https://doi.org/10.1016/S0167-2738(00)00408-2)
- Yang, L.; Kruse, B. Revised Kubelka–Munk theory. I. Theory and application. *J. Opt. Soc. Am. A* **2004**, *21* (10), 1933–1941. <https://doi.org/10.1364/JOSAA.21.001933>

Zeba, I.; Ramzan, M.; Ahmad, R.; Shakil, M.; Rizwan, M.; Rafique, M.; Sarfraz, M.; Ajmal, M.; Gillani, S. S. A. First-principles computation of magnesium doped CaZrO_3 perovskite: A study of phase transformation, bandgap engineering and optical response for optoelectronic applications. *Solid State Commun.* **2020**, *313* (4), 113907. <https://doi.org/10.1016/j.ssc.2020.113907>

Zhang, H.; Fu, X.; Niu, S.; Xin, Q. Synthesis and photoluminescence properties of Eu^{3+} -doped AZrO_3 (A=Ca, Sr, Ba) perovskite. *J. Alloys Compd.* **2008**, *459* (1–2), 103–106. <https://doi.org/10.1016/j.jallcom.2007.04.259>

Zhang, J.; Cai, G.; Wang, W.; Ma, L.; Wang, X.; Jin, Z. Tuning of Emission by Eu^{3+} Concentration in a Pyrophosphate: the Effect of Local Symmetry. *Inorg. Chem.* **2020**, *59* (4), 2241–2247. <https://doi.org/10.1021/acs.inorgchem.9b02949>

Zheng, H.; Reaney, I. M.; Csete de Györgyfalva, G. D. C.; Ubic, R.; Yarwood, J.; Seabra, M. P.; Ferreira, V. M. Raman spectroscopy of CaTiO_3 -based perovskite solid solutions. *J. Mater. Res.* **2004**, *19*, 488–495. <https://doi.org/10.1557/jmr.2004.19.2.488>

Zhou, Q.; Fang, Y.; Li, J.; Hong, D.; Zhu, P.; Chen, S.; Tan, K. A design strategy of dual-ratiometric optical probe based on europium-doped carbon dots for colorimetric and fluorescent visual detection of anthrax biomarker. *Talanta* **2021**, *222*, 121548. <https://doi.org/10.1016/j.talanta.2020.121548>

Performance and stability of femtosecond laser-irradiated Fe₂O₃ materials as photocatalysts for methylene blue dye discoloration

Josiane Carneiro Souza¹⁺, Tiago Almeida Martins¹, Regiane Cristina de Oliveira², Julio Ricardo Sambrano², Cleber Renato Mendonça³, Leonardo de Boni³, Edson Roberto Leite¹, Elson Longo¹

1. Federal University of São Carlos, Center for the Development of Functional Materials, São Carlos, Brazil.
2. São Paulo State University, Faculty of Science, Bauru, Brazil.
3. University of São Paulo, Institute of Physics, São Carlos, Brazil.

+Corresponding author: Josiane Carneiro Souza, **Phone:** +551633066600, **Email address:** josi3souza@gmail.com

ARTICLE INFO

Article history:

Received: July 04, 2021

Accepted: November 23, 2021

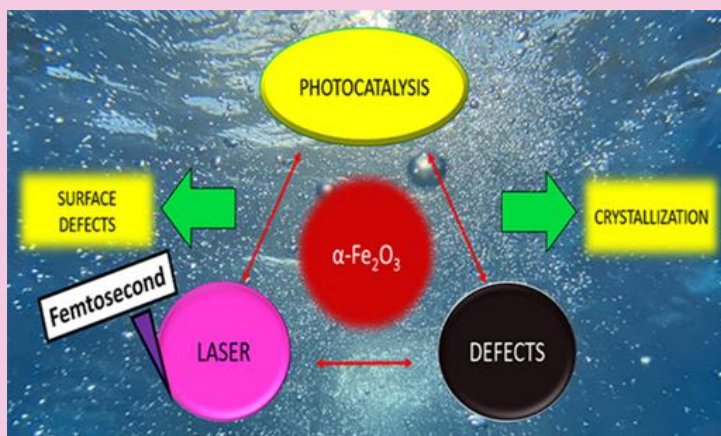
Published: April 11, 2022

Keywords:

1. defect density
2. polymorphism
3. dye
4. pollutant

Section Editors: Elson Longo and Juan Manuel Andrés Bort

ABSTRACT: The disposal of substances pollutant, such as methylene blue dye (MB), into wastewater, arouses the interest of technologies to remove these pollutants. The discoloration of MB by photocatalysis and using femtosecond laser-irradiated Fe₂O₃ materials as photocatalysts proved to be a promising way to treat this pollutant. Here, Fe₂O₃ obtained by the conventional hydrothermal process and heat-treatment, subsequently femtosecond laser-irradiated treatment. Materials obtained with a mixture of irradiated α -Fe₂O₃ and ϵ -Fe₂O₃ phases revealed lower crystallinity than irradiated α -Fe₂O₃ samples. The irradiation treatment and the increase in crystallinity were crucial to improve the performance of α -Fe₂O₃ irradiated sample in the discoloration of MB, which reached 90% in 75 min of dye solution exposure under UV irradiation. The irradiation treatment proved to allow greater exposure of the particle surfaces, which coalesced and presented a greater distribution of medium size, indicating a more heterogeneous morphology in the irradiated samples. As a result, there was an increase in active sites due to the density of defects generated, which facilitated the dye degradation process.



1. Introduction

Hematite (α -Fe₂O₃) and ϵ -Fe₂O₃ are two of the five known iron oxide polymorphs which have different crystal structures under normal conditions of temperature and pressure (CNTP) (Machala *et al.*, 2011; Tuček *et al.*, 2015). Under the conditions of α -Fe₂O₃, the material is more thermodynamically stable and abundant within the polymorphs of Fe₂O₃ (Machala *et al.*, 2011; Sivula *et al.*, 2011). During the period of expansion of the past Inca α -Fe₂O₃ was found on the surface of magmatic rocks due to years of aerobic weathering processes (Gialanella *et al.*, 2010; Sepúlveda *et al.*, 2019), among its first uses as pigments in primitive ruptured paints in prehistoric eras (Marean *et al.*, 2007) and more recently as dyes (Carneiro *et al.*, 2018). α -Fe₂O₃ can be obtained by thermally induced structural transformations of other oxides (Gialanella *et al.*, 2010; Gonçalves *et al.*, 2011) and/or other Fe₂O₃ polymorphs (Darezereshki, 2011; Ding *et al.*, 2007; Zboril *et al.*, 2002), as well as from reactions between iron salts (II) and (III) (Lassoued *et al.*, 2017; Papynov *et al.*, 2018; Sivula *et al.*, 2010).

ϵ -Fe₂O₃ was discovered in 1934 by Forestier and Guiot-Guillain (1934), but only received the name ϵ -Fe₂O₃ 29 years later by the researchers Schrader and Büttner (1963). Its structural characterization was performed for the first time in 1998 by Tronc *et al.* (1998) and in 2005 Kelm and Mader (2005), Sakurai *et al.* (2005) developed a model called refinement to interpret the X-ray crystal structure of ϵ -Fe₂O₃, obtained in coherence with some experimental data, such as lattice parameters and electron density maps (Shabalina *et al.*, 2018). The first thin films of ϵ -Fe₂O₃ were prepared in 2010 (Gich *et al.*, 2010); however, their chemical stability was determined eight years later at pressures up to 27 GPa (Sans *et al.*, 2018). ϵ -Fe₂O₃ is a metastable material between the polymorphs α -Fe₂O₃ and/or γ -Fe₂O₃ (Tronc *et al.*, 1998). Although it is found as biogenic nanoparticles mixed with magnetite and is present in some clays, this material is not very abundant in nature. Additionally, its particles have a low surface energy, which guarantees the formation and existence of ϵ -Fe₂O₃ (Gich *et al.*, 2007; McClean *et al.*, 2001; Petersen *et al.*, 1987).

Since α -Fe₂O₃ is an n-type semiconductor with a gap energy between 1.9 and 2.2 eV, it is considered as a potential sunlight converter, which uses solar energy to generate clean energy, such as electricity or green fuel (e.g., H₂) (Gratzel, 2001; Tamirat *et al.*, 2016). For such reason, it has been widely studied in photoelectrochemical processes (Sivula *et al.*, 2010; 2011; Trindade *et al.*, 2020). Fe₂O₃ materials can also

be applied as carrier of drugs to treat cancer cells (Liong *et al.*, 2008; Mandriota *et al.*, 2019), lithium batteries (Gu *et al.*, 2013), gas sensors (Gou *et al.*, 2008), pigments (Carneiro *et al.*, 2018) and dyes (Ahmed *et al.*, 2013). Many studies have used Fe₂O₃ materials as photocatalysts or adsorbents in the degradation of dyes present in industrial effluents (paper, textiles, leather) especially methylene blue (MB), which is resistant to chemical and biological treatment and can produce more toxic substances than the dye itself during its chemical decomposition (Ahmed *et al.*, 2013; Crini, 2005; Sharma *et al.*, 2011).

The versatility of Fe₂O₃ materials is attributed to their distinct crystal structures, resulting in different physicochemical properties (Machala *et al.*, 2011; Sakurai *et al.*, 2009). What makes these materials versatile with interesting technological applications is the greater understanding of the association of their properties with their crystal structures, especially concerning the effects of structural order and disorder (Pottker *et al.*, 2018). It is known that the structural modification on the surface of particles irradiated using femtosecond laser technology improves the structural and ablation properties of the material (Keller, 2003; Sugioka and Cheng, 2014). Such modification can be assigned to the creation of cations and oxygen vacancies that modulate the electronic states in the valence band of the material (Assis *et al.*, 2020). This study evaluates the performance of thermally treated and femtosecond laser-irradiated Fe₂O₃ samples for the discoloration of methylene blue (MB) dye under UV irradiation.

2. Experimental

The Fe₂O₃ particles were obtained by the conventional hydrothermal process, according to a procedure similar to that reported by Gou *et al.* (2008): 2 mmol of Fe(NO₃)₃·9H₂O, 4 mmol of trisodium citrate dihydrate and 5 mmol of urea were dissolved separately in 10 mL of deionized water and subsequently dissolved and placed in a hydrothermal reactor under constant stirring. The hydrothermal process was carried out at 160 °C for 10 h. After cooling, the precipitates were washed with deionized water and alcohol, and then dried at 90 °C for 6 h. Lastly, they were heat-treated at 860 and 900 °C for 30 min.

Fe₂O₃ samples were irradiated by a Ti:Sapphire laser (CPA-2001 system from Clark-MXR Inc.), at 775 nm, 150 fs (FWHM) and a repetition rate of 1 Hz. The samples were irradiated with an average power of 300 mW and positioned within the Rayleigh range. The

experiment was carried out following Assis *et al.* (2020). The nonirradiated samples were named hematite+epsilon-Fe₂O₃ (EPHE) and hematite-Fe₂O₃ (HE). After irradiation, they were denominated EPHEI and HEI, respectively.

The thermal behavior of Fe₂O₃ particles obtained by the hydrothermal process were evaluated by thermogravimetry (TGA) and differential thermal analysis (DTA), and then heated up to 1300 °C in an O₂ atmosphere with a flow of 50 mL min⁻¹ (NETZSCH - Cell 409).

The structural characterization of Fe₂O₃ samples was performed by X-ray diffraction (XRD), Raman spectroscopy and scanning electron microscopy (SEM). For the XRD measurements, a diffractometer (Shimadzu) with Cu K α radiation ($\lambda = 1.5406 \text{ \AA}$) was used, and the XRD patterns were acquired with steps of 0.02° and an angular range of 10 to 110°. The data obtained were analyzed using the Rietveld (1969) method with the aid of the general structure analysis system (GSAS) software (Von Dreele and Larson, 1994). Raman spectra were obtained in the range of 100–1000 cm⁻¹ using a Senterra spectrometer (Bruker) coupled to a 785 nm He–Ne laser excitation source with a power of 1 mW and a microscope with a 20 \times objective.

The morphology of the Fe₂O₃ samples was analyzed through images obtained in a Zeiss – Supra 35 scanning electron microscope. The images were obtained by secondary electron detection (ETD, Everhart – Thornley detector) with a 10 kV incident beam. Transmission electron microscopy (TEM) images were captured in high resolution (HRTEM) using an FEI – Tecnai F20 microscope operating in the brightfield. One μm -scale scanning electron micrographs were used to construct the frequency histogram and the mean size modal distribution curve versus particle size. The count of 150 particles was inspected and the measurements were performed by the ImageJ software (Schneider *et al.*, 2012) using the linear method.

The UV-Vis spectra were obtained over a range of 800–300 nm in diffuse reflectance mode at room temperature using a Varian Cary 5G spectrometer.

The photocatalytic activity of nonirradiated and irradiated Fe₂O₃ samples was tested for the discoloration of the methylene blue dye (MB; [C₁₆H₁₈ClN₃S]; 99.5% purity, Mallinckrodt) in relation to the exposure time under UV irradiation. The loss of MB coloration was observed by aliquots of Fe₂O₃ materials dispersed in the dye solution under UV radiation at different collection times. The concentration of the aqueous solution of MB used in

the photocatalysis experiments was provided by a calibration curve. The maximum absorbance (λ_{maximum}) measurement of MB was performed using a UV-Vis spectrometer (V-660 Jasco). As the dye follows Beer's Law (Grasse *et al.*, 2016), the calibration curve provided the aqueous concentration of the MB index in the photocatalytic study of nonirradiated and irradiated Fe₂O₃ materials.

The experiments were carried out by dispersing 50 mg of the sample in 50 mL of MB solution in an ultrasound bath inside an open reactor with a controlled temperature of 20 °C and water circulation. The sample-dye adsorption process was performed by stirring this dispersion in the dark for 30 min. The photocatalytic system was obtained by illuminating this dispersion with six UV lamps (TUV Philips, 15 W with maximum intensity of 254 nm). Aliquots were removed at time zero and other predetermined times (5, 10, 20, 30, 45, 60 and 75 min), the absorbance changes were measured by a spectrophotometer (V-660 Jasco), while the photocatalytic stability of the sample with the best performance was obtained from the recycling test results.

3. Results and discussion

There are four thermal events according to the TGA and differential thermal DTA curves of the Fe₂O₃ sample obtained by the conventional hydrothermal process, as showed in Fig. 1. The TGA curve demonstrates that the thermal stability of the sample occurred at 500 °C. The processes with energy absorption were identified at 110 °C, which corresponds to the sample dehydration, and at 650 °C, indicating that above this temperature hematite presents paramagnetic behavior (Liu *et al.*, 1997). At 243 and 860 °C, two exothermic events were observed, the first due to the release of gases and organic impurities from the process of particle obtention, and the second attributed to the $\epsilon\text{-Fe}_2\text{O}_3 \rightarrow \alpha\text{-Fe}_2\text{O}_3$ phase transition (Dézi and Coey, 1973). From this result, it was possible to perform the heat-treatment of the Fe₂O₃ samples.

The vibrational modes of Raman showing EPHE and EPHEI were identified as shown in Fig. 2. The vibrational modes of single-phase $\epsilon\text{-Fe}_2\text{O}_3$ samples phase are not identified in the literature yet. The determination of the wavenumbers referring to the $\epsilon\text{-Fe}_2\text{O}_3$ phase was performed from a Lorentzian fit of the Raman scattering spectrum bands. Thus, it was possible to distinguish the vibrational modes of the $\epsilon\text{-Fe}_2\text{O}_3$ and $\alpha\text{-Fe}_2\text{O}_3$ phases (López-Sánchez *et al.*, 2016). The vibrational modes agree with the

vibrational modes reported by López-Sánchez *et al.* (2016), the ϵ -Fe₂O₃ phase has 117 active Raman vibrational modes: 29A₁ + 30A₂ + 29B₁ + 29B₂, considering that the same has space group Pna21. Sample EPHE (Fig. 2a) showed nine active modes of the ϵ -Fe₂O₃ phase in wavenumbers in the range 120 to 600 cm⁻¹.

According to the literature (Faria *et al.*, 1997), α -Fe₂O₃ exhibits seven modes of active phonons (2A_{1g} + 5E_g) allowed in Raman. Sample EPHE shows two modes in 226 and 496 cm⁻¹, attributed to A_{1g}, and others in 245, 293, 410 and 610 cm⁻¹, assigned to E_g.

The changes observed in the Raman vibrational modes of the irradiated samples (Fig. 2b) are a consequence of the irradiation treatment, which provided an increase in the structural disorder within the crystal lattice of samples EPHEI and HEI. Compared to the nonirradiated samples, the high full-width at half-maximum (FWHM) values of the Raman bands, and the absence of active vibrational modes of the irradiated samples (Tab. 1) indicated that the irradiation treatment caused a distortion in the crystal lattice of the samples and an increase in the defect

density, leading to the breaking of Fe–O bonds. These results contribute to changes in the physicochemical properties of the irradiated samples.

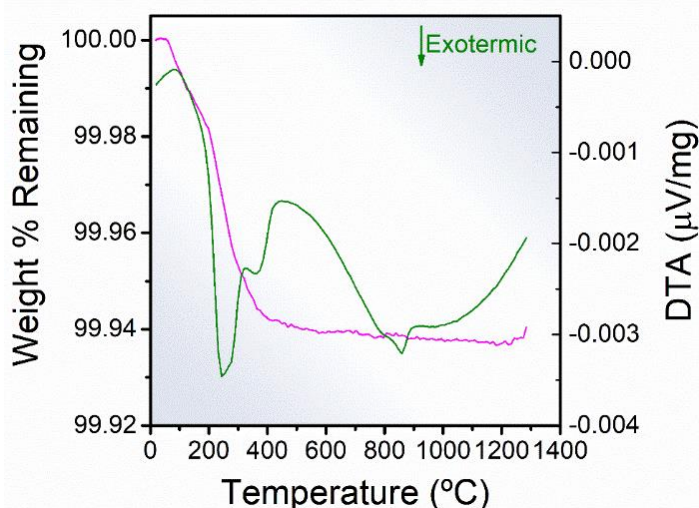


Figure 1. Differential thermal curve (olive line) and TGA curve (magenta line) of Fe₂O₃ sample obtained by the conventional hydrothermal process.

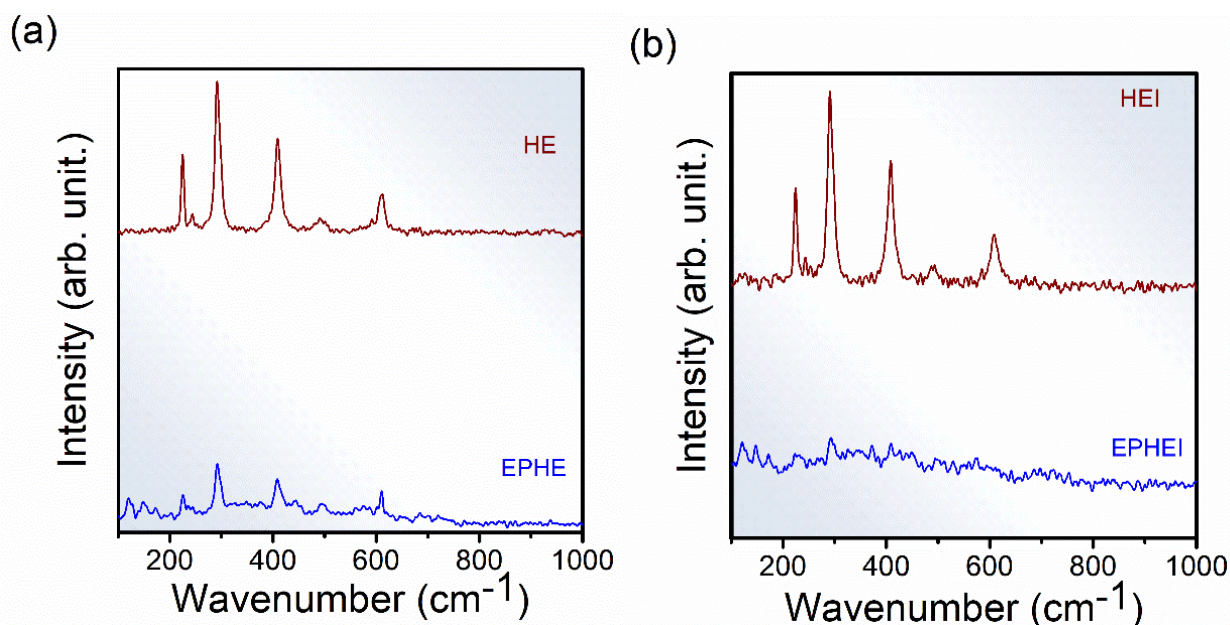


Figure 2. Raman spectra for (a) nonirradiated samples and (b) irradiated samples.

X-ray diffraction patterns of samples EPHE and EPHEI (Fig. 3) presented peaks indexed to the inorganic crystal structure database (ICSD) number 415250 (Kelm and Mader, 2005; Sakurai *et al.*, 2005) and 15840 (Blake *et al.*, 1966), and corresponding to ϵ -Fe₂O₃ to α -Fe₂O₃ phases, respectively, characterizing these materials as multiphase. These phases have an orthorhombic (Pna 21) and rhombohedral (R-3cH)

structure with eight and six molecular formulas per unit cell ($Z = 8$ and 6), respectively. On the other hand, samples HE and HEI are formed by α -Fe₂O₃ and are considered monophasic. This preferential formation is due to the increase in temperature to 900 °C during the heat-treatment when compared to samples EPHE and EPHEI.

Table 1. Wavenumbers (cm^{-1}) and full widths at half maximum (FWHM) for nonirradiated and irradiated samples.

Wavenumber (cm^{-1}) EPHE	FWHM (cm^{-1}) EPHE	Wavenumber (cm^{-1}) EPHEI	FWHM (cm^{-1}) EPHEI	Wavenumber (cm^{-1}) HE	FWHM (cm^{-1}) HE	Wavenumber (cm^{-1}) HEI	FWHM (cm^{-1}) HEI
123.4 ± 0.1	11.3	122.7 ± 0.3	13.8	-	-	-	-
147.9 ± 0.2	9.6	148.2 ± 0.2	13.3	-	-	-	-
172.1 ± 0.3	10.5	172.0 ± 0.3	11.1	-	-	-	-
226.1 ± 0.3	6.8	225.7 ± 0.3	2.8	225.8 ± 0.1	8.9	224.9 ± 0.1	8.7
244.9 ± 0.2	6.2	-	-	244.1 ± 0.2	11.5	245 ± 2	45.0
293.8 ± 0.2	13.8	293.9 ± 0.3	4.9	292.8 ± 0.1	14.7	292.1 ± 0.1	15.7
326.7 ± 0.3	7.1	325.4 ± 0.2	6.0	-	-	-	-
349.6 ± 0.2	6.2	350.6 ± 0.1	4.7	-	-	-	-
375.5 ± 0.2	12.2	373.9 ± 0.1	5.1	-	-	-	-
409.1 ± 0.3	16.6	409.3 ± 0.3	6.9	409.3 ± 0.1	15.6	408.9 ± 0.1	19.0
443.0 ± 0.3	8.4	-	-	-	-	-	-
560.9 ± 0.2	7.8	-	-	-	-	-	-
590.0 ± 0.2	6.7	-	-	-	-	-	-
495.3 ± 0.3	32.5	494.3 ± 0.2	10.4	494.0 ± 2.1	25.2	493.0 ± 0.3	22.3
610.1 ± 0.2	9.9	-	-	610.5 ± 0.2	12.2	608.7 ± 0.1	19.1

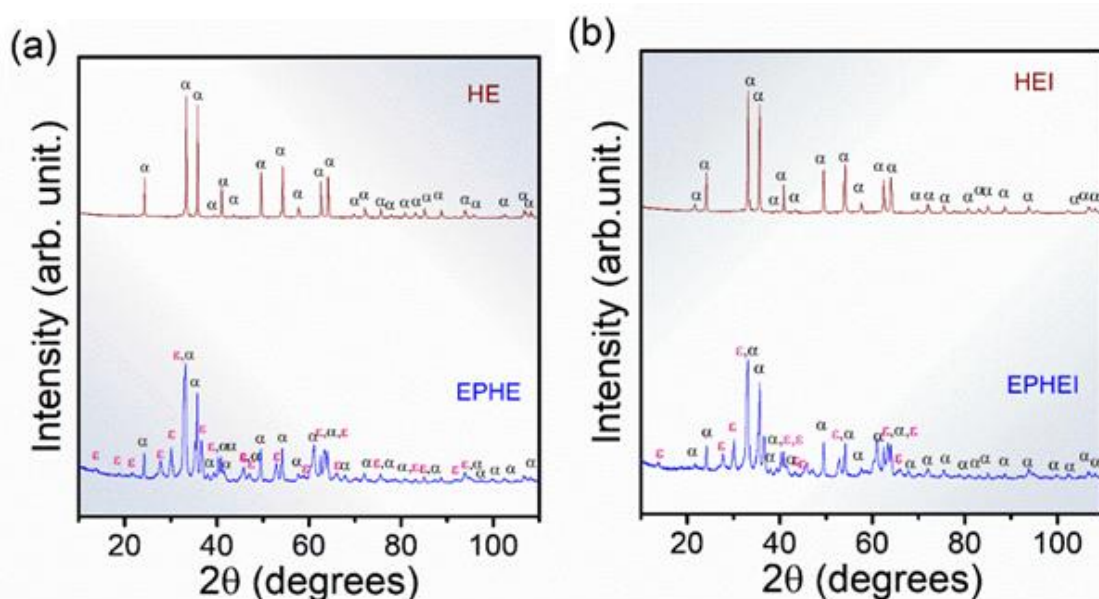


Figure 3. X-ray diffraction patterns for the $\epsilon\text{-Fe}_2\text{O}_3$ and $\alpha\text{-Fe}_2\text{O}_3$ of the samples heat-treated at 860 and 900 °C for 30 min. In (a) nonirradiated samples and (b) irradiated samples.

The results of structural refinement by the Rietveld (1969) method are shown in Tab. 2 and Fig. 4. Table 2 presents the lattice parameters and the percentage of phases of the samples before and after the irradiation treatment, whereas Fig. 4 shows typical Rietveld refinement graphs. It is possible to observe that the diffraction patterns calculated and obtained in Fig. 3 are related to high structural order or long-range and well-defined peaks.

The results of two lattice parameters presented in Tab. 2 are consistent with the previous studies of $\alpha\text{-Fe}_2\text{O}_3$ and $\epsilon\text{-Fe}_2\text{O}_3$ phases (Blake *et al.*, 1966; Kelm and Mader, 2005; Sakurai *et al.*, 2005). In this study, EPHE and EPHEI showed 62% of the $\epsilon\text{-Fe}_2\text{O}_3$ phase,

while HE exhibited crystallized $\alpha\text{-Fe}_2\text{O}_3$ as the preferential phase, which is indicative of the increase in temperature without heat-treatment. These results refer to the nonlinearity of the adjustment parameter (R_w %) for different processes of crystallization, solubilization and recrystallization. Microstrain results from irradiated samples (EPHEI and HEI) revealed higher values than those shown by nonirradiated samples (EPHE and HE), demonstrating that the irradiation treatment favored or increased the density of defects and stress in the crystalline lattice of the materials.

Table 2. Parameters obtained from Rietveld refinements of Fe₂O₃ samples.

Sample		EPHE	EPHEI	HE	HEI	ϵ -Fe ₂ O ₃ *	α -Fe ₂ O ₃ **	
α -Fe ₂ O ₃	Lattice parameters (Å)	a = b	5.035	5.037	5.040	5.035	-	5.038
		c	13.733	13.738	13.758	13.748	-	13.772
	V (Å ³)	301.50	301.93	302.70	301.89	-	302.72	
	Crystallite size (Å)	0.45	0.40	0.84	0.73	-	-	
	Microstrain	1282.7	2215.5	921.9	1390.9	-	-	
% Wt fraction		0.376	0.379	1.000	1.000	-	-	
ϵ -Fe ₂ O ₃	Lattice parameters (Å)	a	5.091	5.091	-	-	5.071	-
		b	8.781	8.789	-	-	8.736	-
		c	9.465	9.470	-	-	9.418	-
	V (Å ³)	423.09	423.74	-	-	417.25	-	
	Crystallite size (Å)	0.25	0.25	-	-	-	-	
	Microstrain	-599.4	-1741.8	-	-	-	-	
	% Wt fraction		0.624	0.621	-	-	-	-
Rw%		9.414	8.943	-	-	-	-	

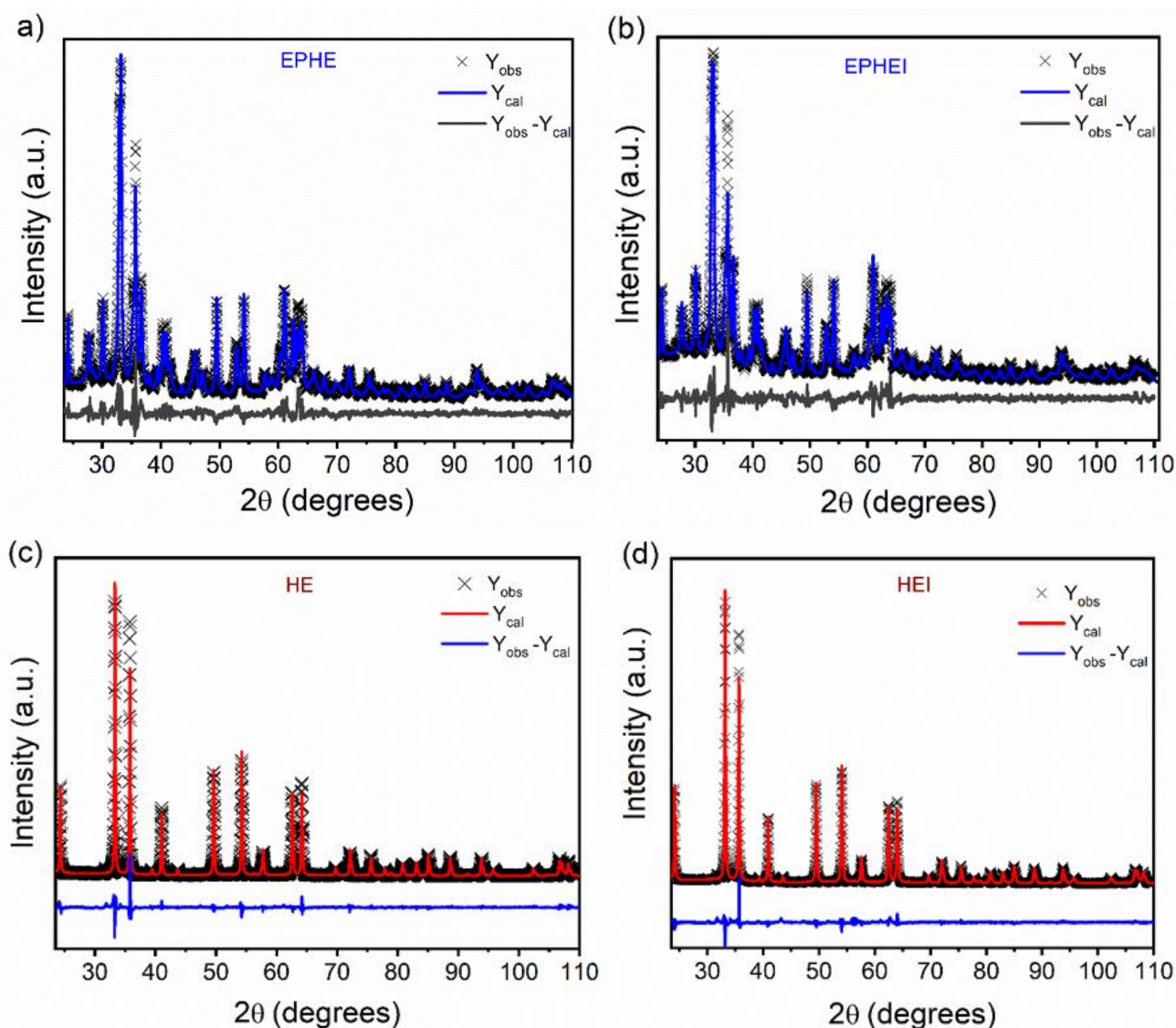


Figure 4. Rietveld refinement plot of nonirradiated in (a, c) and (b, d) irradiated samples.

Figure 5 illustrates the UV-Vis spectra in diffuse reflectance mode in the 250–800 nm range for the nonirradiated and irradiated samples. The absorbance close to the 570 nm region shows that these samples have application as absorbers (Sarma *et al.*, 2020).

The calculations performed to determine the energy of the samples in the forbidden band (E_{gap}) were obtained according to Wood and Tauc (1972) and Chen *et al.* (2013). The indirect transitions of the samples resulted in E_{gap} values consistent with the literature (Pandey *et al.*, 2014). Compared to the nonirradiated

samples, EPHEI and HEI showed a reduction in their E_{gap} value, indicating that the irradiation treatment caused the samples to present a more conductive behavior with greater structural disorder at medium-range (Pinatti *et al.*, 2020). It can be attributed to the presence of electronic levels within the forbidden band, which are associated with crystalline lattice disturbances. These results corroborate those obtained in the Raman and XRD analyses.

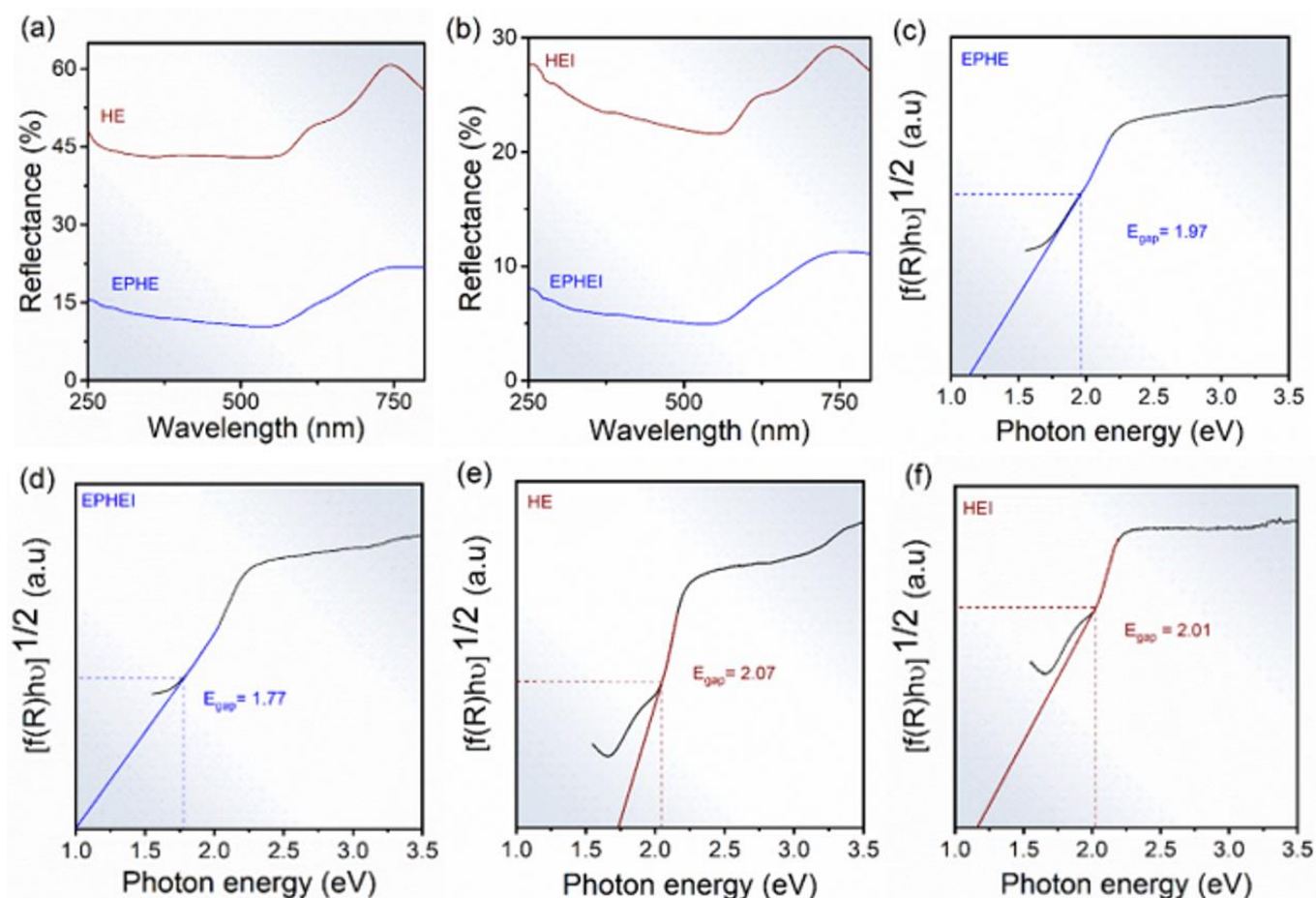


Figure 5. UV-Vis spectra in (a, b) and energy gap. In (c, e) nonirradiated samples and (d, f) irradiated samples.

The electron micrographs in Fig. 6 reveal that sample EPHE has a heterogeneous morphology with clusters in the shape of irregular plates and equiaxed structures on the plates. In turn, HE showed that the α - Fe_2O_3 particles have a homogeneous morphology with clusters of irregular plaques. The same change was

observed in EPHEI and HEI, even though the irradiation treatment allowed the formation of equiaxed particles on the agglomerated structures, including, in some regions of the samples, the phenomenon of coalescence resulting from diffusion processes of matter during irradiation (Anastasiou *et al.*, 2016).

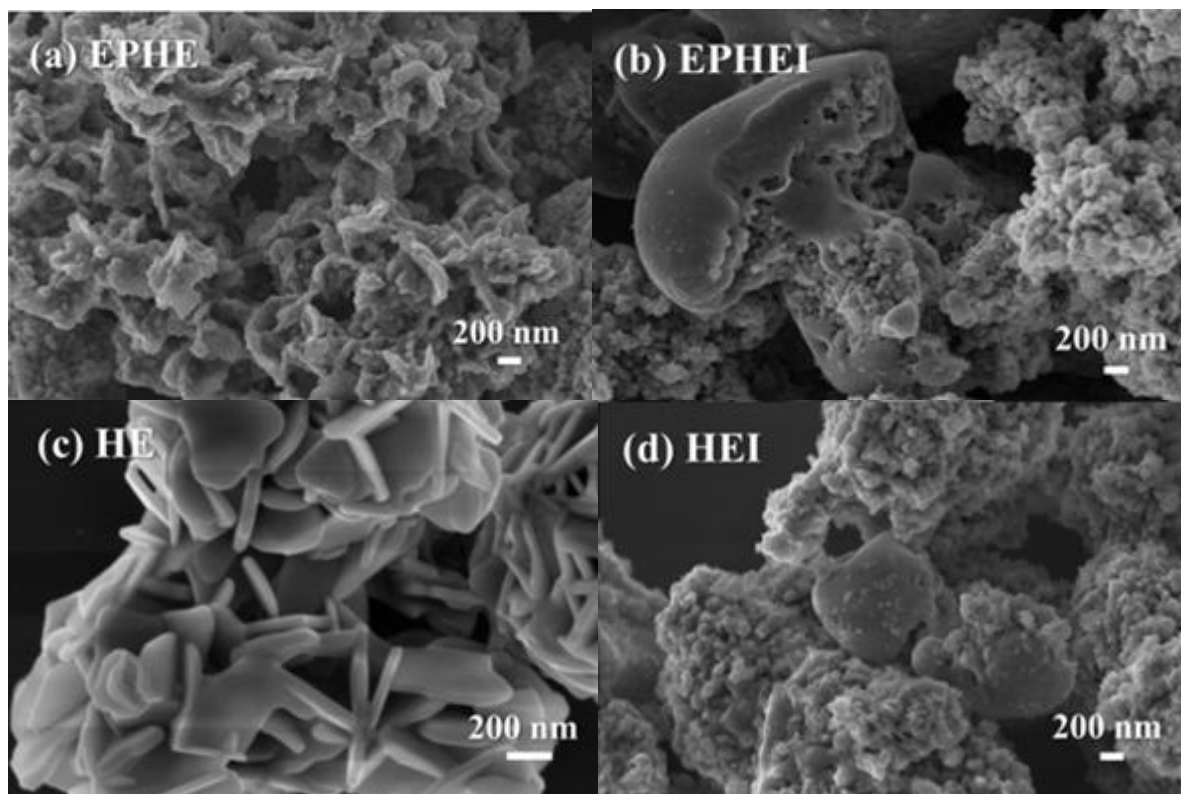
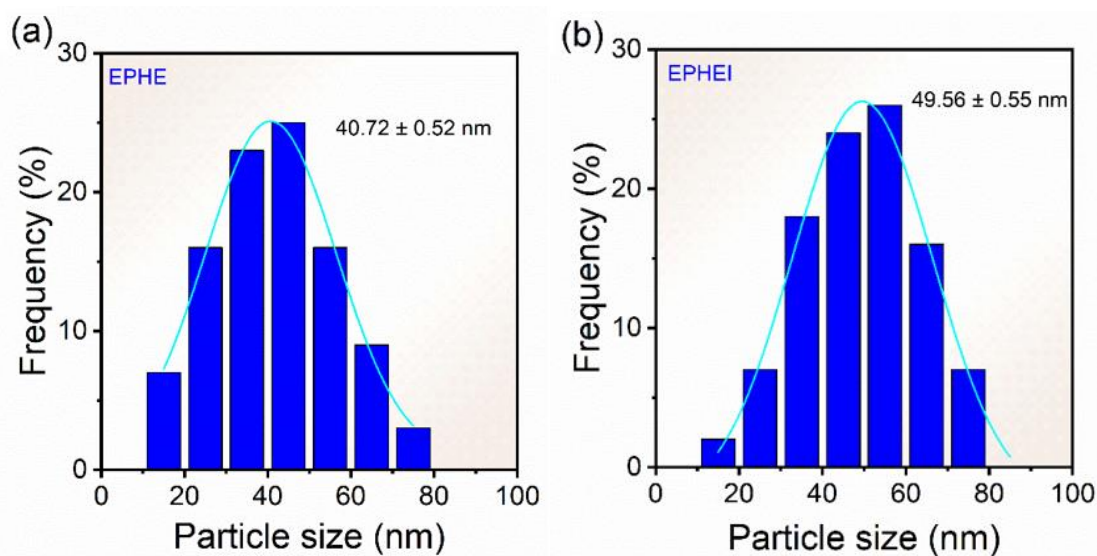


Figure 6. Micrographs of the nonirradiated in (a, c) and (b, d) irradiated samples.

The frequency histograms in Fig. 7 reveal an average size of 41 and 40 nm for the particles of samples EPHE and HE, respectively, and 49 and 54 nm for the irradiated samples EPHEI and HEI, respectively. It can be noted that the mean size distribution curve of the EPHE and EPHEI particles was very similar to each other. On the other hand, the mean size distribution curve of HEI became much broader than that of HE, indicating that there was an increase in the morphological heterogeneity.

Images obtained from high-resolution micrographs (HRTEM) of the nonirradiated and irradiated samples are displayed in Fig. 8. The crystallinity of the samples made it possible to obtain the indexing of the Fe_2O_3 phases. The insets show that the nonirradiated and irradiated samples crystallized in the $\epsilon\text{-Fe}_2\text{O}_3$ and $\alpha\text{-Fe}_2\text{O}_3$ phases, corroborating the results of the Raman spectra and XDR patterns. The irradiation treatment increased the defect density and avoided the $\epsilon\text{-Fe}_2\text{O}_3$ to $\alpha\text{-Fe}_2\text{O}_3$ phase transition in sample EPHEI.



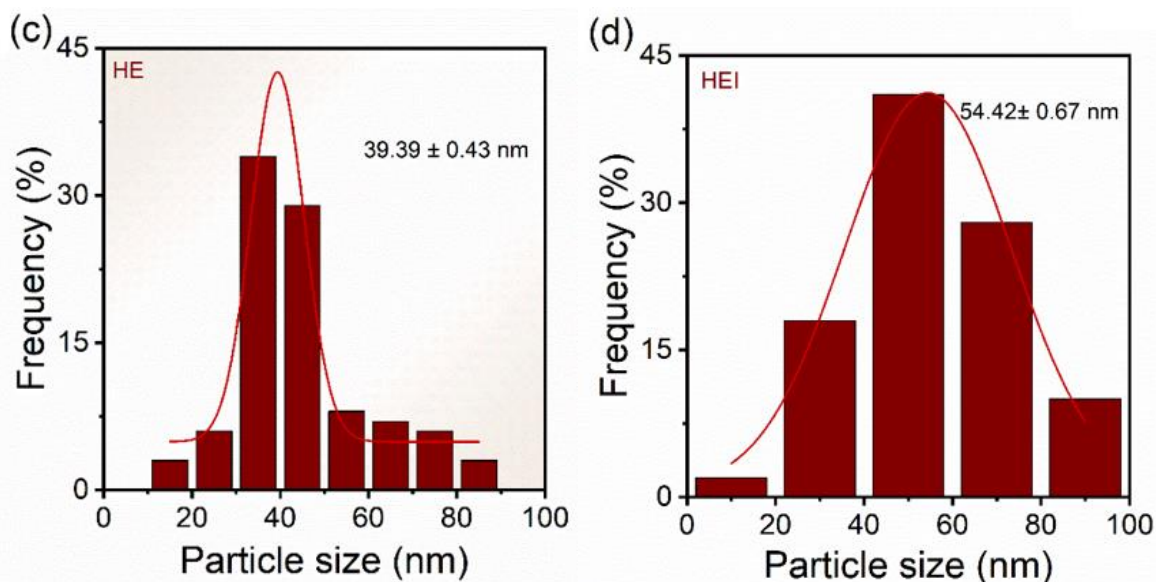


Figure 7. Frequency histograms of the nonirradiated in (a, c) and (b, d) irradiated samples.

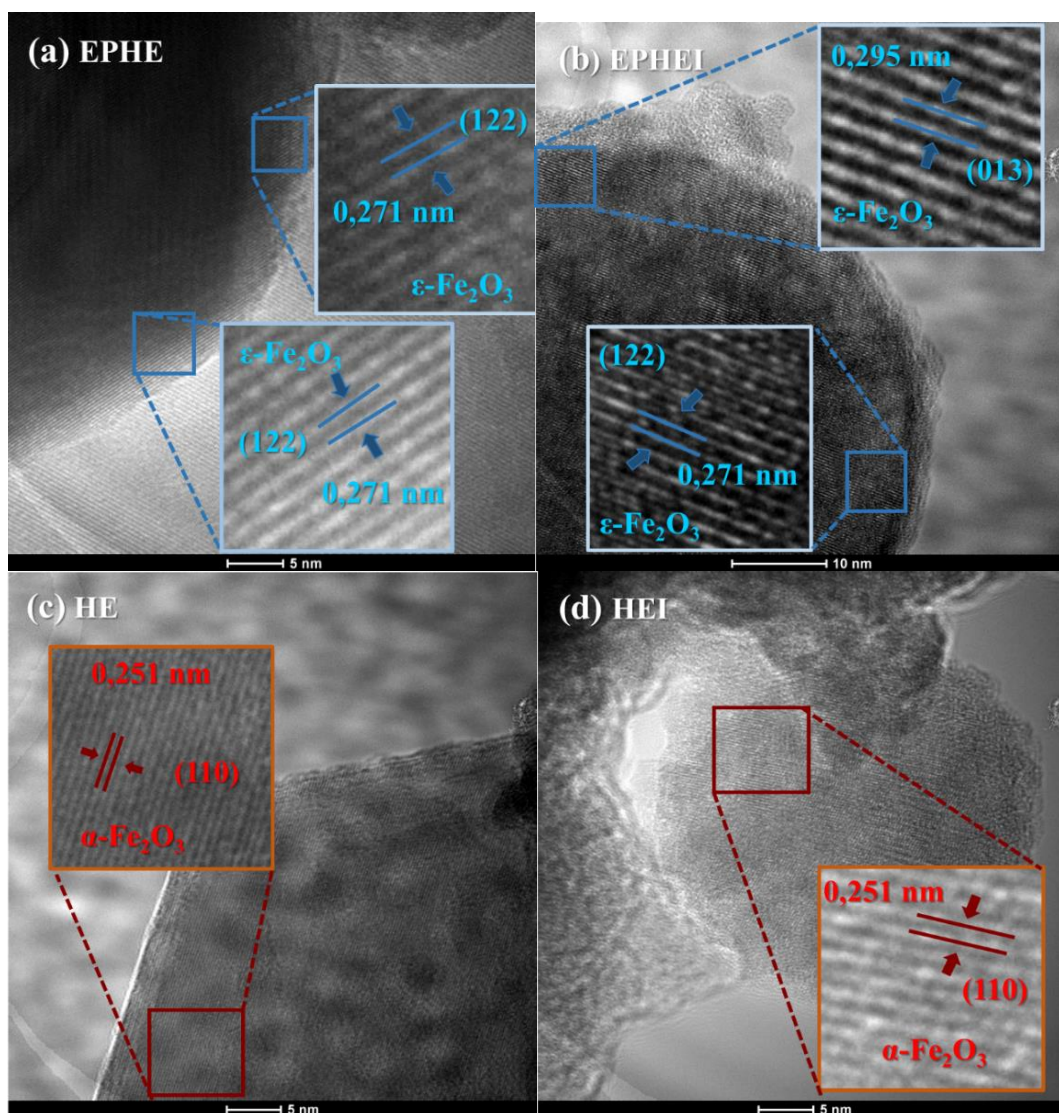


Figure 8. Transmission electron microscopy images of the nonirradiated in (a, c) and (b, d) irradiated samples.

The MB calibration curve (Fig. 9) was constructed from the solutions of the standard MB at pH = 7. The concentration of aqueous solutions of MB was estimated by measuring the absorbance at maximum wavelengths of MB ($\lambda_{\text{maximum}} = 668 \text{ nm}$) (Sheng and Mat Yunus, 2005). The adjustment of the experimental data was given by a straight line with a regression coefficient of $R^2 = 0.9990$. The calibration curve allowed us to determine that the concentration of 52.33 mg L^{-1} of MB had a maximum absorbance value of 1.0067, which is in agreement with the value found by Al-Rubayee *et al.* (2016). This was the concentration used in the photocatalysis test.

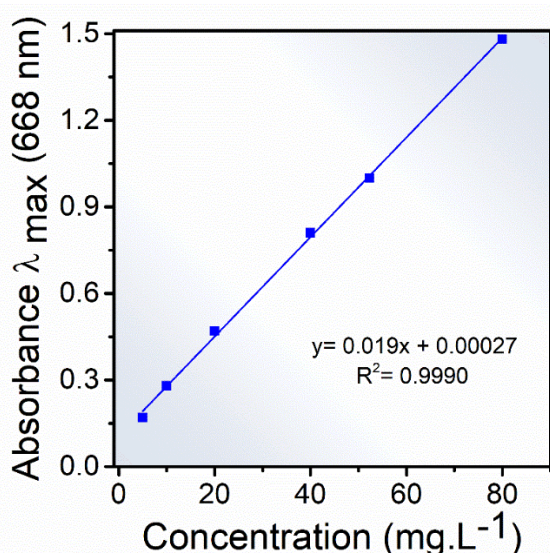


Figure 9. Calibration curve methylene blue at different concentrations 5–80 mg.L^{-1} .

The photocatalytic activity of nonirradiated and irradiated Fe_2O_3 samples was compared when MB was subjected to UV irradiation, in the absence of

photocatalysts and under the same experimental conditions. Figure 10a shows the relationship among the equilibrium adsorption concentration, the concentration after irradiation (C_N/C_0) and the irradiation time. The MB sample without catalyst showed much lower discoloration than catalyzed samples. The discoloration of MB in 75 min photocatalyzed by HEI was 90%. However, HE showed a similar discoloration profile in the absence of a catalyst. In relation to the dye adsorption, samples EPHE and EPHEI reached values of 60 and 35% in the dark, respectively. In contrast, HE ($\alpha\text{-Fe}_2\text{O}_3$) adsorbed 20% of the dye within 30 min of exposure in the dark. Allawi *et al.* (2020) studied the adsorption process of 100 mg of $\alpha\text{-Fe}_2\text{O}_3$ catalyst in a 20 mg L^{-1} MB solution at pH 7.6. They observed that in 6 min of exposure in the dark, the dye adsorption was $\sim 10\%$. Considering the results achieved by samples EPHE and EPHEI, it is possible to then infer that the presence of the $\epsilon\text{-Fe}_2\text{O}_3$ phase significantly influenced the MB adsorption process. During the photocatalysis of EPHE and EPHEI, the discoloration was 8 and 15%, respectively, which is in accordance with the results obtained by Ahmed *et al.* (2013). These findings show that samples EPHE and EPHEI behave as MB adsorbent materials, being promising for MB photocatalysis. Regarding the photocatalytic activity of HEI, the recycling test was performed following the procedure described Trench *et al.* (2018). The effect of photocatalytic activity of each cycle is shown in Fig. 10c. It is possible to observe that the photocatalytic activity of this sample decreased over the cycles, which can be attributed to the loss of material due to washing processes for dye removal. On the other hand, such sample (HEI) showed good stability as a photocatalyst.

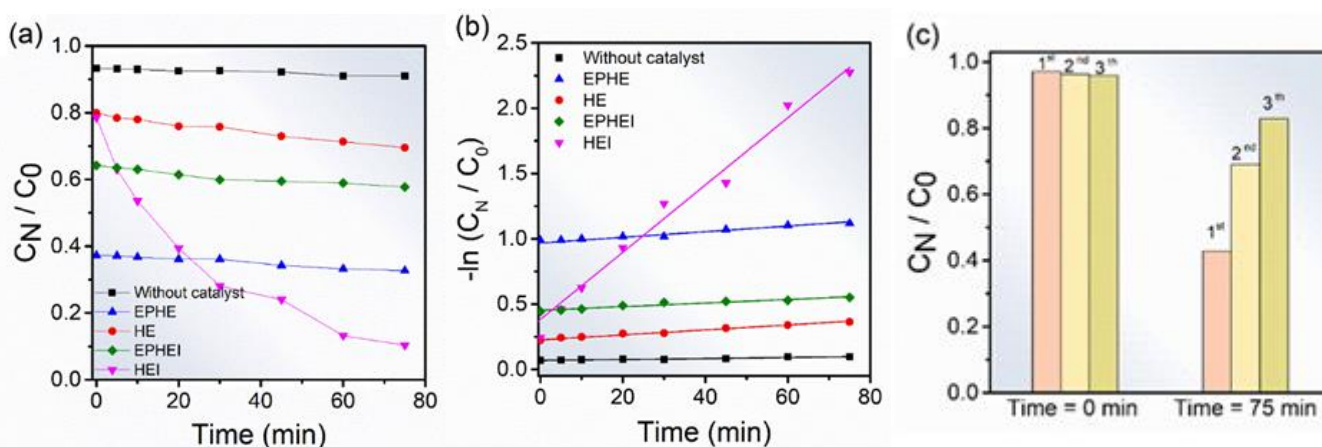


Figure 10. Photocatalytic discoloration of MB (52.33 mg L^{-1}). In (a) without catalyst and Fe_2O_3 nonirradiated and irradiated materials and (b) Determination of the rate constant by log plot and (c) Recycle test of HEI sample.

For the MB dye, the solution concentration was considered very low. In order to quantitatively compare the obtained results, a kinetic study was carried out using a pseudo first-order reaction from the Langmuir–Hinshelwood model, as showed Eq. 1 (Guettaï and Amar, 2005):

$$k't = -\ln\left(\frac{C_N}{C_0}\right) \quad (1)$$

where k' and t represent the constant reaction rate and the irradiation time, respectively. Figure 10b shows the kinetic behavior of MB discoloration. The reaction constants found were 2.67×10^{-2} , 1.39×10^{-3} , 1.80×10^{-3} , 1.87×10^{-3} , $3.52 \times 10^{-4} \text{ min}^{-1}$ for HEI, EPHEI, HE, EPHE and the sample without catalyst, respectively. In comparison with the sample without catalyst, EPHE, EPHEI and HE showed an increase in the reaction speed in one order of magnitude, while HEI exhibited a constant speed with two orders of magnitude.

Figures 6 and 8 illustrate the morphology of the nonirradiated samples (EPHE and HE) under thermal treatment. It could be observed that the femtosecond laser-irradiation treatment led to the formation of different morphologies in EPHEI and HEI that interfere with the absorption and electron transfer processes, presenting different photocatalytic activities (Vu *et al.*, 2019). The lower photocatalytic activity was due to the reduction of active reaction sites in the studied samples (Huang *et al.*, 2015). The irradiation treatment directly affected the surface of the particles, causing an increase in the density of surface defects, thus improving the photocatalytic properties of these samples.

This result is very significant compared to the development of $\alpha\text{-Fe}_2\text{O}_3$ materials as a photocatalyst for MB discoloration at room temperature, which reached a value of 78% in 6 h of UV irradiation (Vu *et al.*, 2019). In fact, the irradiation treatment proved to be very efficient to improve the photocatalytic activity of sample HEI, composed solely of $\alpha\text{-Fe}_2\text{O}_3$. This improvement was also attributed to the defects generated on the surface of the particles (Vu *et al.*, 2019).

The $\alpha\text{-Fe}_2\text{O}_3$ present in the studied samples has short diffusion length of the minority carriers (holes) (Wheeler *et al.*, 2012) and low conductivity of the majority carriers (electrons) (Kennedy and Frese Junior, 1978), resulting in difficulty in separating the photogenerated electron-hole pairs, and consequently influencing the photocatalytic activity results of these materials. On the other hand, $\varepsilon\text{-Fe}_2\text{O}_3$ is a material difficult to be obtained in isolation (Danno *et al.*, 2013;

Dézi and Coey, 1973; Shanenkov *et al.*, 2019; Wang *et al.*, 2019). For such reason, its attention is more focused on its interesting magnetic properties, as the anisotropic particles in this material can lead to the formation of a single magnetic domain, generating a large coercive field compared to other Fe_2O_3 polymorphs, and thus having advanced magnetic applications (Jin *et al.*, 2004; Machala *et al.*, 2011). However, in this study it was very interesting to investigate the photocatalytic properties of this material against $\alpha\text{-Fe}_2\text{O}_3$.

Since the photocatalytic process of HEI occurred by the transfer of surface charge, there was a consequent increase in defect density (Huang *et al.*, 2015). Such sample absorbed energy of the photon generated by UV irradiation to form charge carriers (electron-hole pairs) that participate in the photooxidation on the sample surface. Minority carriers form very reactive hydroxy radicals ($\cdot\text{OH}$), which are the main active species used to decolor MB (Zhao *et al.*, 2004). In contrast, majority carriers captured by dissolved oxygen in the MB solution form superoxide radicals anions ($\cdot\text{O}_2^-$) and/or peroxide radicals, which have the ability to break down MB molecules until mineralizing them into CO_2 and H_2O (Vadivel *et al.*, 2014). In turn, $\cdot\text{O}_2^-$ reacts with minority carriers of the sample, forming peroxides and releasing oxygen and/or active OH radicals and peroxides, partially contributing to the degradation of MB (Huang *et al.*, 2015).

4. Conclusions

The optical properties of femtosecond laser-irradiated $\alpha\text{-Fe}_2\text{O}_3$ materials showed a reduction in their band gap energy values and exhibited a more conductive behavior than nonirradiated samples due to the presence of electronic levels within the band gap range generated by the resulting defect density caused by irradiation.

According to the XRD patterns, the structural characterization showed that the high crystallinity of samples HE compared to EPHE influenced the increase in their photocatalytic activity due to the presence of the $\varepsilon\text{-Fe}_2\text{O}_3$ phase. On the other hand, the femtosecond laser irradiation treatment improved the photocatalytic properties of EPHEI compared to the nonirradiated sample (EPHE). A significant reduction in the Raman modes was observed for irradiated samples, indicating that their structural disorder at medium range was a result from the increase in the density of defects generated on the surface of their particles. Therefore, it was proven that sample HEI presented the best photocatalytic property, which was attributed to the

synergistic effect of the high crystallinity of the α -Fe₂O₃ phase and the generation of defects caused by the irradiation treatment.

The morphological aspect of the samples revealed agglomerated particles that impaired the improvement of the photocatalytic properties of the samples. Therefore, samples EPHE, HE and EPHEI behaved as adsorbent materials for MB discoloration. These materials have the potential to be used together with photocatalysts to enhance MB degradation in a short period of dye exposure. The mean particle size distribution curve of HEI was wider than that of HE, indicating an increase in the morphological heterogeneity of the irradiated sample, which consequently favored the increase in its catalytic activity. The phase indexing in the HRTEM images showed that the irradiation treatment was not energetically favorable to the transformation of ϵ -Fe₂O₃ to α -Fe₂O₃, but sufficiently effective for the generation of surface defects in the particles of the irradiated samples (HEI and EPHEI).

Authors' contribution

Conceptualization: Souza, J. C.; Martins, T. A.; Oliveira, R. C.; Sambrano, J. R.; Boni, L.; Mendonça, C. R.; Leite, E. R.; Longo, E.

Data curation: Not applicable.

Formal Analysis: Souza, J. C.; Martins, T. A.; Oliveira, R. C.; Boni, L.

Funding acquisition: Mendonça, C. R.; Leite, E. R.; Longo, E.

Investigation: Souza, J. C.; Martins, T. A.; Oliveira, R. C.; Sambrano, J. R.

Methodology: Souza, J. C.; Martins, T. A.; Boni, L.

Project administration: Leite, E. R.; Longo, E.

Resources: Souza, J. C.; Martins, T. A.; Oliveira, R. C.; Boni, L.; Mendonça, C. R.; Leite, E. R.; Longo, E.

Software: Not applicable

Supervision: Longo, E.

Validation: Souza, J. C.; Martins, T. A.; Oliveira, R. C.; Sambrano, J. R.; Mendonça, C. R.; Boni, L.

Visualization: Souza, J. C.; Martins, T. A.; Oliveira, R. C.; Sambrano, J. R.; Mendonça, C. R.; Boni, L.

Writing – original draft: Souza, J. C.; Martins, T. A.; Oliveira, R. C.; Sambrano, J. R.; Boni, L.; Mendonça, C. R.; Leite, E. R.; Longo, E.

Writing – review & editing: Souza, J. C.; Martins, T. A.; Oliveira, R. C.; Sambrano, J. R.; Boni, L.; Mendonça, C. R.; Leite, E. R.; Longo, E.

Data availability statement

All data sets were generated or analyzed in the current study

Funding

Coordenação de Aperfeiçoamento de Pessoal de Nível Superior (CAPES). Finance Code: 001.

Fundação de Amparo à Pesquisa do Estado de São Paulo (FAPESP). Grant No: 2013/07296-2; 2019-08928-9; 2018/11283-7; 2021/01651-1.

Conselho Nacional de Desenvolvimento Científico e Tecnológico (CNPq). Grant No: 2019/88887.469176.

Acknowledgments

Not applicable.

References

- Ahmed, M. A.; El-Katori, E. E.; Gharni, Z. H. Photocatalytic degradation of methylene blue dye using Fe₂O₃/TiO₂ nanoparticles prepared by sol–gel method. *J. Alloys Compd.* **2013**, *553*, 19–29. <https://doi.org/10.1016/j.jallcom.2012.10.038>
- Allawi, F.; Juda, A. M.; Radhi, S. W. Photocatalytic degradation of methylene blue over MgO/ α -Fe₂O₃ nano composite prepared by a hydrothermal method. *AIP Conf. Proc.* **2020**, *2290* (1), 030020. <https://doi.org/10.1063/5.0029461>
- Al-Rubayee, W. T.; Abdul-Rasheed, O. F.; Ali, N. M. Preparation of a Modified Nanoalumina Sorbent for the Removal of Alizarin Yellow R and Methylene Blue Dyes from Aqueous Solutions. *J. Chem.* **2016**, *2016*, 4683859. <https://doi.org/10.1155/2016/4683859>
- Anastasiou, A. D.; Thomson, C. L.; Hussain, S. A.; Edwards, T. J.; Strafford, S.; Malinowski, M.; Mathieson, R.; Brown, C. T. A.; Brown, A. P.; Duggal, M. S.; Jha, A. Sintering of Calcium Phosphates with a Femtosecond Pulsed Laser for Hard Tissue Engineering. *Mater. Des.* **2016**, *101*, 346–354. <https://doi.org/10.1016/j.matdes.2016.03.159>
- Assis, M.; Ribeiro, R. A. P.; Carvalho, M. H.; Teixeira, M. M.; Gobato, Y. G.; Prando, G. A.; Mendonça, C. R.; Boni, L.; Oliveira, J. A. de; Bettini, J.; Andrés, J.; Longo, E. Unconventional Magnetization Generated from Electron Beam and Femtosecond Irradiation on α -Ag₂WO₄: A Quantum Chemical Investigation. *ACS Omega.* **2020**, *5*, 10052–10067. <https://doi.org/10.1021/acsomega.0c00542>

- Blake, R. L.; Hessevick, R. E.; Zoltai, T.; Finger, L. W. Refinement of the hematite structure. *Am. Mineral.* **1966**, *51* (1–2), 123–129.
- Carneiro, J.; Tobaldi, D. M.; Hajjaji, W.; Capela, M. N.; Novais, R. M.; Seabra, M. P.; Labrincha, J. A. Red mud as a substitute coloring agent for the hematite pigment. *Ceram. Int.* **2018**, *44* (4), 4211–4219. <https://doi.org/10.1016/j.ceramint.2017.11.225>
- Chen, Z.; Miller, E.; Dinh, H. N. *Photoelectrochemical Water Splitting: Standards, Experimental Methods, and Protocols*. Springer, 2013. <https://doi.org/10.1007/978-1-4614-8298-7>
- Crini, G. Recent developments in polysaccharide-based materials used as adsorbents in wastewater treatment. *Prog. Polym. Sci.* **2005**, *30* (1), 38–70. <https://doi.org/10.1016/j.progpolymsci.2004.11.002>
- Danno, T.; Nakatsuka, D.; Kusano, Y.; Asaoka, H.; Nakanishi, M.; Fujii, T.; Ikeda, Y.; Takada, J. Crystal Structure of β -Fe₂O₃ and Topotactic Phase Transformation to α -Fe₂O₃. *Cryst. Growth Des.* **2013**, *13* (2), 770–774. <https://doi.org/10.1021/cg301493a>
- Darezereshki, E. One-step synthesis of hematite (α -Fe₂O₃) nano-particles by direct thermal-decomposition of maghemite. *Mater. Lett.* **2011**, *65* (4), 642–645. <https://doi.org/10.1016/j.matlet.2010.11.030>
- Dézsi, I.; Coey, J. M. D. Magnetic and thermal properties of ϵ -Fe₂O₃. *Phys. Status Solidi.* **1973**, *15* (2), 681–685. <https://doi.org/10.1002/pssa.2210150239>
- Ding, Y.; Morber, J. R.; Snyder, R. L.; Wang, Z. L. Nanowire Structural Evolution from Fe₃O₄ to ϵ -Fe₂O₃. *Adv. Funct. Mater.* **2007**, *17* (7), 1172–1178. <https://doi.org/10.1002/adfm.200601024>
- Faria, D. L. A. de; Silva, S. V.; Oliveira, M. T. de. Raman microspectroscopy of some iron oxides and oxyhydroxides. *J. Raman Spectrosc.* **1997**, *28* (11), 873–878. [https://doi.org/10.1002/\(SICI\)1097-4555\(199711\)28:11<873::AID-JRS177>3.0.CO;2-B](https://doi.org/10.1002/(SICI)1097-4555(199711)28:11<873::AID-JRS177>3.0.CO;2-B)
- Forestier, H.; Guiot-Guillain, G. Ferromagnetic Variety of Fe₂O₃. *C. R. Acad. Sci.* **1934**, *199*, 720.
- Gialanella, S.; Girardi, F.; Ischia, G.; Lonardelli, I.; Mattarelli, M.; Montagna, M. On the goethite to hematite phase transformation. *J. Therm. Anal. Calorim.* **2010**, *102*, 867–873. <https://doi.org/10.1007/s10973-010-0756-2>
- Gich, M.; Roig, A.; Taboada, E.; Molins, E.; Bonafos, C.; Snoeck, E. Stabilization of metastable phases in spatially restricted fields: the case of the Fe₂O₃ polymorphs. *Faraday Discuss.* **2007**, *136*, 345–354. <https://doi.org/10.1039/B616097B>
- Gich, M.; Gazquez, J.; Roig, A.; Crespi, A.; Fontcuberta, J.; Idrobo, J. C.; Pennycook, S. J.; Varela, M.; Skumryev, V.; Varela, M. Epitaxial stabilization of ϵ -Fe₂O₃ (001) thin films on SrTiO₃ (111). *Appl. Phys. Lett.* **2010**, *96*, 112508. <https://doi.org/10.1063/1.3360217>
- Gonçalves, R. H.; Lima, B. H. R.; Leite, E. R. Magnetite Colloidal Nanocrystals: A Facile Pathway To Prepare Mesoporous Hematite Thin Films for Photoelectrochemical Water Splitting. *J. Am. Chem. Soc.* **2011**, *133* (15), 6012–6019. <https://doi.org/10.1021/ja111454f>
- Gou, X.; Wang, G.; Park, J.; Liu, H.; Yang, J. Monodisperse hematite porous nanospheres: synthesis, characterization, and applications for gas sensors. *Nanotechnology.* **2008**, *19*, 125606. <https://doi.org/10.1088/0957-4484/19/12/125606>
- Grasse, E. K.; Torcasio, M. H.; Smith, A. W. Teaching UV–Vis Spectroscopy with a 3D-Printable Smartphone Spectrophotometer. *J. Chem. Educ.* **2016**, *93* (1), 146–151. <https://doi.org/10.1021/acs.jchemed.5b00654>
- Gratzel, M. Photoelectrochemical Cells. *Nature.* **2001**, *414*, 338–344. <https://doi.org/10.1038/35104607>
- Gu, X.; Chen, L.; Ju, Z.; Xu, H.; Yang, J.; Qian, Y. Controlled Growth of Porous α -Fe₂O₃ Branches on β -MnO₂ Nanorods for Excellent Performance in Lithium-Ion Batteries. *Adv. Funct. Mater.* **2013**, *23* (32), 4049–4056. <https://doi.org/10.1002/adfm.201203779>
- Guettaï, N.; Amar, H. A. Photocatalytic Oxidation of Methyl Orange in Presence of Titanium Dioxide in Aqueous Suspension. Part II: Kinetics Study. *Desalination.* **2005**, *185* (1–3), 439–448. <https://doi.org/10.1016/j.desal.2005.04.049>
- Huang, Y.; Ding, D.; Zhu, M.; Meng, W.; Huang, Y.; Geng, F.; Li, J.; Lin, J.; Tang, C.; Lei, Z.; Zhang, Z.; Zhi, C. Facile synthesis of α -Fe₂O₃ nanodisk with superior photocatalytic performance and mechanism insight. *Sci. Technol. Adv. Mater.* **2015**, *16* (1), 014801 (12pp). <https://doi.org/10.1088/1468-6996/16/1/014801>
- Jin, J.; Ohkoshi, S.; Hashimoto, K. Giant Coercive Field of Nanometer- Sized Iron Oxide. *Adv. Mater.* **2004**, *16* (1), 48–51. <https://doi.org/10.1002/adma.200305297>
- Keller, U. Recent Developments in Compact Ultrafast Lasers. *Nature.* **2003**, *424*, 831–838. <https://doi.org/10.1038/nature01938>
- Kelm, K.; Mader, W. Synthesis and Structural Analysis of ϵ -Fe₂O₃. *Z. Anorg. Allg. Chem.* **2005**, *631* (12), 2383–1389. <https://doi.org/10.1002/zaac.200500283>
- Kennedy, J. H.; Frese Junior, K. W. Photooxidation of Water at α -Fe₂O₃ Electrodes. *J. Electrochem. Soc.* **1978**, *125*, 709–714. <https://doi.org/10.1149/1.2131532>
- Lassoued, A.; Lassoued, M. S.; Dkhil, B.; Gadri, A.; Ammar, S. Synthesis, structural, optical and morphological characterization of hematite through the precipitation method: Effect of varying the nature of the base. *J. Mol. Struct.* **2017**, *1141*, 99–106. <https://doi.org/10.1016/j.molstruc.2017.03.077>

- Liong, M.; Lu, J.; Kovochich, M.; Xia, T.; Ruehm, S. G.; Nel, A. E.; Tamanoi, F.; Zink, J. I. Multifunctional Inorganic Nanoparticles for Imaging, Targeting, and Drug Delivery. *ACS Nano*. **2008**, *2* (5), 889–896. <https://doi.org/10.1021/nn800072t>
- Liu, X. Q.; Tao, S. W.; Shen, Y. S. Preparation and characterization of nanocrystalline α -Fe₂O₃ by a sol-gel process. *Sens. Actuators B Chem.* **1997**, *40* (2–3), 161–165. [https://doi.org/10.1016/s0925-4005\(97\)80256-0](https://doi.org/10.1016/s0925-4005(97)80256-0)
- López-Sánchez, J.; Serrano, A.; Del Campo, A.; Abuín, M.; Fuente, O. R. de la; Carmona, N. Sol-Gel Synthesis and Micro-Raman Characterization of ϵ -Fe₂O₃ Micro- and Nanoparticles. *Chem. Mater.* **2016**, *28* (2), 511–518. <https://doi.org/10.1021/acs.chemmater.5b03566>
- Machala, L.; Tuček, J.; Zbořil, R. Polymorphous Transformations of Nanometric Iron(III) Oxide: A Review. *Chem. Mater.* **2011**, *23*, 3255–3272. <https://doi.org/10.1021/cm200397g>
- Mandriota, G.; Corato, R.; Benedetti, M.; Castro, F. de; Fanizzi, F. P.; Rinaldi, R. Design and Application of Cisplatin-Loaded Magnetic Nanoparticle Clusters for Smart Chemotherapy. *ACS Appl. Mater. Interfaces*. **2019**, *11* (2), 1864–1875. <https://doi.org/10.1021/acsami.8b18717>
- Marean, C. W.; Bar-Matthews, M.; Bernatchez, J.; Fisher, E.; Goldberg, P.; Herries, A. I. R.; Jacobs, Z.; Jerardino, A.; Karkanas, P.; Minichillo, T.; Nilssen, P. J.; Thompson, E.; Watts, I.; Williams, H. M. Early human use of marine resources and pigment in South Africa during the Middle Pleistocene. *Nature*. **2007**, *449*, 905–908. <https://doi.org/10.1038/nature06204>
- McClellan, R. G.; Schofield, M. A.; Kean, W. F.; Sommer, C. V.; Robertson, D. P.; Toth, D.; Gajdardziska-Josifovska, M. Botanical iron minerals: correlation between nanocrystal structure and modes of biological self-assembly. *Eur. J. Mineral.* **2001**, *13* (6), 1235–1242. <https://doi.org/10.1127/0935-1221/2001/0013-1235>
- Pandey, B. K. Shahi, A. K.; Shah, J.; Kotnala, R. K.; Gopal, R. Optical and magnetic properties of Fe₂O₃ nanoparticles synthesized by laser ablation/fragmentation technique in different liquid media. *Appl. Surf. Sci.* **2014**, *289*, 462–471. <https://doi.org/10.1016/j.apsusc.2013.11.009>
- Papynov, E. K.; Portnyagin, A. S.; Modin, E. B.; Mayorov, V. Y.; Shichalin, O. O.; Golikov, A. P.; Pechnikov, V. S.; Gridasova, E. A.; Tananaev, I. G.; Avramenko, V. A. A complex approach to assessing porous structure of structured ceramics obtained by SPS technique. *Mater. Charact.* **2018**, *145*, 294–302. <https://doi.org/10.1016/j.matchar.2018.08.044>
- Petersen, N.; Schembera, N.; Schmidbauer, E.; Vali, H. Magnetization, Mössbauer spectroscopy and structural studies of a ferrimagnetic Fe-Oxide formed by heating nontronite in air. *Phys. Chem. Miner.* **1987**, *14* (2), 118–121. <https://doi.org/10.1007/BF00308215>
- Pinatti, I. M.; Gouveia, A. F.; Doñate-Buendía, C.; Mínguez-Vega, G.; Andrés, J.; Longo, E. Femtosecond-Laser-Irradiation-Induced Structural Organization and Crystallinity of Bi₂WO₆. *Sci. Rep.* **2020**, *10*, 4613. <https://doi.org/10.1038/s41598-020-61524-y>
- Pottker, W. E.; Ono, R.; Cobos, M. A.; Hernando, A.; Araujo, J. F. D. F.D; Bruno, A. C. O.; Lourenço, S. A.; Longo, E.; La Porta, F. A. Influence of order-disorder effects on the magnetic and optical properties of NiFe₂O₄ nanoparticles. *Ceram. Int.* **2018**, *44* (14), 17290–17297. <https://doi.org/10.1016/j.ceramint.2018.06.190>
- Rietveld, H. M. A profile refinement method for nuclear and magnetic structures. *J. Appl. Crystallogr.* **1969**, *2*, 65–71. <https://doi.org/10.1107/S0021889869006558>
- Sakurai, S.; Jin, J.; Hashimoto, K.; Ohkoshi, S. Reorientation Phenomenon in a Magnetic Phase of ϵ -Fe₂O₃ Nanocrystal. *J. Phys. Soc. Japan.* **2005**, *74* (7), 1946–1949. <https://doi.org/10.1143/JPSJ.74.1946>
- Sakurai, S.; Namai, A.; Hashimoto, K.; Ohkoshi, S. First Observation of Phase Transformation of All Four Fe₂O₃ Phases ($\gamma \rightarrow \epsilon \rightarrow \beta \rightarrow \alpha$ -Phase). *J. Am. Chem. Soc.* **2009**, *131* (51), 18299–18303. <https://doi.org/10.1021/ja9046069>
- Sans, J. A.; Monteseuro, V.; Garbarino, G.; Gich, M.; Cerantola, V.; Cuartero, V.; Monte, M.; Irifune, T.; Muñoz, A.; Popescu, C. Stability and nature of the volume collapse of ϵ -Fe₂O₃ under extreme conditions. *Nat. Commun.* **2018**, *9*, 4554. <https://doi.org/10.1038/s41467-018-06966-9>
- Sarma, S. K.; Mohan, R.; Shukla, A. Structural, optoelectronic and photoelectrochemical properties of tin doped hematite nanoparticles for water splitting. *Mater. Sci. Semicond. Process.* **2020**, *108*, 104873. <https://doi.org/10.1016/j.mssp.2019.104873>
- Schneider, C. A.; Rasband, W. S.; Eliceiri, K. W. NIH Image to ImageJ: 25 years of image analysis. *Nat. Methods.* **2012**, *9*, 671–675. <https://doi.org/10.1038/nmeth.2089>
- Schrader, R.; Büttner, G. Eine neue Eisen(III)-oxidphase: ϵ -Fe₂O₃. *Z. Anorg. Allg. Chem.* **1963**, *320* (5–6), 220–234. <https://doi.org/10.1002/zaac.19633200503>
- Sepúlveda, M.; Gallardo, F.; Ballester, B.; Cabello, G.; Vidal, E. El Condor mine: Prehispanic production and consumption of hematite pigments in the Atacama Desert, northern Chile. *J. Anthropol. Archaeol.* **2019**, *53*, 325–341. <https://doi.org/10.1016/j.jaa.2018.04.001>
- Shabalina, I. G.; Porebskia, P. J.; Minor, W. Refining the macromolecular model – achieving the best agreement with the data from X-ray diffraction experiment. *Crystallogr. Rev.* **2018**, *24* (4), 236–262. <https://doi.org/10.1080/0889311X.2018.1521805>
- Shanenkov, I.; Sivkov, A.; Ivashutenko, A.; Medvedeva, T.; Shchetinin, I. High-energy plasma dynamic synthesis of multiphase iron oxides containing Fe₃O₄ and ϵ -Fe₂O₃ with possibility of controlling their phase composition. *J. Alloys*

- Compd.* **2019**, *774*, 637–645. <https://doi.org/10.1016/j.jallcom.2018.10.019>
- Sharma, P.; Kaur, H.; Sharma, M.; Sahore, V. A review on applicability of naturally available adsorbents for the removal of hazardous dyes from aqueous waste. *Environ. Monit. Assess.* **2011**, *183*, 151–195. <https://doi.org/10.1007/s10661-011-1914-0>
- Sheng, C.; Mat Yunus, W. Study of Photobleaching Mechanism in Methylene Blue Sensitized Gelatin Using a Single Beam UV-Vis. Fibre Optics Spectrophotometer. *Pertanika J. Sci. Technol.* **2005**, *13* (1), 23–30.
- Sivula, K.; Zboril, R.; Le Formal, F.; Robert, R.; Weidenkaff, A.; Tucek, J.; Frydrych, J.; Grätzel, M. Photoelectrochemical Water Splitting with Mesoporous Hematite Prepared by a Solution-Based Colloidal Approach. *J. Am. Chem. Soc.* **2010**, *132* (21), 7436–7444. <https://doi.org/10.1021/ja101564f>
- Sivula, K.; Le Formal, F.; Grätzel, M. Solar Water Splitting: Progress Using Hematite (α -Fe₂O₃) Photoelectrodes. *ChemSusChem.* **2011**, *4* (4), 432–449. <https://doi.org/10.1002/cssc.201000416>
- Sugioka, K.; Cheng, Y. Ultrafast lasers—reliable tools for advanced materials processing. *Light Sci. Appl.* **2014**, *3*, e149. <https://doi.org/10.1038/lsa.2014.30>
- Tamirat, A. G.; Rick, J.; Dubale, A. A.; Su, W.-N.; Hwang, B.-J. Using hematite for photoelectrochemical water splitting: a review of current progress and challenges. *Nanoscale Horiz.* **2016**, *1* (4), 243–267. <https://doi.org/10.1039/C5NH00098J>
- Trench, A. B.; Machado, T. R.; Gouveia, A. F.; Assis, M.; Trindade, L. G. da; Santos, C.; Perrin, A.; Perrin, C.; Oliva, M.; Andrés, J.; Longo, E. Connecting structural, optical, and electronic properties and photocatalytic activity of Ag₃PO₄:Mo complemented by DFT calculations. *Appl. Catal. B.* **2018**, *238*, 198–211. <https://doi.org/10.1016/j.apcatb.2018.07.019>
- Trindade, L. G. da; Hata, G. Y.; Souza, J. C.; Soares, M. R. S.; Leite, E. R.; Pereira, E. C.; Longo, E.; Mazzo, T. M. Preparation and characterization of hematite nanoparticles-decorated zinc oxide particles (ZnO/Fe₂O₃) as photoelectrodes for solar cell applications. *J. Mater. Sci.* **2020**, *55*, 2923–2936. <https://doi.org/10.1007/s10853-019-04135-x>
- Tronc, E.; Chanéac, C.; Jolivet, J. P. Structural and Magnetic Characterization of α -Fe₂O₃. *J. Solid State Chem.* **1998**, *139* (1), 93–104. <https://doi.org/10.1006/jssc.1998.7817>
- Tuček, J.; Machala, L.; Ono, S.; Namai, A.; Yoshikiyo, M.; Imoto, K.; Tokoro, H.; Ohkoshi, S.; Zboril, R. Zeta-Fe₂O₃ – A new stable polymorph in iron(III) oxide family. *Sci. Rep.* **2015**, *5*, 1–11. <https://doi.org/10.1038/srep15091>
- Vadivel, S.; Vanitha, M.; Muthukrishnaraj, A.; Balasubramanian, N. Graphene oxide–BiOBr composite material as highly efficient photocatalyst for degradation of methylene blue and rhodamine-B dyes. *J. Water Process. Eng.* **2014**, *1*, 17–26. <https://doi.org/10.1016/j.jwpe.2014.02.003>
- Von Dreele, R. B.; Larson, A. C. *General Structure Analysis System (GSAS)*. Los Alamos National Lab; 1994, p. 86–748. URL. https://permalink.lanl.gov/object/tr?what=info:lanl-repo/lareport/LA-UR-86-0748_REV (accessed 2022-02-04).
- Vu, X. H.; Phuoc, L. H.; Dien, N. D.; Pham, T. T. H.; Thanh, L. D. Photocatalytic Degradation of Methylene Blue (MB) over α -Fe₂O₃ Nanospindles Prepared by a Hydrothermal Route. *J. Electron. Mater.* **2019**, *48*, 2978–2985. <https://doi.org/10.1007/s11664-019-07056-2>
- Wang, T. H.; Lin, C.-A.; Xu, S.; Wang, C.-F.; Chen, C.-W.; Dong, C.-D.; Huang, C. P. Toward concurrent organics removal and potential hydrogen production in wastewater treatment: Photoelectrochemical decolorization of methylene blue over hematite electrode in the presence of Mn(II). *Appl. Catal. B.* **2019**, *244*, 140–149. <https://doi.org/10.1016/j.apcatb.2018.11.048>
- Wheeler, D. A.; Wang, G.; Ling, Y.; Li, Y.; Zhang, J. Z. Nanostructured hematite: synthesis, characterization, charge carrier dynamics, and photoelectrochemical properties. *Energy Environ. Sci.* **2012**, *5*, 6682–6702. <https://doi.org/10.1039/C2EE00001F>
- Wood, D. L.; Tauc, J. Weak Absorption Tails in Amorphous Semiconductors. *Phys. Rev. B.* **1972**, *5* (8), 3144–3151. <https://doi.org/10.1103/PhysRevB.5.3144>
- Zboril, R.; Mashlan, M.; Petridis, D. Iron(III) Oxides from Thermal Processes Synthesis, Structural and Magnetic Properties, Mössbauer Spectroscopy Characterization, and Applications. *Chem. Mater.* **2002**, *14* (3), 969–982. <https://doi.org/10.1021/cm0111074>
- Zhao, W.; Ma, W.; Chen, C.; Zhao, J.; Shuai, Z. Efficient Degradation of Toxic Organic Pollutants with Ni₂O₃/TiO₂-xBx under Visible Irradiation. *J. Am. Chem. Soc.* **2004**, *126* (15), 4782–4783. <https://doi.org/10.1021/ja0396753>

Influence of Zr-metal-organic framework coupling on the morphology and photoelectrochemical properties of SnO₂

Letícia Guerreiro da Trindade¹⁺, Letícia Zanchet², Bianca Lins Zambon da Silva³, Elson Longo⁴, Tatiana Martelli Mazzo³

1. University of São Paulo, São Carlos Institute of Chemistry, São Carlos, Brazil.

2. Federal University of Rio Grande do Sul, Institute of Chemistry, Porto Alegre, Brazil.

3. Federal University of São Paulo, Institute of Marine Sciences, Santos, Brazil.

4. Federal University of São Carlos, Center for the Development of Functional Materials, São Carlos, Brazil.

+Corresponding author: Letícia Guerreiro da Trindade, **Phone:** +551633518214, **Email address:** lgt.trindade@gmail.com

ARTICLE INFO

Article history:

Received: July 05, 2021

Accepted: November 23, 2021

Published: April 11, 2022

Keywords:

1. Zr-MOF

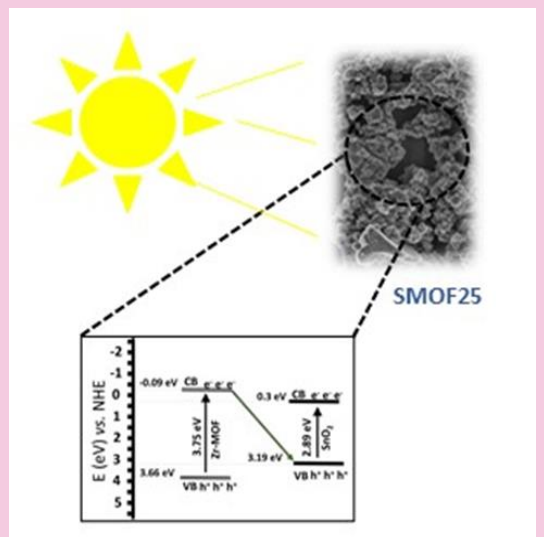
2. solar cells

3. photoelectrode

4. photoelectrochemical properties

Section Editors: Elson Longo and Juan Manuel Andrés Bort

ABSTRACT: In this work, we investigated the effect of the coupling of the Zr-metal-organic framework (MOF) and SnO₂ and its potential for application as photoelectrode in solar cells. Coupling was performed by mechanical mixture followed by heat treatment. The effect of adding two amounts of Zr-MOF (25 and 50 wt%) on morphology and photoelectrochemical properties was investigated. The results of the J-V curves show that the coupling of 25 wt% Zr-MOF with SnO₂ improved the charge transfer characteristics under light irradiated in 1.6 times compared to the pure SnO₂.



1. Introduction

Due to the scarcity of natural resources, the current technological society faces great challenges in relation to its own sustainability (Zhang and Sun, 2019). As a result, the demand for new clean and efficient technologies with lower environmental costs is growing. In this context, solar energy technology stands out, which can be easily found on almost the entire planet.

Research involving solar energy conversion into electricity has drawn a lot of attention, especially in photovoltaic devices such as solar cells (Kojima *et al.*, 2009). Among them, dye-sensitized solar cells (DSSCs) stand out for their low cost and simple fabrication method (Bora *et al.*, 2018; Chen *et al.*, 2018). However, such devices have low power conversion efficiency (PCE), which represents a barrier to the use of these devices in the photovoltaic market (Bashar *et al.*, 2019; Selvaraj *et al.*, 2018). Low PCE is related to the electronic, morphological and optical properties of materials used as photoanodes.

Currently, the most used n-type metal oxide as photoanode in DSSC is TiO₂ (Agbo *et al.*, 2016; Bhogaita *et al.*, 2016). Nevertheless, its material displays some deficiencies, such as low electron mobility and photic instability (W. Yang *et al.*, 2017). In addition, to removing organic compounds of the TiO₂ synthesis of it, it is necessary to use high temperatures, which results in higher production costs (W. Yang *et al.*, 2017). A great candidate to replace the conventional TiO₂ layer is the SnO₂ (Jiang *et al.*, 2017; Ke *et al.*, 2015) due to its wide bandgap, high optical transmittance in the visible, high mobility (240 cm² V⁻¹ s⁻¹), excellent optical and chemical stability, and low-cost preparation at low temperature (Mathiazhagan *et al.*, 2020). However, as the SnO₂ conduction band-edge is more positive than TiO₂ (~ 400 mV), under 1 Sun simulated light (AM 1.5 G) using a solar simulator, the Fermi quasi-equilibrium level will shift down to the redox potential of the liquid electrolyte, resulting in a lower open-circuit voltage compared to TiO₂ (Suresh *et al.*, 2018). These characteristics may make the DSSCs that use SnO₂ as photoanode achieve PCE of only 1.2% while DSSCs working with TiO₂ have a PCE of 5.9% (Concina and Vomiero, 2014). In order to overcome these limitations presented by SnO₂, an alternative found is the modification of its surface (Qian *et al.*, 2009).

The unique characteristics of the metal-organic frameworks (MOFs) such as high porosity, high surface area, accessible active internal energy migration pathways that can increase the electron

transfer and reduce the charge recombination, have motivated research about their photocatalytic and photovoltaic applications (Zhang *et al.*, 2020). MOFs are hybrid materials built by combining the organic ligands and metal nodes through coordinate bonds (Bao *et al.*, 2016; H. Liu *et al.*, 2016; Li *et al.*, 2016).

Recently, our group investigated the coupling of ZnO and Zr-MOF to develop a photoanode to be applied in DSSCs. In this research, the results showed that the ZnO electrode with 25 wt% Zr-MOF has the ability to potentiate charge transport and inhibit charge recombination, making it a promising photoelectrode for solar cells (da Trindade *et al.*, 2021).

Based on our previous results, in this present work, we seek to report the investigation of the Zr-MOF/SnO₂ coupling in the SnO₂ morphology and its photoelectrochemical properties for future application in photoanodes for DSSCs.

2. Experimental

2.1 SnO₂ synthesis

The coprecipitation method in aqueous media was used to prepare the SnO₂ particles. In this method, SnCl₂·2H₂O (6.77 g, Vetec) was mixed with deionized H₂O (30 mL) under constant stirring at room temperature. After dissolution, H₂O₂ (35 mL, Synth) and KOH solution (35 mL/2 mol L⁻¹, Synth) were added. The precipitate was washed with deionized water until pH = 7. The obtained material was oven-dried at 60 °C for 8 h.

2.2 Zr-MOF synthesis

The metal-organic framework synthesis (Zr-MOF) was performed by a solvothermal method as related in our previous work (da Trindade *et al.*, 2019). The ZrCl₄ (1.4 mmol, Aldrich) and terephthalic acid (1.4 mmol, Aldrich) were previously dissolved in N, N-dimethylformamide (DMF, 99.8%, Aldrich) and the solution was put in an autoclave. The reaction was kept in a greenhouse at 125 °C for 24 h. After this time the obtained precipitate was washed with methanol and dried at 60 °C.

2.3 Electrode preparation

The electrodes were prepared with SnO₂ and Zr-MOF using two mass ratios of Zr-MOF, according to Tab. 1. The electrode preparation procedure was performed according to the literature (da Trindade *et*

al., 2018; 2020a). Viscous pastes were prepared by mixing the desired particles with ethanol (200 μL) and sonicated for 30 min. After this, deionized water (60 μL) was added, and the mixture was sonicated again for 30 min. The obtained suspensions were applied onto fluorine-doped tin oxide (FTO) substrates in an area of 1 cm^2 using a micropipette. The films were allowed to dry at 25 $^\circ\text{C}$ for 1 h, and then calcined at 400 $^\circ\text{C}$ for 1 h, at heating and cooling rates of 0.1 $^\circ\text{C min}^{-1}$.

Table 1. Samples designation and composition.

Sample designation	SnO ₂ (g)	Zr-MOF (g)
SnO ₂	0.0125	-
Zr-MOF	0.0125	-
SMOF25	0.0094	0.0031
SMOF50	0.0062	0.0062

2.4 Samples characterization

All samples were characterized by X-ray diffraction (XRD, Rigaku detector (CuK α , $\lambda = 0.15406$ nm), Fourier-transform infrared spectroscopy (FTIR, Bruker EQUINOX 55 spectrometer), thermogravimetry (TG) analysis (TA Instruments Q-50 apparatus), field emission gun-scanning electron microscope (FEG-SEM, ZEISS model 105 DSM940A instrument, 10 keV), UV-Vis spectra (Cary 5 G [Varian] apparatus) and Brunauer-Emmett-Teller (BET) surface area measurements (Micromeritics TriStar II 3020).

The photoelectrochemical measurements were performed in a three-electrode cell where the prepared electrode, Pt wire and Ag/AgCl electrode have been used as working, counter and reference electrodes, respectively. This cell had a quartz glass window, and the electrolyte was acetonitrile solution with LiI (10 mmol L^{-1}), I₂ (1 mmol L^{-1}), and LiClO₄ (0.1 mol L^{-1}). The current density-voltage (J-V) curves of the samples have been analyzed for both illuminated and dark conditions using an Autolab PGSTAT302 N potentiostat and a Newport Sol3A Class AAA solar simulator with a 100 W Xenon lamp.

3. Results and discussion

Figure 1 shows the XRD patterns of all samples. The SnO₂ presents 2θ diffraction angles at 26.4, 33.7, 37.8, 51.6, 54.2, 62.1, 65.5 and 78.6 degrees and (110), (101), (200), (211), (220), (310), (301) and (321) diffraction planes, respectively, corresponding to rutile structure (JCPDS n^o: 41-1445) (Debataraja *et al.*, 2017). The Zr-MOF presents the XRD patterns that

correspond with the Zr-MOF (UiO-66) reported previously (Luan *et al.*, 2015; da Trindade *et al.*, 2020b). When the SnO₂ sample is modified with 25 or 50 wt% of Zr-MOF, it can be observed that the referring to SnO₂ and an absorption peak appears between 5 and 10 $^\circ$, which confirms the presence of Zr-MOF in both samples. It is also possible to observe that in the 50 wt% sample the presence of other diffraction peaks referring to Zr-MOF. This result was expected since there was a significant increase in the Zr-MOF mass amount compared to the 25 wt% sample.

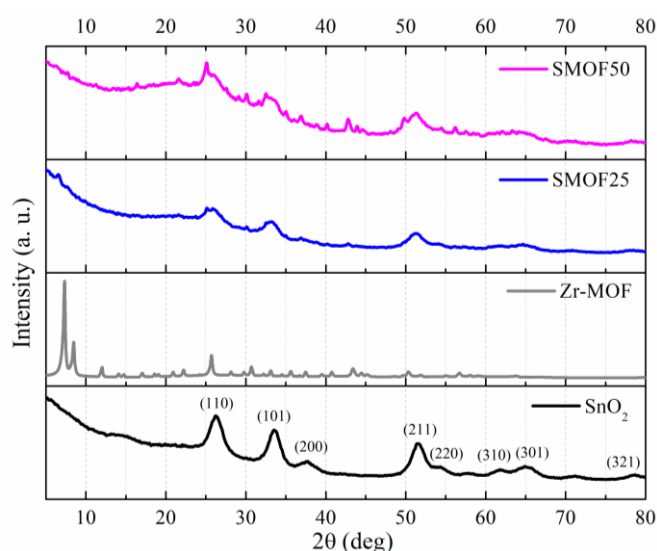


Figure 1. XRD patterns of SnO₂, Zr-MOF, SMOF25 and SMOF50 samples.

Figure 2 shows the FTIR and TG analyzes of SnO₂, Zr-MOF and modified samples. At the SnO₂ FTIR spectrum (Fig. 2a) we observed bands in 3300 and 1640 cm^{-1} that can be attributed to the O-H stretching of adsorbed water molecules. In addition, the band at 640 cm^{-1} refers to framework vibrations of SnO₂ (Zhan *et al.*, 2013). The Zr-MOF spectrum presents broadband at 3300 cm^{-1} that is due to the O-H stretching from water molecules in the MOFs (Zango *et al.*, 2020). The well-defined bands at 1570 and 1387 cm^{-1} refer to the C=O and C-N stretching modes, respectively. The C_{Ar}, δ -H stretching modes and the Zr₆(OH)₄O₄ cluster appears at 750 and 666 cm^{-1} , respectively (Butova *et al.*, 2020; da Trindade *et al.*, 2020b). For the modified samples, SMOF25 and SMOF50, similar spectra can be noted. Characteristic peaks of the SnO₂ and Zr-MOF were observed at both modified samples. However, the intensity of the bands increases with increasing the MOF amount in the sample. These results affirm that the Zr-MOF was successfully coupling into the SnO₂ corroborating the

data observed by XRD. TG measurements were carried out to verify the thermal stability of SnO₂, Zr-MOF and modified samples (Fig. 2b). The pure SnO₂ sample presents only one stage of weight loss of 7% from 25 to 80 °C due to the removal of adsorbed water molecules. Zr-MOF has three stages of mass loss with first up to 125 °C which is attributed to desorption of physisorbed water, the second between 125–550 °C which may be due to the removal of the solvent (DMF) and the dehydroxylation of the zirconium oxo-clusters (X. Liu *et al.*, 2016) and the last stage (550–700 °C) is due to the Zr-MOF decomposition (Q. Yang *et al.*, 2018). When 25 wt % Zr-MOF is coupled to SnO₂ (SMOF25), it can be observed that there is an increase in thermal stability in relation to the pure SnO₂ sample. In the SMOF25 sample, there is an initial weight loss of approximately 3% that can be attributed to the removal of adsorbed water molecules. The increase in the initial thermal stability also is observed for the SMOF50 sample with a mass loss of 6%. However, at 500 °C the beginning of the Zr-MOF decomposition is observed. These data show that adding 25 wt % Zr-MOF to the SnO₂ sample works as a thermal stabilizer.

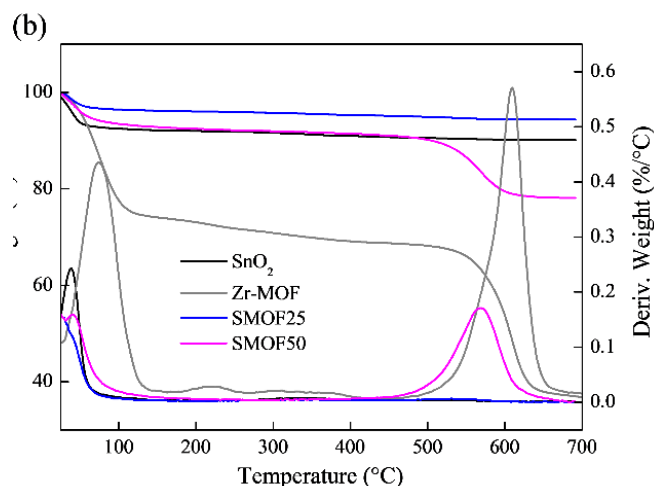
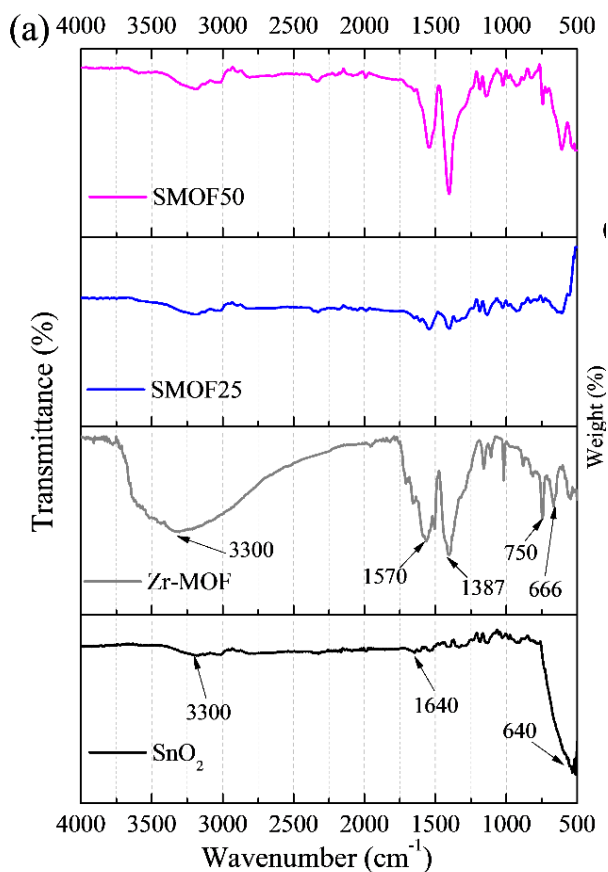
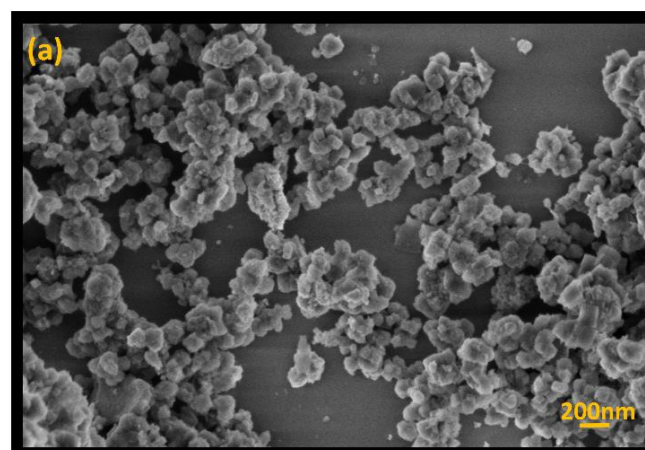


Figure 2. FTIR spectra (a) and TG curves (b) of SnO₂, Zr-MOF, SMOF25 and SMOF50 samples.

FE-SEM images for all samples are shown in Fig. 3. SnO₂ particles (Fig. 3a) tend to form agglomerates with irregular shapes. The Zr-MOF sample has an octahedral shape with different sizes as reported in the literature (Waitschat *et al.*, 2018). When 25 wt% Zr-MOF is coupled to the SnO₂ (Fig. 3c), there is a tendency to form clustered structures which are potentiated by increasing the Zr-MOF mass ratio (Fig. 3d). In the SMOF50 sample, the formation of agglomerates of smaller and fewer uniform particles is observed.



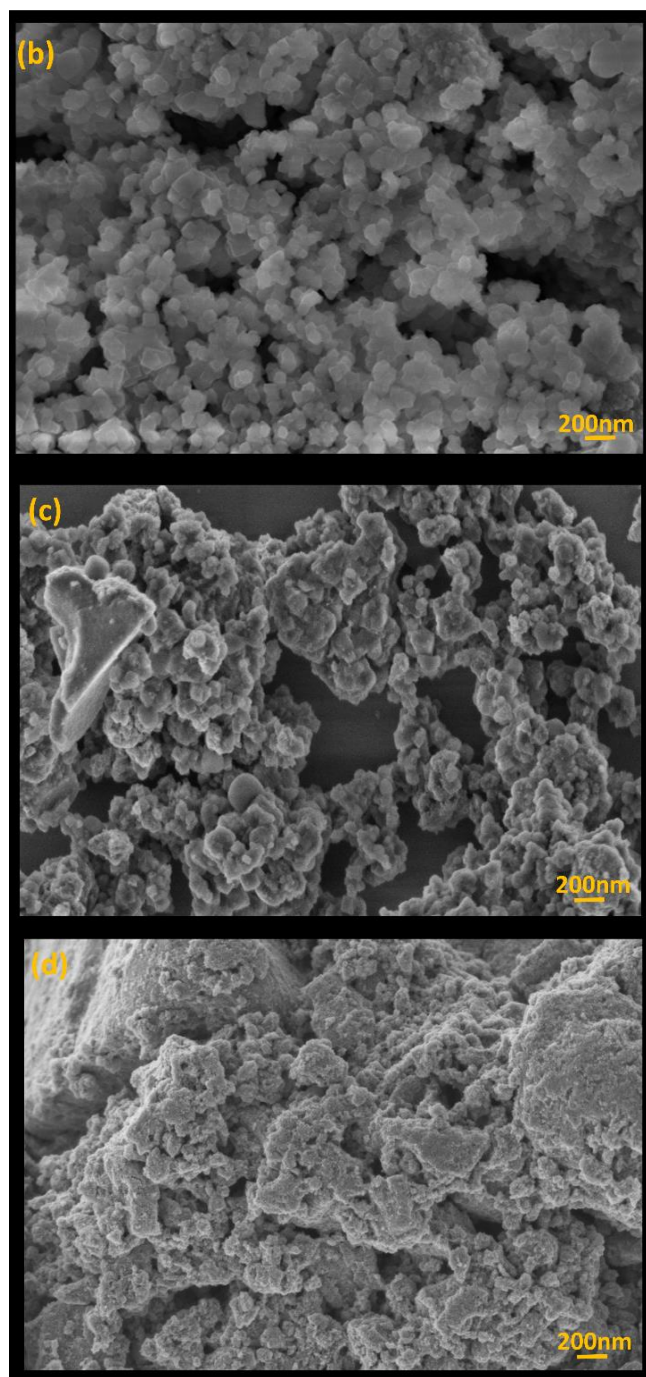
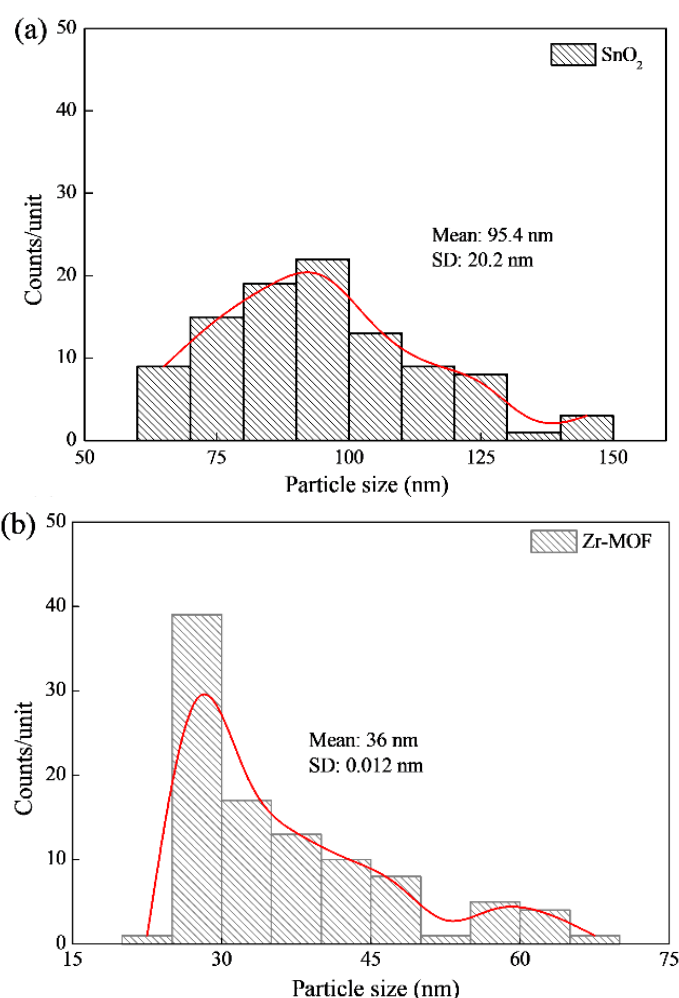


Figure 3. FE-SEM images of SnO₂ (a), Zr-MOF (b), SMOF25 (c), and SMOF50 (d) samples.

Through the FE-SEM images, the particle size was estimated, Fig. 4a–d. The SnO₂ and the Zr-MOF samples present approximately 95.4 and 36 nm particle sizes, respectively. When these two samples are coupled, the particle sizes obtained are approximately 99.6 and 148.7 nm for SMOF25 and SMOF50 samples, respectively. These results reveal that the coupling of SnO₂ with Zr-MOF provokes an increase in particle size. The N₂ adsorption-desorption isotherms of SnO₂,

Zr-MOF, SMOF25 and SMOF50 particles are shown in Fig. 4e. The SnO₂ and SMOF25 samples show typical type IV isotherms with a hysteresis loop and, the Zr-MOF and SMOF50 samples present typical type I isotherms. Type IV isotherms are characteristic of mesoporous nature and the hysteresis loop commonly suggests improved pore size and pore connectivity of the synthesized samples (Malleham *et al.*, 2020). While type I isotherms indicate the microporous nature of the synthesized samples (Q. Yang *et al.*, 2018). It can be hypothesized that the reduction of the specific surface area with the addition of the Zr-MOF implies that the SnO₂/Zr-MOF coupling results in the reduction of the vacancies in the Zr-MOF (Fu *et al.*, 2019).



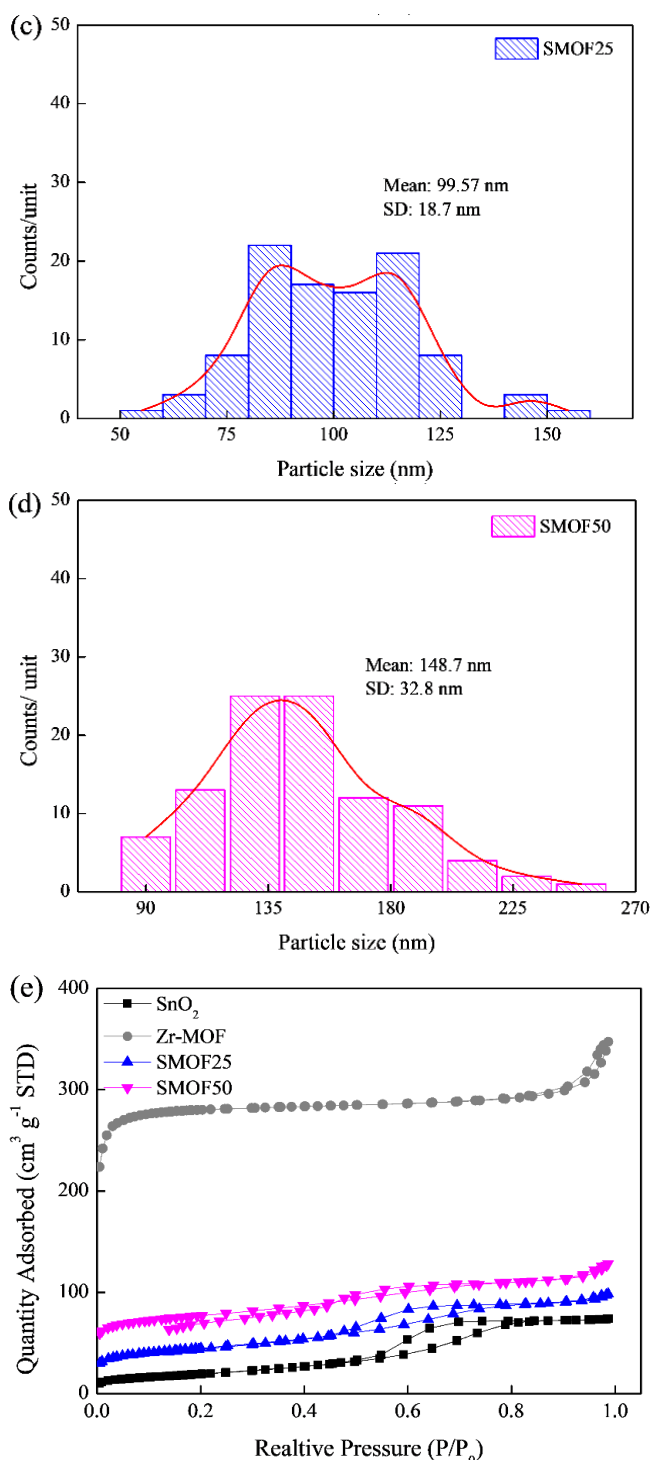


Figure 4. Particle sizes of SnO₂ (a), Zr-MOF (b), SMOF25 (c), and SMOF50 (d), and typical N₂ adsorption–desorption isotherm (e) of the samples.

The BET surface area and pore diameter are presented in Tab. 2. These results show that when SnO₂ is coupling with Zr-MOF the surface area increases from 68.44 m² g⁻¹ to 158 and 270.3 m² g⁻¹ with the addition of 25 and 50 wt% of Zr-MOF (SMOF25 and

SMOF50), respectively. In contrast, the pore diameter decreases with coupling. These changes observed in the surface area and pore diameter can be caused by the increase of clusters formation as a result of the increase of the particles sizes.

Table 2. BET surface area and pore diameter, and FE-SEM average particle size of the samples.

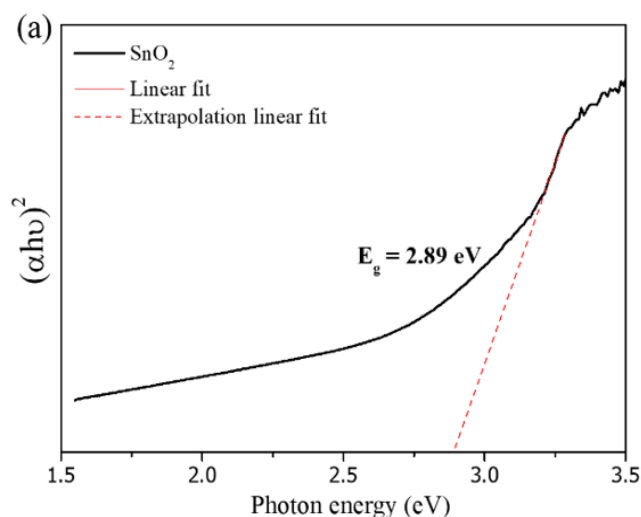
Sample	BET		FE-SEM
	Surface area (m ² g ⁻¹)	Pore diameter (nm)	Average particle size (nm)
SnO ₂	68.44	4.5	95.4
Zr-MOF	985.2	10.0	36.0
SMOF25	158.0	4.3	99.6
SMOF50	270.3	3.4	148.7

The Tauc method was used to determining the bandgap (Coulter *et al.*, 2017), Eq. 1:

$$(\alpha h\nu)^{1/n} = A(h\nu - E_g) \quad (1)$$

where h is Planck's constant, ν is the photon's frequency, α is the absorption coefficient, E_g is the bandgap, and A is the slope of the Tauc plot in the linear region.

The SnO₂ and Zr-MOF are direct bandgap semiconductors with n equal to 1/2 (Ganose and Scanlon, 2016; Hendrickx *et al.*, 2018). The E_g values for all samples are shown in Fig. 5. The bandgap values are 2.89, 3.75, 2.27 and 2.12 eV for SnO₂, Zr-MOF, SMOF25 and SMOF50 samples, respectively. It can be seen that the bandgap is reduced with increasing in Zr-MOF concentration coupled to SnO₂. This behavior can be explained by factors like particle size, optical properties and surface morphology, which influence the penetration of light photons (da Trindade *et al.*, 2021).



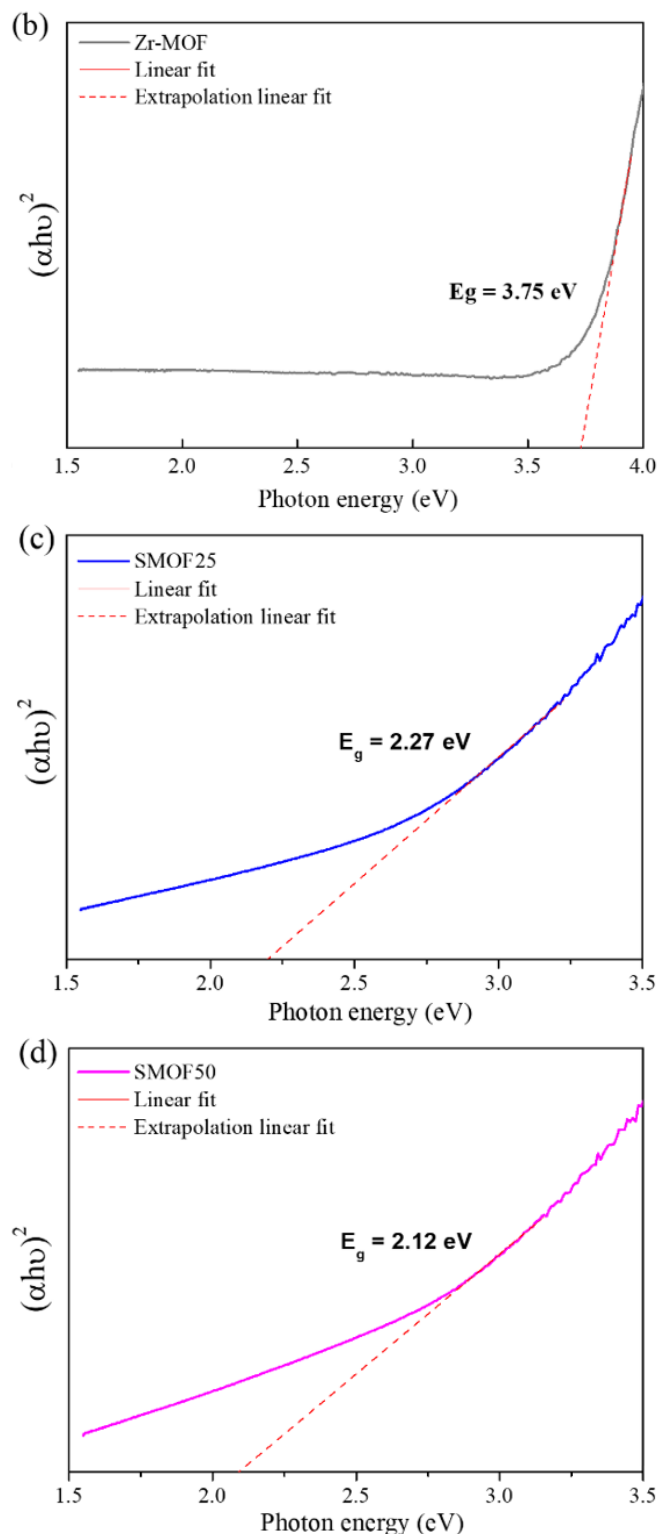


Figure 5. Tauc plot from UV-Vis analysis of SnO₂ (a), Zr-MOF (b), SMOF25 (c) and SMOF50 (d) samples.

The J-V curves of SnO₂, SMOF25 and SMOF50 photoanodes were analyzed in the potential range of 0–1.3 V at 20 mV s⁻¹ in an I₃⁻/I⁻ solution, Fig. 6. Current densities at 1.0 V in the presence of

light are 2.77, 4.5 and 2.23 mA cm⁻² for SnO₂, SMOF25 and SMOF 50, respectively. The results show that the coupling of 25 wt% Zr-MOF with SnO₂ improved the charge transfer characteristics under light irradiated compared to the pure SnO₂ and SMOF50 samples. The SMOF50 sample presented a current density lower than the other samples, indicating that 50 wt% Zr-MOF can reduce the active sites and delay the diffusion process for the electrolyte. This result demonstrates that the coupling of 25 wt% Zr-MOF with SnO₂ is promising for the development of photoanodes for DSSCs considering that the values of short-circuit density (J_{sc}), found in the literature, for the pure TiO₂ can range from 2.51 to 12.9 mA cm⁻² (Concina and Vomiero, 2014; Khannam *et al.*, 2016). In the present work, the DSSC device was not assembled, we only tested the photoanode in I₃⁻/I⁻ solution and without sensitized it by immersing in a dye solution. Therefore, by the obtained results, it is expected that when tested in the DSSC it will reach values similar or superior to cells with TiO₂.

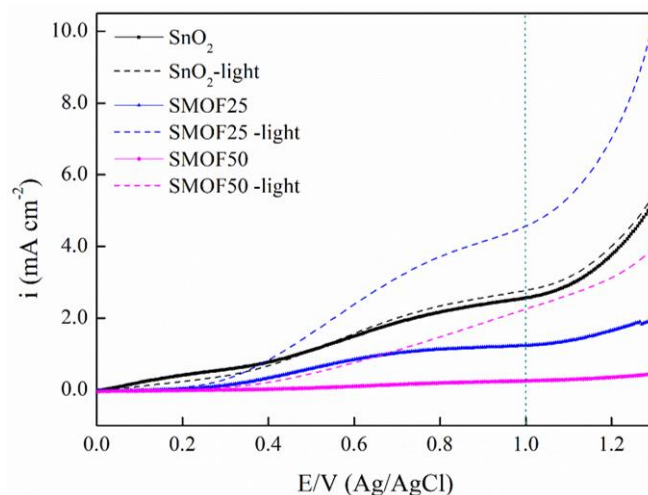


Figure 6. J-V curves of the SnO₂, Zr-MOF, SMOF25 and SMOF50 samples at 20 mV s⁻¹.

The valence band (E_{VB}) and conduction band (E_{CB}) potentials can be calculated by the Mulliken method, Eqs. 2 and 3, respectively (Kandasamy *et al.*, 2018):

$$E_{VB} = \chi - E_e + 0.5E_g \quad (2)$$

$$E_{CB} = E_{VB} - E_g \quad (3)$$

where χ is the electronegativity of the semiconductor and E_e is the energy of the free electrons on the hydrogen scale (4.5 eV) and E_g is the bandgap energy of the material.

The SnO₂ electronegativity is 6.25 eV and the E_{CB} of Zr-MOF is -0.09 eV (vs. NHE); so, we can propose an energy band diagram for Zr-MOF coupling with SnO₂, Fig. 7 (Abdelkader *et al.*, 2015; Wang *et al.*, 2016). In the proposed energy band diagram when the SnO₂/Zr-MOF sample is exposed to visible light, the photogenerated electrons (e⁻) in the Zr-MOF conduction band (CB) migrated to SnO₂, while the holes (h⁺) remained in the Zr-MOF valence band (VB), resulting in the separation of the charge carriers.

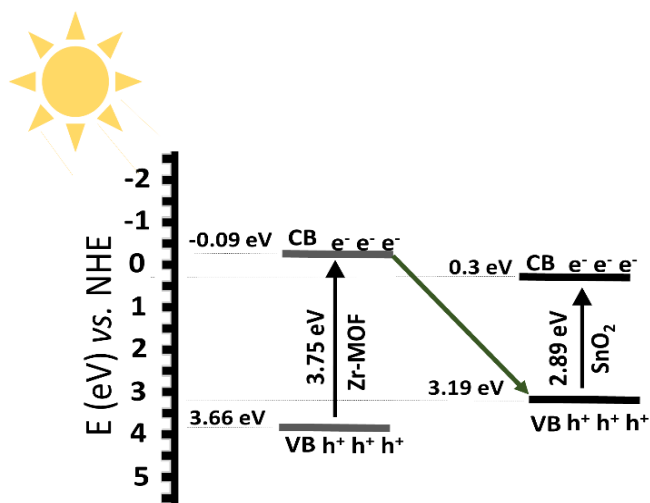


Figure 7. Proposed energy band diagram of the SnO₂/Zr-MOF composite.

4. Conclusions

The Zr-MOF coupling in the SnO₂ was prepared by mechanical mixture followed by heat treatment. The effect of the coupling has been investigated using structural, optical and photoelectrochemical analysis. The XRD and the FTIR reveals the incorporation of Zr-MOF into the SnO₂ lattice. The FE-SEM characterization shows an increase in the tendency to form clusters with an increase in the Zr-MOF concentration. The J-V data show that the coupling of 25 wt% Zr-MOF with SnO₂ improved 1.6 times the charge transfer characteristics under light irradiated compared to the pure SnO₂ and 2 times when compared to the SMOF50 sample. This result demonstrates that the coupling of 25 wt% Zr-MOF with SnO₂ is promising for the development of photoanodes for DSSCs.

Authors' contribution

Conceptualization: da Trindade, L. G.

Data curation: Silva, B. L. Z.; da Trindade, L. G.

Formal Analysis: Silva, B. L. Z.; da Trindade, L. G.; Zanchet, L.

Funding acquisition: Not applicable.

Investigation: da Trindade, L. G.

Methodology: da Trindade, L. G.; Mazzo, T. M.

Project administration: Mazzo, T. M.; da Trindade, L. G.

Resources: Longo, E.

Software: Not applicable.

Supervision: Mazzo, T. M.

Validation: da Trindade, L. G.

Visualization: da Trindade, L. G.

Writing – original draft: da Trindade, L. G.; Zanchet, L.

Writing – review & editing: Mazzo, T. M.; Longo, E.; da Trindade, L. G.

Data availability statement

The data will be available upon request.

Funding

Conselho Nacional de Desenvolvimento Científico e Tecnológico (CNPq). Grant No: 163342/2020-2.

Fundação de Amparo à Pesquisa do Estado de São Paulo (FAPESP). Grant No: 2013/07296-2.

Coordenação de Aperfeiçoamento de Pessoal de Nível Superior (CAPES). Finance Code: 001.

Acknowledgments

Not applicable.

References

Abdelkader, E.; Nadjia, L.; Ahmed, B. Preparation and characterization of novel CuBi₂O₄/SnO₂ p-n heterojunction with enhanced photocatalytic performance under UVA light irradiation. *J. King Saud Univ. Sci.* **2015**, *27* (1), 76–91. <https://doi.org/10.1016/j.jksus.2014.06.002>

Agbo, S. N.; Merdzhanova, T.; Yu, S.; Tempel, H.; Kungl, H.; Eichel, R.-A.; Rau, U.; Astakhov, O. Photoelectrochemical application of thin-film silicon triple-junction solar cell in batteries. *Phys. Status Solidi A* **2016**, *213* (7), 1926–1931. <https://doi.org/10.1002/pssa.201532918>

Bao, C.; Zhou, L.; Shao, Y.; Wu, Q.; Zhu, H.; Li, K. A novel Au-loaded magnetic metal organic framework/graphene multifunctional composite: Green synthesis and catalytic

- application. *J. Ind. Eng. Chem.* **2016**, *38*, 132–140. <https://doi.org/10.1016/j.jiec.2016.04.014>
- Bashar, H.; Bhuiyan, M. M. H.; Hossain, M. R.; Kabir, F.; Rahaman, M. S.; Manir, M. S.; Ikegami, T. Study on combination of natural red and green dyes to improve the power conversion efficiency of dye sensitized solar cells. *Optik* **2019**, *185*, 620–625. <https://doi.org/10.1016/j.jileo.2019.03.043>
- Bhogaita, M.; Yadav, S.; Bhanushali, A. U.; Parsola, A. A.; Nalini, R. P. Synthesis and characterization of TiO₂ thin films for DSSC prototype. *Mater. Today: Proc.* **2016**, *3* (6), 2052–2061. <https://doi.org/10.1016/j.matpr.2016.04.108>
- Bora, A.; Mohan, K.; Phukan, P.; Dolui, S. K. A low cost carbon black/polyaniline nanotube composite as efficient electro-catalyst for triiodide reduction in dye sensitized solar cells. *Electrochim. Acta* **2018**, *259*, 233–244. <https://doi.org/10.1016/j.electacta.2017.10.156>
- Butova, V. V.; Vetlitsyna-Novikova, K. S.; Pankin, I. A.; Charykov, K. M.; Trigub, A. L.; Soldatov, A. V. Microwave synthesis and phase transition in UiO-66/MIL-140A system. *Microporous Mesoporous Mater.* **2020**, *296*, 109998. <https://doi.org/10.1016/j.micromeso.2020.109998>
- Chen, L.; Chen, W.; Wang, E. Graphene with cobalt oxide and tungsten carbide as a low-cost counter electrode catalyst applied in Pt-free dye-sensitized solar cells. *J. Power Sources* **2018**, *380*, 18–25. <https://doi.org/10.1016/j.jpowsour.2017.11.057>
- Concina, I.; Vomiero, A. Metal oxide semiconductors for dye- and quantum-dot-sensitized solar cells. *Small* **2014**, *11* (15), 1744–1774. <https://doi.org/10.1002/smll.201402334>
- Coulter, J. B.; Birnie III, D. P. Assessing Tauc plot slope quantification: ZnO thin films as a model system. *Phys. Status Solidi B* **2017**, *255* (3), 1700393. <https://doi.org/10.1002/pssb.201700393>
- da Trindade, L. G.; Minervino, G. B.; Trench, A. B.; Carvalho, M. H.; Assis, M.; Li, M. S.; Oliveira, A. J. A.; Pereira, E. C.; Mazzo, T. M.; Longo, E. Influence of ionic liquid on the photoelectrochemical properties of ZnO particles. *Ceram. Int.* **2018**, *44* (9), 10393–10401. <https://doi.org/10.1016/j.ceramint.2018.03.053>
- da Trindade, L. G.; Borba, K. M. N.; Zanchet, L.; Lima, D. W.; Trench, A. B.; Rey, F.; Diaz, U.; Longo, E.; Bernardo-Gusmão, K.; Martini, E. M. A. SPEEK-based proton exchange membranes modified with MOF-encapsulated ionic liquid. *Mater. Chem. Phys.* **2019**, *236*, 121792. <https://doi.org/10.1016/j.matchemphys.2019.121792>
- da Trindade, L. G.; Hata, G. Y.; Souza, J. C.; Soares, M. R. S.; Leite, E. R.; Pereira, E. C.; Longo, E.; Mazzo, T. M. Preparation and characterization of hematite nanoparticles-decorated zinc oxide particles (ZnO/Fe₂O₃) as photoelectrodes for solar cell applications. *J. Mater. Sci.* **2020a**, *55*, 2923–2936. <https://doi.org/10.1007/s10853-019-04135-x>
- da Trindade, L. G.; Zanchet, L.; Dreon, R.; Souza, J. C.; Assis, M.; Longo, E.; Martini, E. M. A.; Chiquito, A. J.; Pontes, F. M. Microwave-assisted solvothermal preparation of Zr-BDC for modification of proton exchange membranes made of SPEEK/PBI blends. *J. Mater. Sci.* **2020b**, *55*, 14938–14952. <https://doi.org/10.1007/s10853-020-05068-6>
- da Trindade, L. G.; Borba, K. M. N.; Trench, A. B.; Zanchet, L.; Teodoro, V.; Pontes, F. M. L.; Longo, E.; Mazzo, T. M. Effective strategy to coupling Zr-MOF/ZnO: Synthesis, morphology and photoelectrochemical properties evaluation. *J. Solid State Chem.* **2021**, *293*, 121794. <https://doi.org/10.1016/j.jssc.2020.121794>
- Debataraja, A.; Zuhendri, D. W.; Yulianto, B.; Nugraha; Hiskia; Sunendar, B. Investigation of nanostructured SnO₂ synthesized with polyol technique for CO gas sensor applications. *Procedia Eng.* **2017**, *170*, 60–64. <https://doi.org/10.1016/j.proeng.2017.03.011>
- Fu, Y.; Wu, J.; Du, R.; Guo, K.; Ma, R.; Zhang, F.; Zhu, W.; Fan, M. Temperature modulation of defects in NH₂-UiO-66(Zr) for photocatalytic CO₂ reduction. *RSC Adv.* **2019**, *9*, 37733–37738. <https://doi.org/10.1039/C9RA08097J>
- Ganose, A. M.; Scanlon, D. O. Band gap and work function tailoring of SnO₂ for improved transparent conducting ability in photovoltaics. *J. Mater. Chem. C* **2016**, *4* (7), 1467–1475. <https://doi.org/10.1039/C5TC04089B>
- Hendrickx, K.; Joos, J. J.; De Vos, A.; Poelman, D.; Smet, P. F.; Van Speybroeck, V.; Van Der Voort, P.; Lejaeghere, K. Exploring lanthanide doping in UiO-66: A combined experimental and computational study of the electronic structure. *Inorg. Chem.* **2018**, *57* (9), 5463–5474. <https://doi.org/10.1021/acs.inorgchem.8b00425>
- Jiang, Q.; Zhang, L.; Wang, H.; Yang, X.; Meng, J.; Liu, H.; Yin, Z.; Wu, J.; Zhang, X.; You, J. Enhanced electron extraction using SnO₂ for high-efficiency planar-structure HC(NH₂)₂PbI₃-based perovskite solar cells. *Nat. Energy* **2017**, *2*, 16177. <https://doi.org/10.1038/nenergy.2016.177>
- Kandasamy, M.; Seetharaman, A.; Sivasubramanian, D.; Nithya, A.; Jothivenkatachalam, K.; Maheswari, N.; Gopalan, M.; Dillibabu, S.; Eftekhari, A. Ni-doped SnO₂ nanoparticles for sensing and photocatalysis. *ACS Appl. Nano Mater.* **2018**, *10* (1), 5823–5836. <https://doi.org/10.1021/acsnm.8b01473>
- Ke, W.; Fang, G.; Liu, Q.; Xiong, L.; Qin, P.; Tao, H.; Wang, J.; Lei, H.; Li, B.; Wan J.; Yang, G.; Yan. Y. Low-temperature solution-processed tin oxide as an alternative electron transporting layer for efficient perovskite solar cells.

- J. Am. Chem. Soc.* **2015**, *137* (21), 6730–6733. <https://doi.org/10.1021/jacs.5b01994>
- Khannam, M.; Sharma, S.; Dolui, S.; Dolui, S. K. Graphene oxide incorporated TiO₂ photoanode for high efficiency quasi solid state dye sensitized solar cells based on poly-vinyl alcohol gel electrolyte. *RSC Adv.* **2016**, *6*, 55406–55414. <https://doi.org/10.1039/C6RA07577K>
- Kojima, A.; Teshima, K.; Shirai, Y.; Miyasaka, T. Organometal halide perovskites as visible-light sensitizers for photovoltaic cells. *J. Am. Chem. Soc.* **2009**, *131* (17), 6050–6051. <https://doi.org/10.1021/ja809598r>
- Li, Y.; Xu, H.; Ouyang, S.; Ye, J. Metal–organic frameworks for photocatalysis. *Phys. Chem. Chem. Phys.* **2016**, *18* (11), 7563–7572. <https://doi.org/10.1039/C5CP05885F>
- Liu, H.; Ren, X.; Chen, L. Synthesis and characterization of magnetic metal–organic framework for the adsorptive removal of Rhodamine B from aqueous solution. *J. Ind. Eng. Chem.* **2016**, *34*, 278–285. <https://doi.org/10.1016/j.jiec.2015.11.02>
- Liu, X.; Zhao, X.; Zhou, M.; Cao, Y.; Wu, H.; Zhu, J. Highly stable and active palladium nanoparticles supported on a mesoporous UiO66@reduced graphene oxide complex for practical catalytic applications. *Eur. J. Inorg. Chem.* **2016**, *2016* (20), 3338–3343. <https://doi.org/10.1002/ejic.201600367>
- Luan, Y.; Qi, Y.; Gao, H.; Andriamitantoa, R. S.; Zheng, N.; Wang, G. A general post-synthetic modification approach of amino-tagged metal–organic frameworks to access efficient catalysts for the Knoevenagel condensation reaction. *J. Mater. Chem. A* **2015**, *3* (33), 17320–17331. <https://doi.org/10.1039/C5TA00816F>
- Mallesham, B.; Rangaswamy, A.; Rao, B.G.; Rao, T. V.; Reddy, B. M. Solvent-free production of glycerol carbonate from bioglycerol with urea over nanostructured promoted SnO₂ catalysts. *Catal. Lett.* **2020**, *150*, 3626–3641. <https://doi.org/10.1007/s10562-020-03241-9>
- Mathiazhagan, G.; Seeber, A.; Gengenbach, T.; Mastroianni, S.; Vak, D.; Chesman, A. S. R.; Gao, M.; Angmo, D.; Hirsch, A. Improving the stability of ambient processed, SnO₂-based, perovskite solar cells by the UV-treatment of sub-cells. *Sol. RRL* **2020**, *4* (9), 2000262. <https://doi.org/10.1002/solr.202000262>
- Qian, J.; Liu, P.; Xiao, Y.; Jiang, Y.; Cao, Y.; Ai, X.; Yang, H. TiO₂-coated multilayered SnO₂ hollow microspheres for dye-sensitized solar cells. *Adv. Mater.* **2009**, *21* (36), 3663–3667. <https://doi.org/10.1002/adma.200900525>
- Selvaraj, P.; Baig, H.; Mallick, T. K.; Siviter, J.; Montecucco, A.; Li, W.; Paul, M.; Sweet, T.; Gao, M.; Knox, A. R.; Sundaram, S. Enhancing the efficiency of transparent dye-sensitized solar cells using concentrated light. *Sol. Energy Mater. Sol. Cells* **2018**, *175*, 29–34. <https://doi.org/10.1016/j.solmat.2017.10.006>
- Suresh, S.; Unni, G. E.; Satyanarayana, M.; Nair, A. S.; Pillai, V. P. M. Plasmonic Ag@Nb₂O₅ surface passivation layer on quantum confined SnO₂ films for high current dye-sensitized solar cell applications. *Electrochim. Acta* **2018**, *289*, 1–12. <https://doi.org/10.1016/j.electacta.2018.08.078>
- Waitschat, S.; Fröhlich, D.; Reinsch, H.; Terraschke, H.; Lomachenko, K. A.; Lamberti, C.; Kummer, H.; Helling, T.; Baumgartner, M.; Henninger, S.; Stock, N. Synthesis of MUiO-66 (M = Zr, Ce or Hf) Employing 2,5-Pyridinedicarboxylic Acid as a linker: Defect chemistry, framework hydrophilisation and sorption properties. *Dalton. Trans.* **2018**, *47* (4), 1062–1070. <https://doi.org/10.1039/C7DT03641H>
- Wang, A.; Zhou, Y.; Wang, Z.; Chen, M.; Sun, L.; Liu, X. Titanium incorporated with UiO-66(Zr)-type Metal–Organic Framework (MOF) for photocatalytic application. *RSC Adv.* **2016**, *6* (5), 3671–3679. <https://doi.org/10.1039/C5RA24135A>
- Yang, W. S.; Park, B.-W.; Jung, E. H.; Jeon, N. J.; Kim, Y. C.; Lee, D. U.; Shin, S. S.; Seo, J.; Kim, E. K.; Noh, J. H.; Seok, S. I. Iodide management in formamidinium-lead-halide-based perovskite layers for efficient solar cells. *Science* **2017**, *356* (6345), 1376–1379. <https://doi.org/10.1126/science.aan2301>
- Yang, Q.; Zhang, H.-Y.; Wang, L.; Zhang, Y.; Zhao, J. Ru/UiO-66 catalyst for the reduction of nitroarenes and tandem reaction of alcohol oxidation/knoevenagel condensation. *ACS Omega* **2018**, *3* (4), 4199–4212. <https://doi.org/10.1021/acsomega.8b00157>
- Zango, Z. U.; Sambudi, N. S.; Jumbri, K.; Bakar, N. H. H. A.; Abdullah, N. A. F.; Negim, E.-S. M.; Saad, B. Experimental and molecular docking model studies for the adsorption of polycyclic aromatic hydrocarbons onto UiO-66(Zr) and NH₂-UiO-66(Zr) metal-organic frameworks. *Chem. Eng. Sci.* **2020**, *220*, 115608. <https://doi.org/10.1016/j.ces.2020.115608>
- Zhan, S.; Li, D.; Liang, S.; Chen, X.; Li, X. A novel flexible room temperature ethanol gas sensor based on SnO₂ doped poly-diallyldimethylammonium chloride. *Sensors* **2013**, *13* (4), 4378–4389. <https://doi.org/10.3390/s130404378>
- Zhang, B.; Sun, L. Artificial photosynthesis: Opportunities and challenges of molecular catalysts. *Chem. Soc. Rev.* **2019**, *48* (7), 2216–2264. <https://doi.org/10.1039/C8CS00897C>
- Zhang, Y.; Mao, F.; Wang, L.; Yuan, H.; Liu, P. F.; Yang, H. G. Recent advances in photocatalysis over metal–organic frameworks-based materials. *Sol. RRL* **2020**, *4* (5), 1900438. <https://doi.org/10.1002/solr.201900438>

Influence of Cu-doped TiO₂ on its structural and photocatalytic properties

Vinícius Teodoro¹, Elson Longo¹, Maria Aparecida Zaghete², Leinig Antonio Perazolli²⁺

1. Federal University of Sao Carlos, Center for the Development of Functional Materials, São Carlos, Brazil.
2. São Paulo State University, Institute of Chemistry, Araraquara, Brazil.

+Corresponding author: Leinig Antonio Perazolli, **Phone:** +551633019711, **Email address:** leinig.perazolli@unesp.br

ARTICLE INFO

Article history:

Received: July 26, 2021

Accepted: December 09, 2021

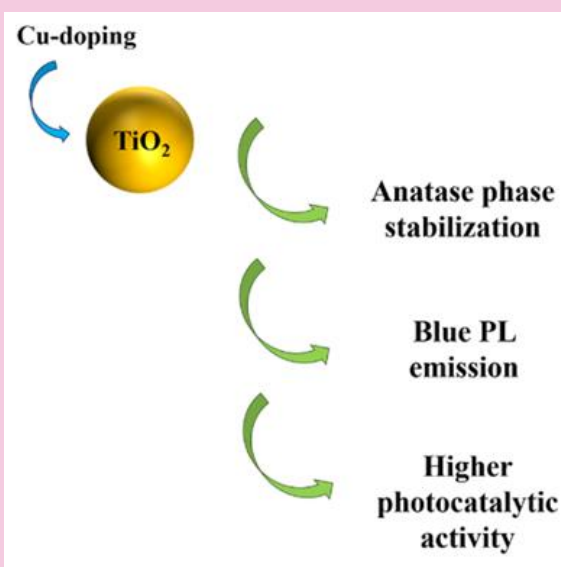
Published: April 11, 2022

Keywords:

1. photocatalysis
2. titanium dioxide
3. doping
4. UV light

Section Editors: Elson Longo and Juan Manuel Andrés Bort

ABSTRACT: Due to the potential of heterogeneous photocatalysis for wastewater treatment, the researches concerning the improvement materials modifications for its photocatalytic activity have been widely increased. One of the most employed methods is the metal doping into semiconductors. Herewith, we demonstrated the influence of Cu doping into TiO₂ in its photocatalytic properties. The powder samples with 0.0 to 0.7% mol were obtained by the Pechini method and characterized by XRD, micro-Raman spectroscopy, FE-SEM, and photoluminescence spectroscopy. The Cu insertion into TiO₂ structure induced the stabilization of anatase phase, increasing its content in the samples in relation to the bare TiO₂. The PL results indicated that a decrease in the PL emission intensity and a shift of the emission band to the blue region. The photocatalytic activity for rhodamine B degradation under UV light irradiation indicated that the Cu-doping into TiO₂ led to an enhancement of the photocatalytic activity compared to the bare one.



1. Introduction

Due to increasing of industrial disposal and domestic effluents on recent years, such as wastewater, it has become necessary an effective treatment alternative to improve the environment quality. Among several methods, heterogeneous photocatalysis has been studied as an alternative to such problem due to its potential degradation of organic compounds, allowing water and air purification (Fujishima *et al.*, 2000; Galindo *et al.*, 2000; Gaya and Abdullah, 2008; Qourzal *et al.*, 2005; Silva *et al.*, 2020). Therefore, the search for materials with high photocatalytic activity and potential to solar applications has been the main target of researches.

The titanium dioxide (TiO₂) is odorless, has high acid resistance and act as a UV absorbent. The most important functions are as a widely used pigment, solar protection and photocatalyst for organic compounds. Titanium dioxide also has been used as a bleaching and opacifying agent in porcelain enamels, giving them brightness, hardness, and acid resistance. TiO₂ is one of the most widely investigated for photocatalytic applications due to its high oxidizing ability for organic pollutants, low cost, photostability, nontoxicity and chemical stability (Dashora *et al.*, 2014; Nakata and Fujishima, 2012; S. Wang *et al.*, 2014). Numerous studies were published on the photocatalytic TiO₂ applications for the decomposition of organic compounds due to the ability of TiO₂ to oxidize organic and inorganic substances in water and air through redox processes (S. Wang *et al.*, 2014), TiO₂ only absorbs ultraviolet (UV) light of broad solar spectrum due to its large bandgap energy ($\lambda < 388$ nm), which was comprised of only 4% of the entire solar spectrum (Dashora *et al.*, 2014; H. Wang *et al.*, 2015).

Furthermore, the high recombination rate of electron/hole pair (e⁻/h⁺) within the semiconductor is the main problem for the photocatalytic performance of the semiconductor, since it disables the photoexcited electron and the hole for redox reactions (Rashad *et al.*, 2014; Li Zhang *et al.*, 2014).

In order to improve the photocatalytic performance of TiO₂, modifications in its structure have been investigated, such as doping with metals ions (Li *et al.*, 2016; Sanchez-Dominguez *et al.*, 2015; Q. Wang *et al.*, 2017; Xiao *et al.*, 2016). The substitution of a Ti⁴⁺ by another transition metal ion promotes changes in the coordination parameters, thus altering the electronic and optical properties, resulting in attractive characteristics for photocatalytic applications (Chen *et al.*, 2018a; Vargas Hernández *et al.*, 2017). Several advantages concerning doping on TiO₂ have been reported, such as increase of specific surface area, light absorption

capacity, and charge transfer rate on particle surface, and band gap energy reduction (Carp *et al.*, 2004; G. Liu *et al.*, 2010). The Cu doping on TiO₂ has shown improvement and desirable results for antibacterial applications (Lan Zhang *et al.*, 2016) and for high-rate capability for lithium-ion batteries (Y. Zhang *et al.*, 2016), possibly making it an attractive dopant metal for photocatalytic applications.

In this work, we report the influence of Cu-doped on TiO₂ powders prepared by the Pechini method and its effects on structural and photocatalytic properties for degradation of rhodamine B dye (RhB) under UV light irradiation. These obtained powders were characterized using XRD, MR spectroscopy, FE-SEM, and PL spectroscopy.

2. Experimental

2.1 Synthesis

All chemical reagents were of analytical grade and used without further treatment. The powders were obtained by the Pechini method, which were used titanium isopropoxide (purity 95%, Alfa Aesar), citric acid (purity 99.5%, Synth) and ethylene glycol (purity 99%, Synth) in a ratio of 1:4:16 moles, respectively. Ethylene glycol was heated to 70 °C and then, titanium isopropoxide was added and stirred for 20 min. Citric acid was added to the mixture and this was stirred for 2 h at 90 °C. The polymeric solution was standardized by gravimetry method in order to define content of TiO₂ generated per gram of solution. For the Cu-doped TiO₂ samples, Cu(NO₃)₂·3H₂O was added to the polymeric solution in stoichiometric contents to obtain 0.3, 0.5 and 0.7 at.% of Cu related to Ti, which the samples were denominated as CTO-0, CTO-0.3, CTO-0.5, and CTO-0.7, respectively. The polymeric solutions were annealed at 380 °C for 4 h to form the root solid, and then 400 °C for 10 h to eliminate organic compounds. All concentrations of Cu-doped and bare TiO₂ samples were annealed 600 °C for 4 h.

2.2 Characterizations

The morphological, structural and optical properties of samples were characterized by field-emission scanning electron microscopy (FE-SEM, JEOL 7500F), X-ray diffraction (XRD, Rigaku-Rotalex Dmax/2500 PC) with Cu K α radiation, micro-Raman spectroscopy (MR, Horiba Jobin Yvon LabRAM iHR550) with a laser wavelength of 514 nm. The optical spectroscopy in UV-Vis on diffuse reflectance mode was performed in a

Perkin Elmer spectrophotometer (Lambda 1050 UV/Vis/NIR). The photoluminescence spectroscopy (PL) was performed at room temperature under air atmosphere using a Monospec 27 monochromator (Thermal Jarrel Ash, USA) coupled to an R955 photomultiplier (Hamamatsu Photonics, Japan). A krypton ion laser (Coherent, Innova 200) with wavelength of 350 nm, with maximum output power maintained at 500 mW and maximum power of 14 mW on the sample due to the passage through an optical chopper. The surface area was measured using Brunauer-Emmett-Teller (BET) methods and Micromeritics ASAP 2010 equipment.

2.3 Photocatalytic experiments

The photocatalytic performance of all samples was carried out in a Philips Ouro reactor, which was fitted with a quartz tube and an inner UV germicide lamp ($\lambda = 254$ nm, 11 W, Osram, Puritec HNS 2G7). The reactor was 9.4 cm of inside diameter and 17.2 cm of height, the quartz tube was 4.1 cm of the inside diameter and 22 cm of height which was sustained by a support. The UV germicide lamp was inside the quartz tube and has dimensions of $1.2 \times 2.6 \times 19$ cm. The experiments were conducted with 700 mL of rhodamine B dye (RhB) solutions (10^{-5} mol L $^{-1}$), 70 mg of catalyst and under constant agitation and pumping air to saturation of O $_2$ dissolved. At certain times, aliquots were withdrawal and centrifuged for absorbance measurements in a Perkin Elmer spectrophotometer (Lambda 1050 UV/Vis/NIR).

3. Results and discussion

Figure 1a shows the XRD patterns of Cu-doped and bare TiO $_2$ samples obtained by the Pechini method. For all samples, the anatase and rutile phases of TiO $_2$ were observed, according to the Inorganic Crystal Structure Database (ICSD) code 9852 and code 9161, respectively. The presence of rutile phase is due to its thermodynamic stability in synthesis temperature from 600 °C (Hu *et al.*, 2003; Zhu *et al.*, 2015). No peaks related to any Cu-related phase were observed, indicating the incorporation of Cu $^{2+}$ into the TiO $_2$ lattice as dopant.

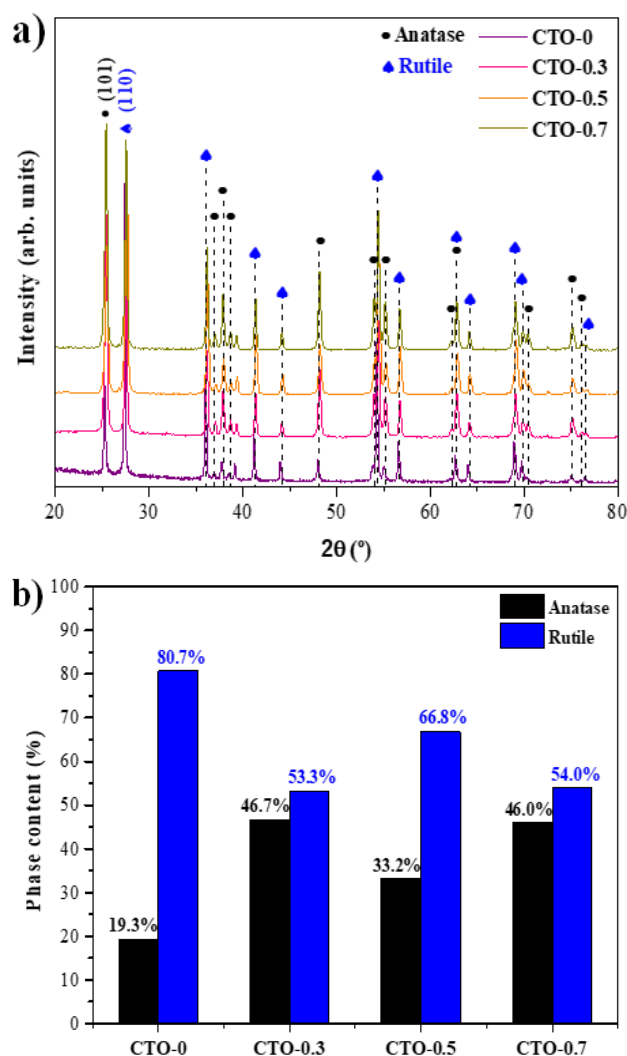


Figure 1. XRD patterns (a) and phase content (b) of CTO-0, CTO-0.3, CTO-0.5, and CTO-0.7 samples.

In order to quantify the proportions of anatase and rutile phases in the prepared samples, the Spurr and Myers (1957) method was employed, according to the Eq. 1, in which, f_a is the anatase percentage in sample, I_R and I_A are the integrated intensity of rutile (110) and anatase (101) peaks.

$$f_a = \frac{1}{\left(1 + 1.265 \frac{I_R}{I_A}\right)} \quad (1)$$

The anatase and rutile crystallite sizes of all prepared samples were calculated according to the Scherrer's Eq. 2 (Alexander and Klug, 1950).

$$D = \frac{k\lambda}{\beta \cos \theta} \quad (2)$$

The k is a constant related to shape factor (about 0.9), λ is the X-ray wavelength of Cu K α radiation

(0.15406 nm), β is the full width at half maximum (FWHM) of the diffraction peak, and θ is the diffraction angle. The values of β and θ used were related to the predominant phase on sample, being the (101) and (110) crystal planes for anatase and rutile phases, respectively. The calculated anatase crystallite sizes were 37.0, 28.8, 23.7, and 27.6 nm for CTO-0, CTO-0.3, CTO-0.5, and CTO-0.7 samples, respectively. For rutile crystallite sizes, the obtained values were 42.3, 35.2, 25.3, and 33.7 nm for CTO-0, CTO-0.3, CTO-0.5, and CTO-0.7 samples, respectively.

It can be observed that the Cu insertion on the TiO₂ lattice promoted an anatase phase stabilization compared to the bare one, as can be seen by the higher weight fractions (Fig. 1b). The anatase to rutile phase transformation in TiO₂ is strongly dependent on the synthesis temperature and also on the intrinsic physicochemical properties and concentration of impurities on lattice (Choi *et al.*, 2010; Shannon and Pask, 1965). As already reported, Cu²⁺ ions are most probably located in interstitial positions into TiO₂ lattice on anatase phase and primarily on grain surface due to its relatively large difference in ionic radius related to Ti⁴⁺ ions, *i.e.*, 73 and 60.5 pm for Cu²⁺ and Ti⁴⁺ in octahedral sites. Besides that, the lower density and higher volume of unit cell of anatase compared to rutile phase also contribute for the Cu²⁺ interstitial occupation (Choi *et al.*, 2010; Gupta and Tripathi, 2011). The interstitial Cu²⁺ into TiO₂ lattice generates Ti–O–Cu bonds that led to an increase in strain energy necessary to anatase to rutile phase transformation, resulting in an inhibition of the grain growth (Choi *et al.*, 2010; Hanaor and Sorrell, 2011; Qi *et al.*, 2011; Shannon and Pask, 1965), as can be observed in the reduction of average crystallite size of anatase with increasing doping concentration. This strain energy needs to be overcome to the rearrangement of [TiO₆] clusters, which have different spatial organizations in both phases. Once Cu²⁺ ions are located at interstitial positions, the energy required for rearrangement has increased due to its interactions with [TiO₆] clusters.

Figure 2a shows the micro-Raman spectra for the Cu-doped and bare TiO₂ samples. Both anatase and rutile phase of TiO₂ exhibits characteristics Raman shift bands, being six vibrational modes Raman active for anatase and four for rutile phase. The characteristics Raman bands of anatase phase are approximately located at 144 cm⁻¹ (E_g), 197 cm⁻¹ (E_g), 399 cm⁻¹ (B_{1g}), 513–519 cm⁻¹ (overlap in Raman shifts values by two vibrational modes with symmetries A_{1g} e B_{1g}), and 639 cm⁻¹ (E_g). For rutile phase, the Raman shifts bands are located at approximately 143 cm⁻¹ (B_{1g}), 447 cm⁻¹ (E_g), 612 cm⁻¹ (A_{1g}), and 826 cm⁻¹ (B_{2g}) (Naumenko *et al.*,

2012; Ohsaka *et al.*, 1978; Ricci *et al.*, 2013; Sahoo *et al.*, 2009). Another band nearly 238 cm⁻¹ for rutile phase is characteristic of a second order scattering due to coupling of two optical phonons (Ohsaka *et al.*, 1978; Ricci *et al.*, 2013; Swamy and Muddle, 2006).

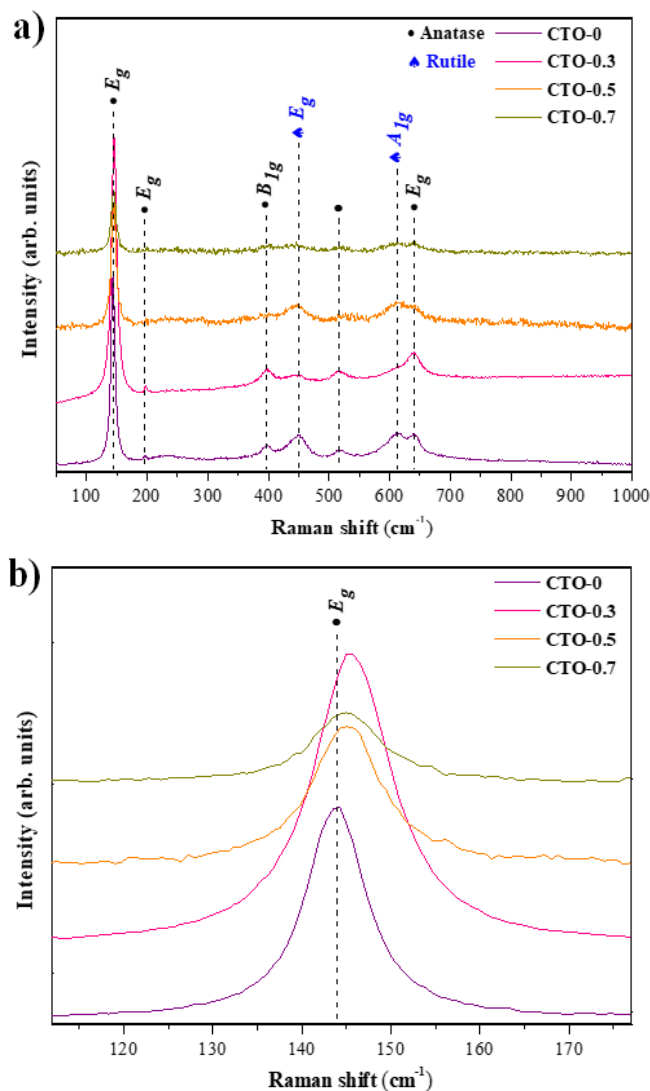


Figure 2. Raman spectra (a) and E_g Raman bands (b) of CTO-0, CTO-0.3, CTO-0.5, and CTO-0.7 samples.

It can be observed that the increase in Cu concentrations into TiO₂ induced a decrease in the intensities of Raman bands compared to the bare one. The structural Ti–O–Cu linkage formed by the interstitial Cu results in a hindrance of the [TiO₆] clusters, reducing its freedom degree for the vibrational modes, hence decreasing the intensity of the Raman bands. Figure 1b shows the E_g Raman band position for the anatase phase for all prepared samples. It can be seen that the insertion of Cu into TiO₂ lattice induced a shift to higher frequencies, thus corroborating with the

presence of Ti–O–Cu linkage that results in an increase in the strain energy.

Figure 2 shows the FE-SEM images of the Cu-doped and bare TiO₂ samples. It can be observed that all samples are composed of agglomerates of nanoparticles, which is characteristic of the Pechini method (Chen *et al.*, 2018b; Neris *et al.*, 2018). Furthermore, the agglomeration of these nanoparticles also arises from the annealing procedure, thus inducing their coalescence.

Photoluminescence spectroscopy emission measurements were performed to understand the effect of Cu insertion into TiO₂ structure in its optical behavior. Figure 3a shows the PL spectra of bare and Cu-doped TiO₂ samples. As can be seen, all spectra indicated the presence of two major emission bands, one located at 400–700 nm and the other centered at approximately 800 nm. The first one is characteristic of anatase phase emission and the second is characteristic of rutile phase emission, corroborating the XRD and Raman results (Jin *et al.*, 2015; Nasr *et al.*, 2015). The PL spectra for all prepared samples indicate a broadband profile, which is assigned to multiphonon processes. These processes arise from the presence of a high density of energy levels within the band gap, in which the electron momentum relaxation and hence photon emission occur in several pathways (Cruz *et al.*, 2020; Tello *et al.*, 2020). It can be seen that all Cu-doped samples presented a lower emission intensity compared to the bare one. This indicates a higher density of intermediate energy levels within the band gap for Cu-doped samples, which results in a lower recombination rate of the electron-hole pairs.

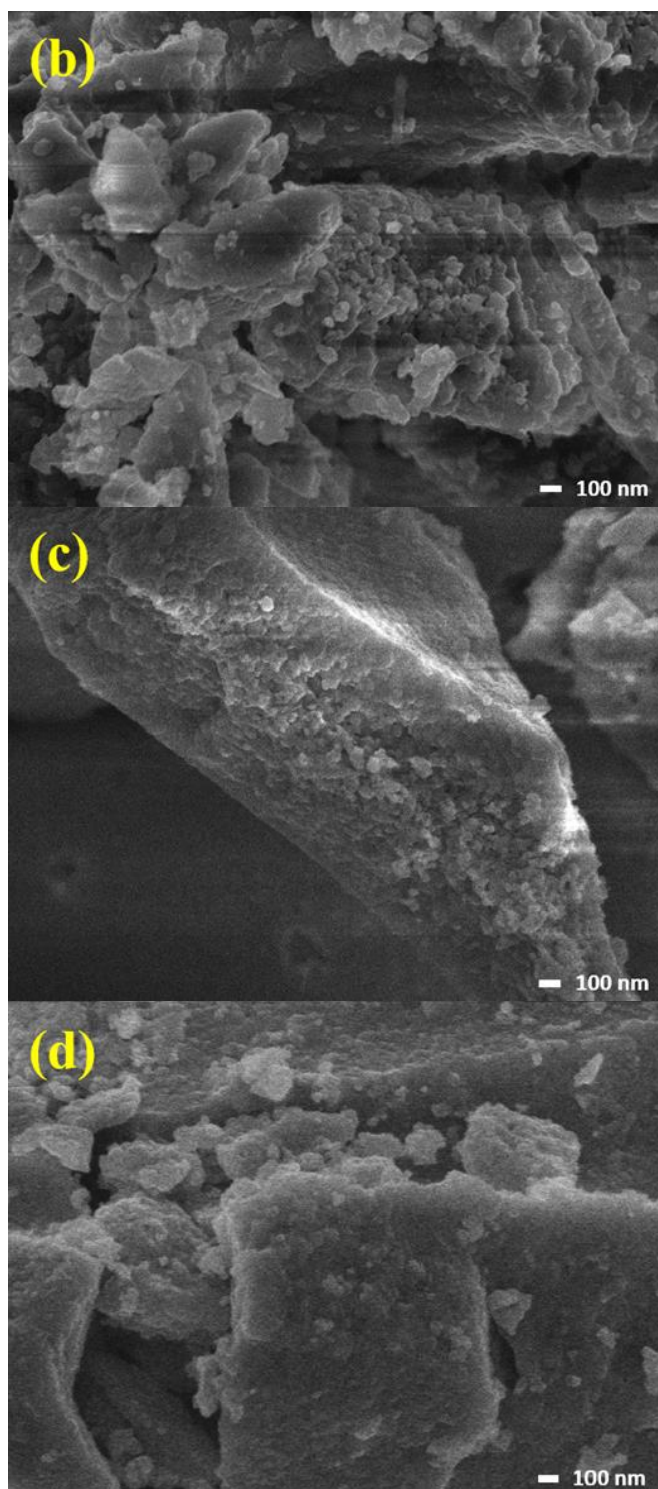
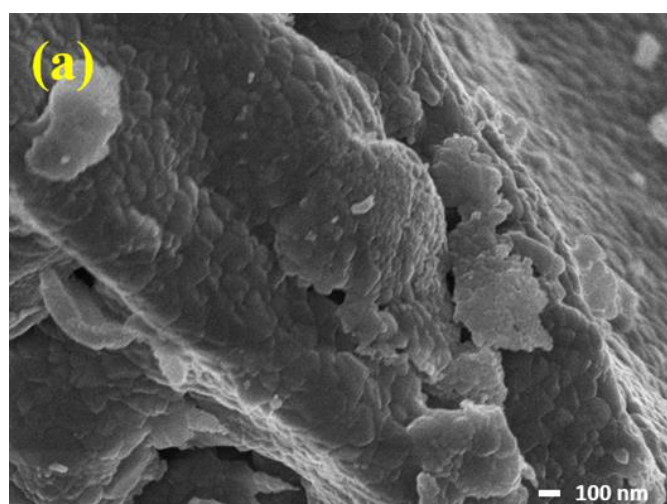


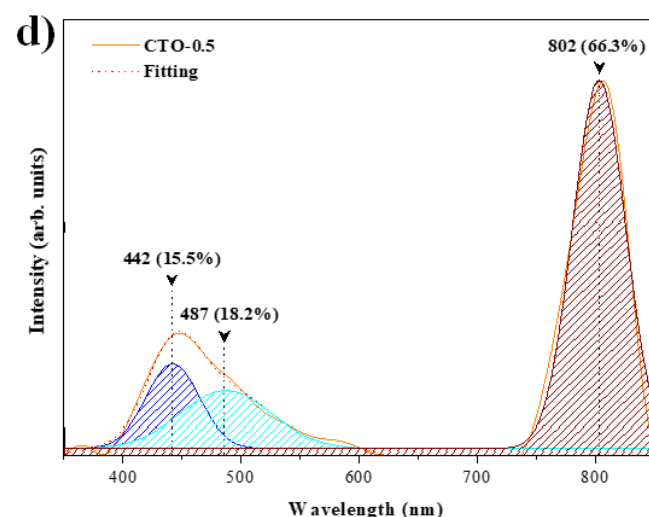
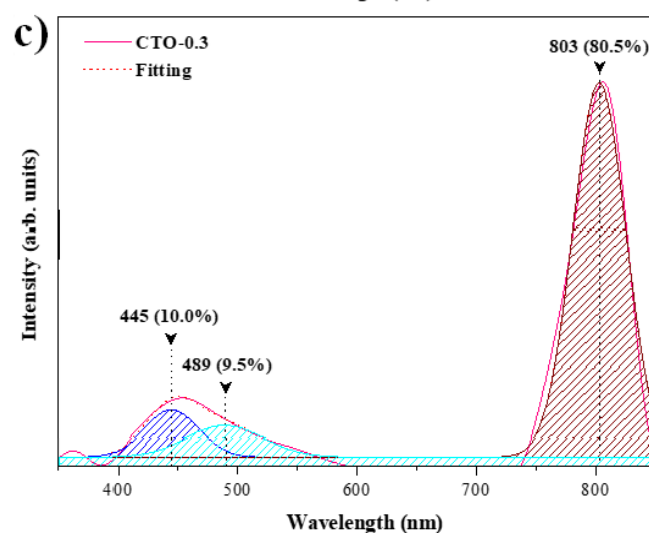
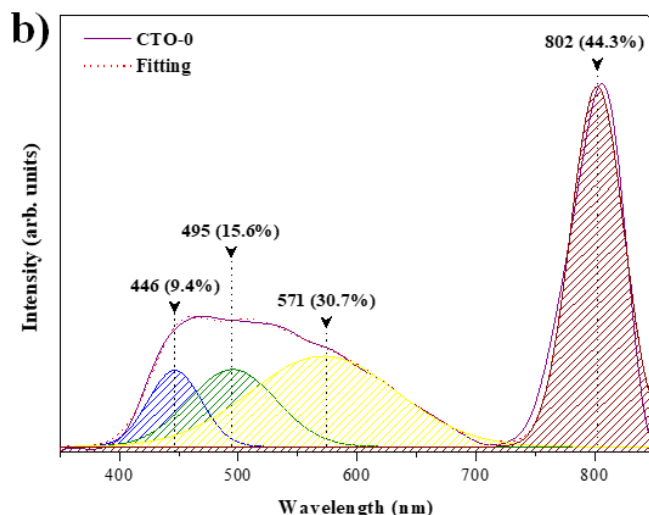
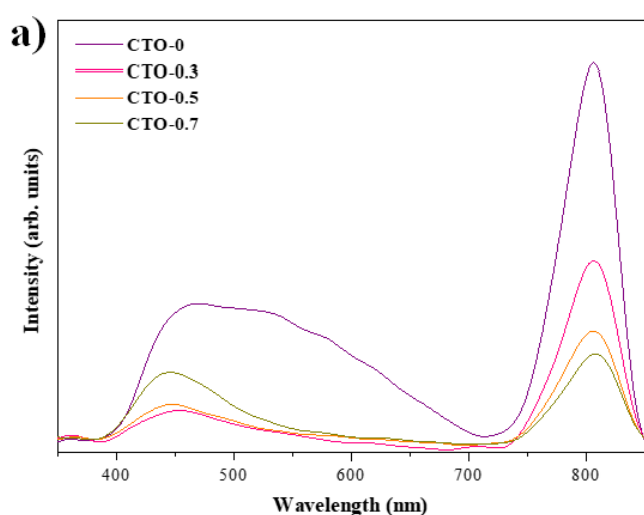
Figure 3. FE-SEM images of CTO-0 (a), CTO-0.3 (b), CTO-0.5 (c), and CTO-0.7 (d) samples.

In order to investigate the contribution of defects for PL emissions in bare and Cu-doped TiO₂ samples, deconvolution of emission bands was performed using the PeakFit v.4 software. It is known that emissions in different color regions are due to different type of defects in the structure that contribute to the electronic

transitions. The blue emissions have been associated with the structural distortions in the composing clusters of the lattice, whereas the green and yellow emissions have been associated with the oxygen vacancies (Longo *et al.*, 2008; Silva Junior *et al.*, 2015). As can be seen, the insertion of Cu into the TiO₂ lattice promoted a shift of the band emission for the blue region, as observed by the maximum emission wavelength and its percentage contribution in the Fig. 3b–e.

For clearer evidence, the contribution percentages of blue emission in function of the Cu-doping content are shown in Fig. 4f. It can be seen that the blue emission percentage directly increases with increasing Cu-doping content. Once the Cu²⁺ ions are occupying interstitial positions in the anatase phase of TiO₂, resulting in a Ti–O–Cu linkage, it is expected higher structural distortions in the [TiO₆] clusters compared to the bare one due to the atomic rearrangement. These structural distortions were confirmed by a higher contribution percentage of blue emission and corroborate the XRD and Raman results. Furthermore, the structural distortions in the [TiO₆] clusters caused by the Cu insertion into the TiO₂ lattice generate intermediate energy levels within the band gap, which decrease the recombination rate of electron-hole pairs and hence the PL emission intensity, as observed in Fig. 4a.

The photocatalytic activity of bare and Cu-doped TiO₂ samples was tested for RhB dye degradation under UV light irradiation. Figure 5a shows the RhB degradation percentage against the irradiation time for all prepared samples and the controlling test (photolysis).



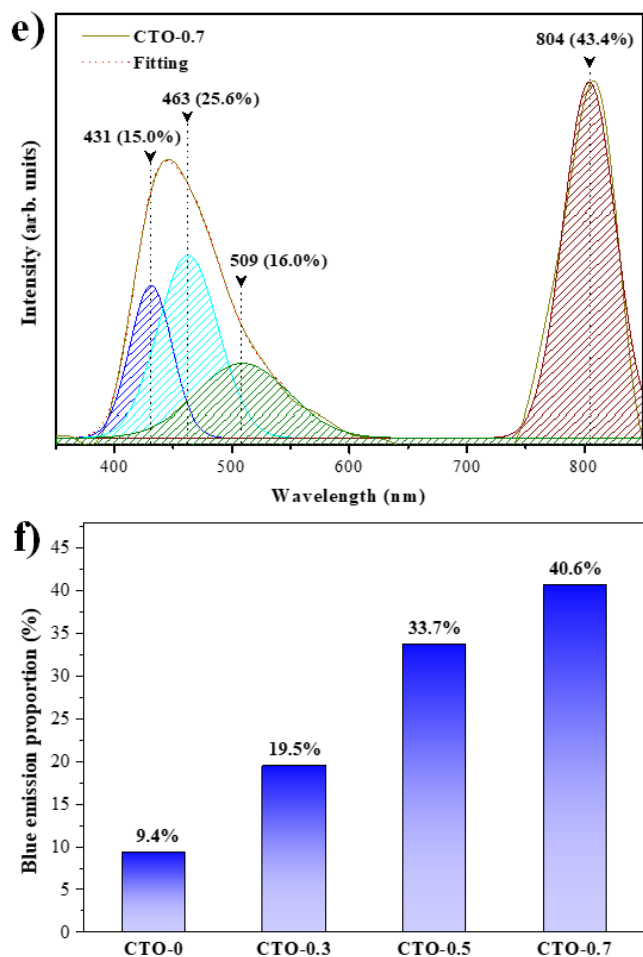


Figure 4. Photoluminescence spectroscopy spectra of all prepared samples (a), deconvolution of emission band of CTO-0 (b), CTO-0.3 (c), CTO-0.5 (d), and CTO-0.7 (e) samples, and blue emission percentage of all prepared samples (f).

It was observed that all Cu-doped samples present a higher photocatalytic activity compared to the bare one. Further, the increase in the Cu-doping content led to an increase in the RhB degradation percentage in 90 min of reaction. However, the CTO-0.5 and CTO-0.7 samples presented similar photocatalytic activity, indicating a saturation of the Cu-content for the improvement of photocatalytic activity of the TiO_2 . According to the Langmuir-Hinshelwood plot (Fig. 4b), the photocatalytic activity of all prepared samples presents a pseudo-first order kinetics (B. Liu *et al.*, 2014). The rate constants for those samples are depicted inset the Fig. 4b.

As previously mentioned, the Cu insertion into the TiO_2 lattice leads to the structural distortions in the $[\text{TiO}_6]$ clusters, which generate a higher density of intermediate energy levels within the band gap. These

energy levels act as traps for the electronic transitions, thus decreasing the recombination rate of electron-hole pairs, as observed by PL analysis. Herewith, the decrease in the recombination rate leads to an increase in the lifetime of electron-hole pairs. Once these pairs have a higher lifetime, their availability to perform the redox reactions with the reaction medium are also increased. Therefore, the Cu insertion into the TiO_2 lattice caused structural distortions in the $[\text{TiO}_6]$ clusters that act as trap for electronic transitions, thus increasing the availability of electrons to promote the reduction reactions and holes to promote the oxidation reactions. These redox reactions rule the RhB degradation mechanism either by the generation of radical species that can degrade the RhB molecules as also by the direct degradation of RhB molecules adsorbed on the TiO_2 particle surface.

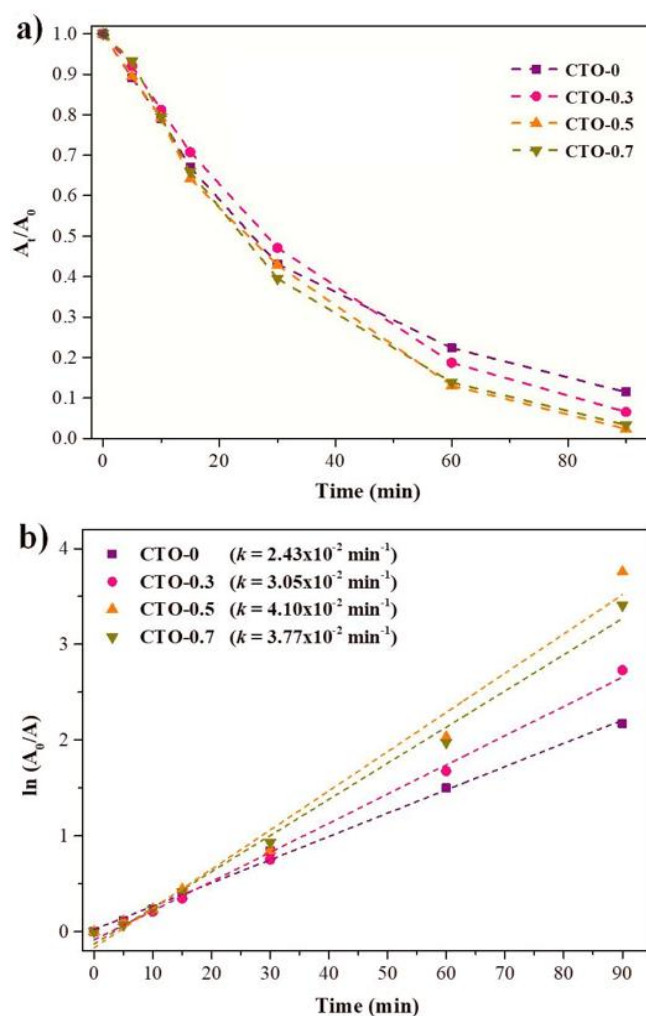


Figure 5. Relative absorbance of RhB dye solution against photocatalytic reaction time (a) and pseudo first-order kinetics plot (b) for CTO-0, CTO-0.3, CTO-0.5, and CTO-0.7 samples.

The prepared CTO-0 sample has a composition very close to Degussa P25 (85% wt rutile and 15% wt anatase), one of the world's most used photocatalysts, but the photocatalytic active of this and of the all the CTOs obtained are small from the P25 activity. This was attributed to surface area difference since the P25 surface are 83 m² g⁻¹ and the obtained is a maximum of 15 m² g⁻¹) for CTO 0.5.

4. Conclusions

The Cu-doping into TiO₂ as powders samples were successfully obtained by the Pechini method. The insertion on Cu²⁺ into the TiO₂ structure promoted the anatase phase stabilization, increasing its content on the samples in relation to the pure TiO₂. This stabilization has been assigned to the interstitial occupation of Cu²⁺ in the anatase phase of TiO₂, thus increasing the strain energy required to the structural rearrangement for the transformation in rutile phase. The shift to higher vibrational frequencies in Raman analysis corroborated the occupation of Cu²⁺ in interstitial positions into TiO₂ structure. PL results indicated that the Cu-doping in TiO₂ induced structural distortions in [TiO₆] clusters, which resulted in shift of PL emission band to blue region and a decrease in the PL emission intensity. The photocatalytic performance of TiO₂ samples under UV light irradiation were enhanced by the Cu-doping, which has been related to the formation of intermediate energy levels within band gap. These levels can act as electron trap, thus decreasing the recombination rate of electron-hole pairs and hence increasing their availability to perform the redox reactions with the reaction medium. Therefore, the Cu-doping into TiO₂ allowed structural and photocatalytic advantages in relation to the pure sample.

Authors' contribution

Conceptualization: Teodoro, V.; Perazolli, L. A.

Data curation: Teodoro, V.

Formal analysis: Teodoro, V.

Funding acquisition: Longo, E.; Zaghete, M. A.; Perazolli, L. A.

Investigation: Teodoro, V. Perazolli, L. A.

Methodology: Teodoro, V.

Project administration: Perazolli, L. A.

Resources: Longo, E.; Zaghete, M. A.; Perazolli, L. A.

Software: Not applicable.

Supervision: Longo, E.; Zaghete, M. A.; Perazolli, L. A.

Validation: Teodoro, V.

Visualization: Teodoro, V.; Longo, E.; Zaghete, M. A.; Perazolli, L. A.

Writing – original draft: Teodoro, V.

Writing – review & editing: Teodoro, V.; Longo, E.; Perazolli, L. A.

Data availability statement

All data sets were generated or analyzed in the current study.

Funding

Fundação de Amparo à Pesquisa do Estado de São Paulo (FAPESP). Grant No: 2013/07296-2.

Conselho Nacional de Desenvolvimento Científico e Tecnológico (CNPq). Grant No: 142035/2017-3.

Coordenação de Aperfeiçoamento de Pessoal de Nível Superior (CAPES). Finance Code: 001.

Acknowledgments

Not applicable.

References

- Alexander, L.; Klug, H. P. Determination of crystallite size with the x-ray spectrometer. *J. Appl. Phys.* **1950**, *21* (2), 137–142. <https://doi.org/10.1063/1.1699612>
- Carp, O.; Huisman, C. L.; Reller, A. Photoinduced reactivity of titanium dioxide. *Prog. Solid State Chem.* **2004**, *32* (1–2), 33–177. <https://doi.org/10.1016/j.progsolidstchem.2004.08.001>
- Chen, W. F.; Chen, H.; Koshy, P.; Nakaruk, A.; Sorrell, C. C. Effect of doping on the properties and photocatalytic performance of titania thin films on glass substrates: Single-ion doping with Cobalt or Molybdenum. *Mater. Chem. Phys.* **2018a**, *205*, 334–346. <https://doi.org/10.1016/j.matchemphys.2017.11.021>
- Chen, W. F.; Mofarah, S. S.; Hanaor, D. A. H.; Koshy, P.; Chen, H.-K.; Yue, J.; Sorrell, C. C. Enhancement of Ce/Cr codopant solubility and chemical homogeneity in TiO₂ nanoparticles through sol-gel versus Pechini syntheses. *Inorg. Chem.* **2018b**, *57* (12), 7279–7289. <https://doi.org/10.1021/acs.inorgchem.8b00926>

- Choi, J.; Park, H.; Hoffmann, M. R. Effects of single metal-ion doping on the visible-light photoreactivity of TiO₂. *J. Phys. Chem. C*. **2010**, *114* (2), 783–792. <https://doi.org/10.1021/jp908088x>
- Cruz, L.; Teixeira, M. M.; Teodoro, V.; Jacomaci, N.; Laier, L. O.; Assis, M.; Macedo, N. G.; Tello, A. C. M.; Silva, L. F.; Marques, G. E.; Zaghete, M. A.; Teodoro, M. D.; Longo, E. Multi-dimensional architecture of Ag/α-Ag₂WO₄ crystals: Insights into microstructural, morphological, and photoluminescence properties. *CrystEngComm*. **2020**, *22* (45), 7903–7917. <https://doi.org/10.1039/D0CE00876A>
- Dashora, A.; Patel, N.; Kothari, D. C.; Ahuja, B. L.; Miotello, A. Formation of an intermediate band in the energy gap of TiO₂ by Cu – N-codoping: First principles study and experimental evidence. *Sol. Energy Mater. Sol. Cells*. **2014**, *125*, 120–126. <https://doi.org/10.1016/j.solmat.2014.02.032>
- Fujishima, A.; Rao, T. N.; Tryk, D. A. Titanium dioxide photocatalysis. *J. Photochem. Photobiol. C Photochem. Rev.* **2000**, *1* (1), 1–21. [https://doi.org/10.1016/S1389-5567\(00\)00002-2](https://doi.org/10.1016/S1389-5567(00)00002-2)
- Galindo, C.; Jacques, P.; Kalt A. Photodegradation of the aminoazobenzene acid orange 52 by three advanced oxidation processes: UV/H₂O₂, UV/TiO₂ and VIS/TiO₂: Comparative mechanistic and kinetic investigations. *J. Photochem. Photobiol. A Chem.* **2000**, *130* (1), 35–47. [https://doi.org/10.1016/S1010-6030\(99\)00199-9](https://doi.org/10.1016/S1010-6030(99)00199-9)
- Gaya, U. I.; Abdullah, A. H. Heterogeneous photocatalytic degradation of organic contaminants over titanium dioxide: A review of fundamentals, progress and problems. *J. Photochem. Photobiol. C Photochem. Rev.* **2008**, *9* (1), 1–12. <https://doi.org/10.1016/j.jphotochemrev.2007.12.003>
- Gupta, S. M.; Tripathi, M. A review of TiO₂ nanoparticles. *Chin. Sci. Bull.* **2011**, *56*, 1639. <https://doi.org/10.1007/s11434-011-4476-1>
- Hanaor, D. A. H.; Sorrell, C. C. Review of the anatase to rutile phase transformation. *J. Mater. Sci.* **2011**, *46*, 855–874. <https://doi.org/10.1007/s10853-010-5113-0>
- Hu, Y.; Tsai, H.-L.; Huang, C.-L. Phase transformation of precipitated TiO₂ nanoparticles. *Mater. Sci. Eng. A* **2003**, *344* (1–2), 209–214. [https://doi.org/10.1016/S0921-5093\(02\)00408-2](https://doi.org/10.1016/S0921-5093(02)00408-2)
- Jin, C.; Liu, B.; Lei, Z.; Sun, J. Structure and photoluminescence of the TiO₂ films grown by atomic layer deposition using tetrakis-dimethylamino titanium and ozone. *Nanoscale Res. Lett.* **2015**, *10*, 95–103. <https://doi.org/10.1186/s11671-015-0790-x>
- Li, J.; Xu, X.; Liu, X.; Yu, C.; Yan, D.; Sun, Z.; Pan, L. Sn doped TiO₂ nanotube with oxygen vacancy for highly efficient visible light photocatalysis. *J. Alloys Compd.* **2016**, *679*, 454–462. <https://doi.org/10.1016/j.jallcom.2016.04.080>
- Liu, B.; Zhao, X.; Terashima, C.; Fujishima, A.; Nakata, K. Thermodynamic and kinetic analysis of heterogeneous photocatalysis for semiconductor systems. *Phys. Chem. Chem. Phys.* **2014**, *16* (19), 8751–8760. <https://doi.org/10.1039/c3cp55317e>
- Liu, G.; Wang, L.; Yang, H. G.; Cheng, H. M.; Lu, G. Q. Titania-based photocatalysts—crystal growth, doping and heterostructuring. *J. Mater. Chem.* **2010**, *20* (5), 831–843. <https://doi.org/10.1039/B909930A>
- Longo, V. M.; Figueiredo, A. T.; Lázaro S.; Gurgel, M. F.; Costa, M. G. S.; Paiva-Santos, C. O.; Varela, J. A.; Longo, E.; Masteralo, V. R.; De Vicente, F. S.; Hernandez, A. C.; Franco, R. W. A. Structural conditions that leads to photoluminescence emission in SrTiO₃: An experimental and theoretical approach. *J. Appl. Phys.* **2008**, *104* (2), 023515. <https://doi.org/10.1063/1.2956741>
- Nakata, K.; Fujishima, A. TiO₂ photocatalysis: Design and applications. *J. Photochem. Photobiol. C Photochem. Rev.* **2012**, *13* (3), 169–189. <https://doi.org/10.1016/j.jphotochemrev.2012.06.001>
- Nasr, M.; Chaaya, A. A.; Abboud, N.; Bachelany, M.; Viter, R.; Eid, C.; Khoury, A.; Miele, P. Photoluminescence: A very sensitive tool to detect the presence of anatase in rutile phase electrospun TiO₂ nanofibers. *Superlattices Microstruct.* **2015**, *77*, 18–24. <https://doi.org/10.1016/j.spmi.2014.10.034>
- Naumenko, A.; Gnatiuk, I.; Smirnova, N.; Eremenko, A. Characterization of sol-gel derived TiO₂/ZrO₂ films and powders by Raman spectroscopy. *Thin Solid Films.* **2012**, *520* (14), 4541–4546. <https://doi.org/10.1016/j.tsf.2011.10.189>
- Neris, A. M.; Schreiner, W. H.; Salvador, C.; Silva, U. C.; Chesman, C.; Longo, E.; Santos, I. M. G. Photocatalytic evaluation of the magnetic core@shell system (Co,Mn)Fe₂O₄@TiO₂ obtained by the modified

- Pechini method. *Mater. Sci. Eng. B*. **2018**, *229*, 218–226. <https://doi.org/10.1016/j.mseb.2017.12.029>
- Ohsaka, T.; Izumi, F.; Fujiki, Y. Raman spectrum of anatase, TiO₂. *J. Raman Spectrosc.* **1978**, *7* (6), 321–324.
- Qi, F.; Moiseev, A.; Deubener, J.; Weber, A. Thermostable photocatalytically active TiO₂ anatase nanoparticles. *J. Nanoparticle Res.* **2011**, *13*, 1325–1334. <https://doi.org/10.1007/s11051-010-0211-0>
- Qourzal, S.; Tamimi, M.; Assabbane, A.; Ait-Ichou, Y. Photocatalytic degradation and adsorption of 2-naphthol on suspended TiO₂ surface in a dynamic reactor. *J. Colloid Interface Sci.* **2005**, *286* (2), 621–626. <https://doi.org/10.1016/j.jcis.2005.01.046>
- Rashad, M. M.; Ismail, A. A.; Osama, I.; Ibrahim, I. A.; Kandil, A.-H. T. Photocatalytic decomposition of dyes using ZnO doped SnO₂ nanoparticles prepared by solvothermal method. *Arab. J. Chem.* **2014**, *7* (1), 71–77. <https://doi.org/10.1016/j.arabjc.2013.08.016>
- Ricci, P. C.; Carbonaro, C. M.; Stagi, L.; Salis, M.; Casu, A.; Enzo, S.; Delogu, F. Anatase-to-rutile phase transition in TiO₂ nanoparticles irradiated by visible light. *J. Phys. Chem. C* **2013**, *117* (15), 7850–7857. <https://doi.org/10.1021/jp312325h>
- Sahoo, S.; Arora, A. K.; Sridharan, V. Raman line shapes of optical phonons of different symmetries in anatase TiO₂ nanocrystals. *J. Phys. Chem. C* **2009**, *113* (39), 16927–16933. <https://doi.org/10.1021/jp9046193>
- Sanchez-Dominguez, M.; Morales-Mendoza, G.; Rodriguez-Vargas, M. J.; Ibarra-Malo, C. C.; Rodriguez-Ridriguez, A. A.; Vela-Gonzalez, A. V.; Perez-Garcia, S. A.; Gomez, R. Synthesis of Zn-doped TiO₂ nanoparticles by the novel oil-in-water (O/W) microemulsion method and their use for the photocatalytic degradation of phenol. *J. Environ. Chem. Eng.* **2015**, *3* (4) (Part B), 3037–3047. <https://doi.org/10.1016/j.jece.2015.03.010>
- Shannon, R. D.; Pask, J. A. Kinetics of the anatase-rutile transformation. *J. Am. Ceram. Soc.* **1965**, *48* (8), 391–398. <https://doi.org/10.1111/j.1151-2916.1965.tb14774.x>
- Silva Junior, E.; La Porta, F. A.; Liu, M. S.; Andrés, J.; Varela, J. A.; Longo, E. A relationship between structural and electronic order–disorder effects and optical properties in crystalline TiO₂ nanomaterials. *Dalt. Trans.* **2015**, *44* (7), 3159–3175. <https://doi.org/10.1039/C4DT03254C>
- Silva, J. S.; Machado, T. R.; Trench, A. B.; Silva, A. D.; Teodoro, V.; Vieira, P. C.; Martins, T. A.; Longo, E. Enhanced photocatalytic and antifungal activity of hydroxyapatite/ α -AgVO₃ composites. *Mater. Chem. Phys.* **2020**, *252*, 123294. <https://doi.org/10.1016/j.matchemphys.2020.123294>
- Spurr, R. A.; Myers, H. Quantitative analysis of anatase-rutile mixtures with an x-ray diffractometer. *Anal. Chem.* **1957**, *29* (5), 760–762. <https://doi.org/10.1021/ac60125a006>
- Swamy, V.; Muddle, B. C. Size-dependent modifications of the Raman spectrum of rutile TiO₂. *Appl. Phys. Lett.* **2006**, *89*, 163118. <https://doi.org/10.1063/1.2364123>
- Tello, A. C. M.; Assis, M.; Menasce, R.; Gouveia, A. F.; Teodoro, V.; Jacomaci, N.; Zaghete, M. A.; Andrés, J.; Marques, G. E.; Teodoro, M. D.; Silva, A. B. F.; Bettini, J.; Longo, E. Microwave-driven hexagonal-to-monoclinic transition in BiPO₄: An in-depth experimental investigation and first-principles study. *Inorg Chem.* **2020**, *59* (11), 7453–7468. <https://doi.org/10.1021/acs.inorgchem.0c00181>
- Vargas Hernández, J.; Coste, S.; García Murillo, A.; Carrillo Romo, F.; Kassiba, A. Effects of metal doping (Cu, Ag, Eu) on the electronic and optical behavior of nanostructured TiO₂. *J. Alloys Compd.* **2017**, *710*, 355–363. <https://doi.org/10.1016/j.jallcom.2017.03.275>
- Wang, H.; Li, Y.; Ba, X.; Huang, L.; Yu, Y. TiO₂ thin films with rutile phase prepared by DC magnetron co-sputtering at room temperature: Effect of Cu incorporation. *Appl. Surf. Sci.* **2015**, *345*, 49–56. <https://doi.org/10.1016/j.apsusc.2015.03.106>
- Wang, Q.; Jin, R.; Zhang, M.; Gao, S. Solvothermal preparation of Fe-doped TiO₂ nanotube arrays for enhancement in visible light induced photoelectrochemical performance. *J. Alloys Compd.* **2017**, *690*, 139–144. <https://doi.org/10.1016/j.jallcom.2016.07.281>
- Wang, S.; Meng, K. K.; Zhao, L.; Jiang, Q.; Lian, J. S. Superhydrophilic Cu-doped TiO₂ thin film for solar-driven photocatalysis. *Ceram. Int.* **2014**, *40* (4), 5107–5110. <https://doi.org/10.1016/j.ceramint.2013.09.028>

Xiao, J.; Xie, Y.; Cao, H.; Nawaz, F.; Zhang, S.; Wang, Y. Disparate roles of doped metal ions in promoting surface oxidation of TiO₂ photocatalysis. *J. Photochem. Photobiol. A Chem.* **2016**, *315*, 59–66. <https://doi.org/10.1016/j.jphotochem.2015.09.013>

Zhang, L.; Guo, J.; Huang, X.; Zhang, Y.; Han, Y. The dual function of Cu-doped TiO₂ coatings on titanium for application in percutaneous implants. *J. Mater. Chem. B* **2016**, *4* (21), 3788–3800. <https://doi.org/10.1039/C6TB00563B>

Zhang, L.; Li, Y.; Zhang, Q.; Wang, H. Well-dispersed Pt nanocrystals on the heterostructured TiO₂/SnO₂ nanofibers and the enhanced photocatalytic properties. *Appl. Surf. Sci.* **2014**, *319*, 21–28. <https://doi.org/10.1016/j.apsusc.2014.07.199>

Zhang, Y.; Meng, Y.; Zhu, K.; Qiu, H.; Ju, Y.; Gao, Y.; Du, F.; Zou, B.; Chen, G.; Wei, Y. Copper-doped titanium dioxide bronze nanowires with superior high rate capability for lithium ion batteries. *Appl. Mater. Interfaces* **2016**, *8* (12), 7957–7965. <https://doi.org/10.1021/acsami.5b10766>

Zhu, S.-C.; Xie, S.-H.; Liu, Z.-P. Nature of rutile nuclei in anatase-to-rutile phase transition. *J. Am. Chem. Soc.* **2015**, *137* (35), 11532–11539. <https://doi.org/10.1021/jacs.5b07734>